

Award Number: W81XWH-19-1-0086

TITLE: Targeting Mitochondrial Metabolism as a Key Vulnerability in Artemisinin-Resistant Plasmodium falciparum Malaria

PRINCIPAL INVESTIGATOR: David A. FIDOCK

CONTRACTING ORGANIZATION: COLUMBIA UNIVERSITY IRVING MEDICAL CENTER

REPORT DATE: March 2021

TYPE OF REPORT: Annual

PREPARED FOR: U.S. Army Medical Research and Materiel Command
Fort Detrick, Maryland 21702-5012

DISTRIBUTION STATEMENT: Approved for Public Release;
Distribution Unlimited

The views, opinions and/or findings contained in this report are those of the author(s) and should not be construed as an official Department of the Army position, policy or decision unless so designated by other documentation.

REPORT DOCUMENTATION PAGE			<i>Form Approved</i> OMB No. 0704-0188		
Public reporting burden for this collection of information is estimated to average 1 hour per response, including the time for reviewing instructions, searching existing data sources, gathering and maintaining the data needed, and completing and reviewing this collection of information. Send comments regarding this burden estimate or any other aspect of this collection of information, including suggestions for reducing this burden to Department of Defense, Washington Headquarters Services, Directorate for Information Operations and Reports (0704-0188), 1215 Jefferson Davis Highway, Suite 1204, Arlington, VA 22202-4302. Respondents should be aware that notwithstanding any other provision of law, no person shall be subject to any penalty for failing to comply with a collection of information if it does not display a currently valid OMB control number. PLEASE DO NOT RETURN YOUR FORM TO THE ABOVE ADDRESS.					
1. REPORT DATE March 2021		2. REPORT TYPE Annual		3. DATES COVERED 03/01/2020 – 02/28/2021	
4. TITLE AND SUBTITLE Targeting Mitochondrial Metabolism as a Key Vulnerability in Artemisinin-Resistant Plasmodium falciparum Malaria			5a. CONTRACT NUMBER W81XWH-19-1-0086		
			5b. GRANT NUMBER PR182303		
			5c. PROGRAM ELEMENT NUMBER		
6. AUTHOR(S) David A. FIDOCK E-Mail: df2260@cumc.columbia.edu			5d. PROJECT NUMBER		
			5e. TASK NUMBER		
			5f. WORK UNIT NUMBER		
7. PERFORMING ORGANIZATION NAME(S) AND ADDRESS(ES) Trustees of Columbia University in the City of New York 630 W 168th St., FL 4, New York NY 10032-3725			8. PERFORMING ORGANIZATION REPORT NUMBER		
9. SPONSORING / MONITORING AGENCY NAME(S) AND ADDRESS(ES) U.S. Army Medical Research and Materiel Command Fort Detrick, Maryland, 21702-5012			10. SPONSOR/MONITOR'S ACRONYM(S)		
			11. SPONSOR/MONITOR'S REPORT NUMBER(S)		
12. DISTRIBUTION / AVAILABILITY STATEMENT Approved for Public Release; Distribution Unlimited					
13. SUPPLEMENTARY NOTES					
14. ABSTRACT Malaria is one of the highest infectious disease priorities for the US Military and the Military Infectious Disease Research Program (MIDRP). Ensuring the future protection of US Military personnel from malaria caused by <i>Plasmodium falciparum</i> requires the development of new therapeutic strategies based on understanding existing mechanisms of antimalarial drug resistance and identifying chemical agents that can effectively eliminate these drug-resistant infections. In recent years, artemisinin (ART) resistance has been shown to result from mutations in the <i>P. falciparum</i> gene K13, which allow circulating young "ring-stage" parasites to survive ART action. Our findings have revealed that these K13 mutations alter multiple features of parasite mitochondria, which is the cellular engine that drives energy production, redox regulation, and synthesis of DNA precursors and heme. Using K13 mutant and "wild-type" parasites, we will implement biochemical assays to determine whether energy production, redox regulation, the respiratory process, and heme synthesis are essential to resistance. We will also search for vulnerabilities in the ART resistance mechanism that we can chemically exploit for future treatments. This work directly supports the mission of the Department of Defense to protect its personnel from drug-resistant malaria.					
15. SUBJECT TERMS Malaria, <i>Plasmodium falciparum</i> , artemisinin, mitochondria, drug resistance, new treatments					
16. SECURITY CLASSIFICATION OF:			17. LIMITATION OF ABSTRACT	18. NUMBER OF PAGES	19a. NAME OF RESPONSIBLE PERSON
a. REPORT U	b. ABSTRACT U	c. THIS PAGE U			USAMRMC
			UU	122	19b. TELEPHONE NUMBER (include area code)

Table of Contents

	<u>Page</u>
Introduction and Keywords.....	2
Body.....	3
Key Research Accomplishments.....	10
Reportable Outcomes.....	10
Conclusion.....	11
References.....	11
Appendices 1-5.....	12

1. Introduction

Malaria is the number one infectious disease threat for American service members serving in endemic areas, including Africa, Asia, the Western Pacific, and South America¹. Constant engagement from civilian and Department of Defense (DoD) researchers is required to confront the emergence and spread of artemisinin (ART)-resistant *Plasmodium falciparum* (Pf) malaria, which is now prevalent throughout Southeast Asia and which threatens all malaria-endemic regions. Investigating the mechanistic basis of resistance is a priority stated in the 2018 Peer Reviewed Medical Research Program (PRMRP) Areas of Encouragement for Malaria research. We are tackling this priority by leveraging our recent discovery of multiple associations between ART resistance and mitochondrial metabolism. This new finding opens an innovative line of enquiry and creates unique opportunities to treat ART-resistant malaria. This research is encapsulated in our two Specific Aims.

In **Aim 1**, we proposed mechanistic studies to test the hypothesis that ART resistance is a result of K13 mutations altering mitochondrial function. This unexpected association was identified following a comprehensive analysis of the global transcriptional, proteomic, and metabolomic profiles of isogenic K13 mutant and wild-type (WT) parasites (**Figure 1**). This systems biology-based approach converged on mutant K13 altering core mitochondrial functionalities, raising the hypothesis that the mitochondria acts as a sensor of ART action and helps protect parasites against ART action.

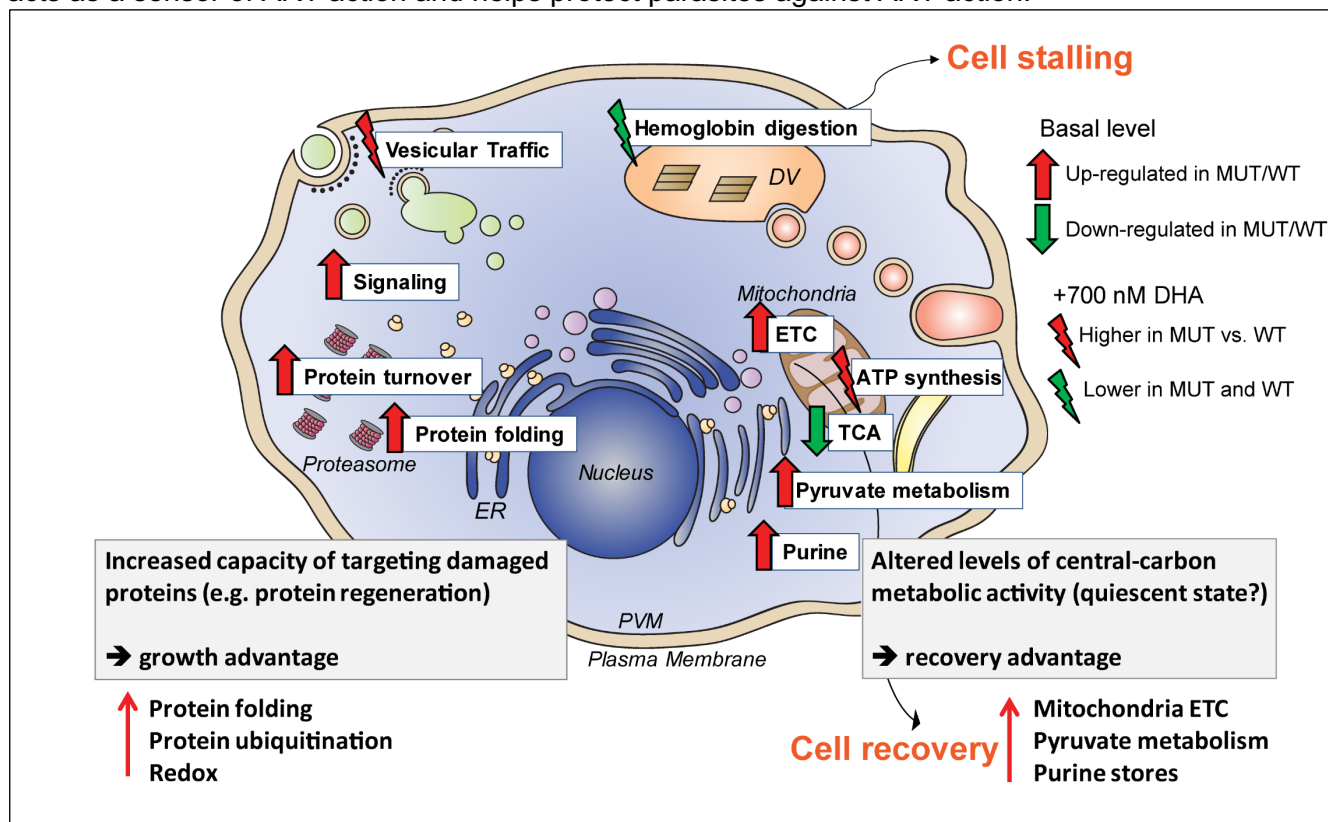


Figure 1. Proposed model for the role of K13 in ART resistance. K13 mutations are associated with an up-regulation of protein folding and proteasome-linked protein turnover, which may provide a growth advantage via a greater capacity of the mutant parasite to target and eliminate damaged proteins caused by the proteotoxic ART drug. K13 protein is involved in other novel pathways including intracellular signaling, pyruvate metabolism, purine salvage, the mitochondrial electron transport chain (ETC), and the tricarboxylic acid cycle (TCA). These functions suggest an altered central carbon metabolism and represent a quiescent state maintained by the parasite that allows for a recovery advantage following exposure to the ART metabolite dihydroartemisinin (DHA). This antimalarial inhibits hemoglobin uptake or degradation and induces stalling in both K13 mutant (MUT) and WT rings. Recovery in K13 mutants may occur through enhanced mitochondrial ATP metabolic function and remodeling of the parasite's secretory and vesicular transport processes. Inhibition of mitochondrial electron transport chain activity increases the susceptibility of K13 mutant ART-resistant parasites to DHA treatment. Published in Mok *et al.*, 2021, **Nature Communications**².

In **Aim 1.1**, we proposed to examine whether resistance involves altered cellular respiration and energy metabolism through the mitochondrial TCA cycle or the electron transport chain (ETC). In **Aim 1.2**, we proposed to test whether heme biosynthesis in the mitochondria regulates ART activation in early rings where mutant K13 is protective. In **Aim 2**, of practical relevance, we posited that we could overcome ART resistance by inhibiting mitochondrial function including pyrimidine biosynthesis and/or targeting the related purine salvage pathway. We have extended this aim substantially in the past year through exciting data showing that ART resistance can also be overcome by inhibiting the parasite proteasome, which serves to remove poly-ubiquitinated proteins damaged by ART action. Progress made is described below based on this project's Statement of Work.

As noted below, we were able to make very good progress on several aspects of the project and have published several studies in highly reputable broad membership journals. Many proposed experiments have been completed. However, the sudden and rapid onset of the COVID-19 pandemic made it impossible to undertake experiments between March and June 2020 when we were not allowed to continue research at CUIMC. Although we were able to progressively ramp up research since July 2020, we have also been restricted in pursuing some of the metabolomics experiments that required access to instrumentation because of restrictions imposed by the COVID-19 pandemic.

Keywords: Malaria, *Plasmodium falciparum* parasites, asexual blood stages, artemisinin, resistance, mitochondria, metabolism

2. Body

Specific Aim 1: Test the hypothesis that mutant K13 achieves ART resistance by altering mitochondrial functionalities.

In **Aim 1** we set out to test the hypothesis that mutant K13 achieves ART resistance in part by altering mitochondrial functionalities. In **Aim 1.1.A** we proposed mass spectrometry methods to examine whether TCA cycle metabolites differ between K13 mutant and WT parasite lines. In **Aim 1.1.B** we proposed to test whether TCA cycle knock-out parasites show a gain of resistance to ART, by profiling parasites with knockouts in the genes α -ketoglutarate dehydrogenase, succinyl-CoA synthase, or succinate dehydrogenase. In **Aim 1.1.C** we proposed to test whether K13 mutations reduce redox perturbations caused by ART action. In **Aim 1.1.D** we proposed to measure mitochondrial respiratory rates via the electron transport chain (ETC) using an extracellular flux analyzer. Progress made is described below for each sub-Aim.

Aim 1.1: Test the hypothesis that cellular respiration and energy metabolism through the tricarboxylic acid cycle (TCA) or the electron transport chain (ETC) are involved in K13-mediated ART resistance.

Sub-Aim 1.1.A: Use metabolite labeling to characterize whether K13 mutations alter the mitochondrial TCA cycle.

Progress: Glucose and glutamine are distinct entry metabolites of the TCA cycle and are differentially processed via glycolysis to acetyl-coA or to glutamate and α -ketoglutarate depending on the Pf parasite's metabolic state. We proposed to incorporate U-¹³C glucose and U-¹³C glutamine into gene-edited K13 mutant and isogenic WT parasite lines and measure the levels of the resulting ¹³C-labeled TCA cycle intermediates. However, we were unable to access the metabolomics instrumentation because of COVID-19 and these studies are pending.

Sub-Aim 1.1.B. Test whether TCA cycle knock-out parasites show a gain of resistance to ART.

Progress: Our studies into the TCA cycle began with immunoprecipitation data that provided evidence of an interaction between K13 and several mitochondrial components, including ones involved in the TCA cycle. These data are shown below in **Table 1**, which was reported by Gnadig *et al.* in 2020 in *PLoS Pathogens*³.

Table. Putative K13-interacting protein partners identified by co-immunoprecipitation and LC/MS-MS..

PlasmoDB Gene ID	Gene Name	Abbreviation	Cellular component and/or functional features	Mean fold change	Number of experiments present (of 6) ¹	Number of samples present (of 13 total, 6 WT, 7 mutant) ²
PF3D7_0708400	Heat shock protein 90	HSP90	Oxidative protein folding in the ER, component of chaperone complexes that interact with BiP	298	5	11 (5,6)
PF3D7_1312600	2-oxoisovalerate dehydrogenase subunit alpha, mitochondrial, putative	BCKDHA	Mitochondrial TCA cycle	270	5	8 (3,5)
PF3D7_1408000	Plasmeprin II	PMII	Digestive vacuole hemoglobinase	264	5	11 (5,6)
PF3D7_1324900	L-lactate dehydrogenase	LDH	Glycolysis	173	4	9 (4,5)
PF3D7_0933600	Mitochondrial-processing peptidase subunit beta, putative	MAS1	Mitochondrial protein degradation	166	5	8 (4,4)
PF3D7_1020900	ADP-ribosylation factor	ARF1	Intracellular traffic, Clathrin, COPI	106	5	9 (3,6)
PF3D7_0523100	Mitochondrial-processing peptidase subunit alpha, putative	MAS2	Mitochondrial protein degradation	92	5	8 (4,4)
PF3D7_0207600	Serine repeat antigen 5	SERA5	Parasitophorous vacuole, parasite egress	87	5	9 (5,4)
PF3D7_0935900	Ring-exported protein 1	REX1	Maurer's cleft exported protein	81	4	6 (2,4)
PF3D7_1446200	M17 leucyl aminopeptidase	LAP	Hemoglobin digestion	76	6	10 (5,5)
PF3D7_1345700	Isocitrate dehydrogenase [NADP], mitochondrial	IDH	Mitochondrial antioxidant system / TCA cycle	74	6	13 (6,7)
PF3D7_0904800	Replication protein A1, small fragment	RPA1	DNA replication / repair	70	3	7 (2,5)
PF3D7_1034400	Flavoprotein subunit of succinate dehydrogenase	SDHA	Mitochondrial respiratory chain complex II (ETC)	60	5	10 (5,5)
PF3D7_0303700	Lipoamide acyltransferase component of branched-chain alpha-keto acid dehydrogenase complex	BCKDH-E2	Mitochondrial antioxidant system	59	3	5 (3,2)
PF3D7_0617200	Conserved <i>Plasmodium</i> protein, unknown function	–	Brl1p family coiled coil protein homolog, putative	59	3	8 (3,5)
PF3D7_0513800	Ras-related protein Rab1A	RAB1A	ER-Golgi translocation and quality control	53	3	6 (2,4)
PF3D7_0919000	Nucleosome assembly protein	NAP1	Histone exchange during transcription elongation	50	4	7 (2,5)
PF3D7_0629200	DnaJ protein, putative	–	Oxidative protein folding in the ER, component of chaperone complexes that interact with BiP	47	6	13 (6,7)
PF3D7_0217100	ATP synthase F1, alpha subunit	–	Mitochondrion, proton-transporting ATP synthase complex, Ca2+ homeostasis	44	4	7 (3,4)
PF3D7_0619400	Cell division cycle protein 48 homologue, putative	p97	ER-associated protein degradation (ERAD)	41	6	11 (5,6)
PF3D7_1239600	Hydroxyethylthiazole kinase	ThzK	Thiamine (Vitamin B) metabolism / glucose metabolism	40	4	9 (4,5)
PF3D7_1246200	Actin I	ACT1	Actin filaments	38	6	13 (6,7)
PF3D7_1022400	Serine/arginine-rich splicing factor 4	SR4	Regulation of mRNA splicing, RNA steady state levels	36	2	5 (2,3)
PF3D7_1302800	40S ribosomal protein S7, putative	–	Ribosome	36	5	9 (4,5)
PF3D7_0103900	Parasite-infected erythrocyte surface protein	ERGIC-53	Intracellular traffic	36	3	6 (3,3)
PF3D7_1118200	Heat shock protein 90, putative	HSP90	Mitochondrial inner membrane	36	6	12 (5,7)
PF3D7_1218500	Dynammin-like protein, putative	–	Mitochondrial division	33	5	9 (4,5)
PF3D7_1340700	Ras-related protein Rab11B	RAB11B	Intracellular traffic / Exocytosis	33	4	9 (4,5)
PF3D7_0817500	histidine triad nucleotide-binding protein 1	–	Ca2+ homeostasis	32	4	7 (4,3)
PF3D7_1108500	Succinyl-CoA synthetase alpha subunit, putative	–	Mitochondrial antioxidant system / TCA cycle	31	6	11 (5,6)
PF3D7_0935800	Cytoadherence linked asexual protein 9	CLAG9	Invasion molecule	30	5	8 (3,5)
PF3D7_0811600	Conserved <i>Plasmodium</i> protein, unknown function	–	No known or predicted function	28	5	7 (4,3)
PF3D7_0302500	Cytoadherence linked asexual protein 3.1	CLAG3.1	Invasion molecule	27	4	6 (4,2)
PF3D7_1407100	rRNA 2'-O-methyltransferase fibrillarin, putative	NOP1	Nucleolus, small nucleolar ribonucleoprotein complex	27	4	8 (3,5)
PF3D7_1144900	Ras-related protein Rab6	RAB6	Intracellular traffic / trans-Golgi network	27	4	8 (3,5)
PF3D7_1230400	ATP-dependent protease subunit ClpQ	ClpQ	Mitochondrial protease complex, protein export	27	6	12 (6,6)
PF3D7_0306400	FAD-dependent glycerol-3-phosphate dehydrogenase, putative	–	Mitochondrial respiratory chain complex II (ETC)	26	4	9 (4,5)
PF3D7_0310400	Parasite-infected erythrocyte surface protein	PIESP1	Exported protein, host cell plasma membrane	25	3	5 (2,3)
PF3D7_1464700	ATP synthase (C/AC39) subunit, putative	–	Digestive vacuole, vacuolar proton-transporting V-type ATPase, Ca2+ homeostasis	25	4	7 (3,4)
PF3D7_1362200	RuvB-like helicase 3	RUVB3	Nucleus / DNA replication and repair	25	3	5 (3,2)
PF3D7_0512600	Ras-related protein Rab1B	RAB1B	ER-Golgi translocation and quality control	25	5	9 (4,5)
PF3D7_1360900	Polyadenylate-binding protein, putative	PABP	Translation initiation	24	5	11 (5,6)
PF3D7_1353100	<i>Plasmodium</i> exported protein, unknown function	–	Maurer's cleft exported protein	23	3	7 (3,4)
PF3D7_0303000	N-ethylmaleimide-sensitive fusion protein	NSF	Exported vesicle-associated protein	21	4	8 (3,5)
PF3D7_0925900	Conserved <i>Plasmodium</i> protein, unknown function	–	No known or predicted function	20	4	8 (4,4)
PF3D7_1135400	Conserved <i>Plasmodium</i> protein, unknown function	–	No known or predicted function	20	2	5 (2,3)
PF3D7_1360800	Falcalysin	FLN	Digestive vacuole, globin peptide degradation	20	4	6 (2,4)
PF3D7_0903200	Ras-related protein Rab7	RAB7	Intracellular traffic, late endosome, digestive vacuole	20	3	5 (3,2)
PF3D7_1212000	Glutathione peroxidase-like thioredoxin peroxidase	TPx(GI)	Mitochondrial antioxidant system	19	3	7 (3,4)
PF3D7_1343000	Phosphoethanolamine N-methyltransferase	PMT	Methionine and phosphatidylcholine metabolism	19	4	6 (2,4)
PF3D7_0532100	Early transcribed membrane protein 5	ETRAPM5	Parasitophorous vacuole membrane protein	19	3	6 (3,3)
PF3D7_1443900	Heat shock protein 90, putative	HSP90	Chaperone protein, putative apicoplast localization	19	4	7 (4,3)
PF3D7_1416100	Protein SEY1, putative	SEY1	Putative mediator of ER membrane fusion	19	4	8 (4,4)
PF3D7_0532300	<i>Plasmodium</i> exported protein (PHISTb), unknown function	–	Exported protein	18	4	6 (2,4)
PF3D7_1431600	Succinyl-CoA ligase [ADP-forming] subunit beta, putative	–	Mitochondrial TCA cycle	17	5	10 (5,5)
PF3D7_1434800	Mitochondrial acidic protein MAM33, putative	–	Mitochondrial matrix, putative	17	6	13 (6,7)
PF3D7_1333000	20 kDa chaperonin	CPN20	Protein chaperone, apicoplast, potentially mitochondrial protein import	15	3	6 (3,3)
PF3D7_0719600	60S ribosomal protein L11a, putative	–	Large ribosomal subunit	15	2	6 (2,4)
PF3D7_0702400	Small exported membrane protein 1	SEMP1	Maurer's cleft exported protein	14	3	7 (3,4)
PF3D7_0831600	Cytoadherence linked asexual protein 8	CLAG8	Putative rhopty protein	14	4	7 (4,3)
PF3D7_1129900	Major facilitator superfamily-related transporter, putative	MFR5	Putative plasma membrane-localized amino acid transporter	12	4	6 (3,3)

We proposed to pursue these studies by generating parasites with TCA cycle genes disrupted. Specifically, we planned to focus on studying parasites with deletions in α -ketoglutarate dehydrogenase, succinyl-CoA synthase, or succinate dehydrogenase. We have not yet pursued this Sub-Aim as we have instead focused on enzymes involved in heme biosynthesis (see **Sub-Aim 1.2.B**).

Sub-Aim 1.1.C. Examine whether K13 mutations reduce redox perturbations caused by ART.

Progress: We have been able to complete this Sub-Aim. For this experiment we developed a redox-sensitive GFP sensor that localizes to the mitochondria, and introduced this via an episomally replicating plasmid electroporated into *in vitro* cultured parasites. Results showed that within 4h of DHA exposure, this drug produced a strong signal of mitochondrial oxidation, and even more so than the mitochondrial ETC inhibitor atovaquone (ATQ) and the reference hemozoin inhibitor chloroquine (CQ). DHA-mediated mitochondrial oxidation was maintained at 24h post exposure. These data were published in Gnadig *et al.*, 2020, *PLoS Pathogens* and are shown in **Figure 2**.

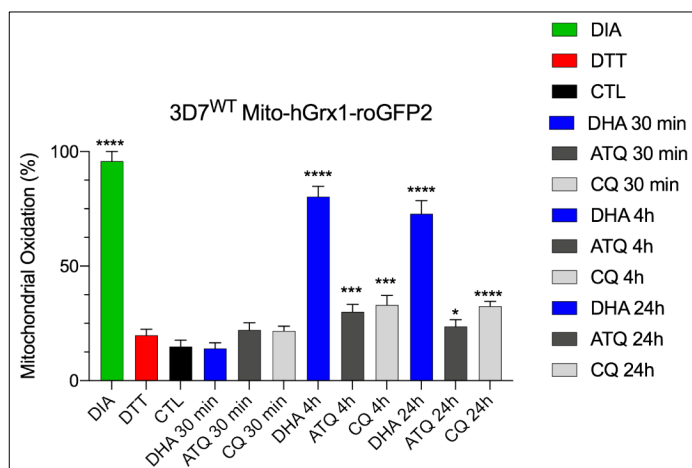


Figure 2. Percent mitochondrial oxidation measured in the 3D7^{WT} Mito-hGrx1-roGFP2 reporter line. Parasites were treated with DHA, ATQ, CQ, a known oxidizing agent (DIA), a known reducing agent (DTT), or vehicle control (CTL). Parasites were exposed for 30 min to 100 μ M drug, for 4h to 5 μ M drug, or for 24h to 50 nM drug. Mean \pm SEM data were collected from three independent occasions, with 10 parasites per experiment examined using confocal laser scanning microscopy. Significance was calculated using two-tailed, unpaired *t* tests comparing drug-treated with mock-treated parasites. **p*<0.05; ***p*<0.01; ****p*<0.001; *****p*<0.0001. ATQ, atovaquone; CQ, chloroquine; DHA, dihydroartemisinin; DIA, diamide; DTT, 1,4-dithiothreitol.

Sub-Aim 1.1.D. Test whether K13 mutations alter mitochondrial respiratory rates via the ETC.

Progress: We proposed to test whether K13 mutant and WT parasite lines differ in their mitochondrial cellular respiratory rates at baseline or upon DHA exposure. This entails saponin-lysing synchronized early rings and measuring oxygen consumption using an extracellular flux analyzer over 3 min⁴, alongside no-cell controls for background correction. Our plan was to undertake these experiments with advice from colleagues specialized in these assays. However, with the COVID-19 disruption and restricted access to specialized equipment, it has not been possible to undertake studies to date.

Aim 1.2: Test the hypothesis that heme synthesized in the mitochondria activates ART in ring-stage parasites and is central to mutant K13-mediated ART resistance.

Sub-Aim 1.2.A. Test whether K13 mutants produce less mitochondrial heme or porphyrin.

We began these studies by measuring the levels of various heme species in isogenic parasite lines expressing mutant or WT K13. Our measurement of free hemin in parasites showed a significant decrease in mutant K13 parasites compared to the isogenic WT control (**Figure 3**). Heme or hemin levels in hemoglobin were unaltered. Mitochondrial heme together with hemoglobin-derived heme constitutes the sum of hemin in parasites. Our data therefore provide evidence that mitochondrial heme must be substantially lower in K13 R539T parasites. To explore this further, we deleted the *P. falciparum* gene encoding DegP2, which is an ortholog of a known mitochondrial protease. K13 WT parasites lacking DegP2 phenocopied mutant K13 parasites in having less total free hemin and similar levels of hemin in hemoglobin, suggesting that DegP2 is also important for mitochondrial heme production. Our collaborator on this project, Dr. Sebastian Lourido at MIT, also identified an association between mutant K13-mediated ART resistance and mitochondrial heme biosynthesis in the related Apicomplexan parasite *Toxoplasma gondii*. These data were published in Harding *et al.*, 2020, *Nature Communications*⁵.

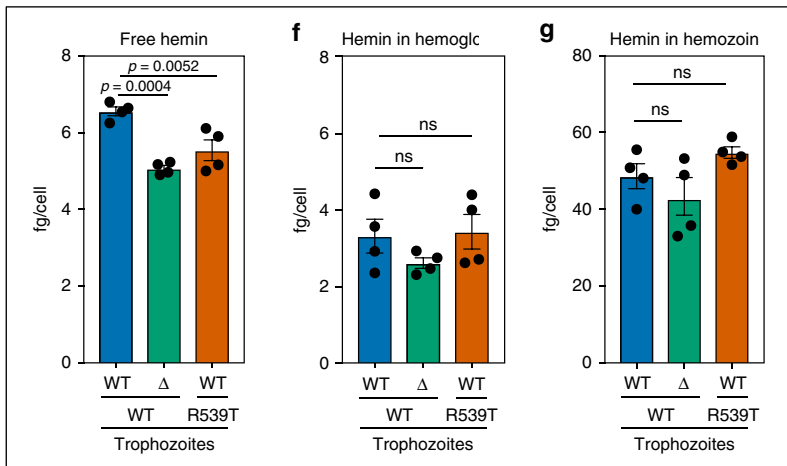


Figure 3. Hemin levels measured from (left) free, (center) hemoglobin-associated, and (right) hemozoin pools from trophozoites for K13 wild-type (WT) or mutant R539T isogenic parasites. The Δ line refers to a parasite that lacks the mitochondrial protease DegP2⁵. Heme concentrations were calibrated to a standard curve and normalized to the number of parasites per sample to calculate fg/cell. Results are mean \pm SD for four independent experiments; p -values from one-way ANOVA.

Sub-Aim 1.2.B. Characterize heme synthesis KO lines to test whether defects in this pathway can phenocopy ART resistance.

Progress: On the basis of these data, we further explored the role of mitochondrial physiology in parasites. In particular, we focused on ferrochelatase (FC) and 5-aminolevulinic acid synthase (ALAS), which are part of the heme biosynthetic pathways that occurs primarily in the mitochondria (**Figure 4**). We also examined the use of succinyl acetone (SA), which inhibits heme biosynthesis and the TCA cycle by competing with the natural substrate succinyl-CoA (**Figure 5**).

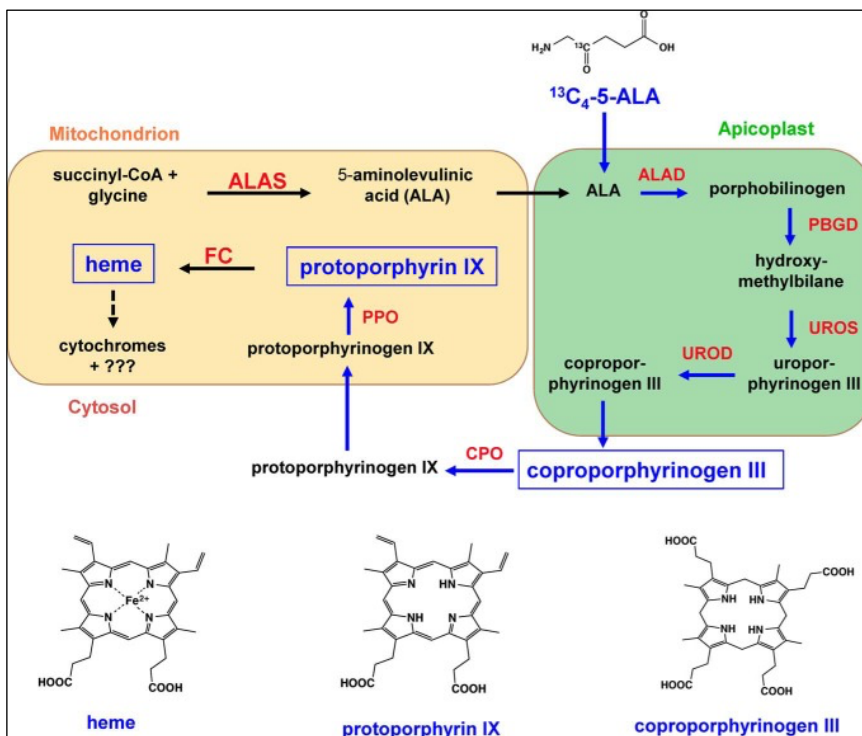


Figure 4. Illustration of the heme biosynthesis pathway in *P. falciparum*. This pathway is composed of eight enzymes that have been localized to the mitochondrion, the cytosol, and the apicoplast⁶. The substrates and products of the pathway are in black. The enzymes involved are in red. The fraction of the pathway labeled by [¹³C]ALA is in blue, and the compounds detected by LC-MS/MS are boxed. The molecular structures of ALA, CPP III, PPIX, and heme are shown. ALAS, 5-aminolevulinic synthase; ALAD, 5-aminolevulinic acid dehydratase; PBGD, porphobilinogen deaminase; UROS, uroporphyrinogen III synthase; UROD, uroporphyrinogen decarboxylase; CPO, coproporphyrinogen oxidase; PPO, protoporphyrinogen oxidase; FC, ferrochelatase.

We then examined the effect of SA on parasites in which FC and ALAS had been genetically disrupted. These parasites, obtained from Dr. Akhil Vaidya at Drexel University, were generated in the K13 WT ART-sensitive D10 strain, and have previously been published⁶. RSA assays with these lines showed that pre-treatment of D10 parasites with SA offered some protection against DHA (**Figure 6**). Parasites lacking both FC and ALAS, however, showed no difference in their survival rates, providing evidence that these enzymatic components are not involved in the survival of DHA-treated parasites. These data are yet to be published.

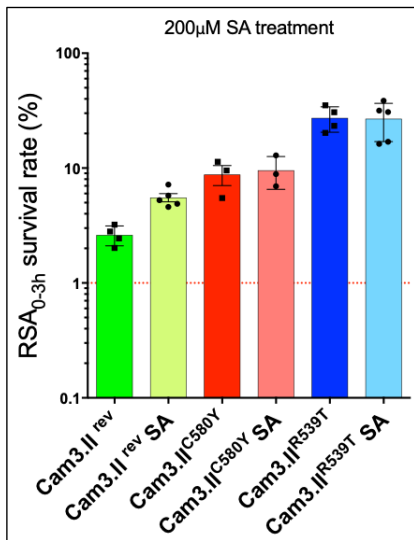


Figure 5. Parasite survival data with K13 mutant or wild-type (WT) lines exposed to the ART metabolite DHA in the presence or absence of the heme biosynthesis inhibitor succinyl acetone (SA). Treatment with 200 mM SA began 12h prior to initiating the 6h treatment with 200 nM DHA, which was applied against early ring-stage parasites. Cam3.II^{C580Y} and Cam3.II^{R539T} express the K13 mutations C580Y or R539T, respectively, and are ART-resistant as indicated by their elevated survival rates in the ring-stage survival assay (RSA, Y-axis values are shown on a log scale). The isogenic Cam3.II^{rev} line expresses WT K13 and is ART-sensitive with low survival rates. Results are mean \pm SD in at least three independent experiments. For the WT parasites, we observed a 2-fold shift in RSA survival rates upon SA treatment, suggesting that blocking heme biosynthesis in the mitochondria might help protect drug-sensitive parasites against ART action. In contrast, no difference was observed for Cam3.II^{C580Y} and Cam3.II^{R539T} parasites.

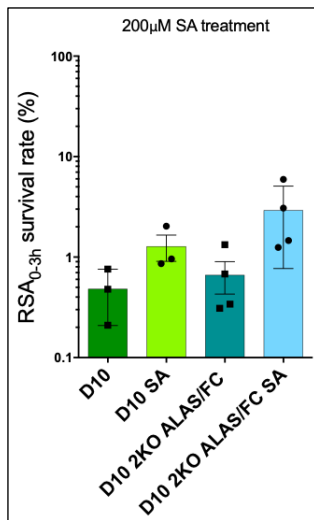


Figure 6. RSA survival rates of early ring stage D10 parasites exposed to 200 nM DHA for 6h. Pre-treatment with 200 mM SA provided some increase in survival. Deletion of ferrochelatase (FC) and 5-aminolevulinic acid synthase (ALAS), however, did not alter parasite survival. Results are mean \pm SD in at least three independent experiments.

Milestone #1. Our progress to date has provided compelling evidence that mitochondrial physiology is central to how *P. falciparum* parasites sense DHA action and that mutations in K13 impact core functionalities in this organelle. We obtained some evidence that mitochondrial heme is reduced in mutant K13 parasites, which is consistent with the idea that this source of heme could be activating drug in early ring-stage parasites. These data provide a compelling rationale to further explore the connection between mitochondrial physiology and mutant K13-mediated ART resistance. We note that this association has also recently been documented in *Toxoplasma gondii*, in a study that we contributed to, as well in recent data from the Wellems lab^{5,7}.

Aim 2: Overcoming ART resistance through inhibition of Pf mitochondrial functionalities and DNA precursor synthesis and salvage. Here, we proposed to test the hypothesis that ART resistance creates vulnerabilities in mitochondrial metabolism, and DNA precursor availability, which can be leveraged to treat ART-resistant parasites. As stated above, this hypothesis arose from the convergence of transcriptional, proteomic, metabolomic and co-immunoprecipitation data that identified the mitochondria as an important component of how mutant K13 impacts parasite physiology (**Figure 7A**).

Aim 2.1. Test whether K13 mutant lines are hypersensitized to inhibitors that target mitochondrial pathways including pyrimidine biosynthesis. Our study focused on inhibitors that target the mitochondrial ETC (using atovaquone), protein translation (fusidic acid), and pyrimidine synthesis (DSM265). Atovaquone inhibits cytochrome B, whereas DSM265 is a clinical drug that targets mitochondrial dihydroorotate dehydrogenase (DHODH), which is essential for pyrimidine synthesis. Fusidic acid inhibits the elongation factor G (EF-G) present in both the apicoplast and mitochondria, leading to cell death within 48h. Of these, atovaquone clearly showed more potency against mutant K13 parasites (Cam3.II^{R539T}) compared to isogenic K13 WT parasites (Cam3.II^{WT}). This is shown as a lower IC₅₀ ratio of Cam3.II^{R539T} vs. Cam3.II^{WT} (**Figure 7B**). We also observed that increasing concentrations of atovaquone synergized with DHA against ART-resistant Cam3.II^{R539T} parasites (**Figure 7C and 8A**), indicating that despite their DHA-induced quiescent state, they retained susceptibility to this ETC-inhibiting drug. These data provide compelling evidence that atovaquone, the first-line drug for traveler's medicine to protect against malaria, could be effective in combination with

DHA in treating ART-resistant parasites. These data were published in Mok *et al.*, 2021, **Nature Communications**.

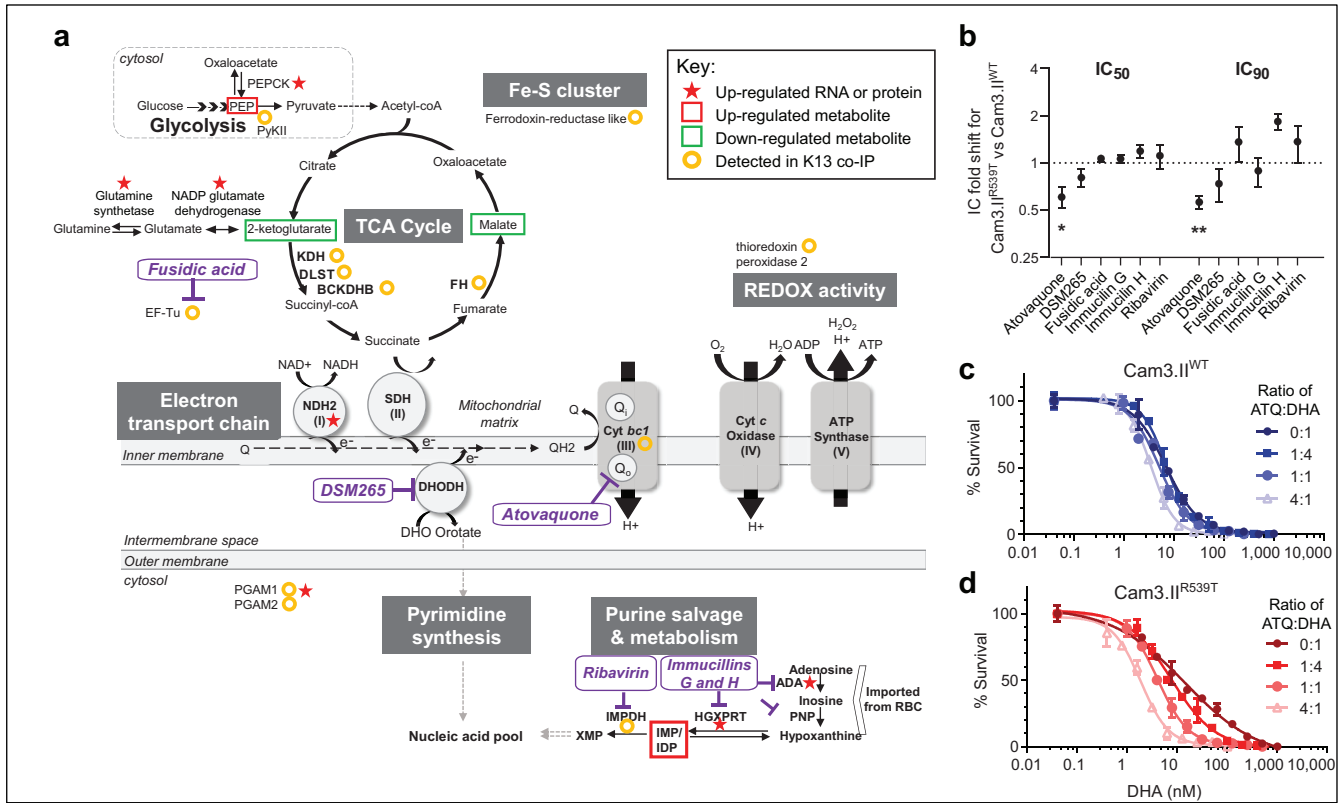


Figure 7. Multi-omics data and dose-response assays reveals K13's role in maintaining mitochondrial ETC functions. **a**, Schematic of the energy and purine metabolism pathways in the parasite mitochondrion. Genes, proteins, metabolites, and co-IP proteins that were detected as differentially regulated between isogenic K13 mutant and WT parasites in multi-omics experiments are highlighted. ADA, adenosine deaminase; DHODH, dihydroorotate dehydrogenase; DLST, dihydrolipoyllysine-residue succinyltransferase; HGXPRT, hypoxanthine-guanine-xanthine phosphoribosyl transferase; IMPDH, inosine 5'-monophosphate dehydrogenase; PNP, purine nucleoside phosphorylase. For full list of protein names, refer to Supplementary Data 5. **b**, IC₅₀ and IC₉₀ fold shifts for Cam3.II^{R539T} vs. Cam3.II^{WT} 0-3 hpi early rings exposed for 4h to a panel of inhibitors targeting mitochondrial processes (atovaquone, DSM265, fusic acid) or purine metabolism (immucilin G and H, ribavirin). Shown are means ± SEM values from two to five independent experiments with technical duplicates. ***P* = 0.008, **P* = 0.024, two-tailed one-sample *t*-tests of the IC fold shift. Individual IC₅₀ and IC₉₀ data are provided in Supplementary Data 8. **c**, 4h dose-response assays conducted on Cam3.II^{WT} 0-3 hpi early rings, depicting no change in the DHA dose response curves in the presence of increased ATQ to DHA ratios. **d**, 4h dose-response curves show increased sensitization of Cam3.II^{R539T} 0-3 hpi early rings to DHA with higher ratios of ATQ to DHA. The mitochondrial ETC inhibitor ATQ displays increased potency when combined with DHA against Cam3.II^{R539T} parasites in 4h drug treatments. Dose-response assays were performed in three to five independent experiments with technical duplicates for each parasite line. The data presented in **c** and **d** are exemplars from one independent experiment with error bars representing the SD between technical duplicates.

To extend these findings, we tested the efficacy of atovaquone with DHA on the set of gene-edited K13 mutant and WT isogenic Dd2 line, which is a long-term *in vitro* culture adapted Pf strain. We observed an additive interaction in Dd2^{R539T} and Dd2^{C580Y} parasites but this killing effect was antagonistic in Dd2^{WT} parasites (**Figure 8A-B**). This suggests that both K13 and the parasite's genetic background may influence the effect of atovaquone on parasite's survival to DHA. We also tested the Cam3.II^{R539T} parasites with the combination of DSM265 and DHA and the effect was additive in both WT and mutant lines (**Figure 8C**; data not published), suggesting that K13-mediated ART resistance is independent of the DHODH pyrimidine synthesis pathway.

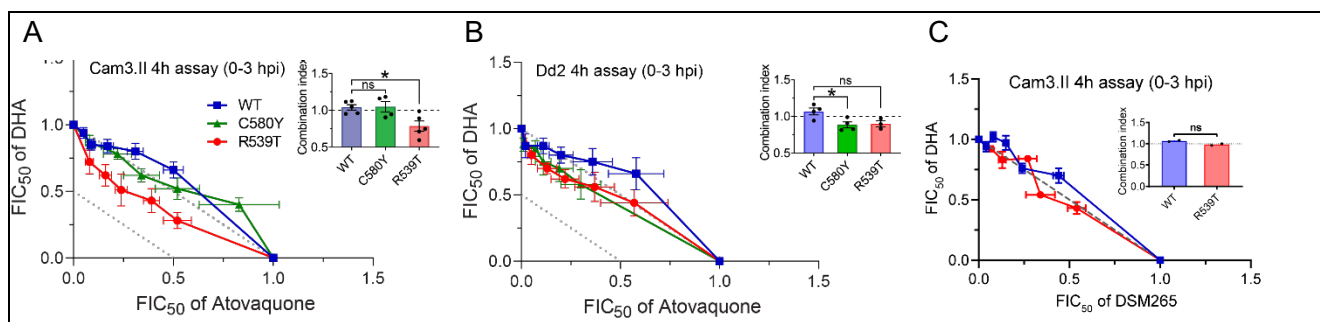


Figure 8. Drug-pair isobologram analyses of Cam3.II and Dd2 K13 mutant vs. wild-type (WT) lines. A-B, Isobolograms showing the fractional IC₅₀ (FIC₅₀) values of DHA + atovaquone combination pairs tested at fixed molar ratios of their individual IC₅₀ values, comprising 1:0, 4:1, 2:1, 1:1, 1:2, 1:4, and 0:1 ratios of atovaquone to DHA. 4h assays were conducted on K13 C580Y or R539T mutants or WT early ring-stage parasites generated in either the Cam3.II or Dd2 backgrounds. FIC₅₀ values are shown as means ± SEM derived from 3-5 biological repeats with technical duplicates. The dashed line at x=y=1 indicates additivity between the two compounds (when the sum FIC₅₀, also known as the Combination Index, equal to 1). Points lying substantially above the dashed line are indicative of an antagonistic interaction, whereas points lying substantially below the line indicate synergy. Combination Index insets depict the average of the sum of the FIC₅₀ values calculated for each experiment across the range of dual-drug combination ratios. The DHA and atovaquone combination was synergistic in killing Cam3.II^{R539T} rings, unlike Cam3.II^{WT} that showed an additive effect. Interactions between these two drugs differed based on their *k13* sequence and genetic background. **P*<0.05 and ***P*<0.01 (paired two-sided *t* tests); ns, not significant. **C,** Isobologram and FIC₅₀ values of the DHA+DSM265 combination pair in Cam3.II K13 mutant and WT parasite lines, which displayed additive interactions.

Aim 2.2. Examine whether ART-resistant parasites are uniquely sensitized to purine salvage inhibitors. We tested this hypothesis using several inhibitors known to target Pf purine metabolism. These inhibitors were immucillin G and immucillin H, which inhibit purine nucleoside phosphorylase (PNP) and block the conversion of adenosine to inosine monophosphate. We also tested ribavirin, which inhibits mammalian and/or bacterial IMPDH, which is central to purine salvage (**Figure 7**). Unlike atovaquone, none of these inhibitors displayed differential activity against parasites expressing mutant vs. WT K13 (**Figure 7B**).

Our studies into the topic of how to block mutant K13-mediated ART resistance led us to undertake a collaboration with Dr. Matt Bogyo and his group at Stanford University (CA). His lab had earlier generated a number of inhibitors of the *P. falciparum* 20S proteasome, which block the ability of the parasite proteasome to eliminate poly-ubiquitinated proteins that result from the proteotoxic action of ART⁸. Recent studies had shown that these inhibitors could synergize with ART derivatives *in vitro*⁹. In our report by Stokes *et al.* (2019, ***PLoS Pathogens***), we documented that proteasome inhibitors synergized with ART derivatives against both K13 mutant and WT parasites. These data showed that K13 mutations did not prevent synergy and that proteasome inhibitors could therefore be effective tools to treat ART-resistant parasites in the field.

Milestone #2. Our findings to date show heightened sensitivity of ART-resistant parasites to the ETC inhibitor atovaquone, suggesting a greater reliance of K13 mutant parasites on the mitochondria. Based on our current data, we exclude the possibility that inhibitors of purine salvage and metabolism prevent K13 mutant parasites from initiating developmental arrest upon exposure to ART. We therefore propose that atovaquone should be further investigated for its ability to prevent mutant K13 from mediating the survival of ART-treated parasites, and thus presents a powerful new therapeutic avenue for exploration.

Given the restrictions on experimental research imposed by the COVID-19 pandemic, we also dedicated considerable time to writing two reviews relevant to this award: Wicht, Mok & Fidock, 2020 in ***Annual Reviews in Microbiology*** and Okombo, Kanai, Deni & Fidock, 2021 in ***Trends in Parasitology***^{10,11}. Thus, despite this pandemic, we had a highly productive year on this project.

Key Research Accomplishments

- Our data provide evidence that ART resistance in *P. falciparum* parasites is achieved via mutations in the K13 gene, and that these mutations cause a differential regulation in energy production by the parasite mitochondria. This is evidenced by the increase in ETC gene transcripts and decrease in TCA cycle metabolites in K13 mutant parasites vs. their isogenic WT controls.
- We find that dihydroartemisinin (DHA), the active metabolite of ART, causes rapid oxidation of the parasite mitochondria, indicative of sudden oxidative stress in this compartment.
- The mitochondrial ETC inhibitor atovaquone, used in traveler's medicine as a prophylactic for malaria, had increased activity against artemisinin-resistant parasites.
- The addition of atovaquone to DHA reversed artemisinin resistance, providing an important new avenue of research into whether this prophylactic drug could be of use in countering artemisinin resistance in field settings of malaria infection and treatment.
- Evidence for a role of mitochondrial perturbation was also obtained in *Toxoplasma gondii* parasites, with an important role identified for mitochondrial heme.
- Parasite proteasome inhibitors were found to synergize with K13 mutant and WT parasites *in vitro*, providing a unique opportunity for synergistic interactions to treat artemisinin-resistant malaria.

Reportable Outcomes

1. Mok S, Stokes BH, Gnadig NF, Ross LS, Yeo T, Amaratunga C, Allman E, Solyakov L, Bottrill AR, Tripathi J, Fairhurst RM, Llinas M, Bozdech Z, Tobin AB & **Fidock DA** (2021). Artemisinin-resistant K13 mutations rewire *Plasmodium falciparum*'s intra-erythrocytic metabolic program to enhance survival. **Nature Communications** 12: 530. PMC7822823. PMID 33483501.
2. Gnadig NF, Stokes BH, Edwards RL, Kalantarov GF, Heimsch KC, Kuderjavy M, Crane A, Lee MCS, Straimer J, Becker K, Trakht IN, Odom John AR, Mok S & **Fidock DA** (2020). Insights into the intracellular localization, protein associations and artemisinin resistance properties of *Plasmodium falciparum* K13. **PLoS Pathogens** 16: e1008482. PMC7192513. PMID 32310999.
3. Harding CR, Sidik SM, Petrova B, Gnadig NF, Okombo J, Herneisen AL, Ward KE, Markus BM, Boydston EA, **Fidock DA** & Lourido S (2020). Genetic screens reveal a central role for heme metabolism in artemisinin susceptibility. **Nature Communications** 11: 4813. PMC7511413. PMID 32968076.
4. Wicht KJ, Mok S & **Fidock DA** (2020). Molecular mechanisms of drug resistance in *Plasmodium falciparum* malaria. **Annual Reviews in Microbiol** 74: 431-54. PMC8130186. PMID 32905757.
5. Okombo J, Kanai M, Deni I & **Fidock DA** (2021). Genomic and genetic approaches to studying antimalarial drug resistance and *Plasmodium* biology. **Trends in Parasitology** 37: 476-492. PMC8162148. PMID: 33715941.

Part of our data were presented at three meetings:

- The 67th Annual Meeting of the American Society of Tropical Medicine and Hygiene. November 2018. Symposium presentations by Drs. Sachel Mok and David Fidock.
- The 3rd New York Parasitology Annual Meeting, December 2018. Presentation by Dr. Sachel Mok.
- The Molecular Approaches to Malaria meeting, held in Lorne, Victoria, Australia, February 2020. Presentations by Drs. Sachel Mok and David Fidock.

Conclusion

Our project has uncovered the parasite mitochondria as a contributor to the mechanism of artemisinin action and parasite resistance. We have also identified increased potency of atovaquone against ART-resistant parasites. We are now focusing on targeting the *P. falciparum* proteasome as a means of treating ART-resistant malaria, leveraging the unique synergy between inhibitors of the proteasome and ART derivatives. Despite COVID-19, this work was highly productive, with three research articles plus two authoritative reviews, all in highly impactful journals.

References

1. Armed Forces Health Surveillance B (2017). Update: Malaria, U.S. Armed Forces, 2016. **MSMR** 24: 2-7.
2. Mok S, Stokes BH, Gnadig NF, Ross LS, Yeo T, Amaratunga C, Allman E, Solyakov L, Bottrill AR, Tripathi J, Fairhurst RM, Llinas M, Bozdech Z, Tobin AB & Fidock DA (2021). Artemisinin-resistant K13 mutations rewire *Plasmodium falciparum*'s intra-erythrocytic metabolic program to enhance survival. **Nat Commun** 12: 530.
3. Gnadig NF, Stokes BH, Edwards RL, Kalantarov GF, Heimsch KC, Kuderjavy M, Crane A, Lee MCS, Straimer J, Becker K, Trakht IN, Odom John AR, Mok S & Fidock DA (2020). Insights into the intracellular localization, protein associations and artemisinin resistance properties of *Plasmodium falciparum* K13. **PLoS Pathog** 16: e1008482.
4. Sakata-Kato T & Wirth DF (2016). A novel methodology for bioenergetic analysis of *Plasmodium falciparum* reveals a glucose-regulated Metabolic shift and enables mode of action analyses of mitochondrial inhibitors. **ACS Infect Dis** 2: 903-16.
5. Harding CR, Sidik SM, Petrova B, Gnadig NF, Okombo J, Ward K, Markus BM, Fidock DA & Lourido S (2020). Genetic screens reveal a central role for heme biosynthesis in artemisinin susceptibility. **Nature Commun**: 4813.
6. Ke H, Sigala PA, Miura K, Morrissey JM, Mather MW, Crowley JR, Henderson JP, Goldberg DE, Long CA & Vaidya AB (2014). The heme biosynthesis pathway is essential for *Plasmodium falciparum* development in mosquito stage but not in blood stages. **J Biol Chem** 289: 34827-37.
7. Connelly SV, Manzella-Lapeira J, Levine ZC, Brzostowski J, Krymskaya L, Rahman RS, Ellis AC, Amin SN, Sa JM & Wellems TE (2021). Restructured mitochondrial-nuclear interaction in *Plasmodium falciparum* dormancy and persists survival after artemisinin exposure. **mBio** May 28: e0075321. doi: 10.1128/mBio.00753-21. Online ahead of print.
8. Yoo E, Stokes BH, de Jong H, Vanaerschot M, Kumar T, Lawrence N, Njoroge M, Garcia A, Van der Westhuyzen R, Momper JD, Ng CL, Fidock DA & Bogyo M (2018). Defining the determinants of specificity of *Plasmodium* proteasome inhibitors. **J Am Chem Soc** 140: 11424-37.
9. Li H, O'Donoghue AJ, van der Linden WA, Xie SC, Yoo E, Foe IT, Tilley L, Craik CS, da Fonseca PC & Bogyo M (2016). Structure- and function-based design of *Plasmodium*-selective proteasome inhibitors. **Nature** 530: 233-6.
10. Wicht KJ, Mok S & Fidock DA (2020). Molecular mechanisms of drug resistance in *Plasmodium falciparum* malaria. **Annu Rev Microbiol** 74: 431-54.
11. Okombo J, Kanai M, Deni I & Fidock DA (2021). Genomic and genetic approaches to studying antimalarial drug resistance and *Plasmodium* biology. **Trends Parasitol** 37: 476-92.








ARTICLE



<https://doi.org/10.1038/s41467-020-20805-w>

OPEN

Artemisinin-resistant K13 mutations rewire *Plasmodium falciparum*'s intra-erythrocytic metabolic program to enhance survival

Sachel Mok ¹, Barbara H. Stokes ¹, Nina F. Gnädig¹, Leila S. Ross¹, Tomas Yeo ¹, Chanaki Amaratunga², Erik Allman³, Lev Solyakov⁴, Andrew R. Bottrill⁴, Jaishree Tripathi⁵, Rick M. Fairhurst^{2,9}, Manuel Llinás ^{3,6}, Zbynek Bozdech ^{5,10}, Andrew B. Tobin ^{7,10} & David A. Fidock ^{1,8}✉

The emergence and spread of artemisinin resistance, driven by mutations in *Plasmodium falciparum* K13, has compromised antimalarial efficacy and threatens the global malaria elimination campaign. By applying systems-based quantitative transcriptomics, proteomics, and metabolomics to a panel of isogenic K13 mutant or wild-type *P. falciparum* lines, we provide evidence that K13 mutations alter multiple aspects of the parasite's intra-erythrocytic developmental program. These changes impact cell-cycle periodicity, the unfolded protein response, protein degradation, vesicular trafficking, and mitochondrial metabolism. K13-mediated artemisinin resistance in the Cambodian Cam3.II line was reversed by atovaquone, a mitochondrial electron transport chain inhibitor. These results suggest that mitochondrial processes including damage sensing and anti-oxidant properties might augment the ability of mutant K13 to protect *P. falciparum* against artemisinin action by helping these parasites undergo temporary quiescence and accelerated growth recovery post drug elimination.

¹Department of Microbiology & Immunology, Columbia University Irving Medical Center, New York, NY, USA. ²Laboratory of Malaria and Vector Research, National Institute of Allergy and Infectious Diseases, National Institutes of Health, Bethesda, MD, USA. ³Department of Biochemistry & Molecular Biology, Huck Center for Malaria Research, Pennsylvania State University, University Park, PA, USA. ⁴Protein Nucleic Acid Laboratory, University of Leicester, Leicester, UK. ⁵School of Biological Sciences, Nanyang Technological University, Singapore, Singapore. ⁶Department of Chemistry, Huck Center for Malaria Research, Pennsylvania State University, University Park, PA, USA. ⁷The Centre for Translational Pharmacology, Institute of Molecular, Cell and Systems Biology, College of Medical, Veterinary and Life Sciences, University of Glasgow, Glasgow, UK. ⁸Division of Infectious Diseases, Department of Medicine, Columbia University Irving Medical Center, New York, NY, USA. ⁹Present address: Astra Zeneca, Gaithersburg, MD 20878, USA. ¹⁰These authors contributed equally: Zbynek Bozdech, Andrew B. Tobin. ✉email: df2260@cumc.columbia.edu

Plasmodium falciparum parasites, the primary etiological agent of severe malaria, caused an estimated 229 million clinical cases and 409,000 deaths in 2019, predominantly in young African children¹. Disease is caused by the asexual blood stages, which complete their intra-erythrocytic developmental cycle (IDC) every ~48 h. Globally, first-line treatment depends on artemisinin (ART)-based combination therapies (ACTs), which benefit from the exceptional potency of ART derivatives. These derivatives are activated in the parasite by hemoglobin-derived Fe²⁺-heme and kill rings and trophozoites via alkylation of proximal proteins, lipids, and heme^{2–4}. *P. falciparum* resistance to ART, which first emerged in western Cambodia, is now present across the Greater Mekong Sub-region (GMS), compromising clinical efficacy^{5–7}. Clinically, resistance is defined as a >5.5 h parasite clearance half-life (i.e. the time required to halve the parasite biomass)^{8,9}. This reduced rate of clearance has increased the selective pressure on the partner drug. The recent appearance and spread across the GMS of resistance to the first-line partner drug piperazine in ART-resistant parasites is causing widespread treatment failures, threatening local malaria control efforts^{9–11}. A spread of ART resistance in Africa would be devastating¹².

Genetic and clinical data, supported by gene editing experiments, have identified point mutations in K13 (also known as Kelch13) as the dominant causal determinant of ART resistance. The degree of resistance is modulated by the specific mutation, which tends to cluster geographically^{7,13}, as well as by the parasite genetic background^{14–19}. With cultured parasites, resistance (or tolerance) is typically defined as >1% survival in the Ring-stage Survival Assay (RSA), in which young rings (0–3 h post invasion (hpi)) are exposed to 700 nM DHA for 4–6 h and their survival measured 3 days later as a percentage of mock-treated parasites²⁰. K13 R539T confers the highest level of in vitro resistance across strains (19–49% survival, with a geometric mean survival of 27%, as determined with four gene-edited strains), and is quite widespread at a relatively low prevalence across Asia²¹. By comparison K13 C580Y, which is the dominant isoform in the GMS, gives a more moderate in vitro resistance phenotype (4–24% survival, with a geometric mean survival of 9.2%, as determined with five gene-edited strains)^{16,22}. K13-independent ART resistance has also been documented in five field isolates originating from Cambodia or Senegal and in two independent selection or transfection studies with the 3D7 parasite line^{23–26}.

The biological role of K13 and the precise mechanism(s) by which its mutations elicit an enhanced survival response to ART remain enigmatic. Studies have suggested roles for reduced endocytosis of hemoglobin leading to less Fe²⁺-heme and reduced drug activation in rings, an endoplasmic reticulum (ER) stress response and an up-regulated unfolded protein response, translational arrest possibly involving enhanced eIF2- α phosphorylation, decreased levels of protein ubiquitination and altered rates of proteasome-mediated protein turnover, and PI3K-dependent intracellular signaling linked to amplified PI3P vesicles^{27–35}. These processes could offset widespread ART-mediated damage to parasite proteins and other biomolecules^{36,37}. One pressing question is whether these cellular effects are a direct result of mutations in K13, or whether they are epistatic phenomena that provide suitable cellular contexts on which mutant K13 can exert ART resistance, or a combination of both.

In this work, to explore the impact of K13 mutations on the parasite and gain further insight into the mechanism of ART resistance, we subjected a panel of *k13* gene-edited isogenic parasites on two different genetic backgrounds to untargeted multi-omics including transcriptomics, proteomics, and metabolomics (Fig. 1). Results provided herein reveal a broad array of intracellular processes affected by K13 mutations and converge

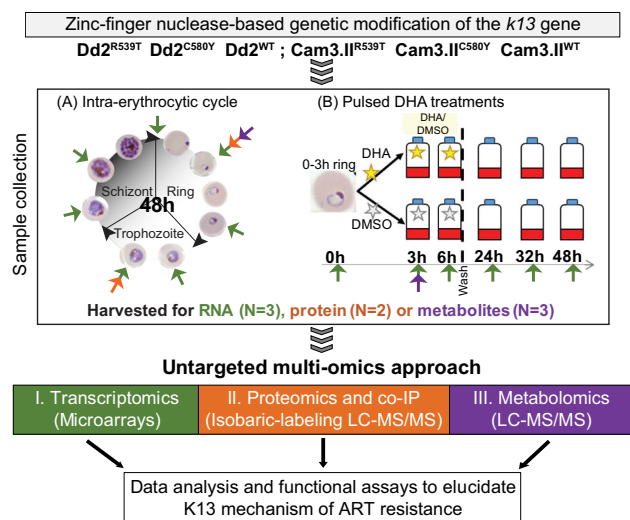


Fig. 1 Outline of experimental workflow and multi-omics approaches applied to examine K13 function in this study. The workflow illustrates the sample collection, processing, and data acquisition steps. The Dd2 laboratory-adapted parasite line and the Cam3.II clinical isolate were genetically modified at the *k13* locus via zinc-finger nuclease-based gene editing to create isogenic lines with either the wild-type (WT) or mutant *k13* alleles¹⁵. RNA, protein, or metabolite samples were collected for each parasite line at 6–7 time points throughout the 48 h asexual blood stage cycle in the absence of drug treatment. Synchronized K13 mutant and WT parasites were also subjected to a pulse of DHA, either at a concentration of 350 nM for 3 h (for metabolomics) or at 700 nM for 6 h (for transcriptomics), in parallel with 0.1% DMSO vehicle control. Samples were collected during DHA exposure and post drug removal. Colored arrows represent times and conditions of harvest for the different omic methods (green for transcriptomics, orange for proteomics and purple for metabolomics). Using microarray gene expression profiling and quantitative mass spectrometry-based proteomics and metabolomics, we generated global transcriptional, proteomic, and metabolomic profiles of gene-edited lines and compared the K13 mutants to their isogenic WT counterparts across the IDC.

on a previously unsuspected role for mitochondria. These data reveal vulnerabilities that could be leveraged to target ART-resistant *P. falciparum*.

Results

K13 mutations rewire the *P. falciparum* transcriptome. To investigate the biological function of K13, we examined the transcriptional profiles of highly synchronized K13 mutant or isogenic wild-type (WT) parasite lines generated in the pre-ART era Dd2 and contemporary Cam3.II SE Asian strains¹⁶ (Dd2^{R539T}, Dd2^{C580Y}, Dd2^{WT}, Cam3.II^{R539T}, and Cam3.II^{WT}) across the 48 h IDC time course (Fig. 1, Table 1 and Supplementary Fig. 1a). Between *k13* genotypes, the Dd2 and Cam3.II sets of parasites mapped to highly similar IDC time points, with the isogenic sets of lines differing in developmental age by up to 1.5 and 4 h, respectively at the 0 h start of sampling. Principal component analyses of transcriptomic profiles showed distinct clustering by parasite stage (0–16 hpi rings vs. 24–40 hpi trophozoites and schizonts for PC1; trophozoites vs. schizonts for PC2), followed by genetic background (PC3) (Fig. 2a). Variation between strains outweighed the impact of K13 mutations on the transcriptomes, underscoring the need to compare isogenic edited parasites in order to identify changes specifically attributable to *k13* sequence variants.

Table 1 Geographic origin, k13 isoform, and DHA response of *P. falciparum* lines.

Parasite	Edited?	K13	Origin (year)	PCt _{1/2} (h)	RSA (% survival)	Omics method
Cam3.II ^{R539T}	No	R539T	Pursat, W. Cambodia (2010)	6.0	40.2 ± 3.0	Transcriptomics, proteomics, co-IP
Cam3.II ^{C580Y}	Yes	C580Y	Pursat, W. Cambodia (2010)	N/A	24.1 ± 2.9	Proteomics, co-IP, metabolomics
Cam3.II ^{WT}	Yes	WT	Pursat, W. Cambodia (2010)	N/A	0.3 ± 0.1	Transcriptomics, proteomics, co-IP, metabolomics
Dd2 ^{R539T}	Yes	R539T	Indochina (1980)	N/A	19.4 ± 0.8	Transcriptomics
Dd2 ^{C580Y}	Yes	C580Y	Indochina (1980)	N/A	4.1 ± 0.4	Transcriptomics
Dd2 ^{WT}	Yes (bsm)	WT	Indochina (1980)	N/A	0.3 ± 0.1	Transcriptomics

bsm binding-site mutant control (no amino acid substitutions), co-IP co-immunoprecipitation, N/A not available, PCt_{1/2} parasite clearance half-life, RSA Ring-stage Survival Assay conducted with 0–3 h post invasion rings, WT wild type. Cam3.II and Dd2 parasites both harbor the PICRT Dd2 haplotype: M74I/N75E/K76T/A220S/Q271E/N326S/I356T/R371I. Dd2 and Cam3.II harbor the PIMDR1 haplotypes N86Y and Y184F, respectively.

Because K13 mutations have been previously linked to prolonged duration of ring-stage development^{29,38}, we used Spearman rank correlations to map parasite ages to a high-resolution 96-time point reference transcriptome (Supplementary Fig. 1b–f). While the R539T mutants and WT parasites progressed similarly in both Dd2 and Cam3.II parasite backgrounds, the Dd2^{C580Y} mutant developed ~4 h slower, most evident at the 24, 32, and 48 h time points (***P* < 0.001, *t*-test, *N* = 3) (Fig. 2b and Supplementary Fig. 2a). This finding suggests that Dd2^{C580Y} has a longer ring phase with a delayed ring to trophozoite transition.

At each sampling time point across the 48 h IDC, we observed ~80–200 genes differentially expressed (DE) between the Dd2^{R539T} mutant line and its isogenic Dd2^{WT} counterpart (*P* < 0.05, *t*-test, *n* = 3). Similar numbers of DE genes were observed in Dd2^{C580Y} rings, with even higher numbers of DE genes observed at later time points (24, 32, and 48 h; Supplementary Fig. 2b and Supplementary Data 1), due to the decelerated development of Dd2^{C580Y} parasites. A significant overlap of 394 genes were DE in the Dd2^{R539T} and Dd2^{C580Y} lines relative to Dd2^{WT} parasites. Of these genes, 123 and 113 were up- and down-regulated, respectively, in both mutants within the same 4 h developmental window of the IDC (Fig. 2c). *K*-means clustering of the 394 DE genes showed a similar pattern of differential expression elicited by both mutants, indicating that the two different K13 mutations impacted expression of these genes in the same manner (Fig. 2c).

Most of these DE genes in Dd2 parasites were up-regulated during the transition from late schizonts to early rings and were enriched for pathways specialized in ubiquitin transfer (including ubiquitin-conjugating enzyme E2 and HECT-domain ubiquitin-transferase), protein phosphorylation, intracellular signaling (including adenylyl cyclase and cAMP protein kinase), sphingolipid and ceramide lipid metabolism, and mitochondrial electron transport chain (ETC) NADH dehydrogenase ubiquinone activity (hypergeometric test; *P* < 0.05) (Fig. 2d; Supplementary Fig. 2d and Data 1 and 2).

These same DE pathways were also observed in the Cam3.II^{R539T} mutant. Interestingly, *k13* was among this set of genes with higher transcript abundance in the K13 mutant early rings. Functional enrichment analysis of DE genes at each sampling time point through the IDC for Dd2 and Cam3.II identified other strain-transcending changes associated with K13 mutations, ranging from elevated histone modifications in late rings, to higher levels of pyruvate metabolic enzyme, phosphoenolpyruvate (PEP) carboxykinase, and exported parasite proteins to the host red blood cell (RBC) cytosol in trophozoites, and increased S-nitrosylation and palmitoylation-modified proteins in schizonts (Fig. 2d and Supplementary Data 2). Several pathways were also exclusive to K13 mutants in Dd2 but not Cam3.II, including the DNA damage checkpoint (GO process) that contained genes that were up-regulated in ring stages in both Dd2 K13 mutant lines compared to Dd2^{WT}.

K13 mutations alter the parasite proteome including protein turnover and glutamate and purine metabolism. In parallel, we performed isobaric labeling-based quantitative proteomics with Cam3.II lines (Cam3.II^{R539T}, Cam3.II^{C580Y}, and Cam3.II^{WT}), and detected a total of 2780 and 2573 proteins (~50% of the *P. falciparum* proteome) in synchronized rings and trophozoites, respectively (*N* = 2; Fig. 1 and Supplementary Fig. 3a). Strikingly, fewer proteins were DE between K13 mutant and WT parasites in trophozoites, as compared to early rings that manifest ART resistance (Fig. 3a and Supplementary Fig. 3b, b). In rings, 87 proteins were more abundant in both K13 mutants relative to the isogenic WT line, in at least one experiment (*P* < 0.05; *t*-tests using normalized spectral intensity of peptides for each protein; Fig. 3a and Supplementary Data 3). Functional enrichment analyses converged on chaperone-mediated protein folding (cyclophilin 19B, ER calcium-binding protein, chaperonin 10 kDa) and protein targeting processes in the proteasome core complex (proteasomal subunits and ubiquitin ligase), redox (superoxide dismutase), and processes within intracellular vesicles and the digestive vacuole (Fig. 3a).

Of note, cyclophilin 19B was the top hit associated with in vivo ART resistance from an earlier transcriptomics study of *P. falciparum* clinical isolates²⁹. Our observations here suggest that its increased protein abundance is regulated by K13 mutations. We also observed new functionalities not previously associated with K13, including carbon metabolism (illustrated by the increased abundance of glutamine synthetase and NADP-specific glutamate dehydrogenase that both help regulate cellular glutamine levels), as well as adenosine deaminase and hypoxanthine-guanine phosphoribosyltransferase (HGXPRT), which are critical for purine metabolism (Supplementary Data 3). While the changes associated with K13 mutations in rings were mostly instances of increased abundance, all 13 DE proteins in trophozoites showed reduced levels in the K13 mutants (Supplementary Fig. 3c). This included 1.8- to 2.0-fold less K13 protein in Cam3.II^{C580Y} and Cam3.II^{R539T} trophozoites (Fig. 3b), as previously reported³⁹. However, unlike Cam3.II^{R539T} rings that showed 1.5-fold reduced K13 protein, there was no detectable difference in Cam3.II^{C580Y} rings (Fig. 3b). In these samples, K13 was identified with 11 unique peptides, covering 17% of the protein (Supplementary Fig. 4). The increased turnover of K13 protein in Cam3.II^{R539T} rings may contribute to this parasite line's relatively high degree of ART resistance and suggests a potential loss-of-function role for the R539T mutation.

Targeted metabolomics reveals altered levels of tricarboxylic acid (TCA) cycle and purine salvage metabolites in K13 mutants. Metabolomic analyses of Cam3.II^{C580Y} and Cam3.II^{WT} ring (*N* = 3) and trophozoite (*N* = 1) extracts, using a previously published dataset⁴⁰, detected a total of 96 metabolites

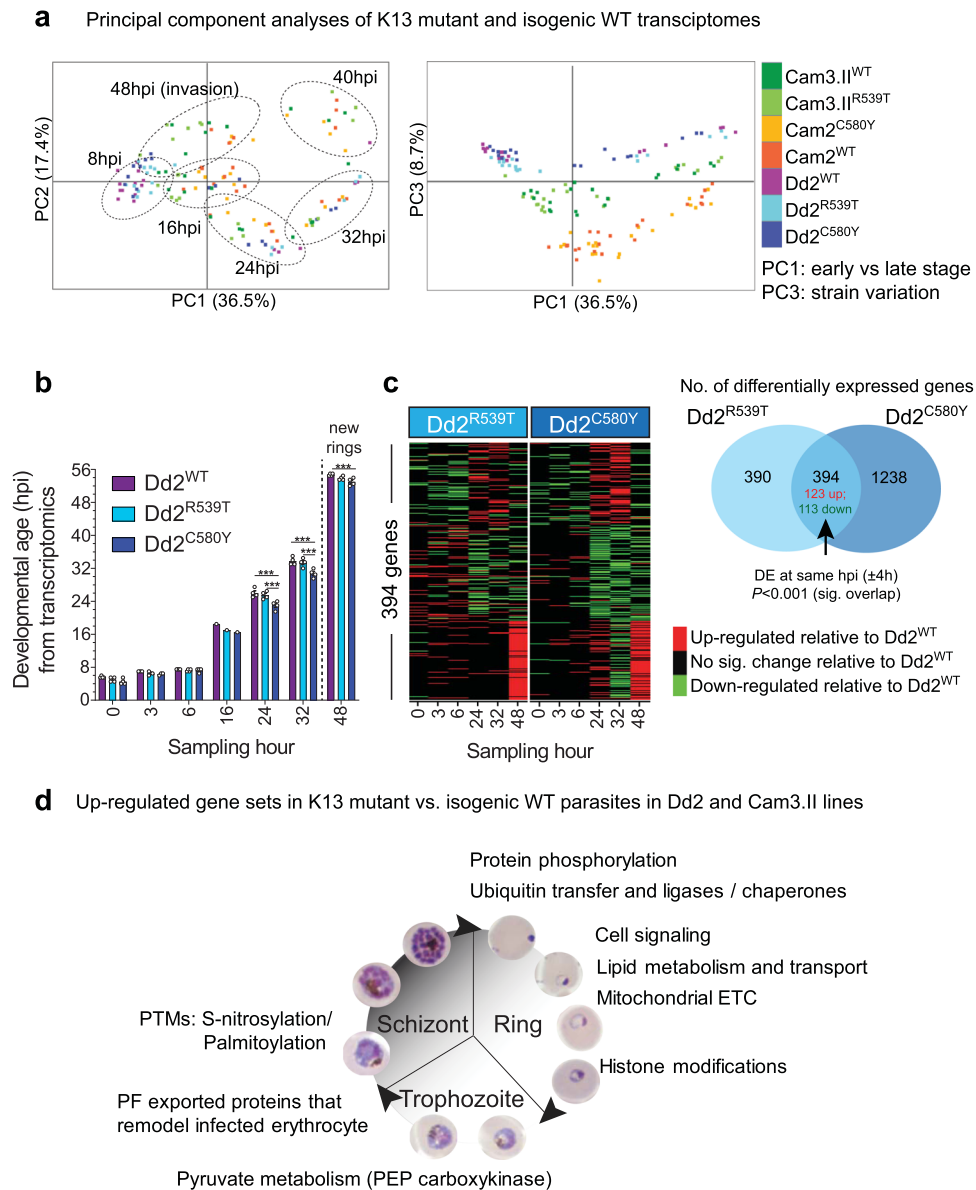


Fig. 2 K13 mutations associate with altered temporal cell-cycle progression and broad transcriptional changes throughout the 48 h IDC. **a** PCA plots for transcriptome samples labeled by parasite line, K13 status, sampling time, and parasite asexual stage. This analysis was conducted on Cam3.II and Dd2 K13 WT, C580Y and R539T samples, as well as the Cam2 isogenic K13 C580Y and WT pair¹⁶. **b** Transcriptomics-based age estimation for R539T and C580Y mutants and isogenic WT Dd2 parasites determined by comparison against a Dd2 reference 48 h IDC⁶⁸. Dd2^{C580Y} mutant parasites showed a significant albeit modest (up to 4 h) slowing of the developmental cycle during the 16–48 h developmental period, relative to Dd2^{WT} and Dd2^{R539T} parasites. Each time point was harvested on three independent occasions (data points are presented as means ± SEM), except for the 16 h time point that was collected only once. Differences between lines were examined using a two-sided *t*-test; ****P* < 0.001. *P* values for each comparison were 24 h time point–Dd2^{C580Y} vs. Dd2^{WT} *P* = 1.7E–6, Dd2^{C580Y} vs. Dd2^{R539T} *P* = 5.1E–5; 32 h time point–Dd2^{C580Y} vs. Dd2^{WT} *P* = 1.7E–6, Dd2^{C580Y} vs. Dd2^{R539T} *P* = 2.6E–5; 48 h time point–Dd2^{C580Y} vs. Dd2^{WT} *P* = 0.002. **c** Venn diagram (right) showing significant overlap of 394 DE genes in pair-wise comparisons between the gene-edited K13 mutant and WT lines at the same developmental stage (± 4 h). Heat map of *k* means-clustered overlapping DE genes in each pair-wise comparison, showing a similar profile of differential expression in both the R539T and C580Y mutants as compared to the WT line. Significant changes in expression levels were defined using a two-sided *t*-test (*P* < 0.05). Results also revealed consistent up-regulation of 80 genes in the 48 h late segmenter/early ring-stage samples of both K13 mutant parasite lines (see lower rows; detailed in Supplementary Data 1). The Venn diagram analysis used a binomial distribution test, with *P* = 5.7E–32. **d** Significantly up-regulated gene sets common to both K13 mutants relative to WT parasites (hypergeometric testing, *P* < 0.05) across the 48 h cycle in both the Cam3.II and Dd2 backgrounds (see Supplementary Data 2). ETC electron transport chain, hpi hours post invasion, PEP phosphoenolpyruvate, PTMs post-translational modifications.

(Supplementary Fig. 5a and Supplementary Data 4). Sample-to-sample correlation of the metabolite expression profiles showed that ring-stage samples clustered separately from trophozoites and uninfected RBC controls, indicating substantial changes in parasite metabolism throughout the IDC (Supplementary

Fig. 5b). Metabolomic set enrichment analyses of untreated ring-stage parasites revealed that the C580Y mutation affected the basal levels of metabolites involved in the TCA cycle, as well as purine, glutamate, and pyruvate metabolism (Fig. 3c). Partial least-squares discriminant analyses revealed several metabolites

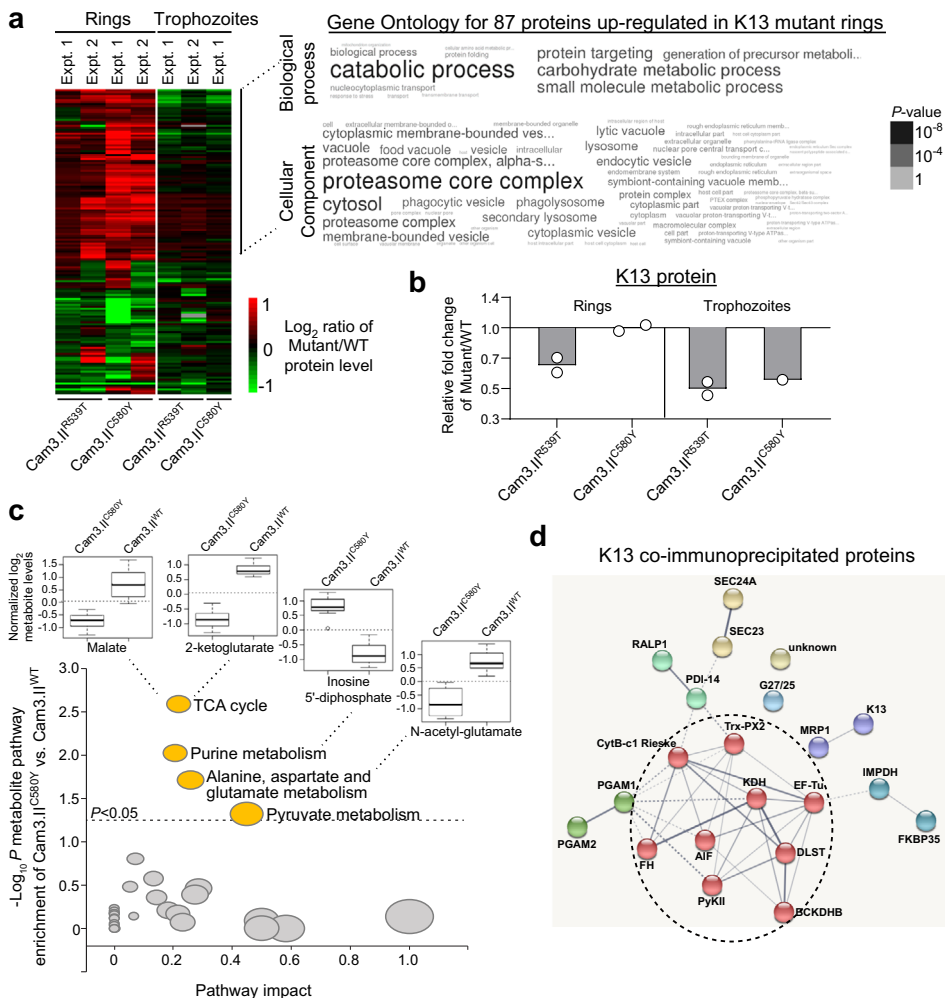


Fig. 3 K13 mutations associate with differential expression of proteins involved in proteasome-mediated turnover and protein folding, and altered levels of TCA cycle, purine, glutamate, and pyruvate metabolites at the ring stage. **a** Heat map of the log₂ fold change of significantly different protein levels in Cam3.11^{R539T} or Cam3.11^{C580Y} mutants relative to the isogenic Cam3.11^{WT} parasites for 155 DE proteins identified from isobaric labeling-based quantitative proteomics. Within each biological replicate, two-sided *t*-tests were performed for peptide levels belonging to each protein between K13 mutant and WT isogenic lines. Word cloud representation of functional analysis of significant biological processes and cellular components (Gene Ontology database) for the 87 up-regulated proteins in K13 mutant rings, along with their corresponding *P* values. **b** Relative fold change of K13 protein levels in Cam3.11^{R539T} and Cam3.11^{C580Y} mutants vs. Cam3.11^{WT}, at the ring and trophozoite stages. K13 protein was ~2-fold lower in the Cam3.11^{R539T} rings and trophozoites, as compared to the isogenic Cam3.11^{WT} line. Data points are shown with means of the averaged normalized peptide abundance across two independent experiments for each strain and stage, except for C580Y trophozoites. **c** Scatterplot of the enrichment -log₁₀ *P* score (using a two-sided *t*-test adjusted for multiple comparisons using the Holm-Bonferroni method) of the metabolite pathway and % pathway impact calculated from metabolite set enrichment analysis comparing Cam3.11^{C580Y} and Cam3.11^{WT} rings at basal level. Differential expression of four pathways (*P* < 0.05; gold color) is shown. Circle sizes reflect the pathway impact value, which represents the cumulative percentage of matched metabolite nodes (i.e. the importance measure) with respect to the total pathway based on pathway topological analyses. Box plots show reduced normalized log₂ levels of the two TCA cycle metabolites, malate, and 2-ketoglutarate, and the glutamate metabolite, *N*-acetyl glutamate, but increased level of the purine metabolite, inosine 5'-diphosphate in Cam3.11^{C580Y} as compared to Cam3.11^{WT} rings. Data are represented as box and whisker plots with medians, interquartile ranges, and 95% confidence intervals (*N* = 3 independent experiments). **d** Interactome network of the 21 putative K13-interacting partners detected by co-immunoprecipitation (co-IP) with the K13-specific monoclonal antibodies E3 and D9 (ref. 41) and mass spectrometry experiments using K13 WT, C580Y, or R539T samples from either the Cam3.11 or CamWT strain background¹⁶. Proteins were clustered using the Markov Cluster Algorithm in STRING. Line thickness depicts the confidence/strength of the relationship between proteins (nodes). Solid lines represent intra-cluster interactions while dashed lines represent the interaction between clusters. Red nodes correspond to mitochondrial proteins, which are over-represented in this list of co-IP proteins. Gene abbreviations are listed in Supplementary Data 5.

with differential levels between the mutant and WT parasite (Supplementary Fig. 5c, d). The Cam3.11^{C580Y} parasite had lower levels of malate and 2-ketoglutarate, both of which serve as TCA cycle intermediates, and *N*-acetyl glutamate, a glutamate metabolite, consistent with higher NADP-specific glutamate dehydrogenase and glutamine synthetase RNA transcripts in the

mutant lines (Fig. 3c). In contrast, we observed higher levels of the nucleoside precursor inosine 5'-diphosphate and pyruvate metabolite phosphoenolpyruvate (PEP). These findings were consistent with higher HGXPRT protein abundance and elevated PEP carboxykinase RNA transcript levels (Fig. 2d and Supplementary Figs. 2d and 5d, e). Collectively, these data suggest a

higher reliance on reverse glutaminolysis, with alterations in glycolysis/gluconeogenesis, the mitochondrial TCA cycle, and purine metabolism in the K13 mutants.

Co-immunoprecipitation assays identify mitochondrial factors as major putative K13-interacting partners. To identify putative interactors of K13 that could drive these RNA, protein, or metabolomic changes described above, we earlier performed co-immunoprecipitation (co-IP) and mass spectrometry experiments using custom-raised K13-specific monoclonal antibodies on *k13*-edited and WT Cambodian isolates. The specificity of these antibodies was validated using western blot and IFA data comparing our K13 signals with results from parasite lines expressing GFP-K13 or 3×HA tagged K13 (ref. 41). These experiments yielded 21 proteins that were present in at least half of the six co-IP experiments, and absent in four negative resin controls. Interactome analyses using the STRING database, which uses published biological data to search for observed and predicted protein–protein interactions⁴², predicted a statistically significant enrichment for interactions among these proteins (protein–protein interaction *P* value of 3.1E−7) (Fig. 3d and Supplementary Data 5). Besides identifying physical associations of K13 with chaperones involved in protein folding and vesicle trafficking, we also observed an over-representation of mitochondrial-localized proteins (in 9 of 21 proteins; Fig. 3d, red nodes). These proteins are important for a range of mitochondrial functions including the TCA cycle (fumarate hydratase and multiple 2-oxoglutarate dehydrogenase components), the ETC (cytochrome *b_c1* complex), translation (elongation factor Tu), Fe–S protein synthesis (ferrodoxin reductase-like protein), and antioxidant processes (thioredoxin peroxidase 2). This evokes a potential functional interplay between mitochondrial metabolism, signaling, and the unfolded protein response in *P. falciparum*.

Metabolomic and transcriptional response of K13 parasites to DHA. We next applied metabolomics and transcriptomics approaches to explore the response of K13 lines to DHA exposure. Metabolomic profiling of parasites after a 3 h treatment with 70 or 350 nM DHA revealed a substantial reduction in the levels of several hemoglobin-derived peptides (including LD, SD, PE, PD, PEE, DLS, DLH, and PVNF) in Cam3.II^{C580Y} and Cam3.II^{WT} (Fig. 4a). This reduction was of a similar magnitude in both Cam3.II K13 mutant and WT lines at ring and trophozoite stages. In the absence of DHA, there was no difference in hemoglobin-derived peptides levels between Cam3.II^{C580Y} and Cam3.II^{WT} rings (Supplementary Fig. 5f). This finding suggests that the reduction in hemoglobin-derived peptides upon treatment with DHA occurs via a K13-independent mechanism, involving either the inhibition of hemoglobin uptake or its digestion by the parasite.

Mutant K13 promotes recovery after initial cell-cycle arrest in DHA-treated parasites. To further characterize the effects of DHA on cell-cycle progression and the protection afforded by K13 mutations, early ring-stage parasites were subjected to a 6 h pulse of 700 nM DHA or 0.1% DMSO vehicle control and samples were collected during and after DHA exposure (Fig. 1). Transcriptional profiling and age mapping of WT and mutant lines ± DHA using Spearman rank correlations revealed that DHA-sensitive K13 WT parasites were completely halted in their developmental progression over the period of 6–48 h post DHA treatment (Fig. 4b, c, see solid purple and green lines, and Supplementary Fig. 1b–f). In contrast, DHA-resistant K13 mutants stalled for up to 16 h from the start of treatment and then resumed normal cell-cycle development asynchronously (Fig. 4b,

c—see solid aqua, blue, and orange lines). The speed of re-initiation of transcriptional activity correlated with the degree of parasite's resistance to ART afforded by the K13 mutation in the Dd2 and Cam3.II backgrounds (Fig. 4b, c). Developmental differences were independently verified by Giemsa smears. Morphologically, we observed that DHA-treated K13 WT parasites failed to develop beyond rings, with pyknotic forms seen 24 h post DHA treatment. In contrast, a subset of DHA-treated K13 mutant parasites recovered after the initial drug-induced developmental arrest, progressed to schizonts, and reinvaded RBCs to form new rings (Fig. 4d and Supplementary Fig. 6).

Differential transcriptional response of K13 mutants and WT lines to DHA treatments. Compared to the transcriptional impact of K13 mutations, DHA treatment affected a much larger number of genes, up to 2530 and 2517 in K13 WT Dd2 and Cam3.II parasites respectively (at *P* < 0.05; with cutoffs of >1.4-fold for either Dd2 or Cam3.II). These transcriptional changes occurred mostly at 32–40 h post treatment (Supplementary Fig. 7). Gene set enrichment analyses with Dd2^{WT} rings revealed that pathways relating to protein metabolism such as protein ubiquitination, degradation, folding, and translation, as well as redox and glycolysis, were significantly down-regulated within 6 h of initiating DHA treatment (*P* < 0.05 and false discovery rate < 0.3; Supplementary Data 6). Our observations agree with a prior report that DHA treatment of K13 WT drug-sensitive parasites caused a rapid drug-triggered shutdown in critical cellular processes⁴³. We note that fewer genes were DE in K13 mutants vs. WT parasites after DHA exposure and the transcriptional changes in these genes were attenuated (Supplementary Fig. 7).

To identify genes that associate with the survival of post DHA-pulsed K13 mutant parasites, we applied two-factor ANOVA on transcriptional responses in the Dd2 and Cam3.II lines, stratified by K13 status (mutant vs. WT) and treatment condition (DHA vs. DMSO control). In total, 667 and 192 genes were DE from 3 to 48 h post initiation of DHA treatment in Dd2 or Cam3.II mutants vs. their WT counterparts respectively (Fig. 4e and Supplementary Data 7). We observed a larger divergence in transcriptional response to DHA between Dd2^{R539T} and Dd2^{WT} than between Dd2^{C580Y} and Dd2^{WT} (Fig. 4e), consistent with the higher survival rate in the R539T mutant compared with C580Y. Further analyses of the initial 3 and 6 h post DHA/DMSO transcriptional responses in Dd2^{R539T} parasites that associated with elevated survival in the early ring stage identified 348 and 234 genes with higher and lower RNA expression, respectively, in the DHA-treated Dd2^{R539T} mutant relative to the Dd2^{WT} line (*t*-test; *P* < 0.05) (Fig. 4f). Functional enrichment analyses revealed highly similar up-regulated gene sets at the initial 6 h time point and throughout the 48 h sampling, including Rab-mediated vesicular trafficking (Rab 1A, 5B, and 11A), secretory and endocytic complexes, organellar transcription, and mitochondrial ATP production (Fig. 4f and Supplementary Fig. 8a). These pathways were also observed in analyses of DHA-treated Cam3.II^{R539T} vs. WT lines (Supplementary Fig. 8a, indicated with #, and Supplementary Data 7). Gene sets specific to 6 h response comprise tRNA modifications and lipid transport and those at 48 h in both backgrounds were limited to redox and DNA excision repair. In contrast, fewer commonalities were seen between down-regulated genes in DHA-treated K13 mutants as compared to WT parasites, in both parasite backgrounds (Supplementary Fig. 8b and Supplementary Data 7). Genes down-regulated in DHA-treated Dd2^{R539T} vs. Dd2^{WT} from 6 to 48 h were enriched for protein folding and ER heat-shock chaperones, autophagy markers (ATG7 and ATG18), and phosphorylated proteins (Fig. 4f). At the 6 h time point, we observed down-regulation of

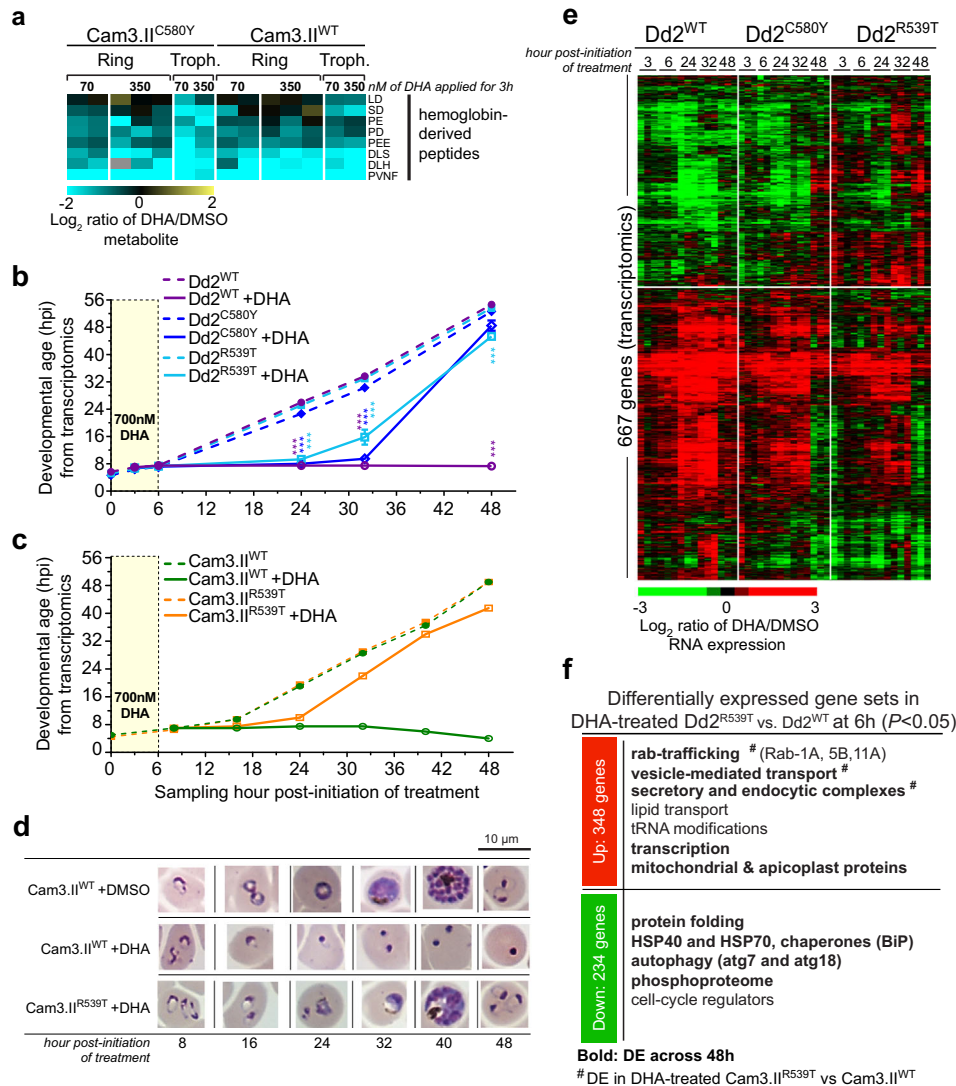


Fig. 4 Short-term DHA exposure results in a decrease of hemoglobin-derived peptides, and a temporary, reversible cell-cycle arrest in K13 mutant parasites, concomitant with distinct transcriptional responses between K13 mutant and WT parasites. **a** Heat map of log₂ fold changes in DHA-treated Cam3.II^{C580Y} or Cam3.II^{WT} parasites vs. DMSO controls for the eight metabolites that showed a significant change in level after parasites were pulsed with either 70 or 350 nM DHA for 3 h. DHA treatment at rings and trophozoites resulted in a consistent down-regulation of host hemoglobin-derived peptides in both lines. For levels in untreated rings, see Supplementary Fig. 4f. **b, c** Transcriptome-based age estimation of the *k13*-edited R539T, C580Y, and WT in Dd2 or Cam3.II parasites after 6 h pulsed exposure to either 700 nM DHA (solid lines) or DMSO vehicle control (dashed lines). Parasites were sampled up to 48 h post treatment and developmental ages were determined using Spearman rank correlations. Results shown as means ± SEM ($N = 3$ for each Dd2 line and $N = 1$ for Cam3.II lines). $***P < 0.001$, unpaired two-sided t -tests. P values in **b** are: 24 h time point—Dd2^{WT} DHA vs. DMSO $P = 1.7E-5$, Dd2^{C580Y} DHA vs. DMSO $P = 1.7E-5$, Dd2^{R539T} DHA vs. DMSO $P = 4.7E-6$; 32 h time point—Dd2^{WT} DHA vs. DMSO $P = 2.5E-6$, Dd2^{C580Y} DHA vs. DMSO $P = 2.4E-6$, Dd2^{R539T} DHA vs. DMSO $P = 0.002$; 48 h time point—Dd2^{WT} DHA vs. DMSO $P = 3.7E-9$, Dd2^{R539T} DHA vs. DMSO $P = 3.8E-6$. **d** Giemsa-stained parasite images showed that DHA-treated Cam3.II^{WT} parasites became pyknotic after 24 h, whereas Cam3.II^{R539T} parasites underwent a lag in progression through the IDC following DHA treatment, compared to DMSO mock-treated controls. These images are representative of the majority (>50%) of parasites observed at each time and condition per parasite line, with additional examples provided in Supplementary Fig. 6. Microscopy analyses were performed for at least 5000 cells counted across three independent experiments, which yielded similar results. **e** Heat map of log₂ ratios of DHA-treated/DMSO-treated mRNA expression levels for the 667 hierarchically clustered genes whose expression differed significantly in the Dd2^{C580Y} and/or Dd2^{R539T} mutants as compared with Dd2^{WT} parasites across 3–48 h post initiation of treatment ($N = 3$ independent experiments; two-factor ANOVA with adjusted $P < 0.05$; pathways listed in Supplementary Fig. 6 and Supplementary Data 7). A more divergent transcriptional response was observed with Dd2^{R539T} parasites that display high levels of ART resistance in vitro compared with Dd2^{C580Y} parasites¹⁶. **f** Functional enrichment analyses identified biological pathways significantly enriched ($P < 0.05$, hypergeometric tests) among the genes that were up- or down-regulated in the DHA-treated Dd2^{R539T} as compared with Dd2^{WT} parasites relative to DMSO controls in early rings after 3 and 6 h post DHA exposure. Up-regulated genes were relatively more abundant, reflecting increased transcript levels induced by DHA-treated Dd2^{R539T} parasites vs. Dd2^{WT} parasites as compared to their respective DMSO controls. Down-regulated genes reflected a reduction in transcription or faster turnover of these transcripts in DHA-treated Dd2^{R539T} parasites vs. Dd2^{WT} parasites, compared to their DMSO controls. Gene sets in bold or labeled as # were differentially expressed over the 48 h period of sampling or between DHA-treated Cam3.II^{R539T} parasites vs. isogenic Cam3.II^{WT} parasites respectively (see Supplementary Data 7 for pathways and genes).

cell-cycle regulators, which may be important for the parasite's exit from a temporary state of DHA-induced quiescence. Our data suggest that in WT parasites DHA causes a shutdown of energy-related processes. In contrast, processes including synthesis of ATP and vesicular transport across the ER, Golgi, and plasma membranes can remain transcriptionally active in resistant K13 mutant parasites even as early as 6 h post DHA exposure and can be sustained up to 48 h post DHA removal. Higher expression of membrane-bound transporters and the ATP synthase complex subunits might reflect the enhanced ability of K13 mutants to maintain their intracellular pH gradients and ATP levels following DHA-induced oxidative stress.

Multi-omics results associate K13 with mitochondria-related energetic processes. Given our multi-omics results that linked K13 to mitochondrial and purine metabolism (Fig. 2d and Fig. 3a, c, d), we assessed the susceptibility of K13 mutant and WT parasites to a panel of mitochondrial and purine metabolism inhibitors (Fig. 5a). Dose-response assays showed that Cam3.II^{R539T} and Cam3.II^{WT} parasites had equivalent sensitivities to inhibitors of mitochondrial protein synthesis (fusidic acid), purine metabolism (immucilin G and H and ribavirin), or pyrimidine metabolism (the DHODH inhibitor DSM265). These results were

obtained in both 4 h assays that measure activity against early rings and 72 h standard assays (Fig. 5b and Supplementary Fig. 9a). In contrast, with the slower-acting mitochondrial ETC inhibitor atovaquone^{44,45} (ATQ), we noted a subtle yet statistically significant 1.6-fold increased sensitivity in Cam3.II^{R539T} rings as compared with isogenic Cam3.II^{WT} rings (shown as lower IC₅₀ and IC₉₀ values in Fig. 5b). Individual IC₅₀ and IC₉₀ data are provided in Supplementary Data 8.

K13 mutant parasites exhibit differential responses to atovaquone plus DHA. We next performed drug combination assays by exposing tightly synchronized early ring-stage parasites to varying concentrations of both DHA and ATQ, as determined by molar ratios of their individual IC₅₀ values. Dose-response curves with early rings exposed for 4 h to increasing ratios of ATQ:DHA showed evidence of increased ATQ sensitization of Cam3.II^{R539T} but not Cam3.II^{WT} parasites to DHA (Fig. 5c, d). At a 4:1 ATQ:DHA ratio, the Cam3.II^{R539T} parasites became fully sensitive to DHA. Isobologram analyses of the 4 h pulsed ATQ and DHA drug-pair combination assays revealed moderate synergy in Cam3.II^{R539T}, whereas an additive interaction was seen in the DHA-sensitive Cam3.II^{WT} line as well as the Cam3.II^{C580Y} line that was less resistant than the R539T mutant (Supplementary

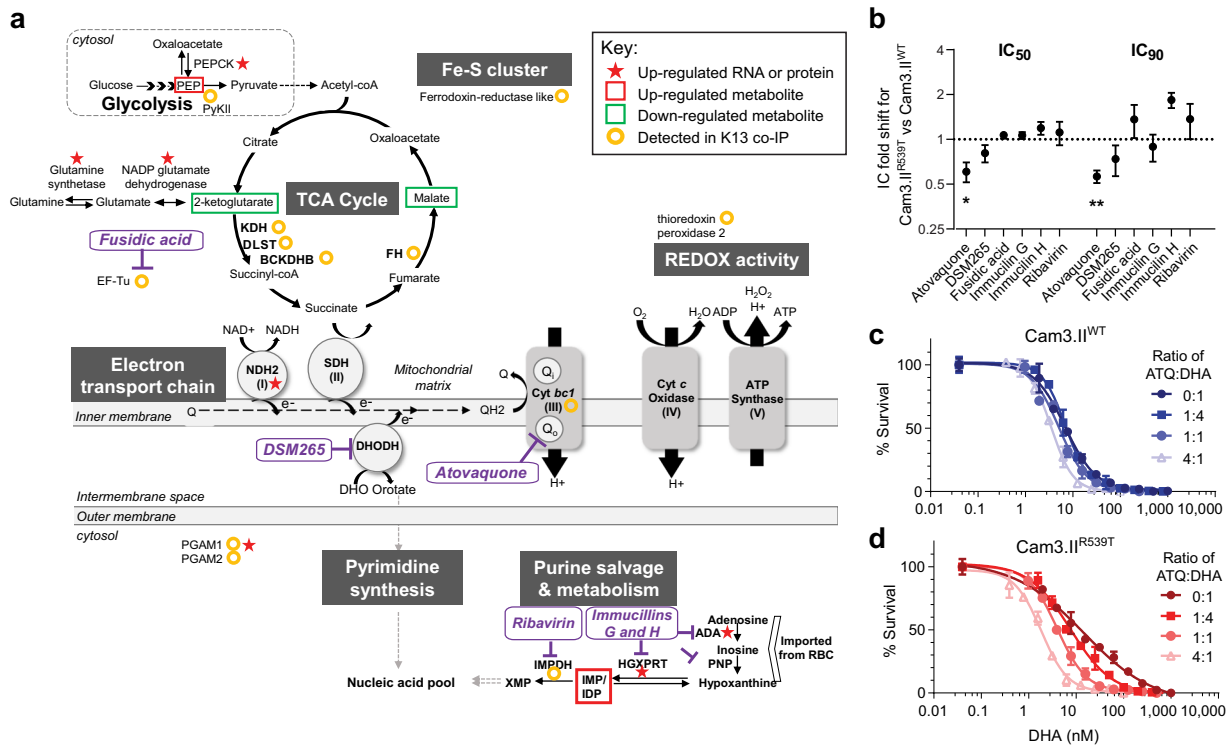


Fig. 5 Multi-omics data and dose-response assays reveals K13's role in maintaining mitochondrial ETC functions. **a** Schematic of the energy and purine metabolism pathways in the parasite mitochondrion. Genes, proteins, metabolites, and co-IP proteins that were detected as differentially regulated between isogenic K13 mutant and WT parasites in multi-omics experiments are highlighted. ADA adenosine deaminase, DHODH dihydroorotate dehydrogenase, DLST dihydrolipoylysine-residue succinyltransferase, HGXPRT hypoxanthine-guanine-xanthine phosphoribosyltransferase, IMPDH inosine 5'-monophosphate dehydrogenase, PNP purine nucleoside phosphorylase. For full list of protein names, refer to Supplementary Data 5. **b** IC₅₀ and IC₉₀ fold shifts for Cam3.II^{R539T} vs. Cam3.II^{WT} 0–3 hpi early rings exposed for 4 h to a panel of inhibitors targeting mitochondrial processes (atovaquone, DSM265, fusidic acid) or purine metabolism (immucilin G and H, ribavirin). Shown are means ± SEM values from two to five independent experiments with technical duplicates. ***P* = 0.008, **P* = 0.024, two-tailed one-sample *t*-tests of the IC fold shift. Individual IC₅₀ and IC₉₀ data are provided in Supplementary Data 8. **c** Four hour dose-response assays conducted on Cam3.II^{WT} 0–3 hpi early rings, depicting no change in the DHA dose-response curves in the presence of increased ATQ to DHA ratios. **d** Four hour dose-response curves show increased sensitization of Cam3.II^{R539T} 0–3 hpi early rings to DHA with higher ratios of ATQ to DHA. The mitochondrial ETC inhibitor ATQ displays increased potency when combined with DHA against Cam3.II^{R539T} parasites in 4 h drug treatments. Dose-response assays were performed in three to five independent experiments with technical duplicates for each parasite line. The data presented in **c** and **d** are exemplars from one independent experiment with error bars representing the SD between technical duplicates. Also see Supplementary Fig. 9b–e for FIC₅₀ curves and isobologram analyses.

Fig. 9b). This synergy was reflected in a significantly lower Combination Index (the averaged sum of fractional IC₅₀ (FIC₅₀) values), in Cam3.II^{R539T} compared to Cam3.II^{WT} parasites (Supplementary Fig. 9b, inset). In 72 h assays, an antagonistic relationship between ATQ and DHA was observed, with its effect being most pronounced in WT parasites and less so in C580Y and especially R539T parasites (Supplementary Fig. 9c). These results were reproduced, albeit to a lesser degree, in Dd2 parasites that carry the same K13 genotypes and that are comparatively less DHA-resistant than the Cam3.II lines (Supplementary Fig. 9d, e). These results suggest that ATQ-mediated inhibition of the mitochondrial cytochrome bc₁ Q_o site can reduce the recovery of K13 mutant ring-stage parasites following treatment with oxidant ART drugs.

Discussion

Our multi-omics analysis of isogenic *P. falciparum* lines expressing mutant or WT isoforms of the ART resistance determinant K13 reveal a striking array of physiological processes in asexual blood stage parasites that are uniquely altered by K13 mutations (Fig. 6). First, cell-cycle periodicity was differentially impacted. The parasite’s developmental progression decelerated during the ring stage in the C580Y mutant but not in the R539T mutant. This contrasted with K13 protein levels that were not significantly altered in the C580Y mutant yet were lower in the R539T mutant. Recent reports highlight an association between K13 inactivation and lowered endocytosis, where less host hemoglobin is taken in and digested, resulting in less liberation of Fe²⁺-heme and reduced ART activation^{27,28,46}. Based on our findings, reduced endocytosis could stem from either lowered K13 protein levels and activity in the R539T mutant or prolonged ring development caused by the C580Y mutation. Upon DHA exposure, K13 mutant trophozoites were earlier reported to show net reductions in heme-DHA adducts, relative to WT counterparts^{39,47}. Our

observation that fewer genes were DE in DHA-treated K13 mutant parasites, as compared to DHA-treated isogenic WT lines, supports the hypothesis that a lower level of activated ART accumulates and exerts its effect in K13 mutant parasites. However, this did not account for the increased rates of survival of DHA-treated rings (0–6 hpi) elicited by K13 mutations and the re-initiation of growth after a temporary arrest, implicating a role for additional survival mechanisms. Furthermore, in our study the reduction in hemoglobin-derived peptides upon treatment with DHA, observed within 3 h of drug exposure, occurred to a similar degree in both K13 mutant and WT parasites. These results suggest that the mechanism of ART resistance afforded by mutant K13 extends beyond a role for reduced hemoglobin endocytosis in rings.

Our transcriptomic analysis revealed that in the absence of DHA, nearly 400 genes were DE in Dd2^{R539T} and Dd2^{C580Y} mutant parasites as compared to isogenic Dd2^{WT} parasites, across the 48 h IDC. The largest number of DE genes was observed in newly invaded rings, when K13 mutations impart ART resistance. Among these genes, most were up-regulated in the mutants. Gene set enrichment analysis revealed up-regulation of pathways involved in post-translational modifications (including phosphorylation and palmitoylation), protein export or turnover, lipid metabolism and transport, and the mitochondrial ETC. Many of these pathways were conserved between Dd2 and Cam3.II parasites, although individual genes often differed, suggesting that the genetic background influences the impact of K13 mutations on the parasite transcriptome. These data provide evidence for pleiotropic effects of mutant K13 that are common across parasite strains. Other loci must nonetheless be important in determining the extent to which mutant K13 mediates ART resistance. This is shown by the greater levels of RSA survival in Cam3.II parasites compared to Dd2 (40.2% vs. 19.4% for the two respective R539T mutants¹⁶), suggesting that K13 also has epistatic interactions with other modifier loci. Intriguingly, K13-mutant Asian parasites

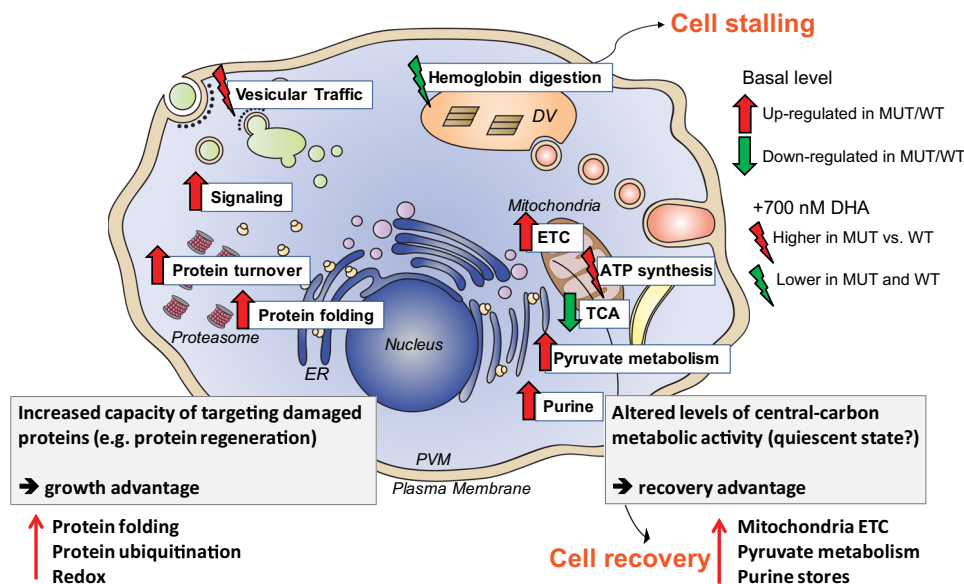


Fig. 6 Proposed model for the role of K13 in ART resistance. K13 mutations are associated with an up-regulation of protein folding as well as proteasome-linked protein turnover that may provide a growth advantage via a greater capacity of the mutant parasite to target and eliminate damaged proteins caused by the proteotoxic ART drug. K13 also appears to be involved in other novel pathways including intracellular signaling, pyruvate metabolism, purine salvage, and the mitochondrial electron transport chain (ETC). These functions suggest an altered central carbon metabolism and represent a quiescent state maintained by the parasite that allows for a recovery advantage following DHA exposure. DHA inhibits hemoglobin uptake or degradation and induces stalling in both K13 mutant (MUT) and wild-type (WT) rings. Recovery in K13 mutants may occur through enhanced mitochondrial ATP metabolic function and remodeling of the parasite’s secretory and vesicular transport processes. Inhibition of mitochondrial ETC activity lowers the survival of K13 mutant parasites to DHA treatment.

were recently found to carry mutant alleles of DNA repair genes that provided enhanced protection against artesunate-mediated DNA damage; several of these genes are also present in Dd2 (ref. 48). Other studies have also reported founder genetic backgrounds on which mutant K13 evolved in Southeast Asia, supporting a role for epistatic interactions that contribute to the resistance phenotype and that may help with a process referred to as cellular healing in ART-treated K13-mutant parasites^{17,49,50}.

K13 C580Y and R539T mutations showed very similar impacts on both parasite transcription and translation in untreated parasites. Transcriptomics and proteomics results overlapped in the up-regulation of chaperone-mediated protein folding and the ubiquitin–proteasome system, as observed in rings of ART-resistant K13-mutant clinical isolates sampled *ex vivo*²⁹. The higher protein abundance of the protein folding factor cyclophilin 19B in K13 mutants reaffirms its earlier report as the top-ranked transcriptional marker in K13 ART-resistant isolates²⁹ and suggest its involvement in enhancing the parasite's capacity to survive the general proteotoxic effects of ART action. In considering these data, we note that experiments had a limited number of independent repeats (generally two) and did not include reference pools or labeling efficiency tests. High reproducibility was nonetheless observed between repeats (Fig. 3a and Supplementary Fig. 3b).

Our combined transcriptomics, proteomics and metabolomics data uncovered new functional modules associated with K13 mutants, including pyruvate and glutamate-linked carbon metabolism, purine metabolism, the mitochondrial ETC, and the TCA cycle (Figs. 5a and 6). Pyruvate and glutamate metabolism are highly connected with mitochondrial functions. Pyruvate metabolism is a core energetics pathway that provides acetyl-coA for the TCA cycle, histone acetylation, and lipid metabolism^{51,52}. Pyruvate and aspartate synthesis can compensate for deficiencies in ETC and membrane potential generation in mammalian cells⁵³. Glutamate is a branch point for carbon and nitrogen metabolism, feeding into the mitochondrial TCA cycle via its conversion into 2-ketoglutarate or into glutamine for nitrogen storage, in preparation for starvation conditions. Our findings of reduced levels of the mitochondrial TCA cycle intermediates malate and 2-ketoglutarate in K13 mutants are consistent with recent modeling predictions based on transcriptional analysis of ART-resistant versus -sensitive clinical isolates⁵⁴. In rodent *Plasmodium* parasites, the addition of malate or succinate promotes oxygen consumption, which contributes to the mitochondrial membrane potential ($\Delta\Psi$) and stimulates complex III activity^{55,56}. The lower levels of malate observed in our metabolomics data suggest that K13-mutant rings might mimic a state of anoxia and lower the ETC complex III activity. Collectively, these findings point towards a rewiring of the energy requirements and metabolic state in K13 mutant parasites, and suggest that a higher reliance on reverse glutaminolysis with altered glycolysis/gluconeogenesis, and lowered mitochondrial TCA cycle and ETC functions, might facilitate the recovery of DHA-treated K13-mutant rings. One question that merits further exploration is whether the reported impact of K13 mutations on reducing hemoglobin endocytosis^{27,28} might trigger a semi-starvation state that accounts for some of our observed metabolic changes. A recent study showed that the Cam3.IR^{539T} Cambodian parasite line¹⁶ showed a threefold better rate of recovery following 72 h of isoleucine starvation as compared with the isogenic Cam3.I^{WT} Cambodian parasite line, suggesting that K13-mutant parasites might be better able to tolerate semi-starvation⁵⁷. Nonetheless, transcriptomic profiling of amino acid-starved 3D7 WT K13 parasites showed a general slowing of transcription across the IDC⁵⁸, without evidence of the specific pathways observed in our study. Metabolomics data in that study also showed minimal

overlap with our results, suggesting that mutant K13-mediated reduction in hemoglobin endocytosis does not readily mimic starvation responses resulting from amino acid deprivation.

Further evidence of mitochondrial-linked function in K13 mutants was seen in K13's physical interaction with mitochondrial factors, which may enable K13 parasites to survive the DHA pulse by reinitiating growth after a temporary 16 h arrest⁴¹. Co-IP experiments identified PGAM2, the parasite ortholog of PGAM5 that is a substrate of the mammalian ubiquitin ligase complex involving the K13 ortholog KEAP1 (refs. 59,60). In mammalian systems, KEAP1 associates physically with NRF2 and PGAM5 on the outer mitochondrial membrane. Upon stress, the mitochondrial unfolded protein response occurs via dissociation of KEAP1 from the NRF2–PGAM5 protein complex, leading to retrograde signaling from the mitochondria to the nucleus and expression of antioxidant and stress response genes⁶⁰. We also observed an increased expression of redox enzymes 48 h after DHA treatment in K13 mutant parasites. These findings evoke a potential functional interplay between mitochondrial metabolism, signaling and the unfolded protein response in *P. falciparum*. We note that our co-IP results differ from the set of K13-interacting proteins identified using a quantitative dimerization-induced bio-ID approach with GFP-tagged K13 (ref. 27). Partial overlap was nonetheless observed between our study and a separate report that used GFP-Trap beads to affinity purify GFP-K13 and then identified the immunoprecipitated proteins¹⁸. These results merit further investigation using independent approaches such as co-IP data with antibodies specific to mitochondrial proteins, which we are to date unable to obtain.

Upon exposure to DHA, survival of K13 mutants was associated with a shutdown of core metabolic functions including protein synthesis, transcription, and glycolysis, accompanied by sustained elevated RNA expression of specific pathways including vesicle-mediated intracellular transport and ATP production. The association with vesicular transport recalls earlier associations between mutant K13 and amplification of PI3P-positive vesicles that were postulated to neutralize ART proteotoxicity³⁴. The speed of re-initiation of transcriptional activity correlated with the degree of ART resistance afforded by K13 mutations in the Dd2 and Cam3.II backgrounds. We hypothesize that this might occur via the regulation of mitochondrial-linked quiescence. This possibility is supported by the greater extent of sensitization to DHA by ATQ (an ETC complex III Q_o ubiquinol oxidation inhibitor) in the Cam3.II mutants compared to the Dd2 K13 mutants (that impart lower resistance) or sensitive WT lines.

In the mitochondria of mammalian cells, redox equilibrium is regulated through functions including oxygen uptake, ATP production, maintenance of membrane potential, and generation of reactive oxygen species. Dysregulation of these processes can drive cells towards senescence or proliferation^{52,61}. In certain cancerous states, cells can switch between senescence and proliferation by modulating their reliance on glycolysis vs. oxidative phosphorylation (involving the TCA cycle and the ETC)^{52,62,63}. Recent research has described drug-induced “low glycolysis-low oxidative phosphorylation” phenotypes that enable mammalian cells to survive drug challenge⁶². A potential role for mitochondria in sensing ART action and regulating cellular quiescence was recently evoked in a study with *Mycobacterium tuberculosis*, which found that ART can inhibit intracellular signaling and persistence via adduct formation with heme-carrying kinases that act as redox or hypoxia sensors⁶⁴. In *P. falciparum*, we also observed substantial mitochondrial oxidation within 4 h of DHA treatment, at levels considerably greater than those observed with either chloroquine or ATQ⁴¹. Our data suggest a metabolic rewiring in *P. falciparum* parasites, with a dysfunctional

mitochondrion that can be perturbed by combining ATQ with DHA. Interestingly, a genome-wide CRISPR/Cas9 screen in the Apicomplexan parasite *Toxoplasma gondii* recently identified components of the TCA cycle and heme biosynthesis as mitochondrial determinants of DHA susceptibility⁶⁵. One important distinction, however, is that unlike *Plasmodium*, *Toxoplasma* parasites do not endocytose or metabolize hemoglobin, thereby removing this pathway for ART activation. Further studies are merited to assess whether altered mitochondrial metabolism might constitute a vulnerability that can be leveraged to overcome ART resistance.

In summary, our findings suggest that interconnected mechanisms might poise K13 mutant parasites to survive DHA treatment and increase the parasite's proteostatic capacity. These mechanisms include an enhanced ability to eliminate damaged proteins through the unfolded protein response and ubiquitin-proteasomal machinery, and remodeling of secretory and vesicular transport processes that impacts hemoglobin endocytosis and protein and lipid trafficking (Fig. 6). K13 mutations may also facilitate rapid recovery post ART exposure by adjusting their central carbon-linked pyruvate and glutamate metabolism, and enabling mitochondrial sensing of cellular damage and the protection and subsequent survival of a subset of drug-exposed parasites (Fig. 6). Further investigation into these mechanisms, which will require additional validation, promises to deliver new approaches to target ART-resistant *P. falciparum*, a goal that is increasingly important given the global dissemination of drug-resistant malaria.

Methods

Parasite lines and culture conditions. *P. falciparum* parasites were cultured at 3% hematocrit in human O⁺ RBCs (Interstate blood bank, USA) and *P. falciparum* culture media comprising RPMI 1640 (Thermo Fisher Scientific) supplemented with 0.5% (w/v) Albumax II, 50 mg/L hypoxanthine, 0.225% NaHCO₃, 25 mM HEPES, and 10 mg/L gentamycin⁶⁶. Parasites were cultured at 37 °C in 5% O₂, 5% CO₂, and 90% N₂. Parasite lines were genotyped by Sanger sequencing *k13* to verify their identities before the start of an experiment. Dd2 and Cam3.II parasites were previously reported¹⁶, with Cam3.II^{WT} earlier referred to as Cam3.II^{ev}. We note that Dd2 was adapted to culture in 1980, decades before the introduction of ART derivatives, whereas Cam3.II was adapted in 2010 a decade after ARTs entered widespread use in the region^{16,67}.

Sample preparation for microarray-based transcriptomics. To obtain tightly synchronized parasites, the K13 mutant or WT lines Dd2^{R539T}, Dd2^{C580Y}, Dd2^{WT}, Cam3.II^{R539T}, and Cam3.II^{WT} (Fig. 1) were doubly synchronized with 5% D-Sorbitol every IDC cycle for at least three cycles, prior to collecting samples for RNA. We confirmed that parasite cultures were highly synchronous by microscopy, which showed that >95% of all parasites were early rings at the start of each time course experiment. We also computationally assessed transcriptomic profiles by applying Spearman rank correlation calculations for each parasite sample to multiple time points across the IDC of a highly synchronized reference transcriptome (see Supplementary Fig. 1b–e). This analysis yielded mean ± SD correlation coefficients of 0.68 ± 0.03 across samples, as expected for highly synchronized cultures based on our earlier studies⁶⁸. RSAs with the synchronized rings used to initiate our transcriptome sampling yielded survival values that agreed closely with our earlier published data¹⁶.

Samples were collected every 8 h throughout the IDC for the Cam3.II^{R539T} and Cam3.II^{WT} lines, and at 0, 3, 6, 24, 32, and 48 hpi for the Dd2^{R539T}, Dd2^{C580Y} and Dd2^{WT} lines. After washing the packed RBC pellets with 1× phosphate-buffered saline (PBS) pH 7.4, a 10× pellet volume of TRIzol was added to the pellet and total RNA was extracted using an acidified phenol-chloroform method⁶⁹. Total RNA was reverse transcribed into cDNA using Superscript II reverse transcriptase and the SMART protocol, with template switching at the cDNA 3' ends⁶⁹. The cDNA was amino allyl-dUTP labeled using 30 cycles of PCR amplification. Four micrograms of each sample was then labeled with Cy5 fluorescent dyes and mixed with an equal amount of a Cy3 labeled pool comprising mixed asexual blood stages of the reference strain 3D7. Samples were hybridized on a custom *P. falciparum* 70-mer long oligonucleotide microarray chip containing 11,400 probes (GEO Platform: GPL18893) at 65 °C for 20 h²⁹. This approach was used to generate transcriptional profiles for 156 samples and was chosen as a cost-effective alternative to RNA-seq. Arrays were washed and scanned using the autogain PMT setting on a Tecan PowerScanner.

Data analyses for transcriptomics. Data processing used GenePix Pro software (Molecular devices) and the R Bioconductor LIMMA package version 3.10.3. Only spots with flag >0, and a feature intensity greater than 1.5-fold higher than the background intensity in either Cy5 or Cy3 channel, were included. Background correction used the *Normexp* algorithm and probe ratios were normalized for each array using the Loess method⁷⁰. Ratios of all probes mapping specifically to each gene were averaged to generate a list of gene log₂-transformed ratios, representing the log₂ ratio of transcript abundance in the sample to transcript abundance in the 3D7 reference pool. For each individual isolate, treatment condition, and replicate IDC, we retained genes present in >66% of the time points, i.e. genes were retained only if they were present in at least 5 out of 7 time points, 4 out of 6 time points, or 8 out of 12 time points. Retained genes also had to be present across the three independent experiments for each parasite line to avoid bias introduced by detection in only one biological experiment. Between 19 and 71 genes were filtered out for each replicate group and these comprised mainly multigene families including *rifins* and *stevors*. Missing data were imputed across all stages and replicates belonging to a given parasite line, using the KNN function applied to a nearest neighbor of 10 genes. This method increased robustness with the imputations while maintaining the specificity for each strain. We used the KNN method to impute missing data, as polynomial fitting or Fast Fourier Transformations did not produce good fits if values were missing at the starting or end points or if sample collection was not regularly spaced over time. After imputing missing data, >4990 (90%) *P. falciparum* genes were analyzed for each parasite strain and were annotated accordingly (PlasmoDB v46).

Generating a high-resolution Dd2 reference transcriptome model. Because *P. falciparum* gene expression is a sine-wave function, we generated a high-resolution transcriptome of the reference Dd2 line by interpolating RNA expression of each gene at 30-min time intervals (from a dataset of samples harvested every 2 h). These interpolations used linear regression of polynomial fitting with strict cutoffs of Fisher's exact test $P < 0.001$, adjusted $R^2 > 0.7$, and the Bayesian's Information Criterion (BIC) to find the optimum degree of fit for each gene. Coefficients of the polynomial equation were applied to generate log₂ expression ratios at 30-min intervals from 0 to 48 hpi, resulting in 96-time points per gene. In total 4342 genes that could be fitted into a polynomial curve were obtained for the Dd2 reference transcriptome. The predicted 96-time point transcriptomes had very high correlations of 0.94 ± 0.05 (mean ± SD) with the actual 24-time-point transcriptomes sampled across the 24 time points. Applying a filter of max-min expression >2-fold gave us 3500 genes that each had a clear peak of expression at a particular stage in the IDC. This was used to calculate the sample age (in hpi) of each parasite sample time point. Principle component analysis (using the TM4 MeV software version 4.8.1) was performed on each sample to identify underlying variables that contributed to expression differences.

To identify DE genes in the K13 mutant lines across the IDC, we performed Student's *t*-tests with replicates of K13 mutant vs. WT samples or between DHA-treated and DMSO vehicle-treated samples, using the log₂ RNA expression levels at each sampling time point for rings, trophozoites, and schizonts. To identify genes that showed a significant difference between the K13 mutant and WT lines in their transcriptional response to DHA exposure, we applied two-factor ANOVA with permutations using subtracted log₂ RNA expression ratios of drug-treated vs. DMSO control samples. This was performed in each parasite background across all sampling time points or at the initial 3 and 6 h treatment time points. Kyoto Encyclopedia of Genes and Genomes (KEGG), Gene Ontology (GO), and Malaria Parasite Metabolic Pathway (MPMP) gene sets derived from PlasmoDB were used for functional enrichment analyses of the DE genes by hypergeometric testing, as described²⁹. DE genes and pathways in K13 mutants vs. WT lines are listed in Supplementary Data 1 and 2. DE pathways in response to DHA in K13 mutants and WT lines are listed in Supplementary Data 6 and 7.

Sample preparation for untargeted liquid chromatography-tandem mass spectrometry (LC-MS/MS) proteomics. Cam3.II^{R539T}, Cam3.II^{C580Y}, and Cam3.II^{WT} parasites were doubly synchronized using 5% D-Sorbitol for each IDC for at least 2–3 cycles. Early-mid rings or trophozoites of each parasite line were harvested by washing with 1× PBS and then lysed with 0.1% saponin in the presence of a protease inhibitor cocktail (Roche). For each parasite line, we harvested ring and trophozoite stages on two independent occasions, except for Cam3.II^{C580Y} trophozoites that were harvested only once. Parasite extracts were lysed to release proteins and 600 µg of protein of each sample was digested with trypsin and processed as described⁷¹. Briefly, the saponin-treated parasite pellets were lysed with TEG buffer (50 mM Tris-HCl, 0.5 mM EDTA, 5% β-glycerol phosphate, 1% NP-40, pH 7.4) containing protease and phosphatase inhibitors on ice for 10 min. Samples were centrifuged at 20,000g for 3 min, and the supernatant collected. The pellet was again resuspended in TEG buffer without NP-40 and sonicated 3 × 15 s on ice and then centrifuged at 20,000g for 3 min. An additional extraction step was performed for ring samples where the pellet was resuspended in the TEG buffer with 2% CHAPS and 0.5% SDS, and sonicated 3 × 15 s on ice and then centrifuged at 20,000g for 3 min. The two (trophozoite) or three (ring) supernatant fractions were then combined. Protein concentrations in the final lysates were in the range of 1.2–4.7 mg/mL for rings and 4.3–6.0 mg/mL for trophozoites in a final volume of 0.6 mL. 0.6 mg of protein from each sample lysate was dissolved in 1 mL TEG

buffer (10 mM Tris, 5 mM EDTA, 20 mM β -glycerol phosphate, pH 7.4) and denatured at 37 °C for 30 min in the presence of 10 mM DTT and 0.1% SDS. Iodoacetamide (1 M solution) was then added to a final concentration of 100 mM, adjusted to pH 8.0, and samples were incubated for 1 h at room temperature in the dark. Protein was precipitated on ice for 10 min by addition of 100% trichloroacetic acid (at a ratio of 1:3) to the samples and harvested by centrifugation for 5 min at 2000g followed by two washes with 1 mL TEAB (triethylammonium bicarbonate, pH 8.5). All washing buffer was removed before the protein pellets were sonicated in 300 μ L of 50 mM TEAB buffer on ice for 3×15 s and digested with trypsin (Promega) at a ratio of 1:20 (w/w) trypsin to protein content, overnight at 37 °C on a rotating platform. Samples were then concentrated to about 0.3–0.5 mL in a Speedvac centrifuge.

For each LC-MS/MS experiment, each parasite line was labeled with a unique isobaric tag (tandem mass tag, TMT 6-plex) and pooled to allow direct comparisons of the proteomic levels of the K13 mutants vs. WT samples. Given the small number of samples, it was not possible to introduce a complete randomization. Instead, we assigned different tags to different samples and runs, as detailed in our data deposited to the ProteomeXchange Consortium (see Data availability section below). Reference pools were not used to internally normalize samples. The experimental design flow chart is shown in Fig. 1. After incubation with TMT reagents, the labeled samples were pooled and concentrated to a volume of 1.2 mL in a Speedvac centrifuge, then mixed with 0.3 mL of 100% acetonitrile and diluted with 10 mM TEAB, pH 8.0 to a final volume of 3 mL. Samples were fractionated using a Resource Q anion-exchange column (GE Healthcare). Peptides were eluted by a linear gradient of 0–1 M NaCl in 10 mM TEAB, pH 8.0, collecting 1 mL fractions. The fractions were concentrated and run on the LTQ-Orbitrap-Velos mass spectrometer (Thermo Scientific). The raw data file was processed using Proteome Discoverer version 2.1 (Thermo Fisher Scientific), searching each file using Mascot version 2.6.0 (Matrix Science Ltd.) against the UniProtKB-Swiss Prot database or a decoy database. To minimize variability, samples were combined on a single MS/MS run. Of note, we identified very few peptides that lacked a TMT tag. Given the abundance of tagged peptides, we estimated the labeling efficiency as >99%.

Data analysis for proteomics. Scaffold Q+ (version Scaffold 4.8.2, Proteome Software Inc., Portland, OR) was used to quantify TMT label-based peptides. We applied the following criteria to confidently assign proteins and generate the global protein expression levels. Peptide identifications were accepted if they could be established at >95% probability. Peptide probabilities from X! Tandem were assigned by the Peptide Prophet algorithm⁷² with Scaffold delta-mass correction. Protein identifications were accepted if they could be established at >48% probability to achieve a false discovery rate <1.0%, and contained at least one identified peptide unique to the assigned protein. Protein probabilities were assigned by the Protein Prophet algorithm version 5.0 (ref. 72). Proteins that contained similar peptides and could not be differentiated based on MS/MS analysis alone were grouped to satisfy the principles of parsimony. Normalization of ion intensities was performed iteratively across samples and spectra, using an ANOVA model to account for variability across MS acquisitions and between channels, as described⁷³. Spectra data were log-transformed, pruned of those that matched to multiple proteins, and weighted by an adaptive intensity weighting algorithm. We then applied an iterative normalization procedure for each run. Individual quantitative samples were median-normalized within each acquisition run. Intensities for each peptide identification were normalized within the assigned protein. Supplementary Figure 10 shows the distribution of reporter ion intensities across the TMT channels for each of the four LC-MS/MS runs using Cam3.II^{R539T}, Cam3.II^{C580Y}, and Cam3.II^{WT} K13 ring and trophozoite stage parasites.

For every sample, we first removed poor quality spectra (large spectral count variation) within a protein if the standard deviation in normalized intensities was greater than the mean ± 2 SD (standard deviations) for experiments with 6-plex TMT (since intensity between spectra should be similar for a protein). If TMT = 3, we removed bad spectra where the SD of the log₂ fold change across spectra was greater than the median log₂ fold change (assuming that differences between strains were consistent with a small SD). On average, for each run 29,259 high-quality spectra (86% of total) were included in the final quantitation. We obtained the median log₂ normalized spectral intensities of exclusive peptides for each protein. In every biological experiment, DE proteins were identified based on performing a *t*-test for each individual protein between the K13 mutant and WT samples. The log₂-transformed fold change of the normalized intensities was used to plot the heat maps for each protein. See Supplementary Data 3 for protein expression levels.

Co-IP and mass spectrometry with monoclonal anti-K13 antibodies. Antibodies were raised against recombinant K13 protein by injecting mice intraperitoneally with two types of immunogens: the BTB-propeller domain (~40 kDa) or the propeller domain only (~32 kDa), as described⁴¹. Immunoprecipitation (IP) studies were performed using the direct IP kit (Fisher Scientific) according to the manufacturer's instructions. Briefly, parasites were released from infected RBCs using 0.05% saponin in PBS and were washed twice in PBS. Pelleted parasites were then resuspended in Pierce IP Lysis Buffer supplemented with 1 \times Halt Protease and Phosphatase Inhibitor Cocktail and 25 U Pierce Universal Nuclease, and lysed on

ice for 10 min with frequent vortexing. Samples were centrifuged at 18,400g for 10 min at 4 °C to pellet cellular debris. Supernatants were collected and protein concentrations therein were determined using the DC protein assay kit (Bio-Rad). IPs were performed using 500 μ g of lysate per test sample. A mix of K13 monoclonal antibodies E3 and D9 (2.5 μ g each per test sample) was used for IP. Antibody coupling to IP columns, IP, and elution steps were performed according to the manufacturer's instructions. Eluates were analyzed by LC-MS/MS to identify immunoprecipitated proteins.

Analysis of K13 protein interactions. We filtered for proteins that were detected with at least three peptide counts in at least three out of six independent co-IP experiments and present in more than 35% samples (5 out of 13 samples). STRING version 11.0 based on seven datasets (textmining, experiments, databases, co-expression, neighborhood, gene fusion, and co-occurrence) was used to generate an interactome of the 21 proteins found to interact with K13. We applied an interaction confidence cutoff of 0.4 and a Markov Clustering with an inflation score of 3. These 21 proteins are listed in Supplementary Data 5.

Sample preparation for untargeted LC-MS metabolomics. Testing for *Mycoplasma* was performed using a MycoAlert PLUS Mycoplasma Detection Kit (Lonza) prior to the start of the sample collection. *Mycoplasma*-free Cam3.II^{C580Y} and Cam3.II^{WT} parasites were doubly synchronized by 5% D-sorbitol in each generation for at least two generations. In all, 0–3 hpi early rings of each parasite line were treated for 3 h at 70 nM or 350 nM DHA along with vehicle-treated 0.05% DMSO controls in two to three independent experiments with one to three technical replicates. Twenty-four hpi trophozoites were similarly treated with DHA or DMSO control in a single experiment with six technical replicates for each parasite line and were subsequently magnetically enriched using MACS CS columns on the SuperMACS™ II Separator (Miltenyi Biotec, Inc.) to remove uninfected RBCs. This protocol followed standard conditions previously used to study the metabolomes of Pf parasites exposed to various antimalarial agents⁴⁰. The K13 mutant and WT ring-stage parasites were run in parallel for each metabolomic experiment to allow direct comparisons of their metabolomic states and the effects of DHA. Metabolites were examined from the saponin-lysed parasites and not from the culture media. Metabolites from saponin-lysed parasites were extracted as described⁴⁰. Briefly, parasites were lysed in 1 mL of 90% cold methanol, containing 0.5 μ M of the internal standard [¹³C₄, ¹⁵N₁]-Aspartate (Cambridge Isotope) to correct for technical variation arising from sample processing in the data analysis phase. Samples were vortexed and centrifuged to remove cell debris. The clarified supernatants were dried under nitrogen prior to resuspension in HPLC-grade water (Chromasolv; Sigma) for LC-MS analysis. Samples were randomized and 10 μ L of extract or processing blank was injected for analysis. Metabolites were analyzed using a previously established reversed phase ion-paired method on a Thermo Exactive Plus Orbitrap LC-MS, scanning from 85 to 1000 *m/z* (*R* = 140,000) and operating in negative ESI mode^{74,75}. Metabolite separation was achieved on a Synergy Hydro-RP column (100 \times 2 mm, 2.5 μ m particle size; Phenomenex, Torrance, CA). Solvent A was 97:3 water:methanol with 10 mM tributylamine and 15 mM acetic acid, and solvent B was methanol (all solvents were HPLC grade).

Data analyses for metabolomics. Data analysis was performed as described⁴⁰. Briefly, raw data files from the Thermo Exactive Plus orbitrap (.raw) were converted to a format compatible with our analysis software (.mzXML) and spectral data (.mzXML files) were visualized in MAVEN version 8.0.3 (ref. 76). The labeled [¹³C₄, ¹⁵N₁]-Aspartate internal standard intensity was assessed for technical reproducibility. Metabolites (level 1 annotation) were identified using an in-house database/library generated from pure standard compounds processed on the same LC-MS platform⁴⁰. The criteria for positive identification was based on peak proximity to standard retention time, the observed mass falling within 10 ppm of the expected *m/z* (calculated from the monoisotopic mass), and the signal/blank ratio (minimum of 10,000 ions). Based upon the above criteria, peaks were further manually inspected and demarcated as good or bad based on peak shape. Peak areas were exported into an R working environment (<http://www.R-project.org>) to calculate log₂ fold changes for each sample compared to control. Metabolites that were not reliably detected across trials were removed prior to additional analysis to minimize the number of “0” values and subsequent imputation bias. The peak areas for any remaining metabolites not detected (“0” value) were imputed to have 10,000 ions, and metabolites that were negative after blank subtraction (sample area < blank area) were maintained as “0” prior to averaging and log₂ calculation.

To investigate the effect of K13 mutations on *P. falciparum* physiology, the log₂ fold change of mutant vs. WT metabolites was calculated for each experimental run using the technical replicate peak areas. Three independent experiments, with two to three technical replicates for samples without DHA treatment and one to three replicates for samples after pulsing with DHA, were conducted with ring stages of Cam3.II^{C580Y} and Cam3.II^{WT} parasites. Spectral data for each technical replicate peak area across all independent trials are listed in Supplementary Data 4. To examine the effects of K13 mutation, we applied metabolomic set enrichment analyses and partial least-squares discriminant analyses (MetaboAnalyst 3.0 package in R). For DHA treatments, the spectral peak areas were averaged and

divided by the average of the DMSO controls for each sample type. Data were log₂ transformed to obtain a single log₂ fold change for each sample.

Drug susceptibility assays. Drug stocks of DHA, atovaquone, fusidic acid, ribavirin, and immucilins G and H were made in dimethyl sulfoxide (DMSO) or ultrapure water (immucilins exclusively), and aliquots were stored at -20°C . All drug assays were conducted such that the final DMSO concentration was $<0.5\%$. Except for immucilins, all assays used standard media as described above. For immucilin assays, we first adapted parasites to low $10\ \mu\text{M}$ hypoxanthine media, as high hypoxanthine levels have been shown to artificially elevate the IC_{50} values of purine salvage inhibitors. We also used blood washed several times in low hypoxanthine media. For standard IC_{50} dose–response assays, ring-stage cultures at 0.4% parasitemia and 1% hematocrit were exposed for 72 h to a range of 10 drug concentrations that were twofold serially diluted, along with drug-free controls. The IC_{50} defines the drug concentration that results in 50% inhibition of parasite growth. IC_{50} can also be reported in the literature (e.g. ref. ²⁴) as EC_{50} . In the 4 h pulsed drug assays, we obtained 0–3 hpi young rings using Percoll-Sorbitol synchronization⁷⁷ and exposed these to the panel of inhibitors. At the end of the pulse, drug was removed by carrying out three washes and a plate transfer using a Tecan EVO 100 automated liquid handler, and parasites were cultured for another 68 h. At least three independent biological replicates were performed, each with technical duplicates. Parasite survival was assessed on an Accuri C6 flow cytometer (BD Biosciences) using SYBR Green I and MitoTracker Deep Red FM (Thermo Fisher Scientific) as stains for DNA and cell viability, respectively. Flow counts were analyzed by gating the live parasites using FlowJo software (FlowJo LLC) as illustrated in Supplementary Fig. 11. Percent parasite survival (normalized to 100%) was plotted against log drug concentrations. A nonlinear regression model was used to determine IC_{50} values (GraphPad Prism). Statistical analyses by one-sample t -tests were used to determine whether there was a significant difference in the response of K13 mutant and WT parasites to these individual compounds.

Drug-pair combination susceptibility assays. Parasites were exposed for 4 or 72 h to a range of ten twofold serially diluted concentrations of atovaquone plus DHA, applied in fixed molar ratios (1:0, 4:1, 2:1, 1:1, 1:2, 1:4, 0:1) of their individual IC_{50} values. For the isobologram analyses, we calculated the fractional IC_{50} values of the fixed ratios of drug combinations vs. DHA or atovaquone alone. The Combination Index for the *Loewe Additivity* was also used to determine whether the relationship between DHA and the test inhibitor was synergistic, additive, or antagonistic. Paired t -tests were used to test for a difference in the combination index values between each mutant and WT line.

Reporting summary. Further information on research design is available in the Nature Research Reporting Summary linked to this article.

Data availability

Microarray gene expression data are available in NCBI's Gene Expression Omnibus with the identifier [GSE151189](https://www.ncbi.nlm.nih.gov/geo/query/acc.cgi?acc=GSE151189). Data for mass spectrometry proteomics are available in ProteomeXchange Consortium (<http://www.proteomexchange.org/>) via the PRIDE repository database with the dataset identifier PXD019612 and <https://doi.org/10.6019/PXD019612> (<https://www.ebi.ac.uk/pride/archive/projects/PXD019612>). LC-MS/MS metabolomics data are available at the NIH Common Fund's National Metabolomics Data Repository (NMDR) website, the Metabolomics Workbench (<https://www.metabolomicsworkbench.org>) with the project ID PR000864, and <https://doi.org/10.21228/M80T2X>. Datasets extracted from PlasmoDB (<https://plasmodb.org>), Kyoto Encyclopedia of Genes and Genomes (<https://www.genome.jp/kegg/>), Gene Ontology (<http://geneontology.org/>), Malaria Parasite Metabolic (<https://mpmp.huji.ac.il/>), and STRING (<https://string-db.org/>) can be accessed using these weblinks. The authors declare that all other data supporting the findings of this study are available within the paper and its Supplementary Information files. Requests for resources and reagents should be directed to D.A.F. (df2260@cumc.columbia.edu). Source data are provided with this paper.

Received: 28 July 2020; Accepted: 17 December 2020;

Published online: 22 January 2021

References

- World Health Organization. *World Malaria Report 2020* (World Health Organization, Geneva, 2020).
- Meshnick, S. R. Artemisinin: mechanisms of action, resistance and toxicity. *Int. J. Parasitol.* **32**, 1655–1660 (2002).
- Tilley, L., Straimer, J., Gnädig, N. F., Ralph, S. A. & Fidock, D. A. Artemisinin action and resistance in *Plasmodium falciparum*. *Trends Parasitol.* **32**, 682–696 (2016).
- Haldar, K., Bhattacharjee, S. & Safeukui, I. Drug resistance in *Plasmodium*. *Nat. Rev. Microbiol.* **16**, 156–170 (2018).
- Dondorp, A. M. et al. Artemisinin resistance in *Plasmodium falciparum* malaria. *N. Engl. J. Med.* **361**, 455–467 (2009).
- Ashley, E. A. et al. Spread of artemisinin resistance in *Plasmodium falciparum* malaria. *N. Engl. J. Med.* **371**, 411–423 (2014).
- Menard, D. et al. A worldwide map of *Plasmodium falciparum* K13-propeller polymorphisms. *N. Engl. J. Med.* **374**, 2453–2464 (2016).
- White, N. J. The parasite clearance curve. *Malar. J.* **10**, 278 (2011).
- van der Pluijm, R. W. et al. Determinants of dihydroartemisinin-piperazine treatment failure in *Plasmodium falciparum* malaria in Cambodia, Thailand, and Vietnam: a prospective clinical, pharmacological, and genetic study. *Lancet Infect. Dis.* **19**, 952–961 (2019).
- Spring, M. D. et al. Dihydroartemisinin-piperazine failure associated with a triple mutant including kelch13 C580Y in Cambodia: an observational cohort study. *Lancet Infect. Dis.* **15**, 683–691 (2015).
- Amaratunga, C. et al. Dihydroartemisinin-piperazine resistance in *Plasmodium falciparum* malaria in Cambodia: a multisite prospective cohort study. *Lancet Infect. Dis.* **16**, 357–365 (2016).
- Conrad, M. D. & Rosenthal, P. J. Antimalarial drug resistance in Africa: the calm before the storm? *Lancet Infect. Dis.* **19**, e338–e351 (2019).
- MalariaGEN *Plasmodium falciparum* Community Project. Genomic epidemiology of artemisinin resistant malaria. *Elife* **5**, e08714 (2016).
- Ariey, F. et al. A molecular marker of artemisinin-resistant *Plasmodium falciparum* malaria. *Nature* **505**, 50–55 (2014).
- Ghorbal, M. et al. Genome editing in the human malaria parasite *Plasmodium falciparum* using the CRISPR-Cas9 system. *Nat. Biotechnol.* **32**, 819–821 (2014).
- Straimer, J. et al. K13-propeller mutations confer artemisinin resistance in *Plasmodium falciparum* clinical isolates. *Science* **347**, 428–431 (2015).
- Miotto, O. et al. Genetic architecture of artemisinin-resistant *Plasmodium falciparum*. *Nat. Genet.* **47**, 226–234 (2015).
- Siddiqui, F. A. et al. Role of *Plasmodium falciparum* Kelch 13 protein mutations in *P. falciparum* populations from northeastern Myanmar in mediating artemisinin resistance. *mBio* **11**, e01134-19 (2020).
- Mathieu, L. C. et al. Local emergence in Amazonia of *Plasmodium falciparum* k13 C580Y mutants associated with in vitro artemisinin resistance. *Elife* **9**, e51015 (2020).
- Witkowski, B. et al. Reduced artemisinin susceptibility of *Plasmodium falciparum* ring stages in western Cambodia. *Antimicrob. Agents Chemother.* **57**, 914–923 (2013).
- Ocan, M. et al. K13-propeller gene polymorphisms in *Plasmodium falciparum* parasite population in malaria affected countries: a systematic review of prevalence and risk factors. *Malar. J.* **18**, 60 (2019).
- Straimer, J. et al. *Plasmodium falciparum* K13 mutations differentially impact ozonide susceptibility and parasite fitness in vitro. *mBio* **8**, e00172-17 (2017).
- Demas, A. R. et al. Mutations in *Plasmodium falciparum* actin-binding protein coronin confer reduced artemisinin susceptibility. *Proc. Natl Acad. Sci. USA* **115**, 12799–12804 (2018).
- Henrici, R. C., van Schalkwyk, D. A. & Sutherland, C. J. Modification of *pfap2mu* and *pfubp1* markedly reduces ring-stage susceptibility of *Plasmodium falciparum* to artemisinin in vitro. *Antimicrob. Agents Chemother.* **64**, e01542-01519 (2019).
- Mukherjee, A. et al. Artemisinin resistance without pfkelch13 mutations in *Plasmodium falciparum* isolates from Cambodia. *Malar. J.* **16**, 195 (2017).
- Rocamora, F. et al. Oxidative stress and protein damage responses mediate artemisinin resistance in malaria parasites. *PLoS Pathog.* **14**, e1006930 (2018).
- Birnbaum, J. et al. A Kelch13-defined endocytosis pathway mediates artemisinin resistance in malaria parasites. *Science* **367**, 51–59 (2020).
- Yang, T. et al. Decreased K13 abundance reduces hemoglobin catabolism and proteotoxic stress, underpinning artemisinin resistance. *Cell Rep.* **29**, 2917–2928 (2019).
- Mok, S. et al. Population transcriptomics of human malaria parasites reveals the mechanism of artemisinin resistance. *Science* **347**, 431–435 (2015).
- Zhang, M. et al. Inhibiting the *Plasmodium* eIF2 α kinase PK4 prevents artemisinin-induced latency. *Cell Host Microbe* **22**, 766–776 (2017).
- Dogovski, C. et al. Targeting the cell stress response of *Plasmodium falciparum* to overcome artemisinin resistance. *PLoS Biol.* **13**, e1002132 (2015).
- Bridgford, J. L. et al. Artemisinin kills malaria parasites by damaging proteins and inhibiting the proteasome. *Nat. Commun.* **9**, 3801 (2018).
- Mbungue, A. et al. A molecular mechanism of artemisinin resistance in *Plasmodium falciparum* malaria. *Nature* **520**, 683–687 (2015).
- Bhattacharjee, S. et al. Remodeling of the malaria parasite and host human red cell by vesicle amplification that induces artemisinin resistance. *Blood* **131**, 1234–1247 (2018).
- Rosenthal, M. R. & Ng, C. L. *Plasmodium falciparum* artemisinin resistance: the effect of heme, protein damage, and parasite cell stress response. *ACS Infect. Dis.* **6**, 1599–1614 (2020).

36. Wang, J. et al. Haem-activated promiscuous targeting of artemisinin in *Plasmodium falciparum*. *Nat. Commun.* **6**, 10111 (2015).
37. Ismail, H. M. et al. Artemisinin activity-based probes identify multiple molecular targets within the asexual stage of the malaria parasites 3D7. *Proc. Natl Acad. Sci. USA* **113**, 2080–2085 (2016).
38. Hott, A. et al. Artemisinin-resistant *Plasmodium falciparum* parasites exhibit altered patterns of development in infected erythrocytes. *Antimicrob. Agents Chemother.* **59**, 3156–3167 (2015).
39. Siddiqui, G., Srivastava, A., Russell, A. S. & Creek, D. J. Multi-omics based identification of specific biochemical changes associated with PfKelch13-mutant artemisinin-resistant *Plasmodium falciparum*. *J. Infect. Dis.* **215**, 1435–1444 (2017).
40. Allman, E. L., Painter, H. J., Samra, J., Carrasquilla, M. & Llinas, M. Metabolic profiling of the Malaria Box reveals antimalarial target pathways. *Antimicrob. Agents Chemother.* **60**, 6635–6649 (2016).
41. Gnädig, N. F. et al. Insights into the intracellular localization, protein associations and artemisinin resistance properties of *Plasmodium falciparum* K13. *PLoS Pathog.* **16**, e1008482 (2020).
42. Franceschini, A. et al. STRING v9.1: protein-protein interaction networks, with increased coverage and integration. *Nucleic Acids Res.* **41**, D808–D815 (2013).
43. Shaw, P. J. et al. *Plasmodium* parasites mount an arrest response to dihydroartemisinin, as revealed by whole transcriptome shotgun sequencing (RNA-seq) and microarray study. *BMC Genomics* **16**, 830 (2015).
44. Vaidya, A. B. & Mather, M. W. Mitochondrial evolution and functions in malaria parasites. *Annu. Rev. Microbiol.* **63**, 249–267 (2009).
45. van Schalkwyk, D. A. et al. Novel endochin-like quinolones exhibit potent in vitro activity against *Plasmodium knowlesi* but do not synergize with proguanil. *Antimicrob. Agents Chemother.* **64**, e02549-19 (2020).
46. Xie, S. C., Ralph, S. A. & Tilley, L. K13, the cytosome, and artemisinin resistance. *Trends Parasitol.* **36**, 533–544 (2020).
47. Heller, L. E., Goggins, E., Roepe, P. D. & Dihydroartemisinin-ferriprotoporphyrin IX adduct abundance in *Plasmodium falciparum* malarial parasites and the relationship to emerging artemisinin resistance. *Biochemistry* **57**, 6935–6945 (2018).
48. Xiong, A. et al. K13-mediated reduced susceptibility to artemisinin in *Plasmodium falciparum* is overlaid on a trait of enhanced DNA damage repair. *Cell Rep.* **32**, 107996 (2020).
49. Cerqueira, G. C. et al. Longitudinal genomic surveillance of *Plasmodium falciparum* malaria parasites reveals complex genomic architecture of emerging artemisinin resistance. *Genome Biol.* **18**, 78 (2017).
50. Sutherland, C., Henrić, R. C. & Artavanis-Tsakonas, K. Artemisinin susceptibility in the malaria parasite *Plasmodium falciparum*: propellers, adaptor proteins and the need for cellular healing. *FEMS Microbiol. Rev.* <https://doi.org/10.1093/femsre/uaa056> (2020).
51. Salcedo-Sora, J. E., Caamano-Gutiérrez, E., Ward, S. A. & Biagini, G. A. The proliferating cell hypothesis: a metabolic framework for *Plasmodium* growth and development. *Trends Parasitol.* **30**, 170–175 (2014).
52. Porporato, P. E., Filigheddu, N., Pedro, J. M. B., Kroemer, G. & Galluzzi, L. Mitochondrial metabolism and cancer. *Cell Res.* **28**, 265–280 (2018).
53. Birsoy, K. et al. An essential role of the mitochondrial electron transport chain in cell proliferation is to enable aspartate synthesis. *Cell* **162**, 540–551 (2015).
54. Carey, M. A., Papin, J. A. & Guler, J. L. Novel *Plasmodium falciparum* metabolic network reconstruction identifies shifts associated with clinical antimalarial resistance. *BMC Genomics* **18**, 543 (2017).
55. Fry, M. & Beesley, J. E. Mitochondria of mammalian *Plasmodium* spp. *Parasitology* **102**, 17–26 (1991).
56. Uyemura, S. A., Luo, S., Vieira, M., Moreno, S. N. & Docampo, R. Oxidative phosphorylation and rotenone-insensitive malate- and NADH-quinone oxidoreductases in *Plasmodium yoelii yoelii* mitochondria in situ. *J. Biol. Chem.* **279**, 385–393 (2004).
57. McLean, K. J. & Jacobs-Lorena, M. *Plasmodium falciparum* Maf1 confers survival upon amino acid starvation. *mBio* **8**, e02317–02316 (2017).
58. Babbitt, S. E. et al. *Plasmodium falciparum* responds to amino acid starvation by entering into a hibernatory state. *Proc. Natl Acad. Sci. USA* **109**, E3278–E3287 (2012).
59. Chaikuad, A. et al. Structures of PGAM5 provide insight into active site plasticity and multimeric assembly. *Structure* **25**, 1089–1099 (2017).
60. O’Mealey, G. B. et al. A PGAM5-KEAP1-Nrf2 complex is required for stress-induced mitochondrial retrograde trafficking. *J. Cell Sci.* **130**, 3467–3480 (2017).
61. Brand, M. D. Mitochondrial generation of superoxide and hydrogen peroxide as the source of mitochondrial redox signaling. *Free Radic. Biol. Med.* **100**, 14–31 (2016).
62. Paudel, B. B. & Quaranta, V. Metabolic plasticity meets gene regulation. *Proc. Natl Acad. Sci. USA* **116**, 3370–3372 (2019).
63. Jia, D. et al. Elucidating cancer metabolic plasticity by coupling gene regulation with metabolic pathways. *Proc. Natl Acad. Sci. USA* **116**, 3909–3918 (2019).
64. Zheng, H. et al. Inhibitors of *Mycobacterium tuberculosis* DosRST signaling and persistence. *Nat. Chem. Biol.* **13**, 218–225 (2017).
65. Harding, C. R. et al. Genetic screens reveal a central role for heme metabolism in artemisinin susceptibility. *Nat. Commun.* **11**, 4813 (2020).
66. Fidock, D. A., Nomura, T. & Wellem, T. E. Cycloguanil and its parent compound proguanil demonstrate distinct activities against *Plasmodium falciparum* malaria parasites transformed with human dihydrofolate reductase. *Mol. Pharmacol.* **54**, 1140–1147 (1998).
67. Wellem, T. E. et al. Chloroquine resistance not linked to *mdr*-like genes in a *Plasmodium falciparum* cross. *Nature* **345**, 253–255 (1990).
68. Foth, B. J. et al. Quantitative time-course profiling of parasite and host cell proteins in the human malaria parasite *Plasmodium falciparum*. *Mol. Cell Proteomics* **10**, M110 006411 (2011).
69. Bozdech, Z., Mok, S. & Gupta, A. P. DNA microarray-based genome-wide analyses of *Plasmodium* parasites. *Methods Mol. Biol.* **923**, 189–211 (2013).
70. Huber, W. et al. Orchestrating high-throughput genomic analysis with bioconductor. *Nat. Methods* **12**, 115–121 (2015).
71. Alam, M. M. et al. Phosphoproteomics reveals malaria parasite protein kinase G as a signalling hub regulating egress and invasion. *Nat. Commun.* **6**, 7285 (2015).
72. Keller, A., Nesvizhskii, A. I., Kolker, E. & Aebersold, R. Empirical statistical model to estimate the accuracy of peptide identifications made by MS/MS and database search. *Anal. Chem.* **74**, 5383–5392 (2002).
73. Oberg, A. L. et al. Statistical analysis of relative labeled mass spectrometry data from complex samples using ANOVA. *J. Proteome Res.* **7**, 225–233 (2008).
74. Lu, W. et al. Metabolomic analysis via reversed-phase ion-pairing liquid chromatography coupled to a stand alone orbitrap mass spectrometer. *Anal. Chem.* **82**, 3212–3221 (2010).
75. Schalkwijk, J. et al. Antimalarial pantothenamide metabolites target acetyl-coenzyme A biosynthesis in *Plasmodium falciparum*. *Sci. Transl. Med.* **11**, eaas9917 (2019).
76. Melamud, E., Vastag, L. & Rabinowitz, J. D. Metabolomic analysis and visualization engine for LC-MS data. *Anal. Chem.* **82**, 9818–9826 (2010).
77. Witkowski, B. et al. Novel phenotypic assays for the detection of artemisinin-resistant *Plasmodium falciparum* malaria in Cambodia: *in-vitro* and *ex-vivo* drug-response studies. *Lancet Infect. Dis.* **13**, 1043–1049 (2013).

Acknowledgements

We are grateful to Dr. Emily Chen at the CUIMC core facility for performing the mass spectrometry runs for the co-IP experiments and to Dr. Mahmood Alam for advice on proteomic analyses and parasite sampling. We are thankful to Dr. Vern L. Schramm, Albert Einstein College of Medicine, USA, for providing immuclin H and G compounds. This work was supported by the National Institute of Allergy and Infectious Diseases at the National Institutes of Health (R01 AI109023 to D.A.F.), the Department of Defense (Discovery Award W81XWH-19-1-0086 to D.A.F.), and in part by the Intramural Research program of NIAID/NIH. S.M. is a recipient of the Human Frontier Science Program Long-term Postdoctoral Fellowship LT000976/2016-L. B.H.S. received funding from T32 AI106711 (PD: D.A.F) that supports the Columbia University Graduate Training Program in Microbiology and Immunology. We also thank the Huck Institutes of Life Sciences Metabolomics Core Facility at Penn State University.

Author contributions

S.M., D.A.F., Z.B., and R.M.F. conceived and designed the study. S.M. performed research, acquired, and analyzed data. B.H.S. acquired and analyzed data. N.F.G., L.S.R., T.Y., C.A., E.A., L.S., A.R.B. and J.T. acquired data. S.M., A.B.T., Z.B., M.L., and D.A.F. contributed reagents and to intellectual discussions. S.M. and D.A.F. wrote the manuscript with input from all the authors.

Competing interests

The authors declare no competing interests.

Additional information

Supplementary information is available for this paper at <https://doi.org/10.1038/s41467-020-20805-w>.

Correspondence and requests for materials should be addressed to D.A.F.

Peer review information *Nature Communications* thanks Adam Reid, Colin Sutherland, Sanjeeva Srivastava and the other, anonymous, reviewer(s) for their contribution to the peer review of this work. Peer reviewer reports are available.

Reprints and permission information is available at <http://www.nature.com/reprints>

Publisher's note Springer Nature remains neutral with regard to jurisdictional claims in published maps and institutional affiliations.


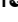


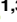


Open Access This article is licensed under a Creative Commons Attribution 4.0 International License, which permits use, sharing, adaptation, distribution and reproduction in any medium or format, as long as you give appropriate credit to the original author(s) and the source, provide a link to the Creative Commons license, and indicate if changes were made. The images or other third party material in this article are included in the article's Creative Commons license, unless indicated otherwise in a credit line to the material. If material is not included in the article's Creative Commons license and your intended use is not permitted by statutory regulation or exceeds the permitted use, you will need to obtain permission directly from the copyright holder. To view a copy of this license, visit <http://creativecommons.org/licenses/by/4.0/>.


© The Author(s) 2021

RESEARCH ARTICLE

Insights into the intracellular localization, protein associations and artemisinin resistance properties of *Plasmodium falciparum* K13

Nina F. Gnädig¹ , Barbara H. Stokes¹ , Rachel L. Edwards² , Gavreel F. Kalantarov³, Kim C. Heimsch⁴, Michal Kuderjavy⁵, Audrey Crane¹, Marcus C. S. Lee⁶, Judith Straimer^{1a}, Katja Becker⁴, Ilya N. Trakht³, Audrey R. Odom John^{2,7,8} , Sachel Mok¹, David A. Fidock^{1,3*} 

1 Department of Microbiology & Immunology, Columbia University Irving Medical Center, New York, NY, United States of America, **2** Department of Pediatrics, Washington University School of Medicine, St. Louis, MO, United States of America, **3** Department of Medicine, Columbia University Irving Medical Center, New York, NY, United States of America, **4** Biochemistry and Molecular Biology, Interdisciplinary Research Center, Justus Liebig University, Giessen, Germany, **5** Laboratory Imaging, Prague, Czech Republic, **6** Wellcome Sanger Institute, Wellcome Genome Campus, Hinxton, United Kingdom, **7** Department of Molecular Microbiology, Washington University School of Medicine, St. Louis, MO, United States of America, **8** Children's Hospital of Philadelphia, Philadelphia, PA, United States of America

 These authors contributed equally to this work.

 Current address: Novartis Institute of Tropical Diseases, Emeryville, CA, United States of America

* df2260@cumc.columbia.edu



OPEN ACCESS

Citation: Gnädig NF, Stokes BH, Edwards RL, Kalantarov GF, Heimsch KC, Kuderjavy M, et al. (2020) Insights into the intracellular localization, protein associations and artemisinin resistance properties of *Plasmodium falciparum* K13. *PLoS Pathog* 16(4): e1008482. <https://doi.org/10.1371/journal.ppat.1008482>

Editor: Michael J. Blackman, Francis Crick Institute, UNITED KINGDOM

Received: August 12, 2019

Accepted: March 17, 2020

Published: April 20, 2020

Copyright: © 2020 Gnädig et al. This is an open access article distributed under the terms of the [Creative Commons Attribution License](https://creativecommons.org/licenses/by/4.0/), which permits unrestricted use, distribution, and reproduction in any medium, provided the original author and source are credited.

Data Availability Statement: All relevant data are within the manuscript and its Supporting Information files.

Funding: Partial funding for this work was provided by the NIH (R01 AI109023 to DAF), the Department of Defense (W81XWH1910086 to DAF) and the Selz Foundation, New York (to GK and IT). SM is a recipient of the Human Frontier Science Program (HFSP) long-term postdoctoral fellowship LT000976/2016-L. BHS was supported

Abstract

The emergence of artemisinin (ART) resistance in *Plasmodium falciparum* intra-erythrocytic parasites has led to increasing treatment failure rates with first-line ART-based combination therapies in Southeast Asia. Decreased parasite susceptibility is caused by K13 mutations, which are associated clinically with delayed parasite clearance in patients and *in vitro* with an enhanced ability of ring-stage parasites to survive brief exposure to the active ART metabolite dihydroartemisinin. Herein, we describe a panel of K13-specific monoclonal antibodies and gene-edited parasite lines co-expressing epitope-tagged versions of K13 *in trans*. By applying an analytical quantitative imaging pipeline, we localize K13 to the parasite endoplasmic reticulum, Rab-positive vesicles, and sites adjacent to cytosomes. These latter structures form at the parasite plasma membrane and traffic hemoglobin to the digestive vacuole wherein artemisinin-activating heme moieties are released. We also provide evidence of K13 partially localizing near the parasite mitochondria upon treatment with dihydroartemisinin. Immunoprecipitation data generated with K13-specific monoclonal antibodies identify multiple putative K13-associated proteins, including endoplasmic reticulum-resident molecules, mitochondrial proteins, and Rab GTPases, in both K13 mutant and wild-type isogenic lines. We also find that mutant K13-mediated resistance is reversed upon co-expression of wild-type or mutant K13. These data help define the biological properties of K13 and its role in mediating *P. falciparum* resistance to ART treatment.

in part by the NIH-supported Columbia University Graduate Program in Microbiology, Immunology and Infection (T32 AI106711; 637 PI DAF). AOJ is supported by R01 AI103280, R21 AI123808, and R21 AI130584, the St. Louis Children's Foundation, and an Investigator in Pathogenesis of Infectious Diseases Award from the Burroughs Wellcome Fund. MCSL is supported by a core grant from Wellcome [206194]. The funders had no role in study design, data collection and analysis, decision to publish, or preparation of the manuscript.

Competing interests: The authors have declared that no competing interests exist.

Author summary

The development of drug resistance in *Plasmodium falciparum* parasites presents a significant impediment to the global fight against malaria. Partial resistance to artemisinin (ART), the core component of current first-line drugs, has swept across Southeast Asia. In *P. falciparum*-infected patients, ART-resistant parasites show slow rates of clearance following treatment with an ART derivative or ART-based combination therapy. Resistance to partner drugs has also emerged in Southeast Asia, leading to frequent treatment failures. Single amino acid mutations in the *P. falciparum* K13 protein constitute the primary genetic cause of ART resistance and predict an increased risk of treatment failure. By generating monoclonal antibodies, we have investigated the subcellular localization of K13 in dihydroartemisinin-treated or untreated parasites. Analytical microscopy data localize K13 to or near the endoplasmic reticulum and vesicles that mediate intracellular trafficking, including plasma membrane-associated cytosomes that import host hemoglobin into the parasite. Co-immunoprecipitation experiments with K13-specific monoclonal antibodies identified multiple proteins associated with the endoplasmic reticulum, vesicular trafficking, the cytosol, or the mitochondria, with no apparent differences between K13 mutant and wild-type parasites. We also observed that overexpression of mutant or wild-type K13 in K13 mutant parasites could restore susceptibility, supporting the hypothesis that K13 mutations cause loss of function.

Introduction

Worldwide, malaria results in an estimated 400,000 or more fatalities each year, afflicting mostly infants and young children in sub-Saharan Africa [1]. Treatment of asexual blood-stage infections caused by *Plasmodium falciparum*, the most virulent human malaria parasite, relies on the efficacy of artemisinin (ART)-based combination therapies (ACTs). These first-line treatments pair a derivative of ART, an exceptionally fast-acting and potent antimalarial, with a longer-lived partner drug [2]. Commonly used partners include the arylaminoalcohol lumefantrine, used primarily in Africa, and piperazine, a bisquinoline used predominantly in Southeast Asia [3].

In parasites, activation of ART or its derivatives requires iron-mediated reductive scission of the compound's central endoperoxide bridge. The activator is thought to be primarily Fe^{2+} heme, a byproduct of parasite-mediated catabolism of host hemoglobin [4]. This cleavage event generates carbon-centered free radicals that can target proteins, lipids, nucleic acids, and heme itself, resulting in rapid cellular damage and parasite death [5–8]. ART is characterized by its ability to eliminate parasites from all stages of the intra-erythrocytic developmental cycle (IDC), including the young ring stages that form shortly after parasites invade host red blood cells (RBCs) [9,10]. This drug is highly potent against trophozoites that undergo maximal endocytosis and degradation of host hemoglobin, thus providing an abundant source of free heme.

Emerging resistance to ACTs threatens to reverse recent progress in reducing the global burden of malaria. Having first appeared in western Cambodia over a decade ago, resistance to ART is now nearly at fixation across Southeast Asia [11–15]. Clinically, ART resistance is defined as delayed parasite clearance after artesunate monotherapy or treatment with an ACT. As resistance to ART has become more widespread, selection pressure on partner drugs has increased. In some cases, delayed parasite clearance has escalated to treatment failure as

partner drugs have succumbed to resistance [16]. In northeastern Thailand, a recent report documented 87% treatment failure rates with dihydroartemisinin (DHA) plus piperazine [15].

In vitro, ART resistance is restricted to early ring-stage parasites, and is quantified as increased survival in the ring-stage survival assay (RSA_{0-3h}), wherein parasites are exposed to a brief pulse (700 nM for 6h) of DHA. This assay distinguishes resistant parasites, which exhibit $\geq 1\%$ survival after three days, from sensitive parasites that do not survive the pulse [17]. This resistance phenotype does not extend to the later trophozoite stage, presumably because parasites cannot counter the substantial toxicity arising from ART-mediated alkylation of the abundant heme moieties generated at this stage.

ART resistance is attributed primarily to individual point mutations in the parasite Kelch protein K13 [18]. Select mutations in K13 associate with delayed parasite clearance in *P. falciparum*-infected patients and with elevated survival in the RSA_{0-3h} [18,19]. These mutations all map to the protein's carboxy-terminal six-bladed beta-propeller domain, a characteristic component of Kelch proteins that often serves as a scaffold for protein-protein interactions. Among the mutations examined *in vitro*, R539T and I543T confer the highest levels of ART resistance [20]. In contrast, the C580Y mutation confers only a modest degree of resistance, yet is the most prevalent in Southeast Asia [20,21]. This finding has been attributed to the relatively minimal fitness cost conferred by the C580Y mutation in Southeast Asian parasites [22].

In addition to its propeller domain, K13 comprises an apicomplexan-specific domain of unknown function and a BTB/POZ dimerization domain. The latter is found in a subset of Kelch proteins that commonly mediate ubiquitin-dependent protein degradation via the proteasome by serving as substrate adaptors for E3 ubiquitin ligases [18,23]. K13 shows homology with the mammalian BTB-Kelch protein Keap1, which controls the cell's adaptive response to oxidative stress [18,24]. In *P. falciparum*, the *K13* gene appears to be essential based on conditional knockout experiments showing that K13-deficient parasites do not progress past the ring stage and transition into non-viable condensed forms, and by a large-scale saturation mutagenesis study that observed no disruptions in the *K13* coding region [25,26].

Mechanistic studies have led to several proposals for how mutant K13 might counter ART-mediated cellular toxicity. These proposals include lowering the levels of the heme activator of ART including via reduced hemoglobin endocytosis in rings [27–30], upregulating endoplasmic reticulum (ER) stress-response pathways [31], reducing the levels of ubiquitinated proteins [32], promoting translational arrest via differential phosphorylation of the translation initiation factor eIF2 α [33], or increasing levels of the phospholipid phosphatidylinositol-3-phosphate (PI3P) [34,35]. To gain additional insight into the biology of this protein, we raised K13-specific monoclonal antibodies (mAbs) and used these to interrogate this protein's subcellular localization in DHA-exposed or vehicle-treated asexual blood-stage parasites. Using co-immunoprecipitation (co-IP), we also identified potential interactions with other parasite proteins and examined their predicted roles in *P. falciparum* metabolism and development. Results presented herein implicate K13 in multiple cellular functions, including vesicular trafficking and ER homeostasis, and suggest an unexpected association with the mitochondria upon DHA treatment.

Results

K13 localizes to the endoplasmic reticulum and to vesicular structures

To probe the subcellular localization of K13, we raised monoclonal antibodies (mAbs) by immunizing mice with recombinant protein fragments consisting of either the K13 propeller domain alone or the propeller domain plus the upstream BTB/POZ domain, and cloning

K13-specific hybridoma populations. Western blot screening identified the E9 clone that recognized the two recombinant K13 immunogens (bands at ~25 kDa and ~35kDa for the propeller domain alone or propeller plus BTB/POZ domains, respectively) (Fig 1A). In parallel, we generated recombinant NF54^{WT}attB parasite lines that express endogenous wild-type (WT) K13 and co-express stably-integrated transgenic copies of WT or C580Y K13, which were N-terminally tagged with GFP or 3HA, respectively. These lines are referred to herein as NF54^{WT}attB-GFP-K13^{WT} or NF54^{WT}attB-3HA-K13^{C580Y} (Table 1 and S1A–S1C Fig).

We tested our E9 mAb by Western blot against asynchronous parasite extracts from the contemporary Cambodian isolate Cam3.II that carries the K13 R539T mutation (referred to herein as Cam3.II^{R539T}) and its isogenic, gene-edited K13 WT counterpart Cam3.II^{WT} [20]. This K13 mAb clearly labeled WT and mutant K13 (both at ~85 kDa), with evidence of reduced K13 labeling in Cam3.II^{R539T} parasites (Fig 1A and S1D Fig). Quantification provided evidence of a slight reduction in K13 protein levels in the Cam3.II^{C580Y} and Cam3.II^{R539T} synchronized ring-stage parasites (these decreases were estimated at ~24% and ~34%, respectively) compared to WT levels (S1E Fig). We also tested the GFP- or HA-tagged NF54^{WT}attB lines expressing K13 *in trans*, revealing bands at ~110 kDa for GFP-K13^{WT} and ~86 kDa for 3HA-K13^{C580Y} (Fig 1A and S1D Fig) that were also recognized by anti-GFP- or anti-HA antibodies respectively.

Our K13-specific E9 mAb was found to be suitable only for Western blots and to not provide a robust signal by immunofluorescence assay (IFA). Further screening led us to identify a second K13-specific mAb, clone E3, which was suitable for IFAs (but not Western blots). This mAb was tested against the parasite lines NF54^{WT}attB-GFP-K13^{WT} and NF54^{WT}attB-3HA-K13^{C580Y}. These assays allowed us to calculate the overlap coefficient (termed the Pearson correlation coefficient, PCC) between the signal from our K13 E3 mAb and that from anti-GFP or anti-HA antibodies tested against epitope-tagged K13 proteins. PCC values range from +1 (indicating complete overlap) to 0 (random association) to -1 (mutually exclusive signals with zero overlap). In both the GFP and HA tagged lines we observed a very high degree of correlation between the signals from the anti-K13 mAb E3 and anti-GFP or anti-HA antibodies, with PCC values of 0.96 and 0.83, respectively (Fig 1B). These Western blot and IFA results with native and epitope or fluorescent protein-tagged lines validated the specificity of our K13-specific mAbs.

Using our E3 mAb, we next examined the subcellular localization of K13 throughout the IDC by IFA. These assays were performed on tightly synchronized parasites and used the Cam3.II^{WT} and Cam3.II^{R539T} isogenic lines. Samples were collected every 12h beginning with early rings (0–3h post invasion (hpi)). Early rings showed a single K13-positive focus within the parasite cytosol in both lines. As parasites progressed into schizonts, the number of K13-positive foci increased. Whereas the majority of these foci appeared to be evenly distributed throughout the parasite cytosol, others appeared to be proximal to specific organelles including the parasite plasma membrane, the ER, and the digestive vacuole (DV). No differences in K13 localization were evident between WT and mutant parasites (Fig 1C). Super-resolution microscopy clearly showed multiple K13 foci in trophozoites of both K13 mutant and WT parasites (Fig 1D; S2A and S2B Fig). Three-dimensional rotations suggested elongated, tunnel-like shapes that might link subcellular compartments (S1 Video). Quantification of the number of visualized K13 foci estimated a 48% reduction in Cam3.II^{R539T} trophozoites compared with Cam3.II^{WT} trophozoites (S2C Fig).

We also examined K13 localization using immunoelectron microscopy (IEM; Fig 1D). These studies were conducted with NF54^{WT}attB-GFP-K13^{WT} and NF54^{WT}attB-3HA-K13^{C580Y} parasites, with K13 detected via anti-GFP or anti-HA colloidal gold-conjugated primary antibodies. In trophozoites, K13 appeared to localize to the parasite cytosol, often

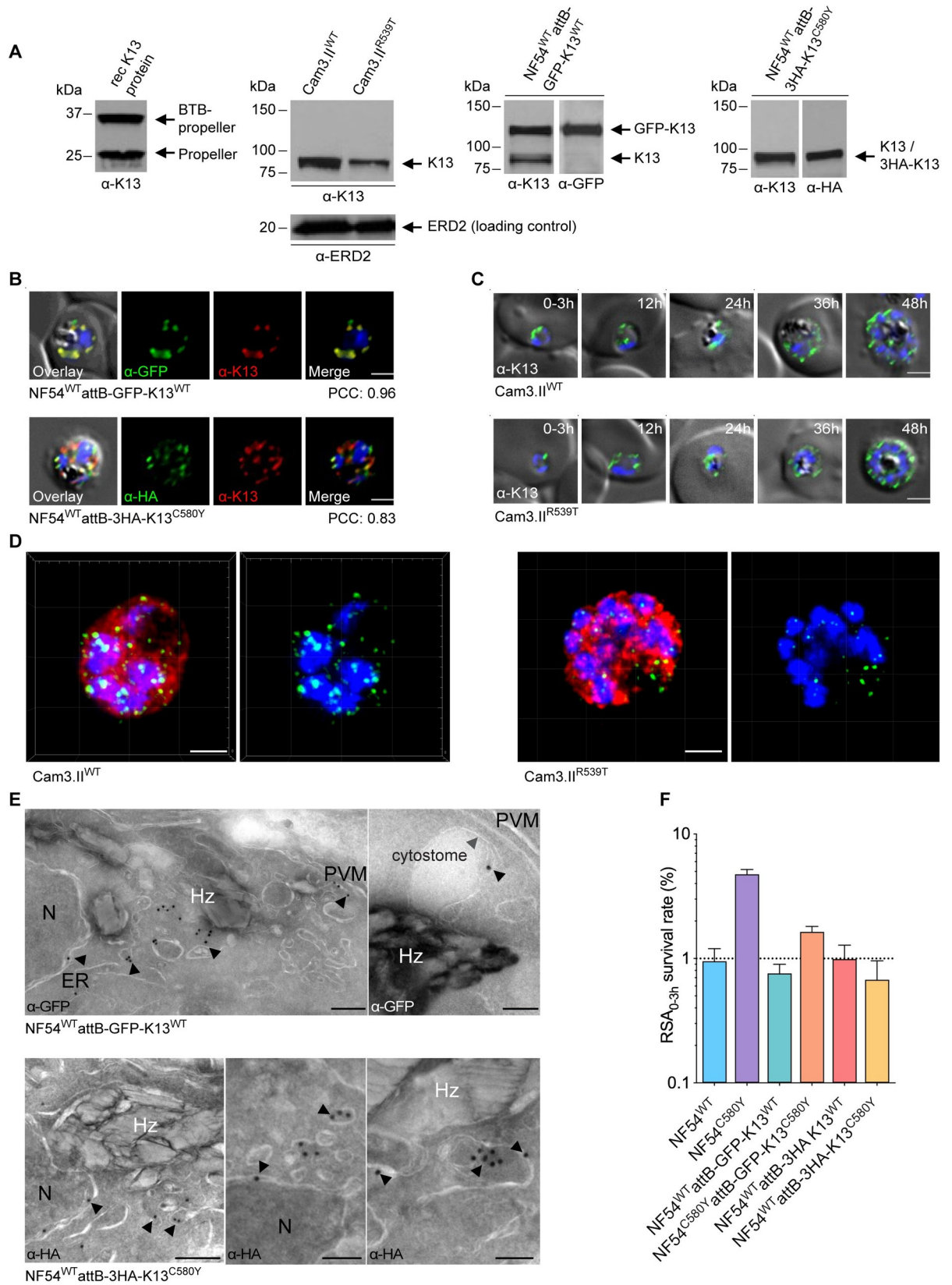


Fig 1. The *P. falciparum* artemisinin resistance determinant K13 localizes to the parasite ER and intracellular vesicles. (A) Western blots probed with the E9 monoclonal antibody (mAb) raised against the K13 propeller domain. Left to right: recombinant K13 protein fragments used as immunogens; Cam3.II^{WT} and Cam3.II^{R539T} asexual blood-stage parasite extracts; and NF54^{WT}attB-GFP-K13^{WT} and NF54^{WT}attB-3HA-K13^{C580Y} extracts. ERD2 was used as a loading control for the Cam3.II lines. The NF54^{WT}attB-GFP-K13^{WT} and NF54^{WT}attB-3HA-K13^{C580Y} blots were also probed with anti-GFP or anti-HA antibodies, respectively. (B) Immunofluorescence assay (IFA) images showing K13 localization in NF54^{WT}attB-GFP-K13^{WT} (top) and NF54^{WT}attB-3HA-K13^{C580Y} (bottom) trophozoites. Parasites were co-stained with the K13 E3 mAb and antibodies specific to GFP or HA. Pearson correlation coefficient (PCC) values indicate the degree of spatial co-localization between the two signals and were calculated by determining the fluorescence intensity correlations of Alexa Fluor 488 (anti-GFP or anti-HA) and 594 (K13 mAb). Nuclei were stained with DAPI (blue). Scale bars: 2 μ m. (C) IFA images depicting K13 localization in Cam3.II^{WT} (top) and Cam3.II^{R539T} (bottom) parasites throughout asexual blood-stage development. Parasites were stained with the K13 E3 mAb. Sampling was performed every 12h, beginning with tightly synchronized 0–3 hpi ring-stage parasites. Scale bars: 2 μ m. (D) Super resolution microscopy of mature parasites labeled with antibodies to K13 (green), the cytosolic marker HAD1 (red) and the nuclear stain DAPI (blue), showing K13-positive punctate foci. Scale bars: 2 μ m. A video representation is shown in [S1 Video](#). (E) Representative immunoelectron microscopy (IEM) images depicting K13 localization in NF54^{WT}attB-GFP-K13^{WT} or NF54^{WT}attB-3HA-K13^{C580Y} parasites stained with 18 nm colloidal gold-conjugated anti-GFP or anti-HA antibodies. Arrowheads highlight locations of interest. ER, endoplasmic reticulum; Hz, hemozoin; N, nucleus; PVM, parasitophorous vacuolar membrane. Scale bars: 100 nm. (F) Ring-stage survival assay (RSA_{0-3h}) results from NF54^{WT}attB-GFP-K13^{WT}, NF54^{C580Y}attB-GFP-K13^{C580Y}, NF54^{WT}attB-3HA-K13^{WT} and NF54^{WT}attB-3HA-K13^{C580Y} transgenic lines, compared to the sensitive and resistant benchmarks NF54^{WT} and NF54^{C580Y}, respectively. Data show mean \pm SEM percent survival of 700 nM dihydroartemisinin (DHA)-treated early ring-stage parasites (0–3 hpi) compared with control dimethyl sulfoxide (DMSO)-treated parasites processed in parallel. Experiments were performed on 2–6 independent occasions with technical duplicates.

<https://doi.org/10.1371/journal.ppat.1008482.g001>

within small vesicles, vesicular clusters, or tubulovesicular networks that likely belong to the ER or the Golgi apparatus. K13 was also frequently associated with the ER itself, as well as with the plasma and nuclear membranes and the DV. We also saw evidence of K13 associating with cytosomes that traffic host-endocytosed hemoglobin from the parasitophorous vacuolar space to the DV ([Fig 1E](#)).

K13 overexpression restores artemisinin sensitivity to K13-mutant parasites

Our epitope-tagged lines made it possible to further explore the relationship between co-expression of mutant or WT K13 *in trans* and endogenous mutated or wild-type K13. The impact of co-expression on *in vitro* resistance was measured using the RSA_{0-3h}. As sensitive and resistant benchmarks, NF54^{WT} and NF54^{C580Y} parasites (expressing K13 WT or C580Y respectively) yielded mean RSA survival values of 1.0% and 4.8% respectively ([Fig 1F](#)). Co-

Table 1. *Plasmodium falciparum* lines employed in this study.

Name	Strain	Endogenous K13 locus	Transgene	Transgene 5' UTR
NF54 ^{WT}	NF54	WT	–	–
NF54 ^{C580Y}	NF54	C580Y	–	–
NF54 ^{WT} attB-GFP-K13 ^{WT}	NF54attB	WT	GFP-K13 ^{WT} (integrated into <i>cg6</i> attB)	<i>K13</i>
NF54 ^{C580Y} attB-GFP-K13 ^{C580Y}	NF54attB	C580Y	GFP-K13 ^{C580Y} (integrated into <i>cg6</i> attB)	<i>K13</i>
NF54 ^{WT} attB-3HA-K13 ^{WT}	NF54attB	WT	3HA-K13 ^{WT} (integrated into <i>cg6</i> attB)	<i>pbef1a</i>
NF54 ^{WT} attB-3HA-K13 ^{C580Y}	NF54attB	WT	3HA-K13 ^{C580Y} (integrated into <i>cg6</i> attB)	<i>pbef1a</i>
Cam3.II ^{R539T}	Cam3.II	R539T	–	–
Cam3.II ^{WT}	Cam3.II	WT	–	–
Cam3.II ^{C580Y}	Cam3.II	C580Y	–	–
CamWT	CamWT	WT	–	–
CamWT ^{C580Y}	CamWT	C580Y	–	–
Dd2 ^{WT} GFP-Rab6	Dd2	WT	Rab6-GFP (episome)	<i>pfsec12</i>
Dd2 ^{R539T} GFP-Rab6	Dd2	R539T	Rab6-GFP (episome)	<i>pfsec12</i>
Dd2 ^{WT} Sec24A-GFP	Dd2	WT	Sec24A-GFP (episome)	<i>pfsyntaxin17</i>
3D7 ^{WT} Mito-hGrx1-roGFP2	3D7	WT	Mito-hGrx1-roGFP2	<i>pfprt</i>

<https://doi.org/10.1371/journal.ppat.1008482.t001>

expression of GFP-K13^{WT} or 3HA-K13^{C580Y} in our NF54^{WT} attB epitope-tagged lines (see above) led to ART sensitivity, with RSA values of 0.8% and 0.7% in the NF54^{WT} attB-GFP-K13^{WT} and NF54^{WT} attB-3HA-K13^{C580Y} lines, respectively. As comparators, we also engineered an NF54^{C580Y} attB line co-expressing GFP-K13^{C580Y} as well as an NF54^{WT} attB line co-expressing 3HA-K13^{WT} (Table 1). The former line expresses mutant K13 in both the endogenous and transgene loci and demonstrated a nominally less sensitive phenotype (with 1.6% mean RSA survival), relative to the fully sensitive NF54^{WT} line. The latter line expresses WT K13 in both loci and was fully sensitive (mean RSA survival 1.0%). These data confirm that mutant K13 does not confer resistance in a dominant-negative manner and suggest that overexpression of the mutant protein mostly reverts K13 mutant parasites to DHA sensitivity. Our results agree with recently published evidence that the RSA_{0-3h} phenotype inversely correlates with K13 abundance and that K13 levels are reduced in mutant parasites relative to WT [27,28].

K13 co-immunoprecipitates with vesicular transport, ER, and mitochondrial proteins

To identify putative K13-interacting partners, we performed six independent HPLC/MS-MS-based co-IP experiments using two K13 mAbs (E3 and D9, which both yielded robust IFA signals). These experiments comprised 13 test samples from parasite cultures enriched in 0–12 hpi rings. These samples were prepared from Cam3.II lines expressing WT, C580Y or R539T K13, as well as from CamWT lines expressing WT or C580Y K13 (Table 1 and S1 Table). For a given sample, we retained only proteins that were identified by ≥ 3 peptide spectra. We then filtered results across all samples by retaining only proteins that were present in ≥ 3 of the 6 independent experiments and ≥ 5 of the 13 test samples, and absent in all of the 10 negative control samples (i.e. that used an unrelated antibody, or used affinity columns without the addition of anti-K13 antibodies). Results showed that K13 was by far the most abundant protein detected, representing 22% of the total number of spectra detected in our filtered list of 83 high-confidence immunoprecipitated proteins (Table 2). In a secondary analysis, we relaxed the criteria to allow for proteins that appeared in 1 to 3 negative control samples (out of 10), while retaining the positive criteria listed above. This yielded an additional 90 proteins as putative interactors (S2 Table).

After K13, the most abundant protein in our co-IPs was S-adenosylmethionine (SAM) synthetase (also known as methionine adenosyltransferase), a redox-regulated enzyme that produces the methyl donor S-adenosylmethionine used in methylation reactions of multiple substrates including nucleic acids, proteins, phospholipids and amines [36]. Adenosylhomocysteinase (also known as adenosylhomocysteine hydrolase), another enzyme involved in the methionine metabolism pathway that produces SAM, was also in the top six most abundant proteins. Phosphoglycerate mutase 1 (PGM1) was the second most abundant protein, with phosphoglucomutase 2 (PGM2) being less abundant. Intriguingly PGM5, the mammalian homolog of PGM2, tethers the K13 ortholog Keap1 to the mitochondria [37,38]). PGM1 is annotated as being involved in parasite glycolysis, a pathway implicated with several other immunoprecipitated proteins. The receptor for activated c kinase (RACK), a cytosolic multi-functional scaffolding protein, was also abundant.

Consistent with our data that localized K13 to intracellular foci, we reproducibly co-immunoprecipitated K13 with several proteins involved in vesicular trafficking (Table 2 and S2 Table). These included multiple members of the Rab family of GTPases, namely Rab1A, Rab1B, Rab5C, Rab6, Rab7, Rab11B, and Rab18B, which function as regulators of vesicular trafficking and endocytosis in eukaryotes [39]. By applying an overrepresentation test in the

Table 2. Putative K13-interacting protein partners identified by co-immunoprecipitation and LC/MS-MS.

PlasmoDB Gene ID	Gene Name	Abbreviation	Cellular component and/or functional features	Mean % total spectral counts, normalized	Number of experiments present (of 6) ¹	Number of samples present (of 13 total, 6 WT, 7 mutant) ²
PF3D7_1343700	Kelch protein K13	K13	Putative CUL3 ubiquitin ligase adaptor protein	22.19%	6	13 (6,7)
PF3D7_0922200	S-adenosylmethionine synthetase	SAMS	Methionine metabolism	5.19%	3	6 (3,3)
PF3D7_1120100	Phosphoglycerate mutase 1, putative	PGM1	Glycolysis	3.58%	4	8 (4,4)
PF3D7_0826700	Receptor for activated c kinase	RACK	Cytosolic multi-functional scaffolding protein	2.47%	5	9 (3,6)
PF3D7_1437900	Heat shock protein 40	HSP40	Cytosolic chaperone	2.33%	5	11 (5,6)
PF3D7_1010700	Dolichyl-phosphate-mannose-protein mannosyltransferase, putative	ALG2	CUL3 ubiquitin ligase adaptor protein, with role in dolichol metabolism	2.32%	6	11 (5,6)
PF3D7_0520900	Adenosylhomocysteinase	SAHH	Methionine metabolism	2.15%	3	6 (3,3)
PF3D7_1026800	40S ribosomal protein S2	RPS2	Small ribosomal subunit	1.76%	6	12 (5,7)
PF3D7_1444800	Fructose-bisphosphate aldolase	FBPA	Glycolysis	1.72%	3	6 (3,3)
PF3D7_0105200	RAP domain-containing protein	–	Altered transcription following inhibition of polyamine and methionine metabolism enzymes	1.51%	5	12 (5,7)
PF3D7_0915400	ATP-dependent 6-phosphofructokinase	PFK9	Cytoplasm	1.50%	3	5 (2,3)
PF3D7_0822600	Protein transport protein Sec23	SEC23	COPII mediated vesicular transport	1.50%	4	7 (3,4)
PF3D7_0934500	V-type proton ATPase subunit E, putative	–	Ca ²⁺ homeostasis	1.49%	5	11 (5,6)
PF3D7_0626800	Pyruvate kinase	PyrK	Glycolysis / Interaction with HDAC1	1.49%	4	6 (3,3)
PF3D7_1008700	Tubulin beta chain	–	Microtubules	1.40%	4	8 (4,4)
PF3D7_1412500	Actin II	ACT2	Actin filaments	1.38%	4	9 (4,5)
PF3D7_0929200	RNA-binding protein, putative	–	RNA-binding protein	1.27%	3	6 (2,4)
PF3D7_0927300	Fumarate hydratase, putative	FH	Mitochondrial TCA cycle	1.24%	6	9 (4,5)
PF3D7_0623500	Superoxide dismutase [Fe]	SOD2	Mitochondrial antioxidant system	1.21%	4	8 (4,4)
PF3D7_0820700	2-oxoglutarate dehydrogenase E1 component	KDH	Mitochondrial TCA cycle	1.20%	3	7 (3,4)
PF3D7_1037100	Pyruvate kinase 2	PyKII	Apicoplast / Isoprenoid metabolism	1.19%	4	8 (4,4)
PF3D7_0608800	Ornithine aminotransferase	OAT	Ornithine metabolism	1.18%	3	5 (2,3)
PF3D7_1302100	Gamete antigen 27/25	Pfs27/25	Early marker of gametocyte development	1.13%	4	8 (3,5)
PF3D7_1327800	Ribose-phosphate pyrophosphokinase, putative	–	Pentose phosphate cycle	1.12%	5	7 (2,5)
PF3D7_0823900	Dicarboxylate/tricarboxylate carrier	DTC	Mitochondrial antioxidant system, TCA cycle	1.07%	4	9 (4,5)
PF3D7_1215000	Thioredoxin peroxidase 2	Trx-Px2	Mitochondrial antioxidant system	1.06%	4	7 (2,5)
PF3D7_1472600	Protein disulfide-isomerase	PDI-14	Oxidative protein folding in the ER, component of chaperone complexes that interact with BiP	1.06%	4	7 (3,4)
PF3D7_0720400	Ferrodoxin NADP+ reductase	–	Mitochondrial iron-sulfur protein biogenesis	1.05%	3	5 (2,3)
PF3D7_1468700	Eukaryotic initiation factor 4A	eIF4A	Eukaryotic translation initiation factor 4F complex	1.02%	4	7 (3,4)

(Continued)

Table 2. (Continued)

PlasmoDB Gene ID	Gene Name	Abbreviation	Cellular component and/or functional features	Mean % total spectral counts, normalized	Number of experiments present (of 6) ¹	Number of samples present (of 13 total, 6 WT, 7 mutant) ²
PF3D7_0722200	Rhoptry-associated leucine zipper-like protein 1	RALP1	Rhoptry neck protein	0.99%	4	6 (4,2)
PF3D7_1410600	Eukaryotic translation initiation factor 2 subunit gamma, putative	eIF2g	Eukaryotic translation initiation factor 2 complex	0.92%	3	7 (3,4)
PF3D7_1338200	60S ribosomal protein L6-2, putative	–	Large ribosomal subunit	0.92%	4	9 (4,5)
PF3D7_1320000	Golgi protein 1	GPI1	ER-Golgi translocation and quality control	0.89%	3	6 (3,3)
PF3D7_1437700	Succinyl-CoA ligase, putative	–	Mitochondrial TCA cycle	0.86%	4	6 (1,5)
PF3D7_0829200	Prohibitin, putative	PHB1	Mitochondrial protein degradation	0.83%	4	9 (4,5)
PF3D7_0621200	Pyridoxine biosynthesis protein PDX1	PDX1	Vitamin B6 synthesis	0.83%	3	6 (3,3)
PF3D7_1330600	Elongation factor Tu, putative	–	Mitochondrial protein translation	0.83%	4	8 (3,5)
PF3D7_0616800	Malate:quinone oxidoreductase, putative	MQO	Mitochondrial TCA cycle, ETC	0.81%	4	7 (2,5)
PF3D7_0624000	Hexokinase	HK	Glycolysis	0.79%	3	6 (3,3)
PF3D7_0920800	Inosine-5'-monophosphate dehydrogenase	IMPDH	Purine metabolism	0.78%	3	5 (2,3)
PF3D7_0511800	Inositol-3-phosphate synthase	INO1	Inositol phosphate metabolism	0.73%	3	5 (3,2)
PF3D7_0727200	Cysteine desulfurase, putative	NFS	Mitochondrial iron-sulfur protein biogenesis	0.72%	3	5 (1,4)
PF3D7_0813900	40S ribosomal protein S16, putative	–	Ribosome	0.70%	3	9 (3,6)
PF3D7_1108400	Casein kinase 2, alpha subunit	CK2a	Cytoplasm, nucleus, calcium dependent protein kinase (CK2 complex)	0.69%	4	9 (4,5)
PF3D7_1115600	Peptidyl-prolyl cis-trans isomerase	CYP19B	Oxidative protein folding in the ER, component of chaperone complexes that interact with BiP	0.69%	3	5 (2,3)
PF3D7_1320800	Dihydrolypoyllysine-residue succinyltransferase component of 2-oxoglutarate dehydrogenase complex	–	Mitochondrial TCA cycle	0.68%	4	7 (3,4)
PF3D7_1408600	40S ribosomal protein S8e, putative	–	Ribosome	0.68%	3	6 (2,4)
PF3D7_0816600	Chaperone protein ClpB	ClpB	Chaperone-assisted protein folding (apicoplast and/or mitochondrion)	0.68%	4	8 (3,5)
PF3D7_1133400	Apical membrane antigen 1	AMA1	Invasion molecule	0.67%	3	6 (2,4)
PF3D7_0709700	Prodrug activation and resistance esterase	PARE	Cytosolic esterase, putative lipase	0.65%	5	9 (4,5)
PF3D7_0401800	<i>Plasmodium</i> exported protein (PHISTb), unknown function	PfD80	Maurer's cleft exported protein	0.64%	4	8 (4,4)
PF3D7_0316800	40S ribosomal protein S15A, putative	–	Ribosome	0.63%	5	9 (5,4)
PF3D7_1465900	40S ribosomal protein S3	–	Ribosome	0.62%	3	6 (2,4)
PF3D7_0106800	Ras-related protein Rab5C	RAB5C	Intracellular traffic / Endocytosis	0.61%	3	6 (3,3)
PF3D7_1025300	Conserved <i>Plasmodium</i> protein, unknown function	–	No known or predicted function	0.60%	3	6 (2,4)
PF3D7_1136300	Tudor staphylococcal nuclease	TSN	mRNA splicing	0.60%	4	7 (2,5)
PF3D7_1361100	Protein transport protein Sec24A	SEC24A	COPII mediated vesicular transport	0.59%	4	6 (2,4)

(Continued)

Table 2. (Continued)

PlasmoDB Gene ID	Gene Name	Abbreviation	Cellular component and/or functional features	Mean % total spectral counts, normalized	Number of experiments present (of 6) ¹	Number of samples present (of 13 total, 6 WT, 7 mutant) ²
PF3D7_1439400	Cytochrome bc1 complex subunit Rieske, putative	–	Mitochondrial cytochrome bc1 complex (ETC)	0.55%	4	7 (3,4)
PF3D7_1452000	Rhoptry neck protein 2	RON2	Invasion molecule	0.54%	3	5 (2,3)
PF3D7_1212500	Glycerol-3-phosphate 1-O-acyltransferase	GAT	ER membrane protein / Glycerolipid synthesis	0.54%	4	8 (3,5)
PF3D7_0922500	Phosphoglycerate kinase	PGK	Glycolysis	0.50%	4	5 (2,3)
PF3D7_1008400	26S proteasome AAA-ATPase subunit RPT2, putative	RPT2	Proteasome	0.49%	4	6 (3,3)
PF3D7_0416800	Small GTP-binding protein Sar1	SAR1	COPII mediated vesicular transport	0.49%	4	7 (4,3)
PF3D7_0810600	ATP-dependent RNA helicase DBP1, putative	DBP1	Helicase	0.48%	3	6 (2,4)
PF3D7_1145400	Dynamin-like protein	DYN1	Clathrin-mediated vesicular transport	0.45%	3	6 (3,3)
PF3D7_0309600	60S acidic ribosomal protein P2	PfP2	Ribosome	0.43%	4	5 (3,2)
PF3D7_0112200	Multidrug resistance-associated protein 1	MRP1	Plasma membrane component / glutathione and redox metabolism	0.41%	3	6 (3,3)
PF3D7_0504600	2-oxoisovalerate dehydrogenase subunit beta, mitochondrial, putative	BCKDHB	Mitochondrial TCA cycle	0.41%	3	6 (3,3)
PF3D7_1306400	26S proteasome AAA-ATPase subunit RPT4, putative	RPT4	Proteasome	0.36%	3	5 (2,3)
PF3D7_0524000	Karyopherin beta	KASb	Import and export through the nuclear pore	0.35%	4	6 (3,3)
PF3D7_0702500	<i>Plasmodium</i> exported protein, unknown function	–	Maurer's cleft exported protein	0.33%	3	7 (3,4)
PF3D7_1361900	Proliferating cell nuclear antigen 1	PCNA1	DNA replication and repair	0.32%	3	6 (2,4)
PF3D7_0507100	60S ribosomal protein L4	RPL4	Ribosome	0.30%	3	6 (3,3)
PF3D7_1247400	Peptidyl-prolyl cis-trans isomerase FKBP35	FKBP35	Cytoplasm, nucleus, centrosome	0.30%	3	5 (1,4)
PF3D7_0213700	Conserved <i>Plasmodium</i> protein, unknown function	–	No known or predicted function	0.30%	3	5 (3,2)
PF3D7_0217900	Conserved <i>Plasmodium</i> protein, unknown function	–	Putative thioesterase	0.29%	3	5 (1,4)
PF3D7_0205900	26S proteasome regulatory subunit RPN1, putative	RPN1	Proteasome	0.29%	3	5 (3,2)
PF3D7_0719700	40S ribosomal protein S10, putative	–	Ribosome	0.28%	3	5 (1,4)
PF3D7_1105000	Histone H4	H4	Nucleus	0.27%	4	5 (3,2)
PF3D7_0413500	Phosphoglucomutase 2, putative	PGM2	Glycolysis	0.25%	3	6 (3,3)
PF3D7_0520000	40S ribosomal protein S9, putative	–	Ribosome	0.23%	3	7 (4,3)
PF3D7_1129200	26S proteasome regulatory subunit RPN7, putative	RPN7	Proteasome	0.22%	3	5 (3,2)

¹A summary of these experiments can be found in S2 Table.

²The 13 samples were derived from Cam3.II^{WT} (4), Cam3.II^{R539T} (4), Cam3.II^{C580Y} (2), CamWT^{WT} (2), and CamWT^{C580Y} (1).

<https://doi.org/10.1371/journal.ppat.1008482.t002>

PANTHER classification system for biological processes, we observed an 18-fold enrichment in Rab proteins, with a p value of 1×10^{-6} (S3 Table; <http://pantherdb.org>; [40,41]). K13-specific mAbs also co-immunoprecipitated Sar1, which assists in COPII coat assembly, and Sec23 and Sec24a, which form a heterodimer associated with the COPII vesicle coat that surrounds

transport vesicles budding from the ER. In *P. falciparum*, Sec24a has been localized to transitional ER sites where it mediates the capture of COPII vesicle cargo [42]. Our co-IP studies also identified other ER-associated proteins, including Sec61, part of the ER-Sec61 translocon complex [43,44], the luminal protein disulfide isomerase (PDI-14), and two peptidyl-prolyl cis-trans isomerases (CYP19B and FKBP35) that catalyze protein folding in the ER.

Multiple members of the eukaryotic translation machinery were also identified, including protein components of the 40S and 60S ribosomes and several translation initiation or elongation factors (EIF1 α , eEF2, eIF2 α , eIF4A), as well as several nucleic acid-binding proteins (including SR1 and SR4). Multiple components of the 19S regulatory particle of the 26S proteasome were observed, notably RPT2, RPT4, RPN1, and RPN7. The 26S proteasome likely has a role in degrading ART-damaged proteins, supporting a potential role for K13 as a ubiquitin ligase adaptor protein that could help deliver polyubiquitinated proteins for proteasome-mediated degradation [45].

We also identified several proteins that localize to the DV, wherein host hemoglobin is degraded leading to the release of reactive heme. These include the hemoglobin-processing enzyme plasmepsin II, and the membrane proteins PfCRT and falcylisin, with the latter also being involved in transit peptide degradation in the apicoplast and mitochondria [46].

Unexpectedly, several proteins were also detected that are known or predicted to localize to mitochondria. These include the Rieske protein that is part of the cytochrome bc1 complex, as well as prohibitin 1 that is implicated in mitochondrial morphogenesis and that is a possible regulator of mitochondrial membrane potential [47]. Components of the TCA cycle (including fumarate hydratase, the 2-oxoglutarate dehydrogenase E1 component, a dicarboxylate/tricarboxylate carrier, succinyl-CoA ligase, malate:quinone oxidoreductase, and the 2-oxoisovalerate dehydrogenase beta subunit) were also observed. We also identified factors thought to be involved in mitochondrial translation (elongation factor Tu), protein degradation (the ATP-dependent protease subunit ClpQ, the ATP-dependent zinc metalloprotease FTSH 1, and the mitochondrial-processing peptidase alpha subunit), iron-sulfur protein biogenesis (ferrodoxin NADP⁺ reductase and cysteine desulfurase), as well as two putative mitochondrial chaperones (HPS40 and CPN20).

Other potential K13-interacting proteins associated with the mitochondria included the ATP synthase F1 alpha subunit (involved in mitochondrial energy metabolism), mitochondrial matrix protein 33, and a putative dynamin (involved in mitochondrial fission). Finally, several proteins were associated with the mitochondrial antioxidant system, including superoxide dismutase, thioredoxin peroxidase 2, isocitrate dehydrogenase, the succinyl-CoA synthetase alpha subunit, a lipoamide acyltransferase, and the glutathione peroxidase-like thioredoxin peroxidase. PANTHER overrepresentation analysis focusing on cellular components revealed a 15-fold enrichment in mitochondrial proteins, with a *p* value of 4×10^{-4} (S4 Table).

In reviewing putative functional features of proteins in our K13 co-IP list (Table 2 and S2 Table), we observed an apparent enrichment of proteins known to undergo post-translational modifications, specifically palmitoylation (73 proteins), glutathionylation (59 proteins), and S-nitrosylation (53 proteins). In comparison, 409, 493 and 319 proteins with these respective modifications were identified from the total asexual blood stage proteome (comprising over 4,800 proteins based on detected expression ([48–51]; <http://mpmp.huji.ac.il>)). This corresponds to an estimated three to five-fold enrichment in these proteins among putative K13-interacting partners.

K13 partially co-localizes with proteins involved in vesicular trafficking and cytostomes

To further interrogate the putative interactors identified by our co-IP studies, we performed quantitative co-localization studies using our K13 mAbs or K13 tagged lines combined with

other epitope-tagged lines or primary antibodies to proteins of interest. Initial experiments focused on the Rab GTPase family and the Sec23/24 heterodimer. For these studies, we prepared highly synchronized early ring-stage parasites (0–3 hpi) and pulsed these for 6h with 700 nM DHA. Control cultures were mock-treated with DMSO vehicle. Parasites were harvested at various time points post drug pulse and subsequently fixed and stained for microscopic analysis (S3 Fig). To increase throughput and reproducibility we developed a quantitative analysis pipeline in collaboration with Nikon software engineers for image processing and determination of PCC values (listed in S5 Table).

We first assayed the Cam3.II^{WT} and Cam3.II^{R539T} lines with antibodies to Rab5A, 5B, or 5C, along with our K13-specific E3 mAb. Samples were collected immediately post drug treatment (0h time point, ~6 hpi), and, in the case of Rab5A, also at 12h post pulse (~18 hpi). IFAs with anti-K13 and anti-Rab5A antibodies showed an intermediate degree of spatial association between the two proteins immediately (0h) post pulse in Cam3.II^{WT} and Cam3.II^{R539T}, with median PCC values for both lines centering around 0.5 (Fig 2A and S4A Fig). At this time point, we observed no effect of DHA treatment on PCC values in either line. At 12h post pulse, however, we observed a statistically significant increase in PCC values for both mutant and WT parasites in DHA-treated cultures as compared to mock (DMSO) treatment (Fig 2B and S4B Fig). At this 12h time point with DHA-treated parasites, the PCC values for K13 and Rab5A were significantly higher for K13 WT parasites compared with their mutant counterparts (median 0.65 vs 0.43; $p < 0.001$; Fig 2B and S5 Table).

The putative K13 associations with Rab5B or Rab5C were also examined immediately post DHA or DMSO treatment. Median PCC values for K13 and Rab5B or Rab5C were slightly lower than for Rab5A in both Cam3.II^{WT} and Cam3.II^{R539T} parasites (Fig 2C and 2D and S4A Fig). For both Rab5B and 5C, a slightly stronger association with K13 was observed in WT parasites compared with the mutants, a trend that became statistically significant upon DHA treatment ($p < 0.05$ and $p < 0.01$, respectively). With all three Rab proteins, there was a trend towards slightly lower PCC values immediately post DHA treatment (0h time point) in the K13 mutant line and slightly increased PCC values in the K13 WT line. These data suggest decreased levels of endocytosis in K13 mutant parasites following DHA exposure.

We subsequently assessed the spatial association between K13 and Rab6, a trans-Golgi marker known to direct exocytic vesicles to the plasma membrane in mammalian cells [52]. These experiments were conducted using Dd2 K13 WT or R539T parasites expressing Rab6-GFP episomally. PCC values were moderately high in both DMSO-treated lines, and were significantly increased in both lines directly post DHA pulse, with the highest levels of association (median 0.73) observed in DHA-treated K13 WT parasites (Fig 2E, S4C Fig and S5 Table).

We continued our IFA analyses with the late endosome marker Rab7 and the post Golgi marker Rab11A, using the Cam3.II^{WT} and Cam3.II^{R539T} lines and antibodies to K13 and the two Rab proteins. For Rab7 we observed relatively high median PCC values, centering around 0.6, regardless of K13 allele status. These remained unchanged immediately post DHA treatment (0h time point; Fig 2F and S4D Fig). For Rab11A we measured high PCC values for colocalization with K13 in Cam3.II^{R539T} parasites for all time points and conditions examined, including 0h and 12h post DHA and DMSO treatments (median 0.70–0.84; Fig 2G and 2H, S4D and S4E Fig, and S5 Table). In contrast, median PCC values for K13 and Rab11A were significantly lower in WT parasites than in mutant parasites at both time points, in particular for DMSO-treated cultures (0.60–0.61; S5 Table). A slight but nonetheless significant increase was observed in K13 and Rab11A association in WT parasites immediately after DHA treatment (0h time point; $p < 0.01$), bringing PCC values to the level of K13 mutant parasites, but these values dropped again at 12h post treatment (Fig 2G and 2H).

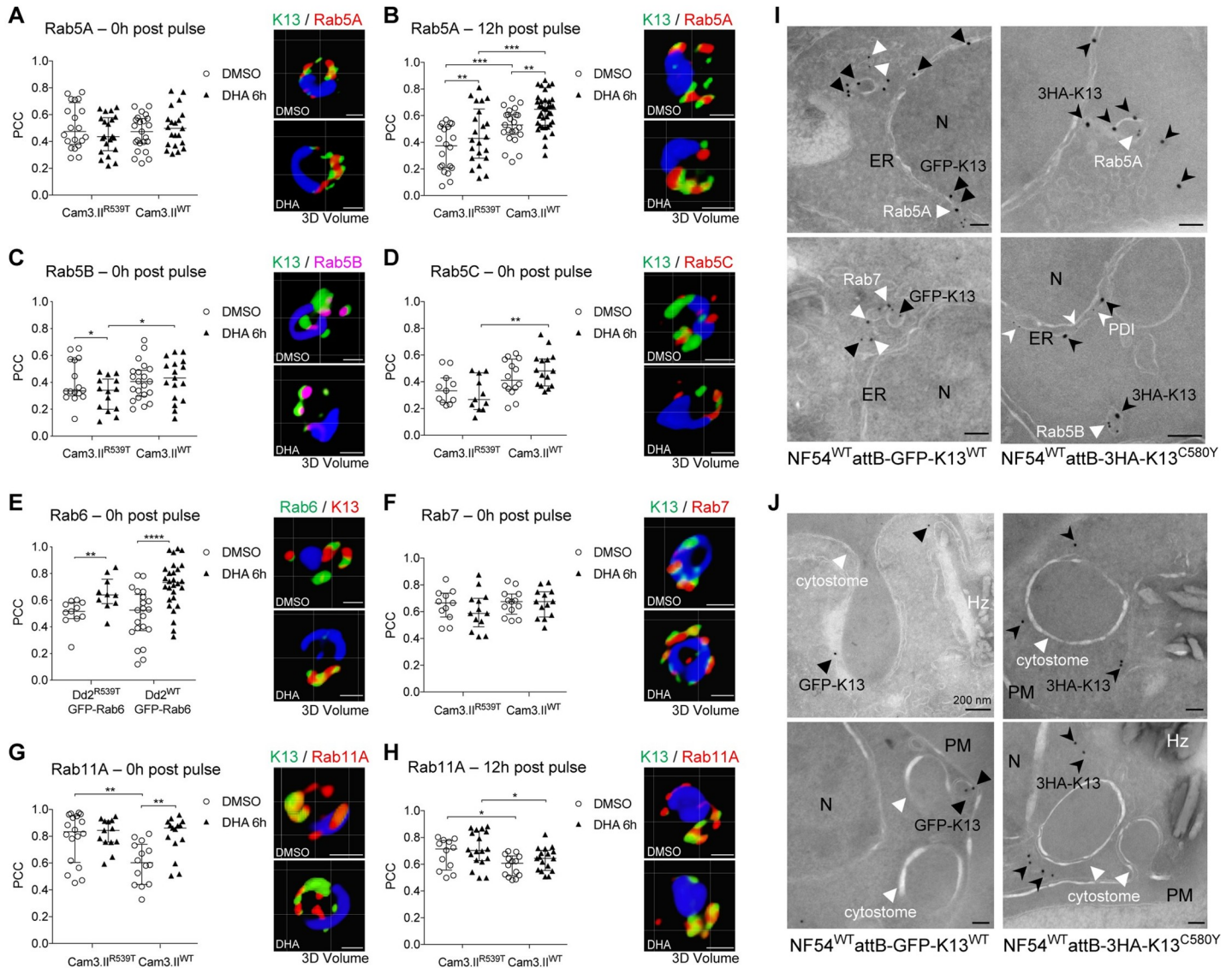


Fig 2. K13 partially co-localizes with vesicular transport proteins and sites adjacent to cytostomes. (A–H) PCC values quantifying the degree of spatial co-localization between K13 and (A, B) Rab5A, (C) Rab5B, (D) Rab5C, (E) Rab6, (F) Rab7, and (G, H) Rab11A, with accompanying representative 3D volume reconstructions of IFA images. Assays were conducted using Cam3.1I^{R539T} or Cam3.1I^{WT} parasites, except in the case of Rab6, where Dd2^{R539T} or Dd2^{WT} parasite lines expressing GFP-Rab6 were employed. Samples were collected either directly following a 6h 700 nM pulse of DHA (A, C–G; denoted 0h) or 12h post pulse (B, H). DMSO was used as a vehicle control. K13 was labeled using the E3 mAb (green). Rab proteins were labeled with specific antibodies (red) or, in the case of Rab6, anti-GFP (green, with K13 this time in red). PCC values were calculated from the fluorescence intensity correlations of Alexa Fluor 488 and either Alexa Fluor 594 or Alexa Fluor 647. For PCC plots, each dot represents an individual parasitized RBC. Horizontal lines represent the median with interquartile range. Two-tailed unpaired *t* tests were used to calculate *p* values. **p* < 0.05; ***p* < 0.01; ****p* < 0.001; *****p* < 0.0001. Scale bars: 1 μm. (I) IEM images of trophozoite-stage NF54^{WT}attB-GFP-K13^{WT} (left) or NF54^{WT}attB-3HA-K13^{C580Y} (right) parasites co-stained with anti-GFP or anti-HA, respectively, and anti-Rab5A (two upper panels), anti-Rab7 (bottom left) or anti-Rab5B plus anti-PDI (bottom right). Secondary antibodies were conjugated to colloidal gold particles of different sizes. Arrowheads highlight locations of interest. ER, endoplasmic reticulum; N, nucleus. Scale bars: 100 nm. (J) IEM images of NF54^{WT}attB-GFP-K13^{WT} (left) or NF54^{WT}attB-3HA-K13^{C580Y} (right) trophozoites stained with anti-GFP or anti-HA, respectively. Arrowheads highlight locations of interest. Hz, hemozoin; N, nucleus; PM, plasma membrane. Scale bars: 100 nm unless otherwise indicated.

<https://doi.org/10.1371/journal.ppat.1008482.g002>

To extend these co-localization studies, we also performed ultrastructural analyses via IEM. These studies used the NF54^{WT}attB-GFP-K13^{WT} and NF54^{WT}attB-3HA-K13^{C580Y} lines, which were stained with anti-GFP or anti-HA colloidal gold-conjugated primary antibodies. Co-staining with antibodies specific for Rab proteins localized K13 (black arrowheads) to sites

either within or adjacent to vesicles containing Rab5A, Rab5B or Rab7 (white arrowheads; [Fig 2I](#) and [S4F Fig](#)). In some IEM images we also observed K13 near cytosomes ([Fig 2J](#)).

Our co-IP data suggested that K13 might also partially associate with the transitional ER marker Sec24a, involved in vesicle budding from the ER. To examine this further, we tested our anti-K13 E3 mAb on a Sec24a-GFP expressing parasite line that harbors WT K13 [42]. Quantitative IFA analyses revealed intermediate to high median PCC values (0.60–0.67) for Sec24a and K13, with no significant changes upon DHA treatment ([S4G and S4H Fig](#)).

K13 partially co-localizes with the ER chaperone BiP but not with the cis-Golgi marker ERD2

Given that K13 also co-immunoprecipitated a number of ER-associated proteins ([Table 2](#) and [S2 Table](#)), we performed imaging analyses using markers for the ER and cis-Golgi, namely BiP and ERD2, respectively. To test for K13 and BiP spatial association, we applied high-resolution 3D structured illumination microscopy to ring- and schizont-stage parasites. These assays employed the Cam3.II K13 WT and R539T mutant lines, which were stained with anti-K13 and anti-BiP antibodies ([Fig 3A](#)). In the ring stages, both mutant and WT K13 proteins localized to foci associated with the BiP-labeled ER, whereas in the schizont stages only R539T K13 showed evidence of a close spatial association with BiP. This association was supported via widefield immunofluorescence microscopy with trophozoites ([S5A Fig](#)). Close proximity between K13 and the ER was also observed by IEM studies with NF54^{WT}attB-GFP-K13^{WT} parasites labeled with anti-BiP and anti-GFP antibodies ([S5B Fig](#)), as well as our previous IEM studies with triple labeling of K13, Rab5B and the ER chaperone PDI (white arrowheads; [Fig 2I](#) and [S4F Fig](#)).

We next assessed the degree of co-localization between K13 and BiP in DMSO- and DHA-treated Cam3.II^{WT} or Cam3.II^{R539T} samples throughout the first half of the IDC, with time points taken at 0h, 3h, 12h and 24h post treatment ([S3 Fig](#)). In DMSO-treated samples we observed a non-significant trend towards lower PCC values in K13 WT samples as compared to mutant samples across all time points tested ([Fig 3B–3E](#) and [S5C Fig](#)). At the 0h time point, for example, PCC values for K13 and BiP averaged 0.72 and 0.64 for Cam3.II^{R539T} and Cam3.II^{WT} respectively ([S5 Table](#)). By comparison, a very recent study using K13-specific polyclonal antiserum reported a PCC value of 0.58 between WT K13 and BiP [53]. Interestingly, following DHA treatment, mutant and WT parasites showed significant differences at 12h post drug pulse ([Fig 3E](#) and [S5C Fig](#)). Whereas PCC values for WT parasites dropped significantly post DHA treatment, PCC values for K13 and BiP in R539T parasites were highest post DHA treatment at this time point (median 0.82; [S5 Table](#)).

In light of the proximity between the cis-Golgi and sites of vesicle budding from the ER, we compared association coefficients obtained with BiP to those measured using ERD2, a marker of the cis-Golgi, using the same lines. In contrast to the high PCC values observed for K13 and BiP in Cam3.II^{WT} or Cam3.II^{R539T}, for K13 and ERD2 we measured moderate to low PCC values regardless of the condition and parasite line tested (median 0.39–0.4; [Fig 3F and 3G](#), [S5D Fig](#) and [S5 Table](#)). These data argue against K13 being present in the cis-Golgi.

To assess whether K13 localization was affected by blocking ER-to-Golgi transport, we exposed parasites to the fungal metabolite brefeldin A (BFA). This agent perturbs secretory traffic in parasites, resulting in retention of secreted proteins within the ER [54]. In these experiments, we treated Cam3.II K13 WT and mutant ring-stage parasites (0–3 hpi) with BFA or vehicle control (EtOH) for 1h before harvesting and co-staining with anti-K13 and antibodies to either BiP or ERD2. After the BFA pulse we observed a significantly higher association between K13 and BiP in K13 mutant parasites, as compared with the ethanol (EtOH) mock-

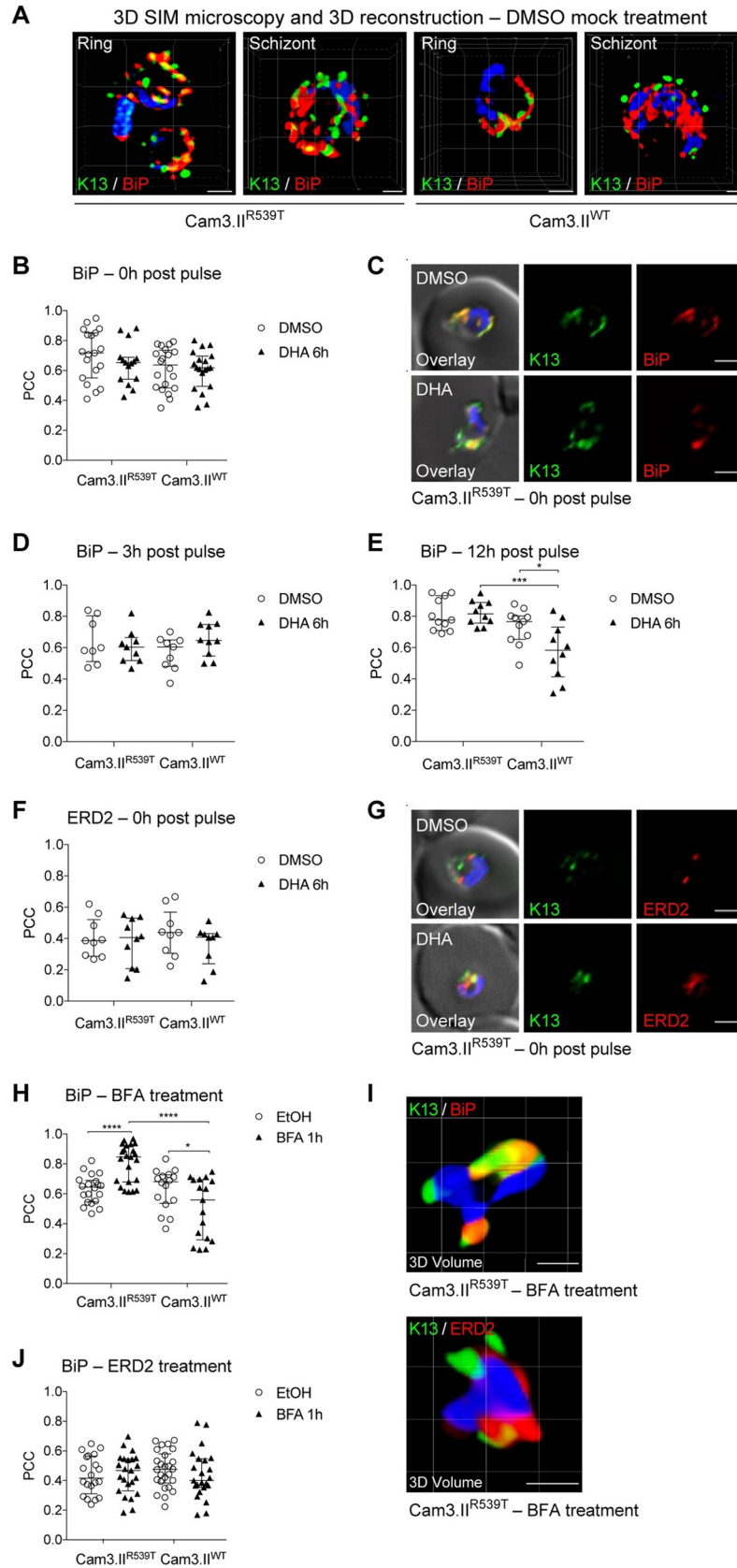


Fig 3. K13 shows substantial co-localization with the ER chaperone BiP but not with the cis-Golgi marker ERD2. (A) 3D SIM microscopy images showing Cam3.II^{R539T} or Cam3.II^{WT} parasites co-stained with the K13 E3 mAb (green) and antibodies to the ER chaperone BiP (red). SIM: structured illumination microscopy. Scale bars: 1 μ m. (B, C) PCC values quantifying co-localization between K13 and BiP at 0h post DHA (6h, 700 nM) pulse, alongside representative IFA images. DMSO was used as a vehicle control. Assays were conducted using the Cam3.II^{R539T} and Cam3.II^{WT} lines. Parasites were co-stained with the K13 E3 mAb and antibodies to BiP. PCC values were calculated and statistics performed as in Fig 2. Scale bars: 2 μ m. (D, E) PCC values for co-localization of K13 and BiP at (D) 3h or (E) 12h post drug pulse. Assays were conducted and PCC values were calculated as in (B). (F, G) PCC values quantifying co-localization between K13 and ERD2 at 0h post DHA pulse, alongside representative IFA images. Parasites were co-stained with the K13 E3 mAb and antibodies to ERD2. Assays were otherwise conducted as in (B). Scale bars: 2 μ m. (H–J) PCC values for co-localization of K13 and BiP or ERD2 following a 1h treatment with Brefeldin A (BFA; 5 μ g/ml). EtOH was used as a vehicle control. Assays were conducted using the Cam3.II^{R539T} and Cam3.II^{WT} lines. (I) 3D volume reconstruction of deconvolved Z-stacks (15 image stacks, step size of 0.2 μ m) of Cam3.II^{R539T} ring-stage parasites treated with BFA and co-stained with anti-K13 mAb E3 and anti-BiP (top) or anti-ERD2 (bottom). Scale bars: 1 μ m.

<https://doi.org/10.1371/journal.ppat.1008482.g003>

treated population (median 0.85 vs 0.64, respectively; **S5 Table**). By comparison, we measured significantly lower PCC values for K13 and BiP in BFA-pulsed vs mock-treated K13 WT parasites (median 0.68 vs 0.56; **Fig 3F** and **S5 Table**). In contrast, PCC values for K13 and ERD2 remained moderate regardless of the treatment (BFA or mock; **Fig 3J**) and were equivalent to those observed in the DHA and DMSO treatments in both lines (**Fig 3F**). The increased association between BiP and mutant K13 upon BFA treatment was further illustrated for Cam3.II^{R539T} in 3D volume reconstructions of K13- and BiP-labeled ring-stage parasites (**Fig 3I**).

K13 shows an elevated association with mitochondria post dihydroartemisinin pulse

To explore the link between K13 and the mitochondrial proteins observed in our co-IP studies (**Table 2** and **S2 Table**), we quantified the degree of co-localization between K13 and mitochondria using our anti-K13 antibodies together with the live mitochondrial dye MitoTracker Deep Red. PCC values were determined either immediately (0h) or 12h post drug pulse (i.e. 6h of DHA or DMSO vehicle). These assays used the NF54^{WT}attB-GFP-K13^{WT} and NF54^{WT}attB-3HA-K13^{C580Y} lines, as well as the isogenic Cam3.II K13 WT and R539T pair. Median PCC values for mock-treated parasites were low (ranging from -0.03 to 0.25), as shown in representative images (**Fig 4A–4E** and **S6 Table**). After DHA treatment we observed significantly increased associations between the mitochondria and K13 at both time points in all parasite lines tested, particularly at the 12h time point in NF54^{WT}attB-GFP-K13^{WT} parasites (median PCC value 0.84 in DHA-treated parasites vs. 0.44 in mock-treated; **S6A Fig** and **S6 Table**). For the isogenic Cam3.II^{R539T} and Cam3.II^{WT} lines, a greater increase was observed in the mutant parasites as compared to their K13 WT counterparts, especially 12h post drug treatment (**Fig 4D**). The increased co-localization observed between parasite mitochondria and K13 following DHA treatment was not detected when MitoTracker-labeled parasites were co-stained with Rab5A, Rabb11A, TRiC or ERD2 (**S6B–S6E Fig**).

IEM studies of NF54^{WT}attB-3HA-K13^{C580Y} parasites stained with colloidal gold-labeled anti-HA antibodies revealed some K13 labeling within parasite mitochondria (**Fig 4F**). Because mitochondria associate with the ER at specialized membrane contact sites [55], we also investigated whether K13 might be present near these signaling hubs (**Fig 4G** and **S6F Fig**). For these studies, untreated Cam3.II^{R539T} or Cam3.II^{WT} trophozoites were incubated with MitoTracker prior to formaldehyde fixation and co-staining with anti-BiP and anti-K13 antibodies. Interestingly, we frequently observed an overlap of all three labels in both mutant and WT K13 parasites, as indicated in the white dotted outlines (**Fig 4G** and **S6F Fig**).

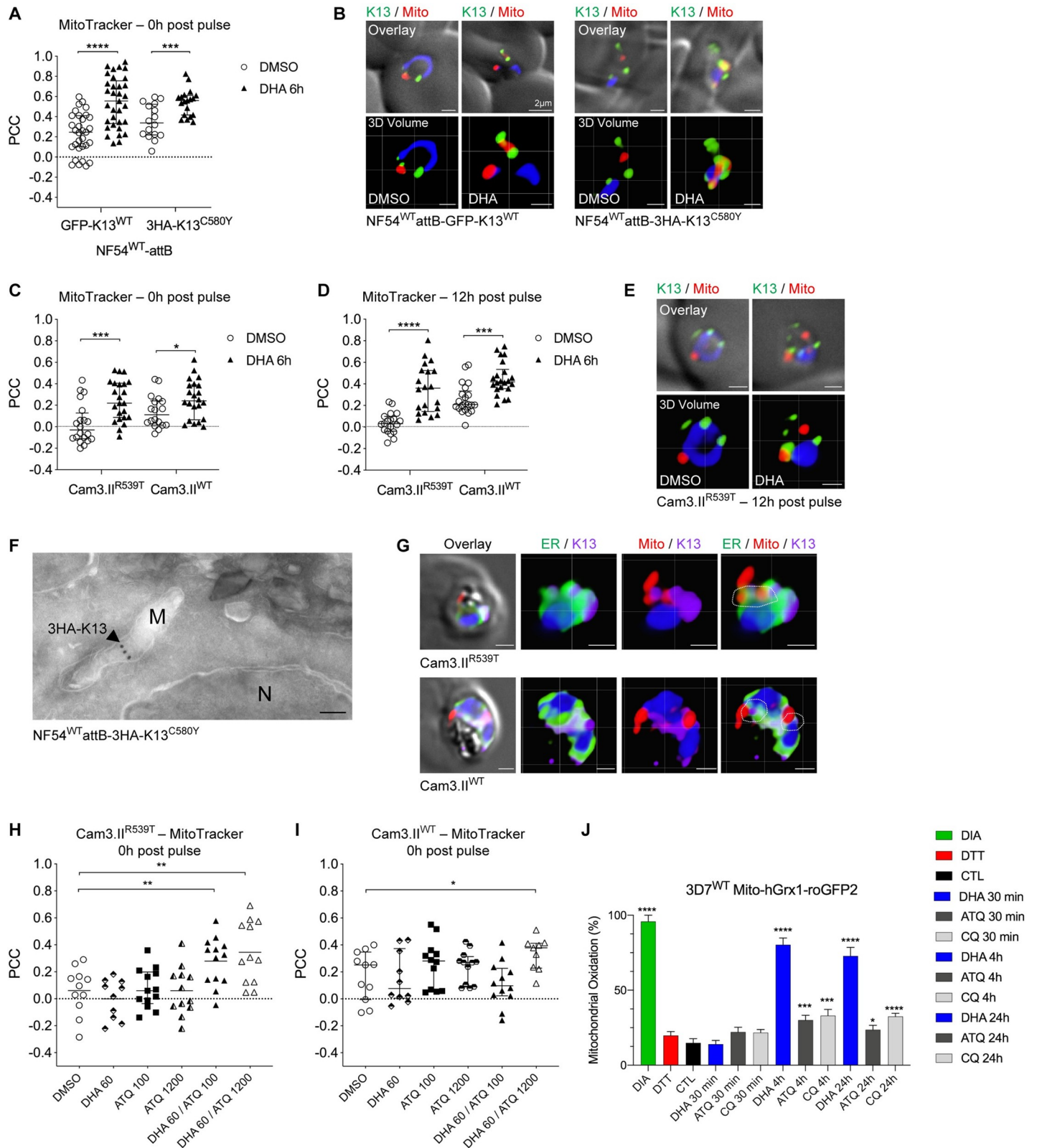


Fig 4. K13 shows an increased association with the mitochondria post DHA pulse. (A) PCC values for the association of K13 with parasite mitochondria in NF54^{WT}-attB-GFP-K13^{WT} or NF54^{WT}-attB-3HA-K13^{C580Y} ring-stage parasites co-stained with MitoTracker Deep Red and anti-GFP antibodies. Samples were collected directly post DHA pulse (6h, 700 nM). DMSO was used as a vehicle control. (B) Representative fluorescence microscopy images and 3D reconstructions of NF54^{WT}-

attB-GFP-K13^{WT} (left) or NF54^{WT}attB-3HA-K13^{C580Y} (right) ring-stage parasites treated and stained as in (A). Scale bars: 1 μ m unless otherwise indicated. (C, D) PCC values for the association of K13 with the mitochondria in Cam3.II^{R539T} or Cam3.II^{WT} ring-stage parasites co-stained with MitoTracker and the K13 mAb E3. Samples were collected either (C) immediately post DHA pulse (6h, 700 nM) or DMSO mock treatment or (D) 12h post pulse. (E) Representative fluorescence microscopy images and 3D reconstructions of Cam3.II^{R539T} ring-stage parasites 12h post DHA pulse or DMSO mock treatment. Scale bars: 1 μ m. (F) Representative IEM images of NF54^{WT}attB-3HA-K13^{C580Y} trophozoites treated with DHA (9 nM for 3h) or a DMSO vehicle control and stained with anti-HA antibodies to detect K13. Arrowhead highlights location of interest. M, mitochondria; N, nucleus. Scale bar: 100 nm. (G) 3D volume reconstruction of untreated late Cam3.II^{R539T} and Cam3.II^{WT} trophozoites triply stained with MitoTracker, anti-BIP (ER, green) and anti-K13 E3 (purple). White dotted outlines indicate spatial overlap between the three labels. Scale bars: 1 μ m. (H, I) PCC values for the association of K13 with mitochondria in (H) Cam3.II^{R539T} or (I) Cam3.II^{WT} ring-stage parasites treated for 4h with 60 nM DHA, or 100 nM or 1200 nM ATQ, or combinations thereof. Samples were co-stained with MitoTracker and the K13 mAb E3. (J) Percent mitochondrial oxidation (OxD; see [Methods](#)) measured in the 3D7^{WT} Mito-hGrx1-roGFP2 reporter line. Parasites were treated with DHA, ATQ, CQ, a known oxidizing agent (DIA), a known reducing agent (DTT), or vehicle control (denoted CTL). Parasites were exposed for 30 min to 100 μ M drug concentrations, for 4h to 5 μ M drug, or for 24h to 50 nM drug. Experiments were performed on three independent occasions, with 10 parasites per experiment examined using confocal laser scanning microscopy. Results are presented as means \pm SEM. Significance was calculated using two-tailed, unpaired *t* tests comparing drug-treated with mock-treated parasites. **p*<0.05; ***p*<0.01; ****p*<0.001; *****p*<0.0001. ATQ, atovaquone; CQ, chloroquine; DHA, dihydroartemisinin; DIA, diamide; DTT, 1,4-dithiothreitol.

<https://doi.org/10.1371/journal.ppat.1008482.g004>

We next examined whether atovaquone (ATQ), an inhibitor of the *Plasmodium* mitochondrial cytochrome bc1 complex, might affect K13 co-localization with the mitochondria. These studies assayed Cam3.II^{R539T} and Cam3.II^{WT} rings treated for 4h with 60 nM DHA and/or ATQ tested at 100 nM or 1,200 nM concentrations. 60 nM DHA produced no change in PCC values for K13 and MitoTracker compared to DMSO ([Fig 4H and 4I](#)). 100 nM or 1,200 nM ATQ also generated no change in PCC values between Cam3.II^{R539T} and Cam3.II^{WT} parasites. In contrast, PCC values increased significantly in Cam3.II^{R539T} parasites exposed to a combination of 60 nM DHA and 100 or 1,200 nM ATQ ([Fig 4H and 4I](#)). This result was observed to a lesser extent in Cam3.II^{WT} parasites but only at the higher ATQ concentration. Elevated ring-stage survival was observed for Cam3.II^{R539T} but not Cam3.II^{WT} parasites following a 6h exposure to 60 nM DHA \pm 100 nM ATQ ([S6G Fig](#)).

DHA leads to an oxidizing effect in the mitochondria

To further investigate a possible role for parasite mitochondria in the response to DHA, potentially as sensors of DHA-induced oxidative stress, we tested whether DHA treatment results in mitochondrial oxidation. For these experiments, we used the ratiometric redox-sensor hGrx1-roGFP2, consisting of human glutaredoxin 1 fused to an oxidation-reduction sensitive GFP and an N-terminal leader sequence that targets this reporter protein to parasite mitochondria. Assays used *P. falciparum* 3D7 parasites episomally transfected with pARL1a-Mito-hGrx1-roGFP2 (referred to herein as 3D7^{WT} Mito-hGrx1-roGFP2) [56] for confocal live-cell imaging. For these studies, we tested DHA, ATQ, and the β -hematin binding drug chloroquine (CQ). Results were compared to mock-treated control parasites. DIA and DTT were included as separate treatments to achieve complete oxidation and reduction, respectively. Results showed that young trophozoites exposed to DHA for 4h underwent a very high degree of mitochondrial oxidation, more than twice the levels observed with ATQ or CQ with similar exposure times and drug concentrations. Increased mitochondrial oxidation with DHA was also observed after 24h. Mitochondrial oxidation was not observed after 30 minutes of parasite exposure to DHA, ATQ or CQ ([Fig 4J](#)).

Discussion

With the rise of ART-resistant *P. falciparum* parasites in Southeast Asia [11,12], the identification of K13 as the molecular marker of ART resistance represented a key breakthrough in tracking their spread and examining the underlying biological basis of resistance [18]. Here, we have explored the biological role of K13 in DHA- and vehicle-treated asexual blood stage parasites with the use of K13-specific mAbs and recombinant lines expressing epitope-tagged

WT or mutant K13. These tools were used in immunofluorescence and IEM-based co-localization studies, and in co-IP experiments to identify putative K13-associated proteins. Our findings suggest an association between K13 and the ER, as well as a role for K13 in vesicular trafficking processes, including cytosomes that transport endocytosed host hemoglobin. We also provide evidence of an association between K13 and mitochondrial proteins and their resident organelle post DHA treatment.

Our IFA results localized K13 to punctate foci that increase in number throughout the parasite IDC. K13 appears to segregate with daughter merozoites, suggesting that the protein is ready to function within very young ring-stage parasites. This observation is consistent with K13-mediated ART resistance occurring in early rings, despite the peak of K13 protein expression occurring in mid trophozoites [17,31,57,58]. Using IEM, we partially co-localized K13 to vesicles in close proximity to the perinuclear ER, the DV and the plasma membrane. We also obtained evidence of K13 localizing near cytosomes, sites where the plasma membrane invaginates to deliver endocytosed hemoglobin to the parasite DV. These results extend prior observations of K13 associating with the ER or vesicular structures as well as sites of cytosomal formation, as defined using GFP-tagged endogenous K13 or polyclonal K13-specific antibodies [25,27,28,35]. Evidence of K13 localizing to cytosomes was also obtained recently using correlative light and electron microscopy [27], a highly-specialized technique that was unavailable for our study. K13 localization patterns were consistent between isogenic WT and mutant Cam3.II lines, as assessed using both K13-specific mAbs and our 3HA- or GFP-tagged NF54^{WT}attB lines, indicating that K13 mutations did not affect subcellular localization.

Of note, the NF54^{WT}attB-3HA-K13^{C580Y} line, which expresses an integrated mutant K13 allele expressed *in trans*, did not show elevated RSA_{0-3h} survival, suggesting that the endogenous WT isoform is dominant and that K13 polymorphisms might be loss-of-function mutations. RSA data also showed that gene-edited NF54^{C580Y}attB-GFP-K13^{C580Y} parasites harboring an integrated second K13 C580Y allele (that results in resistance) reverted to a nearly sensitive phenotype (Fig 1F). These findings are consistent with data recently published using episomally transformed K13 mutant parasites [27].

We also observed less labeling of K13 R539T relative to the WT form both by Western blot and by microscopic quantification of K13-positive foci (S1E and S2C Figs), consistent with quantitative proteomic analyses showing a ~2-fold decrease in K13 protein abundance in Cam3.II^{R539T} rings as compared to isogenic WT rings [59]. These data suggest that the R539T mutation in this Cam3.II background might reduce K13 protein levels and that this might constitute one causal aspect of mutant K13-mediated ART resistance. Increased overall expression of mutant K13 via co-expression of the endogenous protein and second mutant copy *in trans* thus presumably ablates resistance by compensating for a loss of function in the endogenous locus (Fig 1F). In broad agreement with these results, a recent study using K13 conditional knock-sideways parasites showed that mislocalization of K13 can lead to resistance [28]. Further studies will be required to assess whether K13 mutations can differ in their impact on protein stability and activity, how this varies between strains, and to what extent these effects correlate with ART resistance.

Our co-IP experiments resulted in an array of putative K13-associated proteins (Table 2 and S2 Table), suggesting that K13 may interact with multiple proteins across several core pathways including vesicular trafficking, redox regulation and unexpectedly, mitochondrial metabolism and physiology, as discussed below. Our results suggested that few if any interactions were specific to either the WT or mutant K13 isoforms. Many of our candidate K13-associated proteins were also observed in a recent study that used GFP-Trap beads to affinity purify GFP-K13 followed by LC/MS-MS [53]. These proteins included S-adenosylmethionine synthetase (the most abundant protein in our dataset), elongation factor 2, and plasmepsin II.

Our list, however, is distinct from the proteins identified in the recent study by Birnbaum *et al.* [27] that used a quantitative dimerization-induced bio-ID approach (DiQ-BioID) in which GFP-tagged K13 forms a complex with RFP-tagged biotin ligase using dimerization domains regulated by the addition of rapalog. That system enabled biotinylation of K13-proximal proteins, which were then affinity-purified on a streptavidin Sepharose column prior to mass spectrometry and protein identification. One of the proteins identified using this approach, Eps15, was also shown to identify K13 in a reciprocal DiQ-BioID experiment. These proteins were localized to a clathrin-independent AP-2 adaptor complex-labeled compartment involved in hemoglobin endocytosis. Of note, K13 colocalized with AP-2 μ , although this protein was not identified by affinity purification of K13 in either the Birnbaum study or our own. A separate study also did not identify K13 upon affinity purification of HA-tagged AP-2 μ protein [60]. We cannot yet explain the discrepancy between the data we obtained by co-IP with our K13 mAb and that generated using the DiQ-BioID method, although we note that DiQ-BioID will preferentially identify proteins in the same compartment as K13 rather than proteins physically bound to K13. Our list may have preferentially identified the latter. We also note differences in the protein detergent-based extraction protocols. Further work is clearly required to resolve these differences.

Our list of potential interacting partners for K13, based on co-IP and co-localization data, includes multiple Rab GTPases (Fig 5). These included Rabs associated in other eukaryotes with early (Rab5A, 5B, 5C), late (Rab7) or recycling endosomes (Rab 11A, 11B) or the trans-Golgi (Rab6). These and other observed Rabs (e.g. 1A, 1B and 18B) help regulate intracellular cargo trafficking via their association with effector proteins [61,62]. In the case of Rab11A, the consistently high PCC co-localization values with K13 in Cam3.1I^{R539T} parasites (Fig 5) suggest the possibility of increased export and recycling functions in mutant parasites, which may help eliminate damaged and aggregated proteins during the post-drug recovery phase.

DHA treatment differentially impacted certain correlation values obtained for K13 WT and mutant parasites, as evidenced with Rab5A, B and C. For these, we observed significantly higher PCC values for K13 WT parasites post DHA treatment as compared with K13 R539T mutant parasites. Rab5 proteins have been implicated in hemoglobin import processes, suggesting that the differential associations might impact hemoglobin uptake [63–66]. These findings recall the recent report of reduced heme and heme-DHA adducts in K13 mutant parasites [29,30]. Birnbaum *et al.* also recently showed reduced endocytosis of host cytoplasm, which consists mainly of hemoglobin, in ring-stage parasites expressing mutant K13 (compared to an isogenic WT control) or WT K13 parasites in which this protein was conditionally knocked sideways to cause loss of function [27]. The same study also identified several proteins (including K13, Eps15, UBP1 and AP-2 μ) required for hemoglobin endocytosis, of which only K13 was required for rings. This conditional knock sideways system was also recently used by Yang *et al.* to show reduced hemoglobin processing in ring-stage parasites with mislocalized K13 [28]. Stalling of hemoglobin import could have two positive outcomes: less availability of Fe²⁺-heme to activate ART [27,28], and fewer hemoglobin-derived peptides that could trigger a starvation response and entry into a temporary dormant state [67]. Both effects could enable K13 mutant ring stages to survive ART exposure [27,28,68–71].

In mammalian cells, several Rab effector proteins can regulate phosphoinositide metabolism. One of these effectors, a partner of Rab5 and Rab7, is the heterodimeric phosphatidylinositol-3-kinase (PI3K) Vps34/Vps15 complex, which catalyzes the phosphorylation of phosphatidylinositol to phosphatidylinositol-3-phosphate (PI3P) [72–75]. A prior report associated ART resistance with elevated PI3P levels, mediated by an interaction between K13 and PI3K. The rise in PI3P levels in mutant parasites was attributed to reduced binding of K13 to PI3K, resulting in attenuated ubiquitin-mediated degradation of the kinase [34]. PI3K itself

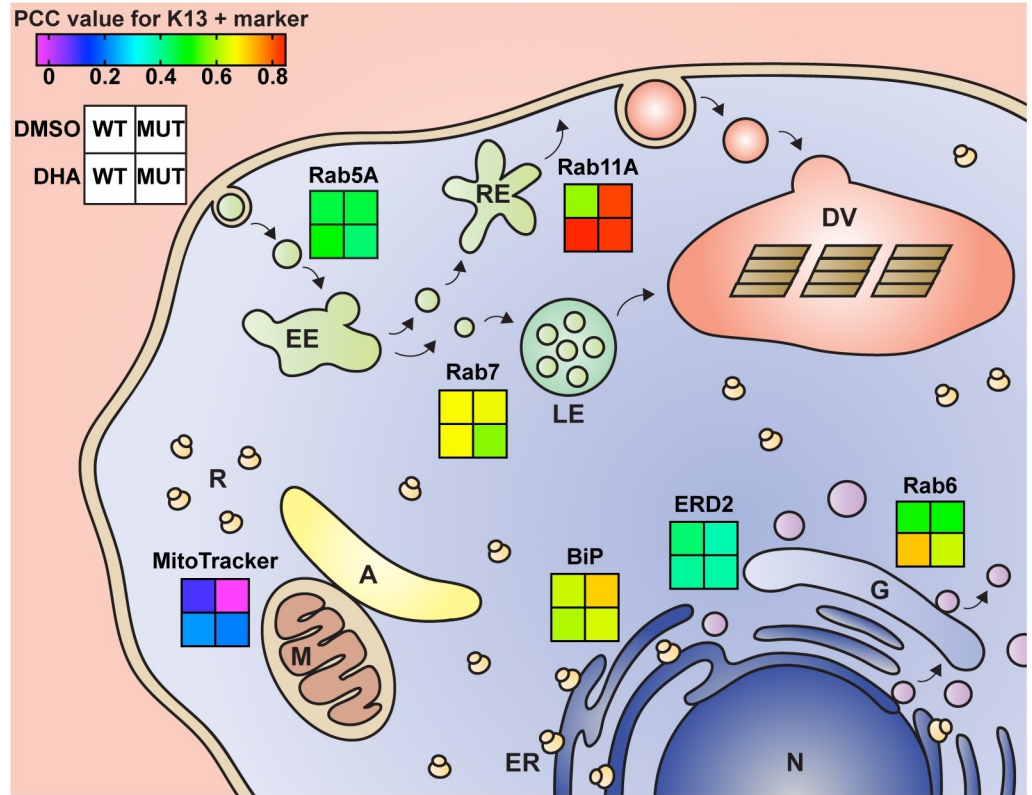


Fig 5. Summary of PCC values for K13 and selected markers upon DHA or DMSO treatment. Schematic showing the subcellular localization of markers used for IFA co-localization studies with K13. The gradient squares illustrate the median PCC values for the spatial association between a given marker and WT or mutant K13. PCC values are shown for DHA- or DMSO-treated parasites and were calculated immediately (0h) post treatment. The Cam3.II^{R539T} and Cam3.II^{WT} lines were employed for all assays, with the exception of those testing the association between K13 and Rab6 that employed the Dd2^{R539T} Rab6-GFP and Dd2^{WT} Rab6-GFP lines. PCC values are also presented in **Figs 2–4**, **S5 Table** and **S6 Table**. A, apicoplast; DHA, dihydroartemisinin; DMSO, dimethyl sulfoxide; DV, digestive vacuole; EE, early endosome; ER, endoplasmic reticulum; G, Golgi apparatus; LE, late endosome; M, mitochondria; MUT, mutant; N, nucleus; PCC, Pearson correlation coefficient; R, ribosome; RE, recycling endosome; WT, wild-type.

<https://doi.org/10.1371/journal.ppat.1008482.g005>

was not observed in our co-IP experiments. Nonetheless, there may be a link between PI3P levels and the association we observed between K13 and Rab5 and Rab7, as Rab GTPase activation contributes to the stimulation of PI3K enzymatic activity, leading to localized synthesis of PI3P and regulation of endocytic trafficking [72–75].

The co-localization we observe between the ER chaperone BiP and K13, notably the R539T variant, supports a link between K13 and protein homeostasis and damage response pathways (Fig 3E). IEM studies also frequently detected K13 close to the perinuclear parasite ER. These results suggest that mutant K13 might act in part by enhancing ER-associated stress responses to damaged proteins [31,53]. Although BiP co-immunoprecipitated with K13 in all samples across all experiments, it was excluded from our list of putative K13-interacting partners (Table 2 and S2 Table) due to its abundant presence in the negative control samples. Nonetheless, we observed several other ER proteins including PDI-14, Sec61, SEY1 and p97 in our co-IP data, corroborating the IFA and IEM data that partially localized K13 to the ER. We note that interactions with ER-luminal proteins may arise after detergent-mediated cell lysis, given that K13 lacks a known signal sequence to access the ER lumen.

The ER is not the sole organelle responsible for sensing and combatting cellular stress. Mitochondria likewise regulate an array of cellular functions including ATP production, intracellular calcium buffering, redox homeostasis, and apoptosis [76,77]. There is increasing evidence that the unfolded protein response, generally viewed as a signaling pathway to overcome proteotoxic ER stress, also regulates mitochondrial proteostasis and function [78]. Communication between these two organelles is achieved via specialized mitochondria-associated membrane contact sites (MAMs), where Ca^{2+} transfer, lipid synthesis and autophagosome assembly take place. In times of stress, Ca^{2+} flow into the mitochondria can augment mitochondrial respiratory chain activity, increasing energy resources to mount an adaptive stress response [78]. Our co-IP data revealed multiple putative K13-interacting mitochondrial proteins whose functions span oxidative stress responses, the electron transport chain, and mitochondrial protein synthesis (Table 2 and S2 Table). Without DHA, an association between K13 and the mitochondria was essentially nonexistent, but PCC values for K13 and MitoTracker increased significantly post DHA treatment, especially for the K13 R539T mutant. This putative association was not tested in the Birnbaum *et al.* study, which did not examine whether treatment with an ART derivative would alter their set of K13-interacting candidates [27]. We caution that our co-IP data associating K13 with mitochondrial proteins might be adversely affected by detergent-based extraction conditions that could lead to false associations with this organelle. Nonetheless, we observed partial colocalization of K13 with MitoTracker-stained mitochondria upon DHA treatment, and note a recent study with *Toxoplasma gondii* parasites that provided evidence of ART targeting the mitochondria, where it affected membrane potential and organelle morphology [79].

The association between K13 and the mitochondria that we observed recalls earlier evidence of ART accumulating in this organelle, as well as in the DV, causing mitochondrial swelling as early as 2h post drug exposure [80]. The mode of action of ART and other endoperoxides has also been linked to the rapid depolarization of the mitochondrial membrane potential, with surviving cells maintaining mitochondrial polarization and activity despite widespread cellular damage [81,82]. Mitochondrial membrane depolarization was attributed to the formation of reactive oxygen species, most likely originating from iron-mediated bioactivation of the ART endoperoxide bridge. Using a genetically-encoded, mitochondria-targeted GFP-fusion redox probe, we found substantial oxidation following 4h or 24h of DHA treatment, which greatly exceeded any oxidative effect of the cytochrome bc1 inhibitor ATQ or the hemozoin inhibitor CQ. These results agree with earlier studies that also showed an impact of ART derivatives on redox potential in the parasite cytosol [56,83,84]. Further studies are merited to elucidate the role of the mitochondria in both DHA action and K13-mediated resistance. One possibility is that this organelle might act as an initial sensor of ART action, with mutant K13 altering mitochondrial functionalities in ways that have downstream impacts across an array of pathways, including reversible entry into quiescence during ART exposure or subsequent recovery of resistant parasites. Further studies into the connection between K13 function and the mitochondria could substantially advance our understanding of parasite physiology and its capacity to counter ART-mediated proteotoxic and oxidative stress.

Materials and methods

Production of monoclonal antibodies to K13

Antibodies were raised against K13 by injecting mice intraperitoneally with two types of immunogens: recombinant BTB plus propeller domain (~40 kDa) or recombinant propeller domain alone (~32 kDa) (Fig 1A). Immunogens were kindly provided by Dr. Raymond Hui (University of Toronto). Mice were immunized five times at three-week intervals. Sera were

collected 9–10 days after the last immunization, and titers of anti-K13 IgG were measured by ELISA using His-tagged versions of the recombinant K13 proteins bound to Ni²⁺-coated ELISA plates. Mice with the highest antibody titers were selected for anti-K13 hybridoma populations, which were generated via polyethylene glycol (PEG)-induced fusion of the MEP-2S fusion partner cell line with murine splenic B cells. Hybridoma cell lines were maintained in RPMI-1640 medium supplemented with 10% FBS, L-glutamine, non-essential amino acids, sodium pyruvate and vitamins. Stable clones were selected in the presence of hypoxanthine-aminopterin-thymidine (HAT) medium. Hybridoma populations producing K13-specific antibodies, as determined by ELISA, were expanded and cloned to assure the monoclonal nature of antibodies. Clones selected via ELISA were further screened for their K13 specificity by IFAs with the NF54^{WT}attB-GFP-K13^{WT} line. Clones were also tested by Western blot against the immunogens. Purified clonal mAbs were generated from K13-positive hybridomas.

Plasmid construction

For GFP-K13 expression studies, the *K13* WT coding sequence (PlasmDB ID PF3D7_1343700) was amplified from genomic DNA using p3947 and p3948 (S7 Table) and cloned into a pDC2-based expression system downstream of GFP using the BglII and XhoI restriction sites [42]. The *K13* 5' untranslated region (UTR) was amplified as a 2000 bp fragment using p4376 and p4377 (S7 Table) and cloned into the ApaI and AvrII restriction sites. We then fused the full-length *K13* coding sequence to an N-terminal GFP tag and placed this sequence under the regulatory control of the endogenous promoter. This plasmid was named pDC-2000-GFP-K13^{WT}-bsd-attP. For 3HA-K13 expression studies, the *K13* C580Y coding sequence was used instead, and the *P. berghei* *ef1α* promoter (PBANKA_1133400) was used as a 5' regulatory element. The N-terminal GFP tag was replaced with an N-terminal 3HA tag at the AvrII and BglII sites. The 3HA sequence was synthetically engineered with the corresponding restriction sites in a pUC57-Amp vector (Genewiz). The resulting plasmid was named pDC2-EF1α-3HA-K13^{C580Y}-bsd-attP. In both plasmids *hsp86* 3'UTR was used as a terminator sequence for the *K13* expression cassette and a *bsd* (blasticidin S-deaminase) cassette was used as a selectable marker [85].

To episomally express the *GFP-Rab6* transgene we amplified the *Rab6* coding sequence (PlasmDB ID PF3D7_1144900) from genomic DNA using poML214 and poML204 (S7 Table) and cloned this fragment into the pDC2-based expression system downstream of GFP using the BglII and XhoI restriction sites [42]. Using p1144 and p1263 (S7 Table), about 1.3 kb of the *Sec12* (PlasmDB ID PF3D7_1116400) 5' UTR was amplified as the promoter and cloned into the ApaI and AvrII restriction sites. The *hsp86* 3'UTR served as a terminator sequence for the expression cassette and human *dhfr* (dihydrofolate reductase) was used as the selectable marker. The plasmid was named pDC2-sec12-GFP-PfRab6-hDHFR.

Parasite culture and transfection

P. falciparum asexual blood-stage parasites were cultured in human erythrocytes (3% hematocrit) and RPMI-1640 medium supplemented with 2 mM L-glutamine, 50 mg/L hypoxanthine, 25 mM HEPES, 0.225% NaHCO₃, 10 mg/L gentamycin and 0.5% w/v Albumax II (Invitrogen). Parasites were maintained at 37°C in 5% O₂, 5% CO₂, and 90% N₂. Cultures were stained with Giemsa, and monitored by blood smears fixed in methanol and viewed by light microscopy.

NF54^{WT}attB-GFP-K13^{WT} and NF54^{WT}attB-3HA-K13^{C580Y} parasite lines were generated by attB×attP crossover-mediated integration of either the pDC-2000-GFP-K13^{WT}-bsd-attP or the pDC2-EF1α-3HA-K13^{C580Y}-bsd-attP plasmid into the *cg6* locus in the NF54^{WT}attB parasite

line [86] (S1 Fig). Crossover events were mediated by Bxb1 serine integrase, which was expressed on the pINT plasmid that contains the neomycin selectable marker and that was co-electroporated with either pDC2 plasmid. The NF54^{C580Y}attB-GFP-K13^{C580Y} line was generated using a *K13*-specific CRISPR/Cas9 system that enabled us to edit both the endogenous and transgene copies of *K13* in the NF54^{WT}attB-GFP-K13^{WT} line (Stokes *et al.*, manuscript in preparation). This system was also used to generate the NF54^{WT}attB-3HA-K13^{WT} line by CRISPR/Cas9-editing the *K13* C580Y transgene locus in the NF54^{WT}attB-3HA-K13^{C580Y} line. Dd2^{WT} or Dd2^{R539T} GFP-Rab6 parasite lines were generated via transfection of the pDC2-sec12-GFP-PfRab6-hDHFR plasmid and episomal selection using 2.5 nM WR99210 (Jacobus Pharmaceuticals, Princeton, NJ).

Transfections were performed by electroporating ring-stage parasites at 5–10% parasitemia with 50 µg of purified circular plasmid DNA in resuspended in Cytomix [87]. Transfected parasites were maintained under 2.5 µg/mL blasticidin (Thermo Fisher) or 2.5 nM WR99210 drug pressure to select for maintenance of the pDC2-based *bsd* or *hdhfr* plasmids respectively, and 125 µg/mL G418 (Fisher) to select for pINT. Blasticidin or WR99210 pressure was maintained until parasites were detected microscopically, whereas G418 pressure was applied for only the first six days post electroporation. Parasite cultures were monitored by microscopy for up to six weeks post electroporation. To test for successful integration of the attP plasmids, trophozoite-infected erythrocytes were harvested and saponin-lysed, and genomic DNA was isolated using QIAamp DNA Blood Mini kit (Qiagen). PCR-based screening for integration is shown in S1 Fig, with primers listed in S7 Table. Integrated parasites were cloned via limiting dilution, and flow cytometry was used to screen for positive wells after 17–20 days. Parasites were stained with 1×SYBR Green (Thermo Fisher) and 100 nM MitoTracker Deep Red (Invitrogen) and detected using an Accuri C6 flow cytometer (Becton Dickinson; [88]). Expression of the tagged proteins in the clonal lines was verified via Western blot and IFA with anti-GFP or anti-HA primary antibodies, as described below.

Western blotting

Parasite lysates for Western blotting were prepared on ice. Infected erythrocytes were washed twice in cold 1× phosphate-buffered saline (PBS), and parasites were isolated from RBCs by treatment with 0.05% saponin in PBS. Released parasites were resuspended in cold lysis buffer (0.15 M NH₄Cl, 1 mM NaHCO₃, 0.1 mM Na₂EDTA, pH 7.4) supplemented with 1× protease inhibitors (Halt Protease Inhibitors Cocktail, Thermo Fisher) and incubated on ice for 30 min. RBC membranes were lysed with 0.1% Triton X100 in PBS supplemented with protease inhibitors for 10 min, with frequent vortexing and trituration. Samples were centrifuged at 14,000 rpm for 10 min at 4°C to pellet cellular debris. Supernatants were collected and protein concentrations were determined using the DC protein assay kit (Bio-Rad). Laemmli Sample Buffer (Bio-Rad) was added to lysates and samples were denatured at 90°C for 10 min. Proteins were electrophoresed on 10% Bis-Tris gels (Bio-Rad) and transferred onto a nitrocellulose membrane. Western blots were probed with primary antibodies to K13 or to GFP or 3×HA epitope tags (1:1,000 dilutions for all) and incubated with HRP-conjugated secondary antibodies (1:10,000 dilution). Western blots were revealed using ECL Western Blotting Substrate (Thermo Fisher). For primary antibodies, we used Living Colors full-length anti-GFP polyclonal antiserum (Takara (Clontech)), anti-HA antibodies produced in rabbit (Sigma), rabbit anti-ERD2 antibodies (BEI Resources) and mouse anti-β actin antibodies (clone AC-15, Invitrogen). As secondary antibodies, we used goat anti-rabbit IgG H&L (HRP) (Abcam) or goat anti-mouse IgG H&L (HRP) (Abcam).

Immunofluorescence assays

Parasites were synchronized with 5% D-sorbitol treatment and harvested either every 12h throughout the 48h life cycle, or were pulsed with DHA (6h, 700 nM) or Brefeldin A (1h, 5 μ g/mL) (Sigma Aldrich) and then harvested post treatment. DMSO was used as vehicle control in the case of DHA treatments and EtOH in the case of BFA (S3 Fig). DHA-treated parasites were harvested either immediately (0h) post treatment, or 3, 12, or 24h post treatment. BFA-treated parasites were harvested 1h post treatment.

IFAs were performed with cells in suspension. Harvested cells were washed twice in 1 \times PBS and fixed in 4% v/v formaldehyde (Fisher) supplemented with 0.0075% v/v glutaraldehyde (Sigma) in PBS for 30 min at room temperature. Cell membranes were permeabilized in 0.1% Triton X-100 in PBS for 30 min. Autofluorescence was quenched using 0.1 M glycine in PBS for 15 min. Blocking was performed with 3% w/v bovine serum albumin (BSA) for at least 1h at room temperature, or overnight at 4°C. Cells were incubated with primary antibodies for 90 min at room temperature or overnight at 4°C, with dilutions ranging from 1:50–1:200, followed by incubation with a species-specific fluorophore-conjugated secondary antibody (Alexa Fluor 488-, 594- or 647-conjugated goat anti-mouse, -rabbit or -rat antibody, Thermo Fisher) diluted 1:2,000 to 1:4,000 in 3% BSA and 0.1% Tween in PBS. As primary antibodies, we used rabbit anti-BiP (kindly provided by Min Zhang), rabbit anti-ERD2 (BEI Resources), rabbit anti-Rab5A, -Rab5C, or -Rab11A, rat anti-Rab5B or -Rab7 (kindly provided by Dr. Gordon Langsley), rabbit anti-TRiC (kindly provided by Zbynek Bozdech), rabbit anti-HAD1 (kindly provided by Dr. Audrey Odom John), rabbit anti-GFP ((Takara (Clontech)), or rabbit anti-HA (Sigma). MitoTracker Red CMXRos (Thermo Fisher) was used to stain mitochondria.

Thin blood smears of stained RBCs were prepared on microscope slides and mounted with cover slips using Prolong Diamond Antifade Mountant with DAPI (Thermo Fisher). Slides were imaged using a Nikon Eclipse Ti-E wide-field microscope equipped with a sCMOS camera (Andor) and a Plan-apochromate oil immersion objective with 100 \times magnification (1.4 numerical aperture). A minimum of 15 Z-stacks (0.2 μ m step size) were taken for each parasitized RBC. NIS-Elements imaging software (Version 5.02, Nikon) was used to control the microscope and camera as well as to deconvolve images and perform 3D reconstructions. Deconvolution was performed using 25 iterations of the Richardson-Lucy algorithm for each image. Quantitative co-localization analysis of the deconvolved Z-stacks was performed using the GA3 pipeline (General analysis Pipeline 3; NIS-Elements software; developed in collaboration with Nikon). ImageJ (Fiji version 2.0.0-rc-68/1.52h) was used to crop images, adjust brightness and intensity, overlay channels and prepare montages. For super resolution imaging, we used either a Nikon N-SIM S Super Resolution Microscope or a W1-Yokogawa Spinning Disk Confocal with a CSU-W1 SoRa Unit. For 3D image analysis, we used Imaris x64 version 6.7 (Bitplane).

Immunoelectron microscopy

Trophozoites were magnetically sorted from uninfected RBCs and ring-stage parasites via MACS LD separation columns (Miltenyi Biotech). Parasites were collected by centrifugation and fixed for 1h at 4°C in 4% paraformaldehyde (Polysciences Inc.) in 100 mM PIPES with 0.5 mM MgCl₂ (pH 7.2). Samples were embedded in 10% gelatin and infiltrated overnight with 2.3 M sucrose and 20% polyvinyl pyrrolidone in PIPES/MgCl₂ at 4°C. Samples were trimmed, frozen in liquid nitrogen, and sectioned with a Leica Ultracut UCT7 cryo-ultramicrotome (Leica Microsystems Inc.). 50 nm sections were blocked with 5% fetal bovine serum and 5% normal goat serum for 30 min, and subsequently incubated with primary antibodies for 1h at

room temperature (anti-PDI (1D3) mouse diluted 1:50, anti-GFP rabbit 1:200, anti-GFP mouse 1:200, anti-HA rabbit 1:50–1:250, anti-BiP rabbit 1:100, anti-Rab5A rabbit 1:50, anti-Rab5B rat 1:50, or anti-Rab7 rabbit 1:50; Rab11A antibodies could not be used as they failed to give signals under our conditions). Species-specific colloidal-gold conjugated secondary antibodies (6 nm, 12 nm or 18 nm particles; Jackson ImmunoResearch) were added at a 1:30 dilution for 1h at room temperature. Sections were stained with 0.3% uranyl acetate and 2% methyl cellulose, and viewed on a JEOL 1200 EX transmission electron microscope (JEOL USA Inc.) equipped with an AMT 8-megapixel digital camera and AMT Image Capture Engine V602 software (Advanced Microscopy Techniques). All labeling experiments were conducted in parallel with controls omitting the primary antibodies. These controls were consistently negative at the concentration of colloidal gold-conjugated secondary antibodies used in these studies.

Co-immunoprecipitation (Co-IP) studies

Co-IP studies were performed using the Pierce Direct IP kit (Thermo Fisher). Briefly, parasites were extracted from infected erythrocytes as described above, resuspended in Pierce IP Lysis Buffer supplemented with 1× Halt Protease and Phosphatase Inhibitor Cocktail and 25U Pierce Universal Nuclease, and lysed on ice for 10 minutes with frequent vortexing. Samples were centrifuged at 14,000 rpm for 10 min at 4°C to pellet cellular debris. Supernatants were collected and protein concentrations were determined using the DC protein assay kit (Bio-Rad). IPs were performed using 500 µg of lysate per test sample. A mix of K13 E3 and D9 mAbs (2.5 µg each per test sample) was used for IP. Antibody coupling to IP columns, IP, and elution steps were performed according to Pierce instructions. Eluates were analyzed by liquid chromatography-tandem mass spectrometry (LC-MS/MS) to identify immunoprecipitated proteins.

Ring-stage survival assays (RSA_{0-3h})

RSA_{0-3h} assays were carried out as previously described [17], with minor modifications. In brief, parasite cultures were synchronized 1–2 times using 5% sorbitol (Fisher). Synchronous schizonts were incubated in RPMI-1640 containing 15 units/mL sodium heparin (Fisher) for 15 min at 37°C to disrupt agglutinated erythrocytes, concentrated over a gradient of 75% Percoll (Fisher), washed once in RPMI-1640, and incubated for 3h with fresh RBCs to allow time for merozoite invasion. Cultures were subjected again to sorbitol treatment to eliminate remaining schizonts. 0–3h post-invasion rings were adjusted to 1% parasitemia and 2% hematocrit and exposed to 700 nM DHA or 0.1% DMSO (vehicle control) for 6h. Alternatively, early rings were exposed to 4h to 60 nM, 100 nM or 1200 nM ATQ, or combinations thereof. These concentrations were selected based on separate studies from our lab showing synergy between DHA and ATQ against Cam3.II^{R539T} parasites at these concentrations. Cells were washed to remove drug and returned to standard culture conditions for an additional 66h. Parasite growth in each well was assessed using flow cytometry. Parasites were stained with 1x SYBR Green and 100 nM MitoTracker Deep Red (Thermo Fisher), and parasitemias were measured on a BD Accuri C6 Plus Flow Cytometer with a HyperCyt attachment sampling 60,000–100,000 events per well. After 72h, cultures generally expanded to 3–5% parasitemia in DMSO-treated controls. Percent survival of DHA-treated parasites was calculated relative to the corresponding DMSO-treated control.

Confocal live-cell imaging

P. falciparum 3D7 parasites were episomally transfected with pARL1a-Mito-hGrx1-roGFP2, which expresses an oxidation-reduction sensitive GFP fused at its N-terminus to human glutaredoxin 1 (Table 1). This fusion protein is targeted to the mitochondria using the citrate synthase leader sequence, as described previously [56]. Transfected parasites were used to test the oxidizing effects of antimalarials on the parasite mitochondria. For 30 min exposure experiments we incubated trophozoites with 100 μ M DHA, ATQ, or CQ. For mid-term 4h incubations we exposed young trophozoites to 5 μ M DHA, ATQ, or CQ. Long-time 24h exposures began with young ring-stage parasites, which were exposed to 50 nM DHA, ATQ, or CQ.

Following drug exposure, parasites were blocked with 2 mM N-ethylmaleimide (NEM) for 15 min. Trophozoite-stage parasites were magnetically enriched and eluted in pre-warmed Ringer's solution and seeded on poly-lysine coated μ -slides VI (Ibidi, Martinsried, Germany). Live-cell imaging was performed on a Leica confocal system TCS SP5 inverted microscope equipped with an HCX PL APO 63.0 x 1.30 GLYC 37°C UV objective and a 37°C temperature chamber, as previously described [83]. Smart gain was set to 222.0 V, smart offset was 12.3% and argon laser power was set to 20%. To calibrate the microscope, we used parasites whose redox state was either fully reduced with 10 mM DTT or fully oxidized with 1 mM DIA. Data were analyzed using Leica LAS AF software. The degree of mitochondrial oxidation (OxD) was calculated as follows:

$$\text{OxD} = \frac{R - R_{\text{red}}}{\frac{I_{488\text{ox}}}{I_{488\text{red}}} (R_{\text{ox}} - R) + (R - R_{\text{red}})}$$

R represents the ratio of the fluorescence intensity measured at 405 nm and 488 nm ($R = \frac{405 \text{ nm}}{488 \text{ nm}}$); R_{red} and R_{ox} are the ratios of the fluorescence intensity of fully reduced or fully oxidized parasites, respectively; $I_{488\text{ox}}$ is the fluorescence intensity at 488 nm for fully oxidized parasites; and $I_{488\text{red}}$ is the fluorescence intensity at 488 nm for fully reduced parasites [89]. Graphs were plotted using GraphPad Prism version 8.

Ethics statement

Human RBCs used in this study were purchased from the Interstate Blood Bank (Memphis, TN) as whole blood from anonymized donors. Approval to use this material for *P. falciparum* *in vitro* culture was granted by the Columbia University Medical Center Institutional Review Board, which has classified this work as not being human subjects research. The use of mice in this study was described in protocol AC-AAM8301, which was reviewed and approved by the Columbia University Institutional Animal Care and Use Committee. Our animal use and care protocol adheres to the NIH Guidelines for Pain and Distress in Laboratory Animals.

Supporting information

S1 Fig. Generation of NF54^{WT}attB-GFP-K13^{WT} and NF54^{WT}attB-3HA-K13^{C580Y} parasites. (A) Schematic of GFP-K13^{WT} or 3HA-K13^{C580Y} gene sequence integration into NF54^{WT} parasites containing an attB site in the *cg6* locus [90]. The two plasmids used for co-transfection are represented at the top. pINT codes for the integrase expression unit (Int) and a neomycin resistance cassette (Neo). pDC-2000-GFP-K13^{WT}-bsd-attP contains an N-terminal GFP-K13^{WT} fusion protein under the control of the endogenous *K13* promoter (*k13* 5'UTR), and a blasticidin S-deaminase (BSD) resistance cassette adjacent to the attP coding site. pDC-EF1 α -3HA-K13^{C580Y}-bsd-attP contains an N-terminal 3HA-K13^{C580Y} fusion protein under the control of the *pbef1 α* promoter, and a BSD resistance cassette. Integrase-mediated

recombination between the attP and attB sequences resulted in integration of the full-length pDC2-based plasmids, yielding the NF54^{WT}attB-GFP-K13^{WT} and NF54^{WT}attB-3HA-K13^{C580Y} transgenic parasite lines. **(B)** Primer combinations and expected amplicon sizes used for PCR-based integration screening. Primer positions are indicated with arrows in **(A)** and primer sequences are listed in **S7 Table**. **(C)** PCR analysis of the two transgenic lines using the primer sets listed in **(B)**. **(D)** Western blots of parasite extracts probed with the anti-K13 mAb E9. This antibody recognizes full-length K13 (~85 kDa) and lower molecular weight bands. We attribute the latter to N-terminal degradation products, based on our observation of very high co-localization values between K13 mAbs and antibodies to either GFP or 3HA in K13 transgenic lines, as well as the finding that antibodies to GFP or 3HA both recognized fusion proteins consistent with a K13 mass of ~85 kDa (as seen in **Fig 1A**). **(E)** Representative Western blot analysis of synchronized 0–6h ring-stage parasites from the K13- isogenic lines Cam3.II^{WT}, Cam3.II^{C580Y} and Cam3.II^{R539T}, probed with K13 mAb E9 and mouse monoclonal anti-β actin. The right panel shows ImageJ-generated quantification of K13 C580Y or K13 R539T protein compared to K13 WT protein, with all proteins normalized to the β-actin loading control. These data yielded relative mean ± SEM expression levels of 76 ± 3% and 66 ± 4% for Cam3.II^{C580Y} and Cam3.II^{R539T} relative to the WT control, corresponding to mean K13 protein percent reductions of 24% and 34% for these two mutant proteins respectively. (PDF)

S2 Fig. Additional super resolution imaging of **(A)** Cam3.II^{WT} and **(B)** Cam3.II^{R539T} trophozoites, labeled with antibodies to K13 and the cytosolic marker HAD1. Images were acquired using a W1-Yokogawa Spinning Disk Confocal microscope equipped with a CSU-W1 SoRa Unit. **(C)** Quantification of antibody-labeled K13 foci in Cam3.II^{WT} and Cam3.II^{R539T} trophozoites, yielding an estimated 48% reduction in K13 R539T protein compared to the K13 WT levels. (PDF)

S3 Fig. Schematic of the protocol used for synchronizing and treating parasites for immunofluorescence co-localization studies. DHA, dihydroartemisinin; DMSO, dimethyl sulfoxide; MACS, magnetic-activated cell sorting. (PDF)

S4 Fig. K13 partially co-localizes with Rab GTPases and Sec24a. **(A)** Representative IFA images showing DMSO-treated Cam3.II^{WT} ring-stage parasites co-stained with anti-K13 mAb E3 and antibodies to Rab5A, Rab5B, or Rab5C (top, middle and bottom panels, respectively). Samples were collected immediately post treatment. Scale bars: 2 μm. **(B)** Fluorescence microscopy/DIC overlay and 3D volume reconstruction showing the spatial association between K13 and Rab5A in Cam3.II^{WT} parasites sampled 12h post DMSO mock treatment. Scale bars are indicated. **(C)** Representative IFA images showing GFP-Rab6-expressing parasites co-stained with K13 mAb E3. Assays were conducted with Dd2^{WT} (top) and Dd2^{R539T} (bottom) ring-stage parasites episomally expressing GFP-Rab6, and samples were collected immediately post DMSO treatment. Scale bars: 2 μm. **(D)** Representative IFA images showing DMSO-treated Cam3.II^{WT} ring-stage parasites co-stained with anti-K13 mAb E3 and antibodies to Rab7 (top) or Rab11A (bottom). Samples were collected immediately post treatment. Scale bars: 2 μm. **(E)** Fluorescence microscopy/DIC overlay and 3D volume reconstruction showing the spatial association between K13 and Rab11A in Cam3.II^{WT} parasites sampled 12h post DMSO treatment. **(F)** Representative IEM images of NF54^{WT}attB-GFP-K13^{WT} (left) or NF54^{WT}attB-3HA-K13^{C580Y} (right) trophozoites stained with anti-GFP or anti-HA antibodies, and either co-stained with antibodies to Rab5A (top), or Rab5B (bottom left), or triply labeled with anti-

Rab5B and anti-PDI antibodies (bottom right). Arrows highlight locations of interest. ER, endoplasmic reticulum; Hz, Hemozoin; M, mitochondria; N, nucleus. Scale bars: 100 nm. (G) PCC values for the spatial association between K13 and Sec24a immediately post DHA pulse (6h, 700 nM) or DMSO mock treatment. Assays were conducted on Dd2^{WT} ring-stage parasites episomally expressing Sec24a-GFP. Parasites were stained with anti-GFP and the K13 mAb E3. Right panels show representative 3D volume reconstructions of DMSO-treated or DHA-pulsed Sec24a-GFP expressing parasites. PCC values were calculated and statistics performed as in Fig 2. Scale bars: 1 μ m. (H) Representative IFA images showing Dd2^{WT} Sec24a-GFP-expressing parasites co-stained with K13 mAb E3 and anti-GFP. Samples were collected immediately post DMSO mock treatment. Scale bars: 2 μ m. Several DIC images as well as montages showing the individual color channels complement the 3D volume view of parasites shown in Fig 2.

(PDF)

S5 Fig. K13 exhibits extensive co-localization with the parasite ER. (A) Fluorescence microscopy/DIC overlay and 3D volume reconstructions of deconvolved Z-stacks showing the spatial association between K13 and BiP in Cam3.II^{WT} (top) and Cam3.II^{R539T} (bottom) trophozoites (untreated). Parasites were co-stained with the K13 E3 mAb and anti-BiP antibodies. Scale bars: 2 μ m. (B) Representative IEM images of NF54^{WT}attB-GFP-K13^{WT} trophozoites co-stained with anti-GFP and anti-BiP antibodies. Arrows highlight locations of interest. Hz, hemozoin; N, nucleus. Scale bars: 100 nm. (C) PCC values for the spatial association of K13 and BiP in Cam3.II^{R539T} and Cam3.II^{WT} ring-stage parasites treated and analyzed as in Fig 3B–3E. (D) Representative IFA images showing Cam3.II^{WT} ring-stage parasites co-stained with anti-K13 E3 and either anti-BiP (left) or anti-ERD2 (right) antibodies. Parasites were sampled immediately post DHA pulse (6h, 700 nM) or DMSO mock treatment. Scale bars: 2 μ m.

(PDF)

S6 Fig. K13 localizes to mitochondria-associated membranes. (A) PCC values for the association of K13 with parasite mitochondria in NF54^{WT}attB-GFP-K13^{WT} ring-stage parasites co-stained with MitoTracker Deep Red and anti-GFP. Samples were collected either 0h or 12h post DHA pulse (6h, 700 nM). DMSO was used as a vehicle control. PCC values were calculated and statistics performed as in Fig 2. (B–E) PCC values for the association of (B) ERD2, (C) TRiC, (D) Rab5A, or (E) Rab11A with parasite mitochondria in Cam3.II^{R539T} and Cam3.II^{WT} ring-stage parasites. Samples were collected 0h post DHA pulse (6h, 700nM). Parasites were co-stained with MitoTracker Deep Red and marker-specific antibodies. (F) Additional representative 3D volume reconstructions of untreated late (left) Cam3.II^{R539T} and (right) Cam3.II^{WT} trophozoites triply stained with MitoTracker, anti-BIP (ER, green) and anti-K13 E3 (purple). White dotted outlines indicate spatial overlap between the three labels. Scale bars: 1 μ m. (G) Percent survival for Cam3.II^{R539T} and Cam3.II^{WT} 0–3 hpi rings treated for 4h with DHA and/or ATQ at the concentrations indicated (in nM). Data show mean \pm SEM for three independent experiments performed in duplicate.

(PDF)

S1 Video. 3D rotations of a Cam3.II^{WT} late trophozoite labeled with anti-K13 (green) and anti-HAD1 (red) antibodies.

(MP4)

S1 Table. Co-immunoprecipitation experimental details.

(PDF)

S2 Table. Putative K13-interacting protein partners identified by co-immunoprecipitation and LC/MS-MS (relaxed criteria).

(PDF)

S3 Table. PANTHER overrepresentation test for biological processes.

(PDF)

S4 Table. PANTHER overrepresentation test for cellular components.

(PDF)

S5 Table. Pearson correlation coefficient values for IFA studies.

(PDF)

S6 Table. Pearson correlation coefficient values for MitoTracker Deep Red imaging studies.

(PDF)

S7 Table. Oligonucleotides used in this study.

(PDF)

Acknowledgments

Recombinant K13 protein was kindly provided by Dr. Raymond Hui at the University of Toronto. We thank Wendy Beatty at Washington University for technical assistance with electron microscopy. We also thank Gordon Langsley for sharing antibodies to Rab5A, 5B, and 5C, Rab7, and Rab11A. We would like to thank the Columbia University Zuckerman Institute's Cellular Imaging platform for instrument use and technical advice.

Author Contributions

Conceptualization: Nina F. Gnädig, Barbara H. Stokes, Judith Straimer, Audrey R. Odom John, Sachel Mok, David A. Fidock.

Data curation: Nina F. Gnädig, Barbara H. Stokes, Rachel L. Edwards, Gavreel F. Kalantarov, Sachel Mok.

Formal analysis: Nina F. Gnädig, Barbara H. Stokes, Michal Kuderjavy, Marcus C. S. Lee, David A. Fidock.

Funding acquisition: David A. Fidock.

Investigation: Kim C. Heimsch.

Methodology: Nina F. Gnädig, Barbara H. Stokes, Gavreel F. Kalantarov, Kim C. Heimsch, Michal Kuderjavy, Audrey Crane, Marcus C. S. Lee, Judith Straimer, Katja Becker, Ilya N. Trakht, Audrey R. Odom John, Sachel Mok, David A. Fidock.

Resources: Ilya N. Trakht, David A. Fidock.

Supervision: Katja Becker, David A. Fidock.

Validation: Nina F. Gnädig, Barbara H. Stokes, Gavreel F. Kalantarov, Ilya N. Trakht.

Visualization: Nina F. Gnädig, Barbara H. Stokes, Rachel L. Edwards, Sachel Mok.

Writing – original draft: Nina F. Gnädig, Barbara H. Stokes, David A. Fidock.

Writing – review & editing: Nina F. Gnädig, Barbara H. Stokes, Marcus C. S. Lee, Audrey R. Odom John, David A. Fidock.

References

1. World Health Organization. World malaria report. 2019; <https://www.who.int/publications-detail/world-malaria-report-2019>.
2. White NJ, Pukrittayakamee S, Hien TT, Faiz MA, Mokuolu OA, et al. Malaria. *Lancet*. 2014; 383: 723–35. [https://doi.org/10.1016/S0140-6736\(13\)60024-0](https://doi.org/10.1016/S0140-6736(13)60024-0) PMID: 23953767
3. Blasco B, Leroy D, Fidock DA. Antimalarial drug resistance: linking *Plasmodium falciparum* parasite biology to the clinic. *Nat Med*. 2017; 23: 917–28. <https://doi.org/10.1038/nm.4381> PMID: 28777791
4. Meshnick SR. Artemisinin: mechanisms of action, resistance and toxicity. *Int J Parasitol*. 2002; 32: 1655–60. [https://doi.org/10.1016/s0020-7519\(02\)00194-7](https://doi.org/10.1016/s0020-7519(02)00194-7) PMID: 12435450
5. Ismail HM, Barton V, Phanchana M, Charoensutthivarakul S, Wong MH, et al. Artemisinin activity-based probes identify multiple molecular targets within the asexual stage of the malaria parasites *Plasmodium falciparum* 3D7. *Proc Natl Acad Sci USA*. 2016; 113: 2080–5. <https://doi.org/10.1073/pnas.1600459113> PMID: 26858419
6. Wang J, Zhang CJ, Chia WN, Loh CC, Li Z, et al. Haem-activated promiscuous targeting of artemisinin in *Plasmodium falciparum*. *Nat Commun*. 2015; 6: 10111. <https://doi.org/10.1038/ncomms10111> PMID: 26694030
7. Gopalakrishnan AM, Kumar N. Antimalarial action of artesunate involves DNA damage mediated by reactive oxygen species. *Antimicrob Agents Chemother*. 2015; 59: 317–25. <https://doi.org/10.1128/AAC.03663-14> PMID: 25348537
8. Gupta DK, Patra AT, Zhu L, Gupta AP, Bozdech Z. DNA damage regulation and its role in drug-related phenotypes in the malaria parasites. *Sci Rep*. 2016; 6: 23603. <https://doi.org/10.1038/srep23603> PMID: 27033103
9. Klonis N, Xie SC, McCaw JM, Crespo-Ortiz MP, Zaloumis SG, et al. Altered temporal response of malaria parasites determines differential sensitivity to artemisinin. *Proc Natl Acad Sci USA*. 2013; 110: 5157–62. <https://doi.org/10.1073/pnas.1217452110> PMID: 23431146
10. Xie SC, Dogovski C, Hanssen E, Chiu F, Yang T, et al. Haemoglobin degradation underpins the sensitivity of early ring stage *Plasmodium falciparum* to artemisinins. *J Cell Sci*. 2016; 129: 406–16. <https://doi.org/10.1242/jcs.178830> PMID: 26675237
11. Dondorp AM, Nosten F, Yi P, Das D, Phyo AP, et al. Artemisinin resistance in *Plasmodium falciparum* malaria. *N Engl J Med*. 2009; 361: 455–67. <https://doi.org/10.1056/NEJMoa0808859> PMID: 19641202
12. Noedl H, Socheat D, Satimai W. Artemisinin-resistant malaria in Asia. *N Engl J Med*. 2009; 361: 540–1. <https://doi.org/10.1056/NEJMc0900231> PMID: 19641219
13. MalariaGEN *Plasmodium falciparum* Community Project. Genomic epidemiology of artemisinin resistant malaria. *Elife*. 2016; 5: e08714. <https://doi.org/10.7554/eLife.08714> PMID: 26943619
14. Menard D, Khim N, Beghain J, Adegnika AA, Shafiul-Alam M, et al. A worldwide map of *Plasmodium falciparum* K13-propeller polymorphisms. *N Engl J Med*. 2016; 374: 2453–64. <https://doi.org/10.1056/NEJMoa1513137> PMID: 27332904
15. van der Pluijm RW, Imwong M, Chau NH, Hoa NT, Thuy-Nhien NT, et al. Determinants of dihydroartemisinin-piperaquine treatment failure in *Plasmodium falciparum* malaria in Cambodia, Thailand, and Vietnam: a prospective clinical, pharmacological, and genetic study. *Lancet Infect Dis*. 2019; 19: 952–61. [https://doi.org/10.1016/S1473-3099\(19\)30391-3](https://doi.org/10.1016/S1473-3099(19)30391-3) PMID: 31345710
16. World Health Organization. WHO status report on artemisinin resistance and ACT efficacy. 2018; <https://www.who.int/malaria/publications/atoz/artemisinin-resistance-august2018/en>.
17. Witkowski B, Amaratunga C, Khim N, Sreng S, Chim P, et al. Novel phenotypic assays for the detection of artemisinin-resistant *Plasmodium falciparum* malaria in Cambodia: *in-vitro* and *ex-vivo* drug-response studies. *Lancet Infect Dis*. 2013; 13: 1043–9. [https://doi.org/10.1016/S1473-3099\(13\)70252-4](https://doi.org/10.1016/S1473-3099(13)70252-4) PMID: 24035558
18. Ariey F, Witkowski B, Amaratunga C, Beghain J, Langlois AC, et al. A molecular marker of artemisinin-resistant *Plasmodium falciparum* malaria. *Nature*. 2014; 505: 50–5. <https://doi.org/10.1038/nature12876> PMID: 24352242
19. Ashley EA, Dhorda M, Fairhurst RM, Amaratunga C, Lim P, et al. Spread of artemisinin resistance in *Plasmodium falciparum* malaria. *N Engl J Med*. 2014; 371: 411–23. <https://doi.org/10.1056/NEJMoa1314981> PMID: 25075834
20. Straimer J, Gnädig NF, Witkowski B, Amaratunga C, Duru V, et al. K13-propeller mutations confer artemisinin resistance in *Plasmodium falciparum* clinical isolates. *Science*. 2015; 347: 428–31. <https://doi.org/10.1126/science.1260867> PMID: 25502314

21. Ghorbal M, Gorman M, Macpherson CR, Martins RM, Scherf A, et al. Genome editing in the human malaria parasite *Plasmodium falciparum* using the CRISPR-Cas9 system. *Nat Biotechnol.* 2014; 32: 819–21. <https://doi.org/10.1038/nbt.2925> PMID: 24880488
22. Straimer J, Gnädig NF, Stokes BH, Ehrenberger M, Crane AA, et al. *Plasmodium falciparum* K13 mutations differentially impact ozonide susceptibility and parasite fitness *in vitro*. *mBio.* 2017; 8: e00172–17. <https://doi.org/10.1128/mBio.00172-17> PMID: 28400526
23. Adams J, Kelso R, Cooley L. The kelch repeat superfamily of proteins: propellers of cell function. *Trends Cell Biol.* 2000; 10: 17–24. [https://doi.org/10.1016/s0962-8924\(99\)01673-6](https://doi.org/10.1016/s0962-8924(99)01673-6) PMID: 10603472
24. Zhang DD, Lo SC, Cross JV, Templeton DJ, Hannink M. Keap1 is a redox-regulated substrate adaptor protein for a Cul3-dependent ubiquitin ligase complex. *Mol Cell Biol.* 2004; 24: 10941–53. <https://doi.org/10.1128/MCB.24.24.10941-10953.2004> PMID: 15572695
25. Birnbaum J, Flemming S, Reichard N, Soares AB, Mesen-Ramirez P, et al. A genetic system to study *Plasmodium falciparum* protein function. *Nat Methods.* 2017; 14: 450–6. <https://doi.org/10.1038/nmeth.4223> PMID: 28288121
26. Zhang M, Wang C, Otto TD, Oberstaller J, Liao X, et al. Uncovering the essential genes of the human malaria parasite *Plasmodium falciparum* by saturation mutagenesis. *Science.* 2018; 360: eaap7847. <https://doi.org/10.1126/science.aap7847> PMID: 29724925
27. Birnbaum J, Scharf S, Schmidt S, Jonscher E, Hoeijmakers WAM, et al. A Kelch13-defined endocytosis pathway mediates artemisinin resistance in malaria parasites. *Science.* 2020; 367: 51–9. <https://doi.org/10.1126/science.aax4735> PMID: 31896710
28. Yang T, Yeoh LM, Tutor MV, Dixon MW, McMillan PJ, et al. Decreased K13 abundance reduces hemoglobin catabolism and proteotoxic stress, underpinning artemisinin resistance. *Cell Rep.* 2019; 29: 2917–28 e5. <https://doi.org/10.1016/j.celrep.2019.10.095> PMID: 31775055
29. Heller LE, Goggins E, Roepe PD. Dihydroartemisinin-ferriprotoporphyrin IX adduct abundance in *Plasmodium falciparum* malarial parasites and relationship to emerging artemisinin resistance. *Biochemistry.* 2018; 57: 6935–45. <https://doi.org/10.1021/acs.biochem.8b00960> PMID: 30512926
30. Heller LE, Roepe PD. Quantification of free ferriprotoporphyrin IX heme and hemozoin for artemisinin sensitive vs delayed clearance phenotype *Plasmodium falciparum* malarial parasites. *Biochemistry.* 2018; 57: 6927–34. <https://doi.org/10.1021/acs.biochem.8b00959> PMID: 30513202
31. Mok S, Ashley EA, Ferreira PE, Zhu L, Lin Z, et al. Population transcriptomics of human malaria parasites reveals the mechanism of artemisinin resistance. *Science.* 2015; 347: 431–5. <https://doi.org/10.1126/science.1260403> PMID: 25502316
32. Dogovski C, Xie SC, Burgio G, Bridgford J, Mok S, et al. Targeting the cell stress response of *Plasmodium falciparum* to overcome artemisinin resistance. *PLoS Biol.* 2015; 13: e1002132. <https://doi.org/10.1371/journal.pbio.1002132> PMID: 25901609
33. Zhang M, Gallego-Delgado J, Fernandez-Arias C, Waters NC, Rodriguez A, et al. Inhibiting the *Plasmodium* eIF2alpha kinase PK4 prevents artemisinin-induced latency. *Cell Host Microbe.* 2017; 22: 766–76 e4. <https://doi.org/10.1016/j.chom.2017.11.005> PMID: 29241041
34. Mbengue A, Bhattacharjee S, Pandharkar T, Liu H, Estiu G, et al. A molecular mechanism of artemisinin resistance in *Plasmodium falciparum* malaria. *Nature.* 2015; 520: 683–7. <https://doi.org/10.1038/nature14412> PMID: 25874676
35. Bhattacharjee S, Coppens I, Mbengue A, Suresh N, Ghorbal M, et al. Remodeling of the malaria parasite and host human red cell by vesicle amplification that induces artemisinin resistance. *Blood.* 2018; 131: 1234–47. <https://doi.org/10.1182/blood-2017-11-814665> PMID: 29363540
36. Pretzel J, Gehr M, Eisenkolb M, Wang L, Fritz-Wolf K, et al. Characterization and redox regulation of *Plasmodium falciparum* methionine adenosyltransferase. *J Biochem.* 2016; 160: 355–67. <https://doi.org/10.1093/jb/mvw045> PMID: 27466371
37. Lo SC, Hannink M. PGAM5, a Bcl-XL-interacting protein, is a novel substrate for the redox-regulated Keap1-dependent ubiquitin ligase complex. *J Biol Chem.* 2006; 281: 37893–903. <https://doi.org/10.1074/jbc.M606539200> PMID: 17046835
38. Lo SC, Hannink M. PGAM5 tethers a ternary complex containing Keap1 and Nrf2 to mitochondria. *Exp Cell Res.* 2008; 314: 1789–803. <https://doi.org/10.1016/j.yexcr.2008.02.014> PMID: 18387606
39. Langsley G, van Noort V, Carret C, Meissner M, de Villiers EP, et al. Comparative genomics of the Rab protein family in Apicomplexan parasites. *Microbes Infect.* 2008; 10: 462–70. <https://doi.org/10.1016/j.micinf.2008.01.017> PMID: 18468471
40. Mi H, Muruganujan A, Ebert D, Huang X, Thomas PD. PANTHER version 14: more genomes, a new PANTHER GO-slim and improvements in enrichment analysis tools. *Nucleic Acids Res.* 2019; 47: D419–D26. <https://doi.org/10.1093/nar/gky1038> PMID: 30407594

41. Mi H, Muruganujan A, Huang X, Ebert D, Mills C, et al. Protocol update for large-scale genome and gene function analysis with the PANTHER classification system (v.14.0). *Nat Protoc.* 2019; 14: 703–21. <https://doi.org/10.1038/s41596-019-0128-8> PMID: 30804569
42. Lee MC, Moura PA, Miller EA, Fidock DA. *Plasmodium falciparum* Sec24 marks transitional ER that exports a model cargo via a diacidic motif. *Mol Microbiol.* 2008; 68: 1535–46. <https://doi.org/10.1111/j.1365-2958.2008.06250.x> PMID: 18410493
43. Marapana DS, Dagley LF, Sandow JJ, Nebl T, Triglia T, et al. Plasmepsin V cleaves malaria effector proteins in a distinct endoplasmic reticulum translocation interactome for export to the erythrocyte. *Nat Microbiol.* 2018; 3: 1010–22. <https://doi.org/10.1038/s41564-018-0219-2> PMID: 30127496
44. Coffey MJ, Jennison C, Tonkin CJ, Boddey JA. Role of the ER and Golgi in protein export by Apicomplexa. *Curr Opin Cell Biol.* 2016; 41: 18–24. <https://doi.org/10.1016/j.ceb.2016.03.007> PMID: 27019341
45. Bridgford JL, Xie SC, Cobbold SA, Pasaje CFA, Herrmann S, et al. Artemisinin kills malaria parasites by damaging proteins and inhibiting the proteasome. *Nat Commun.* 2018; 9: 3801. <https://doi.org/10.1038/s41467-018-06221-1> PMID: 30228310
46. Ponpuak M, Klemba M, Park M, Gluzman IY, Lamppa GK, et al. A role for falcilysin in transit peptide degradation in the *Plasmodium falciparum* apicoplast. *Mol Microbiol.* 2007; 63: 314–34. <https://doi.org/10.1111/j.1365-2958.2006.05443.x> PMID: 17074076
47. Matz JM, Goosmann C, Matuschewski K, Kooij TWA. An unusual prohibitin regulates malaria parasite mitochondrial membrane potential. *Cell Rep.* 2018; 23: 756–67. <https://doi.org/10.1016/j.celrep.2018.03.088> PMID: 29669282
48. Ginsburg H. Progress in *in silico* functional genomics: the Malaria Metabolic Pathways database. *Trends Parasitol.* 2006; 22: 238–40. <https://doi.org/10.1016/j.pt.2006.04.008> PMID: 16707276
49. Kehr S, Jortzik E, Delahunty C, Yates JR 3rd, Rahlfs S, et al. Protein S-glutathionylation in malaria parasites. *Antioxid Redox Signal.* 2011; 15: 2855–65. <https://doi.org/10.1089/ars.2011.4029> PMID: 21595565
50. Jones ML, Collins MO, Goulding D, Choudhary JS, Rayner JC. Analysis of protein palmitoylation reveals a pervasive role in *Plasmodium* development and pathogenesis. *Cell Host Microbe.* 2012; 12: 246–58. <https://doi.org/10.1016/j.chom.2012.06.005> PMID: 22901544
51. Wang L, Delahunty C, Prieto JH, Rahlfs S, Jortzik E, et al. Protein S-nitrosylation in *Plasmodium falciparum*. *Antioxid Redox Signal.* 2014; 20: 2923–35. <https://doi.org/10.1089/ars.2013.5553> PMID: 24256207
52. Grigoriev I, Splinter D, Keijzer N, Wulf PS, Demmers J, et al. Rab6 regulates transport and targeting of exocytotic carriers. *Dev Cell.* 2007; 13: 305–14. <https://doi.org/10.1016/j.devcel.2007.06.010> PMID: 17681140
53. Siddiqui FA, Boonhok R, Cabrera M, Mbenda HGN, Wang M, et al. Role of *Plasmodium falciparum* Kelch 13 protein mutations in *P. falciparum* populations from northeastern Myanmar in mediating artemisinin resistance. *mBio.* 2020; 11: e01134–19. <https://doi.org/10.1128/mBio.01134-19> PMID: 32098812
54. Crary JL, Haldar K. Brefeldin A inhibits protein secretion and parasite maturation in the ring stage of *Plasmodium falciparum*. *Mol Biochem Parasitol.* 1992; 53: 185–92. [https://doi.org/10.1016/0166-6851\(92\)90020-k](https://doi.org/10.1016/0166-6851(92)90020-k) PMID: 1501638
55. Stacchiotti A, Favero G, Lavazza A, Garcia-Gomez R, Monsalve M, et al. Perspective: mitochondria-ER contacts in metabolic cellular stress assessed by microscopy. *Cells.* 2018; 8: E5. <https://doi.org/10.3390/cells8010005> PMID: 30577576
56. Mohring F, Rahbari M, Zechmann B, Rahlfs S, Przyborski JM, et al. Determination of glutathione redox potential and pH value in subcellular compartments of malaria parasites. *Free Radic Biol Med.* 2017; 104: 104–17. <https://doi.org/10.1016/j.freeradbiomed.2017.01.001> PMID: 28062360
57. Saralamba S, Pan-Ngum W, Maude RJ, Lee SJ, Tarning J, et al. Intrahost modeling of artemisinin resistance in *Plasmodium falciparum*. *Proc Natl Acad Sci USA.* 2011; 108: 397–402. <https://doi.org/10.1073/pnas.1006113108> PMID: 21173254
58. Mok S, Imwong M, Mackinnon MJ, Sim J, Ramadoss R, et al. Artemisinin resistance in *Plasmodium falciparum* is associated with an altered temporal pattern of transcription. *BMC Genomics.* 2011; 12: 391. <https://doi.org/10.1186/1471-2164-12-391> PMID: 21810278
59. Siddiqui G, Srivastava A, Russell AS, Creek DJ. Multi-omics based identification of specific biochemical changes associated with PfKelch13-mutant artemisinin-resistant *Plasmodium falciparum*. *J Infect Dis.* 2017; 215: 1435–44. <https://doi.org/10.1093/infdis/jix156> PMID: 28368494
60. Henrici RC, Edwards RL, Zoltner M, van Schalkwyk DA, Hart MN, et al. The *Plasmodium falciparum* artemisinin susceptibility-associated AP-2 adaptin mu subunit is clathrin independent and essential for

- schizont maturation. *mBio*. 2020; 11: e02918–19. <https://doi.org/10.1128/mBio.02918-19> PMID: 32098816
61. Wandinger-Ness A, Zerial M. Rab proteins and the compartmentalization of the endosomal system. *Cold Spring Harb Perspect Biol*. 2014; 6: a022616. <https://doi.org/10.1101/cshperspect.a022616> PMID: 25341920
 62. Stenmark H. Rab GTPases as coordinators of vesicle traffic. *Nat Rev Mol Cell Biol*. 2009; 10: 513–25. <https://doi.org/10.1038/nrm2728> PMID: 19603039
 63. Quevillon E, Spielmann T, Brahimi K, Chattopadhyay D, Yeramian E, et al. The *Plasmodium falciparum* family of Rab GTPases. *Gene*. 2003; 306: 13–25. [https://doi.org/10.1016/s0378-1119\(03\)00381-0](https://doi.org/10.1016/s0378-1119(03)00381-0) PMID: 12657463
 64. Elliott DA, McIntosh MT, Hosgood HD 3rd, Chen S, Zhang G, et al. Four distinct pathways of hemoglobin uptake in the malaria parasite *Plasmodium falciparum*. *Proc Natl Acad Sci USA*. 2008; 105: 2463–8. <https://doi.org/10.1073/pnas.0711067105> PMID: 18263733
 65. Abu Bakar N, Klonis N, Hanssen E, Chan C, Tilley L. Digestive-vacuole genesis and endocytic processes in the early intraerythrocytic stages of *Plasmodium falciparum*. *J Cell Sci*. 2010; 123: 441–50. <https://doi.org/10.1242/jcs.061499> PMID: 20067995
 66. Howe R, Kelly M, Jimah J, Hodge D, Odom AR. Isoprenoid biosynthesis inhibition disrupts Rab5 localization and food vacuolar integrity in *Plasmodium falciparum*. *Eukaryot Cell*. 2013; 12: 215–23. <https://doi.org/10.1128/EC.00073-12> PMID: 23223036
 67. Babbitt SE, Altenhofen L, Cobbold SA, Istvan ES, Fennell C, et al. *Plasmodium falciparum* responds to amino acid starvation by entering into a hibernatory state. *Proc Natl Acad Sci USA*. 2012; 109: E3278–87. <https://doi.org/10.1073/pnas.1209823109> PMID: 23112171
 68. Witkowski B, Lelievre J, Barragan MJ, Laurent V, Su XZ, et al. Increased tolerance to artemisinin in *Plasmodium falciparum* is mediated by a quiescence mechanism. *Antimicrob Agents Chemother*. 2010; 54: 1872–7. <https://doi.org/10.1128/AAC.01636-09> PMID: 20160056
 69. Teuscher F, Chen N, Kyle DE, Gatton ML, Cheng Q. Phenotypic changes in artemisinin-resistant *Plasmodium falciparum* lines *in vitro*: evidence for decreased sensitivity to dormancy and growth inhibition. *Antimicrob Agents Chemother*. 2012; 56: 428–31. <https://doi.org/10.1128/AAC.05456-11> PMID: 21986828
 70. Cheng Q, Kyle DE, Gatton ML. Artemisinin resistance in *Plasmodium falciparum*: A process linked to dormancy? *Int J Parasitol Drugs Drug Resist*. 2012; 2: 249–55. <https://doi.org/10.1016/j.ijpddr.2012.01.001> PMID: 23420506
 71. Shaw PJ, Chaotheing S, Kaewprommal P, Piriyaopongsa J, Wongsombat C, et al. *Plasmodium* parasites mount an arrest response to dihydroartemisinin, as revealed by whole transcriptome shotgun sequencing (RNA-seq) and microarray study. *BMC Genomics*. 2015; 16: 830. <https://doi.org/10.1186/s12864-015-2040-0> PMID: 26490244
 72. Christoforidis S, Miaczynska M, Ashman K, Wilm M, Zhao L, et al. Phosphatidylinositol-3-OH kinases are Rab5 effectors. *Nat Cell Biol*. 1999; 1: 249–52. <https://doi.org/10.1038/12075> PMID: 10559924
 73. Murray JT, Panaretou C, Stenmark H, Miaczynska M, Backer JM. Role of Rab5 in the recruitment of hVps34/p150 to the early endosome. *Traffic*. 2002; 3: 416–27. <https://doi.org/10.1034/j.1600-0854.2002.30605.x> PMID: 12010460
 74. Stein MP, Feng Y, Cooper KL, Welford AM, Wandinger-Ness A. Human VPS34 and p150 are Rab7 interacting partners. *Traffic*. 2003; 4: 754–71. <https://doi.org/10.1034/j.1600-0854.2003.00133.x> PMID: 14617358
 75. Stein MP, Cao C, Tessema M, Feng Y, Romero E, et al. Interaction and functional analyses of human VPS34/p150 phosphatidylinositol 3-kinase complex with Rab7. *Methods Enzymol*. 2005; 403: 628–49. [https://doi.org/10.1016/S0076-6879\(05\)03055-7](https://doi.org/10.1016/S0076-6879(05)03055-7) PMID: 16473626
 76. Griffiths EJ, Rutter GA. Mitochondrial calcium as a key regulator of mitochondrial ATP production in mammalian cells. *Biochim Biophys Acta*. 2009; 1787: 1324–33. <https://doi.org/10.1016/j.bbabi.2009.01.019> PMID: 19366607
 77. Wang C, Youle RJ. The role of mitochondria in apoptosis. *Annu Rev Genet*. 2009; 43: 95–118. <https://doi.org/10.1146/annurev-genet-102108-134850> PMID: 19659442
 78. Rainbolt TK, Saunders JM, Wiseman RL. Stress-responsive regulation of mitochondria through the ER unfolded protein response. *Trends Endocrinol Metab*. 2014; 25: 528–37. <https://doi.org/10.1016/j.tem.2014.06.007> PMID: 25048297
 79. Rosenberg A, Luth MR, Winzeler EA, Behnke M, Sibley LD. Evolution of resistance *in vitro* reveals mechanisms of artemisinin activity in *Toxoplasma gondii*. *Proc Natl Acad Sci USA*. 2019; Dec 5: 201914732. <https://doi.org/10.1073/pnas.1914732116> PMID: 31806760

80. Maeno Y, Toyoshima T, Fujioka H, Ito Y, Meshnick SR, et al. Morphologic effects of artemisinin in *Plasmodium falciparum*. *Am J Trop Med Hyg.* 1993; 49: 485–91. <https://doi.org/10.4269/ajtmh.1993.49.485> PMID: 8214279
81. Peatey CL, Chavchich M, Chen N, Gresty KJ, Gray KA, et al. Mitochondrial membrane potential in a small subset of artemisinin-induced dormant *Plasmodium falciparum* parasites *in vitro*. *J Infect Dis.* 2015; 212: 426–34. <https://doi.org/10.1093/infdis/jiv048> PMID: 25635122
82. Wang J, Huang L, Li J, Fan Q, Long Y, et al. Artemisinin directly targets malarial mitochondria through its specific mitochondrial activation. *PLoS One.* 2010; 5: e9582. <https://doi.org/10.1371/journal.pone.0009582> PMID: 20221395
83. Mohring F, Jortzik E, Becker K. Comparison of methods probing the intracellular redox milieu in *Plasmodium falciparum*. *Mol Biochem Parasitol.* 2016; 206: 75–83. <https://doi.org/10.1016/j.molbiopara.2015.11.002> PMID: 26593282
84. Rahbari M, Rahlfs S, Przyborski JM, Schuh AK, Hunt NH, et al. Hydrogen peroxide dynamics in subcellular compartments of malaria parasites using genetically encoded redox probes. *Sci Rep.* 2017; 7: 10449. <https://doi.org/10.1038/s41598-017-10093-8> PMID: 28874682
85. Mamoun CB, Gluzman IY, Goyard S, Beverley SM, Goldberg DE. A set of independent selectable markers for transfection of the human malaria parasite *Plasmodium falciparum*. *Proc Natl Acad Sci U S A.* 1999; 96: 8716–20. <https://doi.org/10.1073/pnas.96.15.8716> PMID: 10411941
86. Nkrumah LJ, Muhle RA, Moura PA, Ghosh P, Hatfull GF, et al. Efficient site-specific integration in *Plasmodium falciparum* chromosomes mediated by mycobacteriophage Bxb1 integrase. *Nat Methods.* 2006; 3: 615–21. <https://doi.org/10.1038/nmeth904> PMID: 16862136
87. Fidock DA, Nomura T, Wellems TE. Cycloguanil and its parent compound proguanil demonstrate distinct activities against *Plasmodium falciparum* malaria parasites transformed with human dihydrofolate reductase. *Mol Pharmacol.* 1998; 54: 1140–7. <https://doi.org/10.1124/mol.54.6.1140> PMID: 9855645
88. Eklund EH, Schneider J, Fidock DA. Identifying apicoplast-targeting antimalarials using high-throughput compatible approaches. *FASEB J.* 2011; 25: 3583–93. <https://doi.org/10.1096/fj.11-187401> PMID: 21746861
89. Schuh AK, Rahbari M, Heimsch KC, Mohring F, Gabryszewski SJ, et al. Stable integration and comparison of hGrx1-roGFP2 and sfroGFP2 redox probes in the malaria parasite *Plasmodium falciparum*. *ACS Infect Dis.* 2018; 4: 1601–12. <https://doi.org/10.1021/acsinfecdis.8b00140> PMID: 30129748
90. Adjalley SH, Johnston GL, Li T, Eastman RT, Eklund EH, et al. Quantitative assessment of *Plasmodium falciparum* sexual development reveals potent transmission-blocking activity by methylene blue. *Proc Natl Acad Sci USA.* 2011; 108: E1214–23. <https://doi.org/10.1073/pnas.1112037108> PMID: 22042867








ARTICLE



<https://doi.org/10.1038/s41467-020-18624-0>

OPEN

Genetic screens reveal a central role for heme metabolism in artemisinin susceptibility

Clare R. Harding^{1,2,8}, Saima M. Sidik^{1,8}, Boryana Petrova^{1,8}, Nina F. Gnädig³, John Okombo³, Alice L. Herneisen ¹, Kurt E. Ward ^{3,4}, Benedikt M. Markus ^{1,5}, Elizabeth A. Boydston ¹, David A. Fidock ^{3,6} & Sebastian Lourido ^{1,7} 

Artemisinins have revolutionized the treatment of *Plasmodium falciparum* malaria; however, resistance threatens to undermine global control efforts. To broadly explore artemisinin susceptibility in apicomplexan parasites, we employ genome-scale CRISPR screens recently developed for *Toxoplasma gondii* to discover sensitizing and desensitizing mutations. Using a sublethal concentration of dihydroartemisinin (DHA), we uncover the putative transporter Tmem14c whose disruption increases DHA susceptibility. Screens performed under high doses of DHA provide evidence that mitochondrial metabolism can modulate resistance. We show that disrupting a top candidate from the screens, the mitochondrial protease DegP2, lowers porphyrin levels and decreases DHA susceptibility, without significantly altering parasite fitness in culture. Deleting the homologous gene in *P. falciparum*, *PfDegP*, similarly lowers heme levels and DHA susceptibility. These results expose the vulnerability of heme metabolism to genetic perturbations that can lead to increased survival in the presence of DHA.

¹Whitehead Institute for Biomedical Research, Cambridge, MA, USA. ²Wellcome Centre for Molecular Parasitology, Institute of Infection, Immunity & Inflammation, University of Glasgow, Glasgow, UK. ³Department of Microbiology and Immunology, Columbia University Irving Medical Center, New York, NY, USA. ⁴Department of Microbiology and Immunology, University of Otago, Dunedin, New Zealand. ⁵Faculty of Biology, University of Freiburg, Freiburg, Germany. ⁶Division of Infectious Diseases, Department of Medicine, Columbia University Irving Medical Center, New York, NY, USA. ⁷Biology Department, Massachusetts Institute of Technology, Cambridge, MA, USA. ⁸These authors contributed equally: Clare R. Harding, Saima M. Sidik, Boryana Petrova. ✉email: lourido@wi.mit.edu

Since their discovery and characterization as potent anti-malarials, artemisinin (ART), and its synthetic derivatives have emerged as important drugs in treating infectious diseases, and are being actively investigated in cancer therapy^{1,2}. Notably, artemisinin-based combination therapies (ACTs) have transformed malaria treatment, particularly in response to widespread resistance to previous classes of antiparasitic compounds. ARTs require activation within cells by scission of an endoperoxide bridge through the Fe²⁺ center of heme^{1,3}. Cleavage of this bond produces ART radicals that react with a multitude of proteins^{4,5}, lipids⁶, and metabolites⁷, rapidly leading to cell death.

ARTs are labile, and their short half-lives (~1 h in humans) enable modest, stage-specific reductions in parasite susceptibility to translate into reduced clinical efficacy. This reduced activity was first noted in Southeast Asia a decade ago, and is increasingly frequent^{8–11}. Clinical resistance has been associated with genetic polymorphisms in *Plasmodium falciparum* Kelch13 (K13), most notably K13^{C580Y}^{12,13}. Two recent publications attributed this decreased susceptibility to a hemoglobin import defect that presumably renders parasites less able to activate ART^{14,15}. This hypothesis may help explain how mutants in other components of the endocytic machinery, such as coronin¹⁶ and clathrin adaptors^{17–19}, and in hemoglobin digestion²⁰ also confer decreased susceptibility to ART. Previous studies have also postulated that the altered ART susceptibility of K13^{C580Y} parasites involves changes in the unfolded protein response, autophagy, and PI3K activity, which may contribute to cellular survival following protein alkylation^{21–24}. Some *P. falciparum* strains without identified causative mutations have also displayed decreased clearance^{25,26}, suggesting that aspects of ART susceptibility have yet to be elucidated.

Directed evolution coupled with whole-genome sequencing has identified targets and resistance pathways for many antiparasitic compounds^{16,27–29}. Such approaches can be time-consuming, may fail to detect minor mutations or those that negatively impact parasite fitness, and can only be used for positive selection schemes. Recently, whole-genome CRISPR-based mutational approaches have uncovered drug-resistance mechanisms in cancer^{30–32}. Analogously, we have shown that CRISPR screens in *Toxoplasma gondii* provide a comparatively fast method to identify causal mutations using both positive and negative selection^{33,34}.

Despite species-specific differences that could impact ART susceptibility—such as the lack of substantial hemoglobin uptake by *T. gondii*—here, we demonstrate that a point mutation in K13, homologous to the canonical *P. falciparum* K13^{C580Y}, reduced the susceptibility of *T. gondii* to dihydroartemisinin (DHA). Genome-wide screens in *T. gondii* further identified mutants in a putative porphyrin transporter (Tmem14c) that are more susceptible to DHA, as well as mutations in several genes involved in mitochondrial metabolism that decreased drug susceptibility. In particular, we identified a mitochondrial protease (DegP2), disruption of which decreases porphyrins and DHA susceptibility without impacting parasite fitness. We provide evidence that DegP2 interacts with several mitochondrial proteins, including one that contains a NifU domain that is predicted to be involved in transferring nascent iron–sulfur clusters to client proteins. In keeping with this observation, Δ DegP2 parasites have alterations in the electron transport chain (ETC) and the tricarboxylic acid cycle (TCA)—two iron–sulfur cluster-dependent processes.

Results

Using *T. gondii* to understand apicomplexan DHA susceptibility. Previous studies have demonstrated the susceptibility of

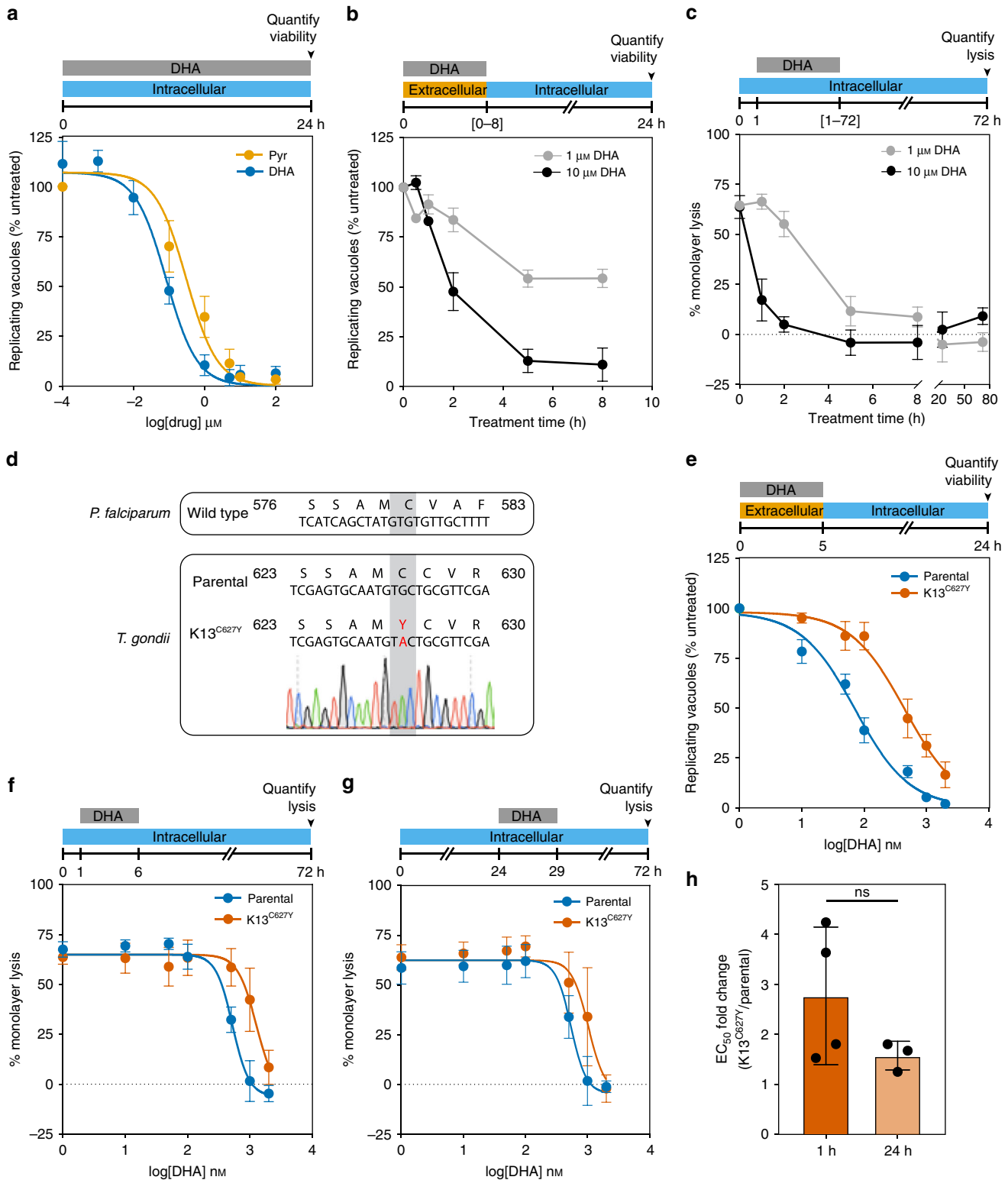
T. gondii to ART and its derivatives^{35–37}. To establish the susceptibility of *T. gondii* to DHA in our assays, we treated intracellular parasites with varying concentrations of DHA or pyrimethamine (the frontline treatment for toxoplasmosis) for 24 h. Parasite viability was measured by counting the number of vacuoles containing two or more parasites in vehicle- or drug-treated conditions. Both drugs completely blocked parasite replication at 10 μ M, which did not affect the integrity of the host monolayers (Fig. 1a). Our results recapitulate the reported EC₅₀ for pyrimethamine³⁸ and underscore the potency of DHA against *T. gondii*. Nevertheless, we recognize that *T. gondii* is far less susceptible to DHA than blood-stage malaria parasites, a fact that contributes to the use of other compounds as frontline drugs for toxoplasmosis³⁹.

We next determined the length of time required for DHA to kill extracellular and intracellular parasites. Measuring the susceptibility of extracellular parasites to DHA allowed us to exclude possible effects of the compound on host cells. Isolated parasites were treated with DHA for increasing lengths of time before removing the compound and allowing parasites to infect host cells and replicate for 24 h. The effect of DHA (both at 1 μ M and at 10 μ M) plateaued after 5 h of treatment (Fig. 1b). We similarly determined the treatment window for intracellular parasites. We added 1 or 10 μ M DHA to intracellular parasites 1 h post invasion (1 h.p.i.), washed out the compound after different lengths of time, then assessed parasite viability based on the proportion of the host cell monolayer that was lysed 72 h.p.i. (Fig. 1c). Based on these results, we used 5 h treatments for both intracellular and extracellular parasites⁴⁰.

Homologous Kelch13 mutations decrease DHA susceptibility in *P. falciparum* and *T. gondii*. In *P. falciparum*, point mutations in *Kelch13* (*K13*), such as C580Y and R539T, correlate with delayed clearance and increased survival of ring-stage parasites^{12,13,41,42}. Although *K13* is conserved among apicomplexans, its role in DHA susceptibility has not been examined in *T. gondii*. We chose to make a C627Y mutation in the *T. gondii* ortholog of *K13* (TGGT1_262150), corresponding to *P. falciparum* C580Y¹³ (Fig. 1d). Extracellular K13^{C627Y} parasites were sevenfold less susceptible to DHA compared to the parental strain (Fig. 1e; EC₅₀ values provided in Supplementary Table 1), indicating that the effect of *K13* on DHA susceptibility transcends genera. As in *P. falciparum*, K13^{C627Y} parasites were still susceptible to prolonged DHA exposure and did not form plaques under continuous DHA treatment (Supplementary Fig. 1).

DHA susceptibility is known to change over the *P. falciparum* erythrocytic cycle, with trophozoites displaying greater susceptibility than rings or schizonts^{43,44}. To determine whether active replication affects DHA susceptibility in *T. gondii*, we treated intracellular parasites immediately after invasion (Fig. 1f and Supplementary Table 1) before most parasites have initiated replication—or 24 h after invasion when most parasites are replicating⁴⁵ (Fig. 1g and Supplementary Table 1). K13^{C627Y} parasites were at least twofold more resistant to DHA compared to the parental line, regardless of the timing of treatment (Fig. 1h), and we conclude that replication does not affect the reduced DHA susceptibility of K13^{C627Y} *T. gondii*.

A genome-wide screen identifies a mutant that is hypersensitive to DHA. We performed CRISPR-based screens to identify genes that when disrupted would increase *T. gondii* susceptibility to DHA. Transfecting a library containing ten guide RNAs (gRNAs) per gene into a large population of parasites that constitutively expressed the Cas9 nuclease, we created a diverse population of mutants. From previous work, we know that



parasites acquire on average a single gRNA that directs Cas9 to create a double-stranded break in the coding sequence of the specified gene^{33,34,46}. Insertions and deletions introduced during DNA repair lead to loss-of-function mutations in the targeted genes, and the prevalence of different mutants in the population can be inferred from the relative abundance of gRNAs against each gene. Following generation of the pool of mutants, we propagated this pool in the presence or absence of a sublethal dose (50 nM) of DHA for 7 days (three passages for the untreated

population; Fig. 2a). Guides against a single gene (TGGT1_228110) were substantially depleted under drug treatment compared to the untreated control (Fig. 2b and Supplementary Data 1). TGGT1_228110 encodes a previously unstudied *T. gondii* gene with three to four transmembrane domains, predicted to be dispensable under standard growth conditions³⁴. Structural prediction using HHPred⁴⁷ indicated that TGGT1_228110 is homologous to TMEM14C ($p = 5 \times 10^{-21}$), a recently identified porphyrin transporter found in mammals⁴⁸.

Fig. 1 DHA kills wild-type *T. gondii* efficiently and its effect is influenced by mutation of K13. **a** Treatment with increasing concentrations of dihydroartemisinin (DHA) or pyrimethamine (Pyr) over 24 h resulted in a reduction in parasite viability, measured as the number of vacuoles with two or more parasites normalized to untreated wells. Results are mean \pm SEM for $n = 4$ independent experiments. **b** Viability was similarly assessed for extracellular parasites treated with 1 or 10 μ M DHA for varying periods of time, then washed and allowed to invade host cells. Viable vacuoles were normalized to untreated parasites kept extracellular for equal periods of time. Results are mean \pm SEM for $n = 3$ independent experiments, each performed in technical triplicate. **c** Quantification of host monolayer lysis after treatment with 1 or 10 μ M DHA for the indicated time, normalized to uninfected monolayers. Results are mean \pm SEM for $n = 4$ independent experiments. **d** Alignment of the mutated region of K13 in *P. falciparum* and *T. gondii* displaying the chromatogram for the K13^{C627Y} *T. gondii* line. **e** Extracellular dose-response curve for parental or K13^{C627Y} parasites treated with DHA for 5 h. Results are mean \pm SEM for $n = 7$ or 5 independent experiments with parental or K13^{C627Y} parasites, respectively. **f** Monolayer lysis following infection with parental or K13^{C627Y} parasites for 1 h, prior to a 5 h treatment with varying concentrations of DHA. Results are mean \pm SEM for $n = 4$ independent experiments. **g** Monolayer lysis following infection with parental or K13^{C627Y} parasites for 24 h, prior to 5 h treatment with varying concentrations of DHA. Results are mean \pm SEM for $n = 4$ or 3 independent experiments with parental or K13^{C627Y} parasites, respectively. **h** Graph summarizing the fold change in DHA EC₅₀ between parental and K13^{C627Y} parasites, treated 1 or 24 h after invasion. Results are mean \pm SD for $n = 4$ or 3 independent experiments, p -value calculated from two-tailed unpaired t -test.

Based on this homology, we named the *T. gondii* gene *Tmem14c*. *Tmem14c* is conserved in coccidia but absent from *Plasmodium* spp., suggesting that this gene plays an accessory role in heme synthesis.

To validate the effect of *Tmem14c* depletion on DHA susceptibility, we replaced the coding region of *Tmem14c* with an mNeonGreen expression cassette (Supplementary Fig. 2). Although Δ *Tmem14c* grew normally under standard conditions, treating mutant parasites with 100 nM DHA for 7 days abolished plaque formation, with minimal effects on the parental line (Fig. 2c). We quantified the change in DHA susceptibility by treating extracellular parasites with varying concentrations of DHA, then measuring their viability. Results showed a modest (twofold) increase in DHA susceptibility for Δ *Tmem14c* parasites compared to the parental line (Fig. 2d and Supplementary Table 1).

We considered that treating intracellular parasites would better resemble the conditions of the CRISPR screens, which maintained DHA pressure throughout the lytic cycle. We therefore assessed the DHA susceptibility of Δ *Tmem14c* parasites by treating with DHA for 5 h immediately after invasion or during replication (Fig. 2e and Supplementary Table 1). In contrast to the parental and K13^{C627Y} parasite lines (Fig. 1h), the susceptibility of Δ *Tmem14c* to DHA was significantly more pronounced during replication, when it was sevenfold greater than that of the parental strain.

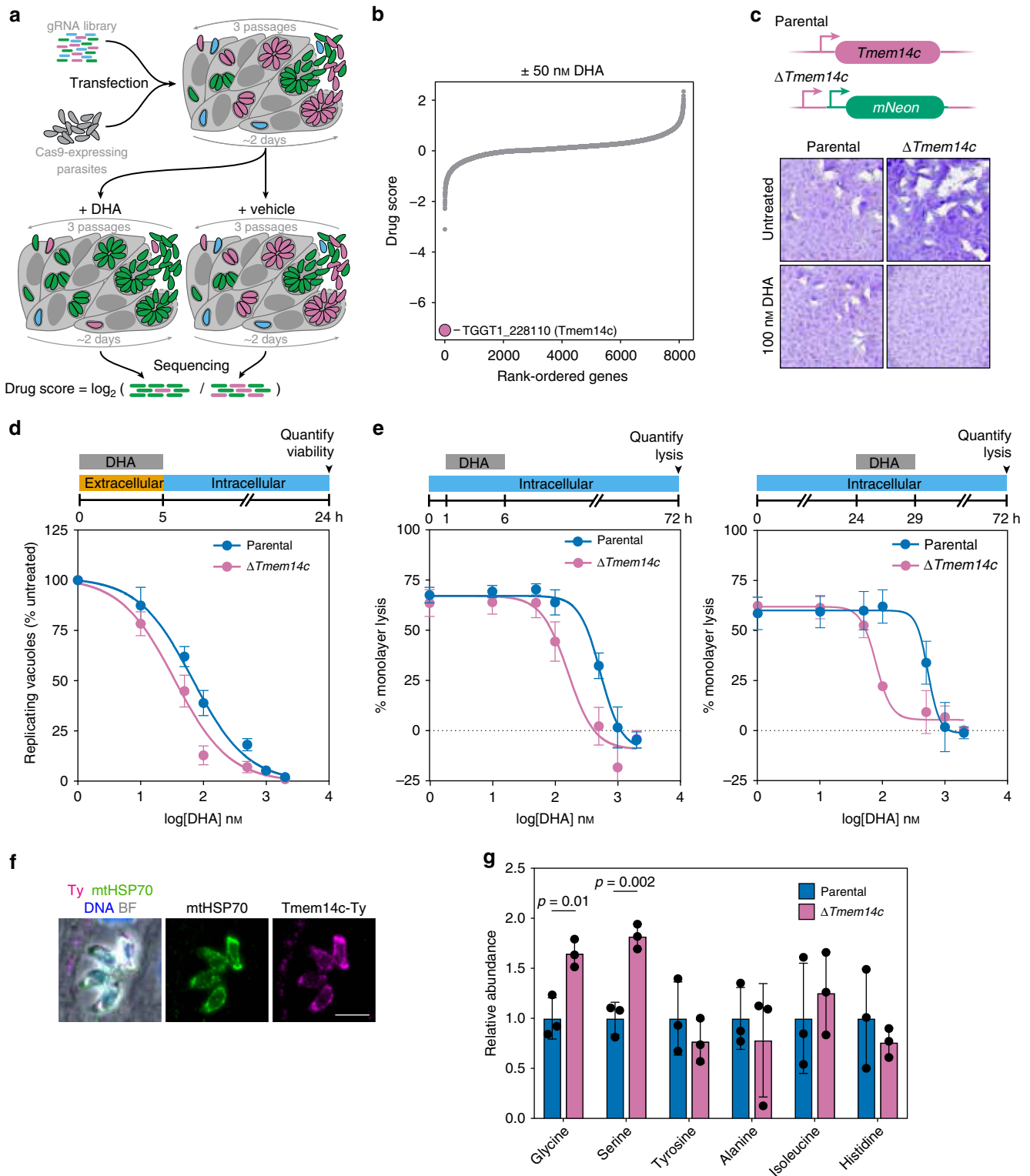
To examine the function of *Tmem14c*, we determined its subcellular localization and the effect of its deletion. A C-terminally Ty-tagged copy of *Tmem14c* was found to localize to the parasite mitochondrion (Fig. 2f), in agreement with the localization of the mammalian homolog to the inner mitochondrial membrane⁴⁸. We then probed for global metabolic changes in intracellular Δ *Tmem14c* parasites by targeted metabolomics (Fig. 2g and Supplementary Data 2). We observed changes in glycine-serine metabolism, as well as TCA cycle intermediates, which supports the link between *Tmem14c* and mitochondrial function.

Genome-wide screens implicate TCA and heme biosynthesis pathways in DHA susceptibility. We performed three genome-wide CRISPR screens, similar to those described above, to identify genes that when disrupted decrease susceptibility to DHA. Following selection for integration of the gRNAs, parasite populations were treated with DHA or vehicle, then cultured for the time required to passage the untreated population three times (~6 days). The log₂-fold change of gRNA abundance between the drug-treated and untreated populations (drug score) was used to rank all protein-coding genes (Fig. 3a and Supplementary Data 1). Two replicates of this screen were performed using 0.5

μ M DHA, pooled, and analyzed using Model-based Analysis of Genome-wide CRISPR/Cas9 Knockout (MaGCK)49. A third screen performed with 10 μ M DHA was analyzed separately. In total, gRNAs against eight genes were significantly enriched in DHA-treated populations in at least two of the three high-dose screens (Supplementary Table 2). A further 65 genes were significantly enriched in individual screens (Supplementary Data 3). The likelihood of identifying a given candidate depends on the gene's contribution to overall fitness, as well as the gene's impact on DHA susceptibility. For every iteration of the screen, the rate at which mutants are lost from the population will fluctuate such that certain fitness-conferring mutants may be completely lost from the population before they have a chance to impact survival under DHA treatment. Even candidates identified in a single screen are significant based on the concordant effect of multiple gRNAs; however, we have the highest confidence in hits obtained from multiple independent screens and focused subsequent analyses on these candidates. Because *K13* mutants are exceedingly difficult to recover by selection with DHA in culture¹² and *K13* is necessary for *T. gondii* fitness³⁴, we did not expect enrichment of gRNAs targeting *K13*, which would predominantly cause loss-of-function mutations.

We performed metabolic pathway analysis on the 73 candidate genes identified by the screens (65 genes identified in single replicates and 8 genes identified in multiple replicates) and found that TCA cycle enzymes were significantly enriched (Bonferroni-adjusted p -value = 1.67×10^{-5}). The TCA cycle and heme biosynthesis are linked through the production of succinyl-CoA, which is a substrate for δ -aminolevulinic acid synthase (ALAS; Fig. 3b). Two enzymes from the heme biosynthesis pathway were among the candidates: porphobilinogen deaminase (TGGT1_271420) and protoporphyrinogen oxidase (TGGT1_272490). We also identified pyridoxal kinase, which functionalizes the cofactor pyridoxal phosphate. This cofactor is required by several enzymes, including ALAS, which catalyzes the first step of heme biosynthesis⁵⁰. Taken together, these screens support the conclusion that genetically inhibiting heme biosynthesis reduces the DHA susceptibility of *T. gondii*.

Chemical modulation of heme biosynthesis decreases DHA susceptibility. We investigated whether inhibitors of the TCA cycle (sodium fluoroacetate, abbreviated as NaFAC)⁵¹ or heme biosynthesis (succinyl acetone, abbreviated as SA)⁵² would recapitulate our genetic results. After pretreating extracellular parasites for 2 h with NaFAC or SA, we treated them for a further 5 h with increasing concentrations of DHA before determining parasite viability. Consistent with our genetic results, both NaFAC and SA significantly increased the EC₅₀ of DHA compared to untreated parasites (Fig. 3c, d and Supplementary Table 1). To



ensure that metabolic modulation alone did not impact DHA susceptibility, we blocked glycolysis using 5 mM 2-deoxyglucose (2-DG)^{51,53}, as glycolysis is dispensable for TCA activity in the presence of glutamine⁵⁴. Pretreatment with 2-DG did not change the susceptibility of parasites to DHA (Fig. 3e and Supplementary Table 1).

To confirm the effect of the inhibitors on heme production, we quantified total levels of porphyrins—including heme and its precursor protoporphyrin IX (PPIX)—by measuring porphyrin

fluorescence⁵⁵. Porphyrin levels were slightly increased by treatment with 2-DG, whereas treatment with NaFAC or SA significantly depressed porphyrin levels (Fig. 3f). We also monitored the effects of 2-DG, NaFAC, and SA by global polar metabolite profiling. Only subtle changes resulted from SA treatment. However, we observed the expected changes in TCA cycle or glycolytic intermediates and neighboring pathways after NaFAC or 2-DG treatment, respectively (Supplementary Fig. 3 and Supplementary Data 4). These results demonstrate that the

Fig. 2 Genome-wide screen under sublethal DHA concentration reveals that loss of Tmem14c increases DHA susceptibility. **a** Screening workflow. The drug score is defined as the \log_2 -fold change in the relative gRNA abundance between the DHA-treated and vehicle populations, where lower scores are indicative of genes that enhance drug susceptibility when disrupted. **b** Results of a genome-wide CRISPR screen (calculated as described in **a**) comparing treatment with 50 nM DHA (equivalent to EC_{50}) to vehicle-treated parasites. Guides against one gene, Tmem14c, were significantly depleted by the sublethal DHA concentration, but were retained in the vehicle control. **c** Δ Tmem14c parasites formed plaques normally under standard growth conditions, but their plaquing ability was attenuated in the presence of 100 nM DHA. The parental strain proliferated normally in both conditions. **d** Extracellular Δ Tmem14c parasites had a decreased EC_{50} compared to the parental line ($p = 0.0003$, extra-sum-of-squares F -test). Results are mean \pm SEM for $n = 7$ independent experiments. **e** Monolayer lysis following infection with parental or Δ Tmem14c parasites and treatment with varying concentrations of DHA during hours 1–6 (top panel) or 24–29 (bottom panel) post infection. Results are mean \pm SEM for $n = 4$ or 3 independent experiments for parental or Δ Tmem14c parasites, respectively. **f** Overexpression of Tmem14c-Ty co-localized with mitochondrial marker mtHSP70. Scale bar is 5 μ m. **g** Relative abundance of selected amino acids from targeted metabolomics of intracellular parental or Δ Tmem14c parasites. Results are mean \pm SD for $n = 3$ technical replicates, with p -values calculated by one-way ANOVA.

TCA cycle is required to maintain porphyrin pools in *T. gondii*, joining the metabolic pathways identified in our screens and confirming that modulation of heme levels can result in decreased DHA susceptibility in apicomplexans.

To test whether increased flux through the heme biosynthesis pathway could hypersensitize parasites to DHA, we supplemented the growth medium with ALA, a precursor that stimulates heme biosynthesis in many organisms^{56–58}. While ALA treatment increased total porphyrin levels it did not alter DHA susceptibility, leading us to suspect that this increase in porphyrins was due to a buildup of PPIX, and is not reflective of increased heme levels (Supplementary Fig. 3).

DegP2 mutants have decreased porphyrin levels and decreased DHA susceptibility. Having verified the relationship between heme biosynthesis and DHA susceptibility, we turned our attention to TGGT1_290840—the most significant hit in our lethal dose DHA screen lacking a known relationship to heme biosynthesis (Fig. 3a). Previously uncharacterized in *T. gondii*, TGGT1_290840 shares homology with the DegP family of serine proteases. A related *T. gondii* rhoptry protease was recently named DegP⁵⁹, so we named TGGT1_290840 DegP2. DegP2 possesses an identifiable catalytic serine (S569), evident in an alignment with the *Arabidopsis thaliana* plastid protease Deg2^{60–62}.

We generated a panel of strains to study the localization and function of DegP2. These included a DegP2 knockout made by replacing the coding sequence with YFP (Δ DegP2; Fig. 4a). We complemented this knockout with a C-terminally HA-tagged allele expressed from the *TUB1* promoter (Δ DegP2/DegP2-HA). We also endogenously tagged DegP2 with a C-terminal Ty epitope, then mutated DegP2's catalytic serine, creating two strains that we refer to as DegP2-Ty and DegP2^{S569A}-Ty, respectively (Fig. 4b). Both the endogenously Ty-tagged and ectopically expressed HA-tagged DegP2 were co-localized with the mitochondrial marker mtHSP70 (Fig. 4b).

Finally, we generated a DegP2 conditional knockdown (cKD) using the U1 system⁶³. Using a parental strain expressing a rapamycin-dimerizable Cre recombinase (DiCre), the DegP2 locus is appended with a floxed synthetic 3' untranslated region (UTR) followed by multiple U1-binding sites. Adding rapamycin to this strain activates Cre, and leads to excision of the 3'-UTR and positioning U1-binding sites directly after the DegP2 coding sequence, altering the stability of the mRNA (Fig. 4c). We used immunofluorescence microscopy (Fig. 4c) and immunoblotting (Fig. 4d) to show that a 2 h pulse of rapamycin leads to robust DegP2 depletion.

Plaque assays showed that both Δ DegP2 and the complemented strain Δ DegP2/DegP2-HA had significant growth defects (Fig. 5a). By contrast, DegP2-Ty and DegP2^{S569A}-Ty lines formed plaques similarly to the parental strain (Fig. 5b). This led us to

suspect that Δ DegP2 harbors alterations that extend beyond the activity of the protease. Therefore, we have only attributed to DegP2 those phenotypes that could be complemented in Δ DegP2/DegP2-HA or determined using the DegP2 cKD.

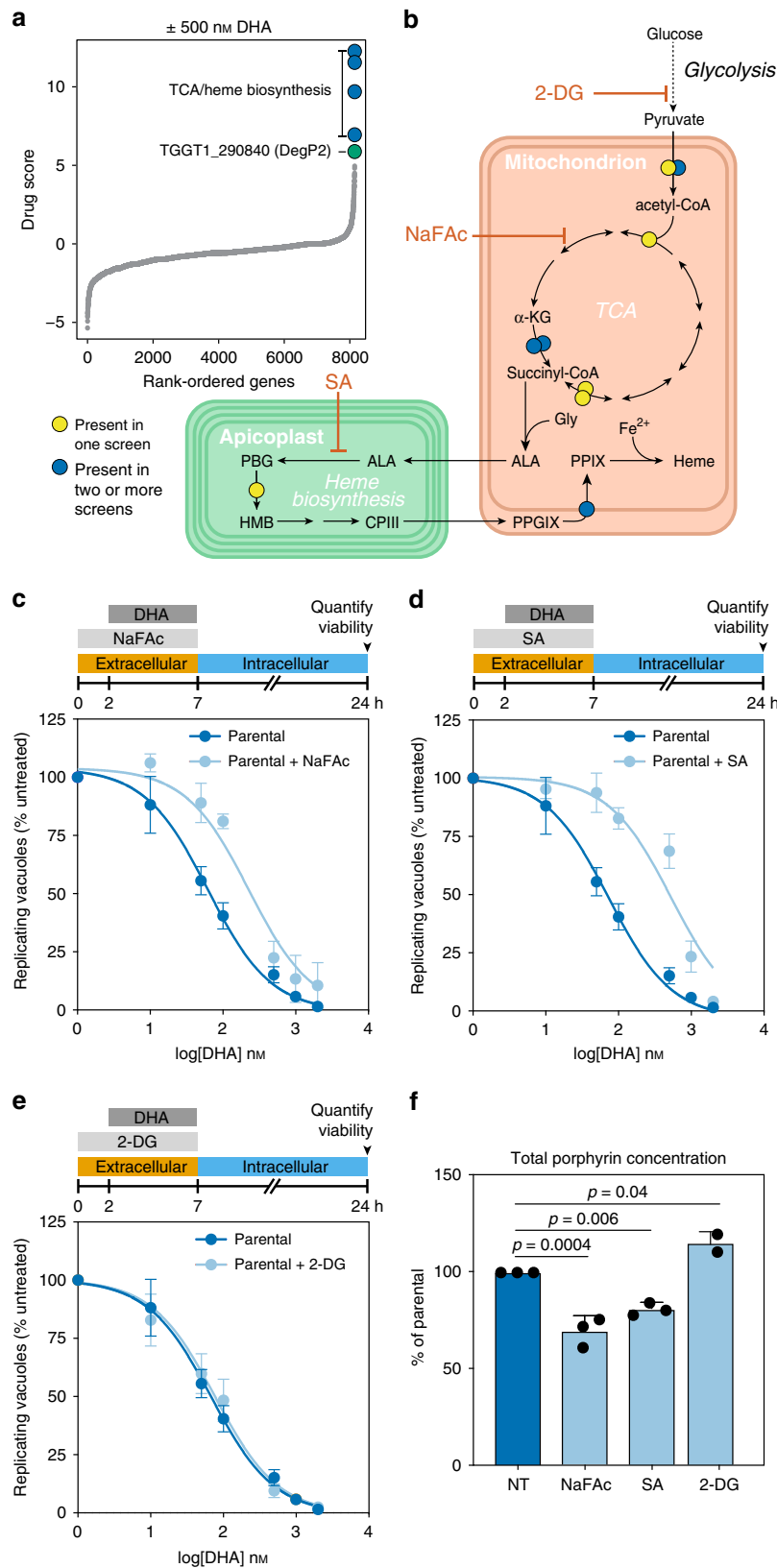
As many of the hits from our lethal dose DHA screen were related to heme biosynthesis—a process that takes place partially in the mitochondrion, where DegP2 is found—we wondered if disrupting DegP2 might also decrease parasite heme levels. By measuring porphyrin fluorescence, we found that Δ DegP2 and DegP2^{S569A}-Ty both had significantly reduced porphyrin levels, and porphyrin abundance was partially restored in Δ DegP2/DegP2-HA (Fig. 5c).

To confirm that Δ DegP2's decreased heme levels correspond to a decrease in DHA susceptibility, we determined the EC_{50} of DHA against the DegP2 knockout and catalytically inactive strains, along with their respective controls (Fig. 5d and Supplementary Fig. 4). As expected, we observed a significantly higher EC_{50} for Δ DegP2 compared to the parental strain (358 nM compared to 76 nM). This effect was largely reversed in Δ DegP2/DegP2-HA (105 nM). Likewise, DegP2^{S569A}-Ty had a significantly higher EC_{50} than DegP2-Ty (153 nM compared to 63 nM). When we looked for a correlation between porphyrin levels and DHA EC_{50} , we found a strong negative relationship between these strain's porphyrin levels and DHA susceptibility ($r^2 = 0.75$; Fig. 5e).

We confirmed the relationship between DegP2, porphyrin levels, and DHA susceptibility using the DegP2 cKD. Rapamycin-treated DegP2 cKD parasites form plaques similarly to DiCre parasites (Fig. 5f). Using fluorescence to quantify the porphyrin levels in the DegP2 cKD revealed a drop of ~30% in response to rapamycin treatment, similar to the difference observed between Δ DegP2 and its parental strain (Fig. 5g).

To assess the ability of DegP2 cKD parasites to survive DHA treatment, we treated the DegP2 cKD strain with rapamycin, or vehicle, then mixed it in a 1:1 ratio with rapamycin-treated DiCre parasites expressing tdTomato. Rapamycin treatment of the DiCre strain had no effect on its fitness and provided an ideal control for treatment of the cKD. We cultured the resulting populations in the presence or absence of DHA for 8 days and used flow cytometry to analyze the composition of the populations every 2 days (Fig. 5h). Rapamycin-treated DegP2 cKD parasites consistently outcompeted DiCre parasites in the presence of DHA, whereas levels of both strains remained close to 50% under control conditions. Collectively, these results confirm that reducing DegP2 levels reduces porphyrin levels, resulting in decreased susceptibility to DHA.

The decreased porphyrin levels in Δ DegP2 prompted us to examine metabolic changes in other mutants that modulate DHA susceptibility. Δ Tmem14c and K13^{C627Y} parasites displayed similar levels of porphyrins as their isogenic controls (Supplementary Fig. 2). Analysis of polar metabolites in the K13^{C627Y} strain revealed that the metabolic pathway for alanine, aspartate,



and glutamate production changed significantly ($FDR < 0.05$). The TCA cycle was also affected ($FDR < 0.1$), with several intermediates displaying decreased abundance compared to the control (Supplementary Fig. 2 and Supplementary Table 3). Unlike for NaFAc (Supplementary Fig. 3) or $\Delta DegP2$ (discussed below), this effect does not point to a specific block in the TCA

cycle, but rather a global dysregulation of the pathway. Our results suggest that in *T. gondii*, $\Delta Tmem14c$ and K13^{C627Y} mutations affect DHA susceptibility independently from the steady-state heme pools. However, we cannot rule out changes in subcellular localization of heme, as may be expected from the predicted role of Tmem14c in porphyrin transport^{14,15,48}.

Fig. 3 Genome-wide CRISPR screen under high DHA pressure identifies TCA and heme biosynthetic pathways as determinants of DHA susceptibility.

a Aggregated drug scores from two independent genome-wide CRISPR screens performed with a lethal dose of 500 nM DHA. Drug scores defined as the \log_2 -fold change in the relative gRNA abundance between the DHA-treated and vehicle populations, where higher scores are indicative of genes that reduce drug susceptibility when disrupted. Genes with consistently high drug scores are highlighted, indicating that their disruption favored parasite survival under otherwise lethal concentrations of DHA. **b** Diagram of key metabolic pathways highlighting genes with high drug scores in the screens from **a** and a third screen performed with 10 μ M DHA, analyzed separately. Predicted localization of enzymes within organelles for the TCA cycle and heme biosynthesis pathways. 2-DG 2-deoxyglucose, α -KG α -ketoglutarate, ALA δ -aminolevulinic acid, CPIII coproporphyrinogen III, Gly glycine, HMB hydroxymethylbilane, NaFAc sodium fluoroacetate, PGB porphobilinogen, PPIX protoporphyrin IX, PPGIX protoporphyrinogen IX, SA succinyl acetone. Hits found in two or more replicates (blue) or only one replicate (yellow) are indicated. **c** Pretreatment with 500 mM NaFAc for 2 h significantly increased the EC_{50} of DHA (extra-sum-of-squares *F*-test, $p < 0.0001$). Results are mean \pm SEM for $n = 7$ or 4 independent experiments with vehicle or NaFAc treatment, respectively. **d** Pretreatment with 10 mM SA significantly increased the EC_{50} of DHA (extra-sum-of-squares *F*-test, $p < 0.0001$). Results are mean \pm SEM for $n = 7$ or 5 independent experiments with vehicle or SA treatment, respectively. **e** Pretreatment with 5 mM 2-DG did not significantly affect the EC_{50} of DHA (extra-sum-of-squares *F*-test, $p = 0.6$). Results are mean \pm SEM for $n = 7$ or 3 independent experiments with vehicle or 2-DG treatment, respectively. **f** Porphyrin levels (combination of heme and PPIX) in parasites exposed to various compounds, measured by fluorescence and normalized to untreated parasites (NT). Results are mean \pm SD for $n = 3$ independent experiments, each performed in technical duplicate; *p*-values from a one-way ANOVA with Tukey's test.

DegP2 influences the intersection of the TCA cycle, heme biosynthesis, and the ETC.

We attempted to use immunoprecipitations with either wild type or catalytically dead DegP2 to define DegP2's binding partners, but we were unable to reliably detect interactions. Instead, we turned to thermal proteome profiling (TPP) to identify proteins that change in thermal stability when DegP2 is knocked down^{64–67}, implying a direct or indirect interaction with DegP2. We collected DegP2 cKD parasites that had been treated with rapamycin or a vehicle control, then heated them to temperatures between 37 °C and 67 °C. After lysis and ultracentrifugation, only non-denatured proteins remained in the supernatant. Using liquid chromatography mass spectrometry (LC–MS), we compared the abundances of non-denatured proteins across the range of temperatures and identified proteins that had altered melting temperatures in the absence of DegP2. We calculated melting temperatures for 1669 proteins across two replicates of the TPP experiment and identified 13 proteins that displayed greater than average changes in both replicates ($p < 0.2$ by *z*-test; Fig. 6a and Supplementary Data 5). Of these 13 proteins, three are mitochondrial^{68,69} a NifU domain-containing protein (TGGT1_212930), the ATP synthase γ subunit (TGGT1_231910), and an unannotated protein (TGGT1_226500; Fig. 6b).

Two of these three mitochondrial proteins are related to the ETC. The yeast homolog of TGGT1_212930, Nfu1, transfers nascent iron–sulfur clusters to complex II, as well as to the TCA cycle enzyme aconitase⁷⁰. The γ subunit of the ATP synthase is another critical component of the ETC⁵³. These observations motivated us to examine the susceptibility of Δ DegP2 parasites to the complex II inhibitor thenoyltrifluoroacetone (TTFA)^{71,72}, and the cytochrome *b* inhibitor atovaquone (ATQ)^{73,74}. Parental and Δ DegP2/DegP2-HA parasites showed similar responses to TTFA, while Δ DegP2 parasites were significantly more resistant (Fig. 6c and Supplementary Table 1). By contrast, the EC_{50} of ATQ was unchanged between Δ DegP2 and the parental line (Fig. 6d and Supplementary Table 1). This specific effect of DegP2 on complex II is consistent with the known role of Nfu1 in transferring iron–sulfur clusters to complex II.

To determine whether this apparent alteration in complex II activity resulted in a mitochondrial polarization defect, we loaded Δ DegP2 and its parental strain with MitoTracker, then analyzed their fluorescence using flow cytometry (Supplementary Fig. 4). Both strains displayed similar fluorescence profiles, indicating that Δ DegP2 parasites polarize their mitochondrial membrane to a similar extent as the wild type, despite altered complex II activity.

The TCA cycle is a common thread connecting heme biosynthesis and the ETC. Succinate, a TCA intermediate, is a substrate for both heme biosynthesis and the SDHB subunit of complex II, which converts it to the subsequent TCA intermediate, fumarate. In addition, yeast Nfu1 binds aconitase, which uses an iron–sulfur cluster to catalyze the second step in the TCA cycle⁷⁰. To gain further insight into the mitochondrial dysregulation of Δ DegP2 parasites, we used polar metabolite profiling via LC–MS to compare the levels of TCA cycle intermediates in Δ DegP2 and its parental strain (Fig. 6e and Supplementary Data 6). We observed reduced levels of succinate, in addition to altered levels of pyruvate, glutamine, malate, and GABA in Δ DegP2 parasites. These results show that disrupting DegP2 dysregulates multiple aspects of mitochondrial homeostasis, centering around the intersection between the ETC, the TCA cycle, and heme biosynthesis.

***P. falciparum* DegP (PfDegP) deletion alters heme concentrations and reduces DHA susceptibility during the erythrocytic cycle.**

To investigate the role of the *P. falciparum* DegP2 ortholog, PfDegP (PF3D7_0807700), in ART susceptibility, we disrupted the gene in the Cam3.II strain expressing wild-type K13 (Fig. 7a, b). Cam3.II K13^{WT} is derived from the Cambodian isolate Cam3.II K13^{R539T}, which shows decreased susceptibility to DHA¹³. We compared the susceptibility of Cam3.II Δ PfDegP to Cam3.II K13^{WT}, and found that Cam3.II Δ PfDegP parasites were less susceptible to DHA in both the ring and schizont stages than Cam3.II K13^{WT} parasites. For comparison, the parental strain, Cam3.II K13^{R539T}, displayed low DHA susceptibility in the ring stage, as previously described¹³. Surprisingly, Cam3.II Δ PfDegP and Cam3.II K13^{R539T} showed similar DHA susceptibility in the schizont stage (Fig. 7c, d).

To test whether the changes in DHA susceptibility were correlated with changes in heme concentrations, we fractionated infected cells and measured free heme, as well as heme associated with hemoglobin and hemozoin^{75,76}. Trophozoites from either the Cam3.II Δ PfDegP and Cam3.II K13^{R539T} strains had significantly lower levels of free heme (Fig. 7e), while heme associated with hemoglobin or hemozoin remained unchanged (Fig. 7f, g). The effect of the K13 mutation on trophozoites points to a link between DHA susceptibility and the availability of free heme within the parasite. Taken together, these data also demonstrate that screens in *T. gondii* can identify resistance alleles that act through mechanisms conserved across the Apicomplexan phylum.

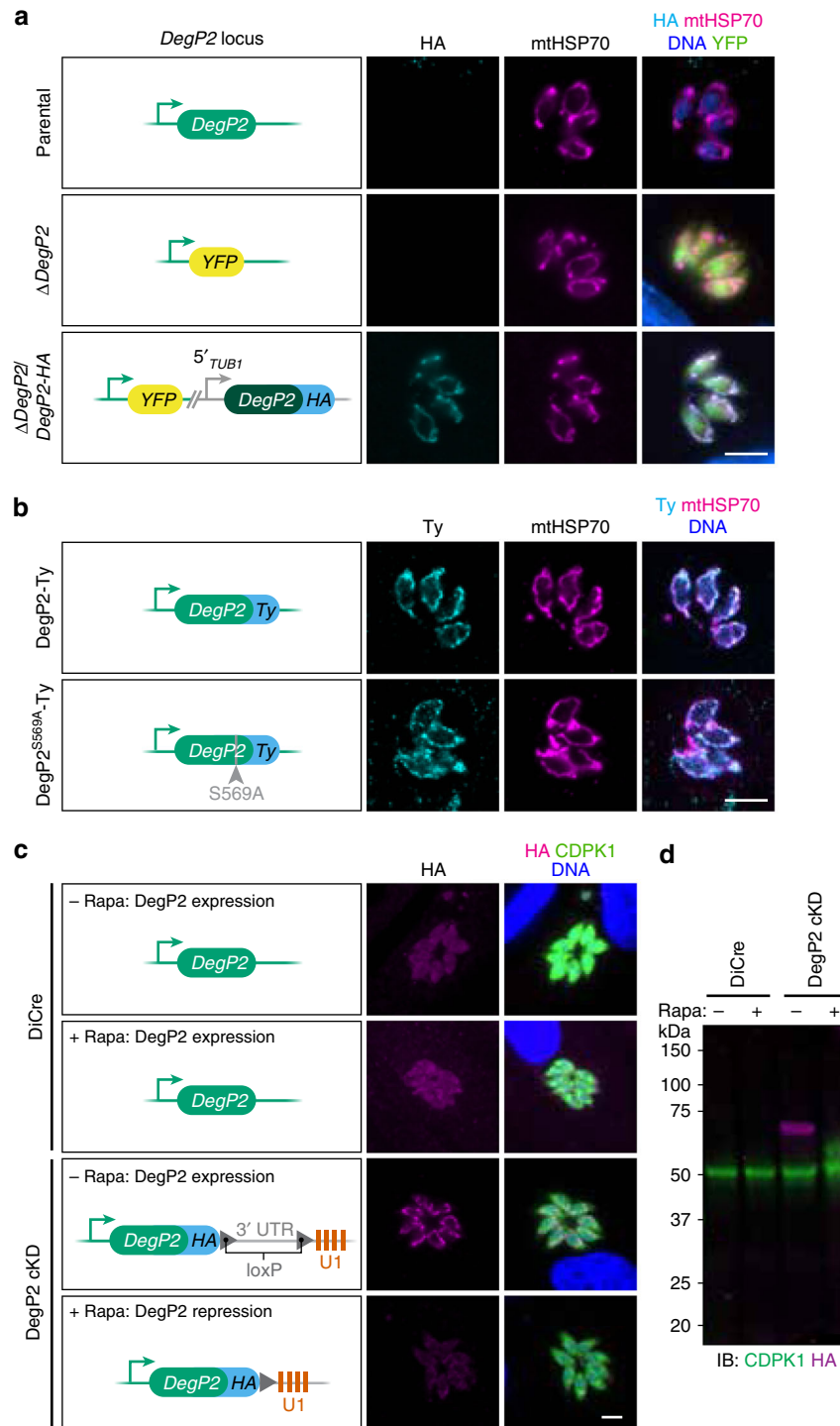


Fig. 4 Strains generated to study the function and localization of DegP2. **a, b** The *DegP2* coding sequence was replaced with *YFP* to generate the Δ *DegP2* line, which was subsequently complemented with an HA-tagged copy of *DegP2* (dark green) under the regulation of the *TUB1* promoter (**a**). Separately, the endogenous locus of *DegP2* was first tagged with the Ty epitope, and a point mutation was introduced at the catalytic serine (**b**). *DegP2*-HA, *DegP2*-Ty, and *DegP2*^{S569A}-Ty co-localized with the mitochondrial marker mtHSP70. Merged image additionally displays YFP (green) for Δ *DegP2* strains and DNA stain (blue) for the HA-stained samples. Scale bar is 5 μ m. **c** A *DegP2*-inducible mutant constructed using the U1 system. Staining for the HA tag appended to the *DegP2* cKD locus showed the expected localization of the protein to the mitochondrion. Individual parasites are visualized by staining for CDPK1. Scale bar is 5 μ m. **d** Immunoblotting for *DegP2*'s HA tag showed robust depletion of *DegP2* 48 h after a 2 h rapamycin treatment. CDPK1 was used as a loading control.

Discussion

Recent studies have shown that modulating hemoglobin import changes *P. falciparum*'s susceptibility to ART^{14,15}, and here we extend these results to show that heme biosynthesis plays a role in

T. gondii's susceptibility to this drug. Heme has long been thought to activate ART^{4,20,57,77}, and our results support the conclusion that heme abundance influences ART susceptibility. These observations help explain why blood-stage *P. falciparum*,

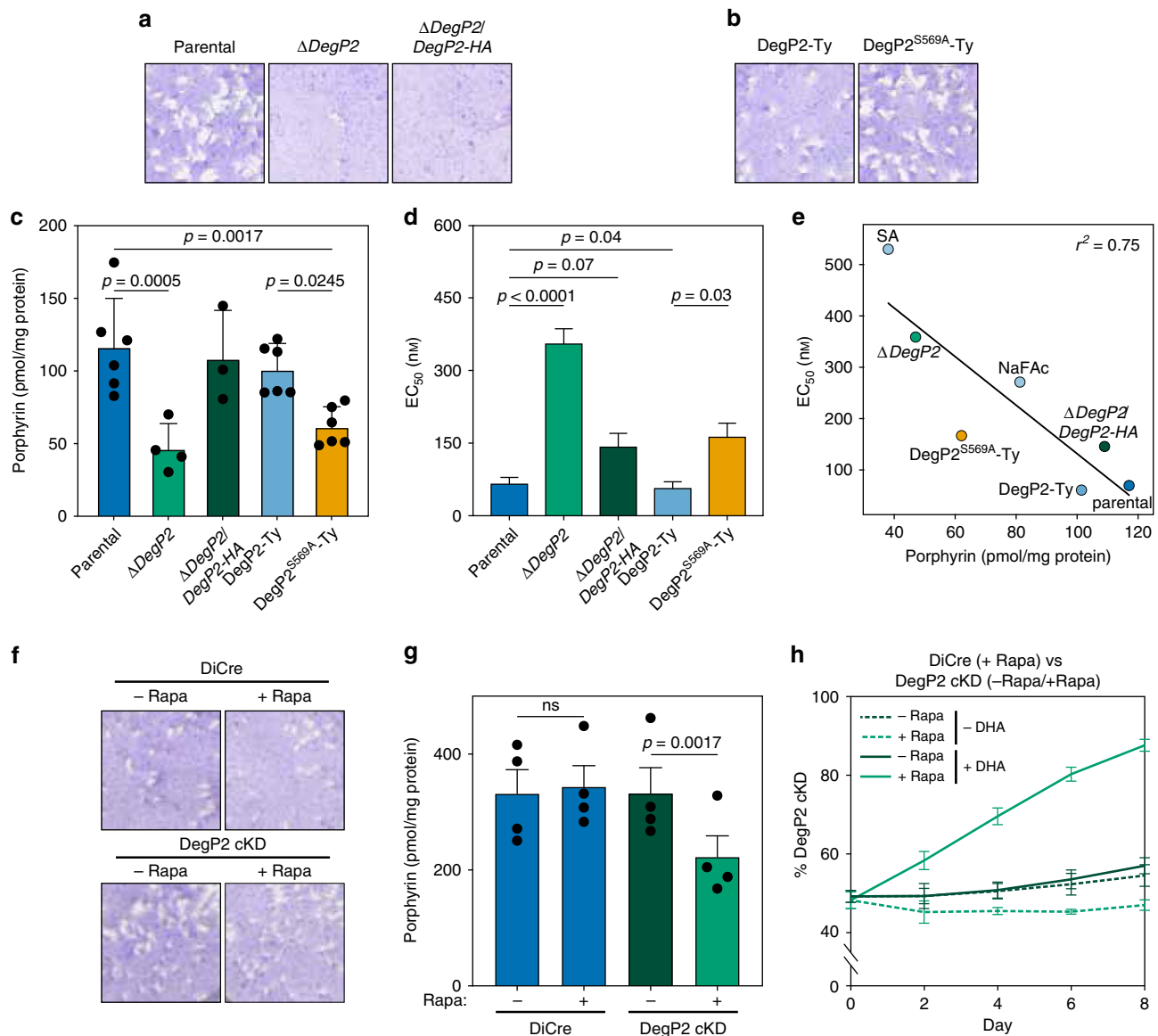


Fig. 5 Deletion of *DegP2* alters porphyrin concentrations and DHA susceptibility. **a** Δ *DegP2* and Δ *DegP2/DegP2-HA* parasites formed smaller plaques than their parental strains, indicating a growth defect. **b** Endogenously Ty-tagged *DegP2* (*DegP2-Ty*) parasites and a derived line bearing a mutation in the protease domain (*DegP2^{S569A-Ty}*) formed plaques normally. **c** Total porphyrin concentrations (pmol/mg protein) showing reduced porphyrin concentrations for both Δ *DegP2* and *DegP2^{S569A-Ty}* parasites. Results are mean \pm SD for $n = 3$ –4 independent experiments; p -values are from one-way ANOVA with Sidak's multiple comparison test. **d** DHA Mean EC_{50} values \pm SD were calculated by curve-fitting 4–7 independent experiments together. **e** Porphyrin levels show a negative correlation with DHA EC_{50} ($r^2 = 0.75$) in the strains and conditions tested. **f** *DegP2* cKD parasites formed plaques similarly to DiCre, both in the presence or absence of rapamycin. **g** Total porphyrin concentrations for DiCre and *DegP2* cKD in the presence or absence of rapamycin. Results are mean \pm SEM for $n = 4$ independent experiments; p -values are from a two-way ANOVA. **h** *DegP2* cKD parasites outcompeted DiCre parasites in the presence of DHA. The fraction of the population composed of mutant parasites was calculated at each time point by flow cytometry. Results are mean \pm SEM for $n = 3$ independent experiments.

releasing large amounts of heme from the digestion of hemoglobin, is more susceptible to ART than *T. gondii*^{78–80}. Interestingly, *Babesia* spp., which live within erythrocytes but do not take up hemoglobin, have an intermediate susceptibility to ART^{81,82}, while *Cryptosporidium parvum*—which lacks genes necessary for heme biosynthesis^{83,84} shows little response to ART⁸⁵.

T. gondii and *P. falciparum* differ in their reliance on de novo heme biosynthesis. Inhibiting heme biosynthesis either chemically⁵² or genetically^{34,86} reduces the fitness of *T. gondii*, highlighting the importance of de novo heme biosynthesis to this parasite. Modulation of heme biosynthesis in cancer cells has similarly been found to alter their susceptibility to ART⁵⁷. By

contrast, heme biosynthesis pathways are dispensable for *P. falciparum* growth during blood stages, although this pathway appears to be necessary during the mosquito stages^{87,88}. Although de novo heme synthesis is dispensable for blood-stage *P. falciparum*, the components of this pathway are still expressed, and studies using radiolabeled substrates for heme biosynthesis have shown that the process remains active^{89–91}. Our results indicate that there are important parallels between *T. gondii* and *P. falciparum* responses to DHA, despite *T. gondii*'s reduced susceptibility to such compounds. Our results also demonstrate the utility of CRISPR screens in identifying pathways that should be considered when designing ACTs.

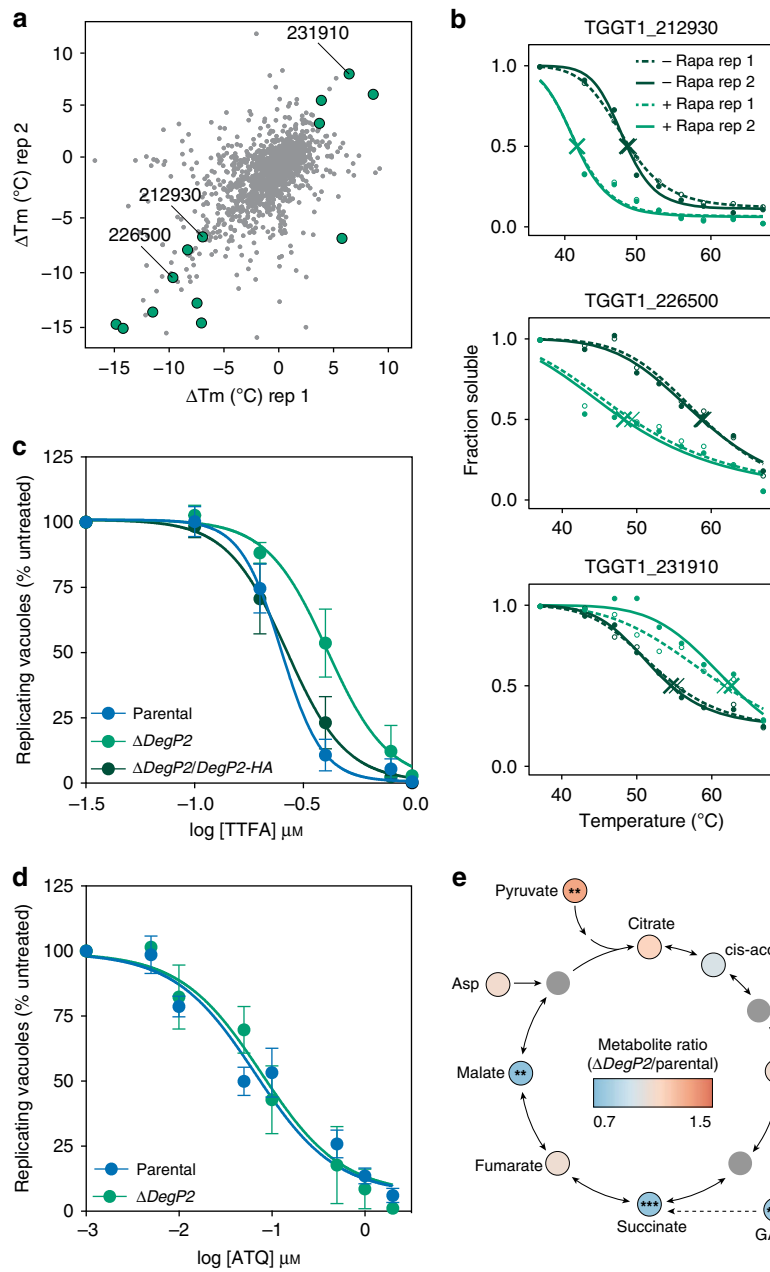


Fig. 6 DegP2 influences the intersection of heme biosynthesis, the TCA cycle, and the ETC. **a** TPP revealed that depleting DegP2 reliably changed the melting temperatures of 13 proteins (highlighted in green, $p < 0.2$ by z-test in each of two replicates). Three mitochondrial proteins are indicated by their gene IDs. **b** Melting curves for three mitochondrial proteins identified as hits by TPP. **c** Dose-response curve for parasites treated with the complex II inhibitor TTFA. Results are mean \pm SEM for $n = 4$ or 3 independent experiments, for the parental and Δ DegP2 or Δ DegP2/DegP2-HA strains, respectively. Δ DegP2 is significantly more resistant to TTFA compared to the parental; $p < 0.0001$ from extra-sum-of-squares F -test. **d** Dose-response curve for parasites treated for 5 h with increasing concentrations of atovaquone (ATQ). Results are mean \pm SEM for $n = 5$ or 3 independent experiments for the parental or Δ DegP2 strains, respectively. Both strains displayed similar susceptibility to ATQ; $p = 0.59$ from extra-sum-of-squares F -test. **e** Summary of changes in metabolites between parental and Δ DegP2 parasites in the TCA cycle and closely related pathways. Full results can be found in Supplementary Data 6. Asp aspartate, α -KG α -ketoglutarate, Gln glutamine, Glu, glutamate. Asterisks indicate significant change from parental, * $p < 0.05$, ** $p < 0.005$, *** $p < 0.0005$, by two-way ANOVA.

Mutations in *P. falciparum* K13, particularly K13^{C580Y}, are major determinants of ART susceptibility in the field. We now know that K13 helps mediate hemoglobin uptake, and that the C580Y mutation reduces DHA susceptibility by reducing protein abundance and limiting flux through this pathway^{14,15}. We constructed an analogous mutation in *T. gondii* K13, and found that this mutation also rendered *T. gondii* less susceptible to DHA. *T. gondii* ingests host cytosolic proteins⁹², and may take up host

heme or precursors at low levels through endocytosis. Some of *T. gondii*'s heme biosynthesis enzymes can be disrupted—although at a large fitness cost to the parasite^{86,93} further suggesting that parasites can scavenge intermediates from the host's heme biosynthetic pathway to sustain viability, but are insufficient for normal growth. It is therefore possible that K13 confers decreased DHA susceptibility through similar mechanisms in *T. gondii* and in *P. falciparum*. Alternatively, recent results show that K13 can

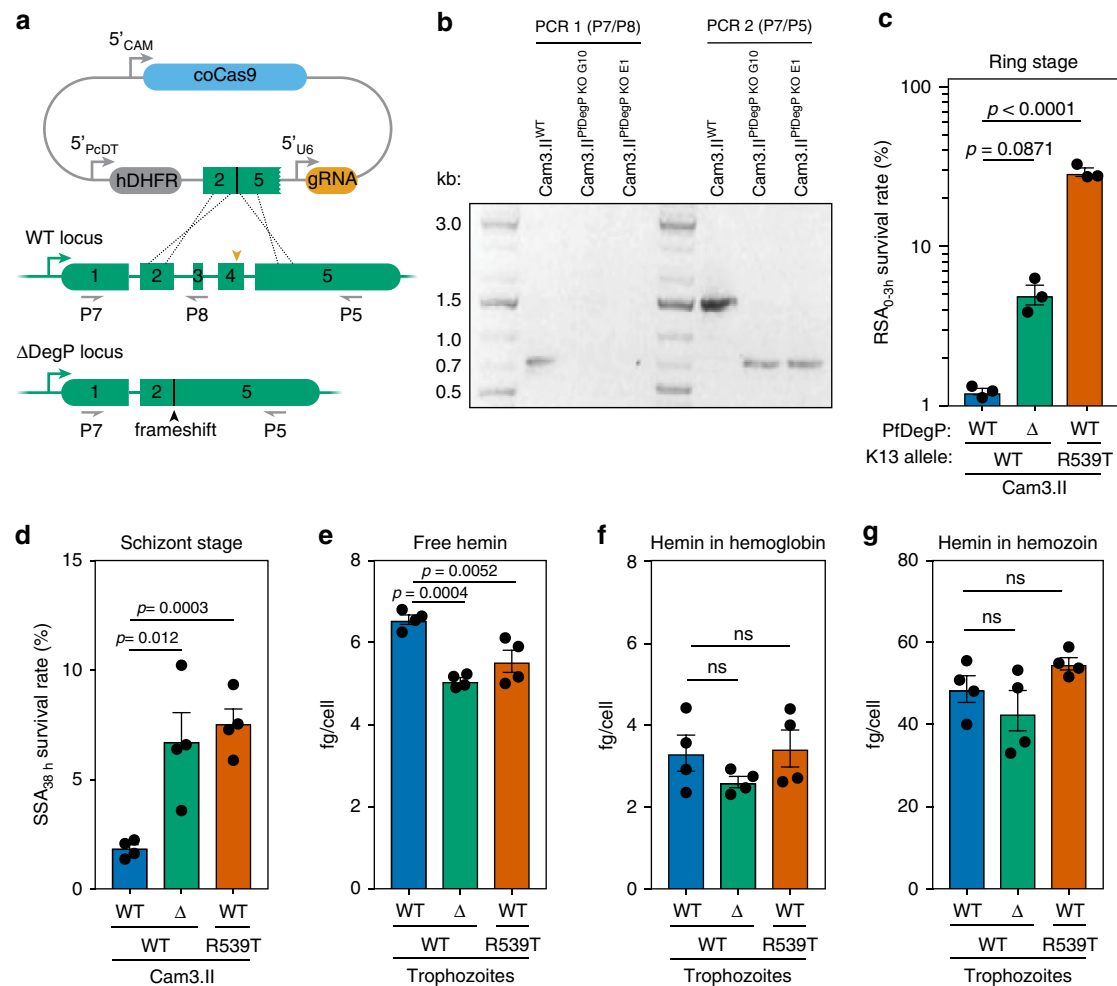


Fig. 7 Mutating the ortholog of *DegP2* in *P. falciparum* reduces susceptibility to DHA. **a** Diagram showing strategy to knockout *PfDegP* in the Cam3.II^{WT} background. **b** PCR confirmation of successful KO of *PfDegP*. PCR 1 (using primers P7 and 8) confirmed the loss of exons 3 and 4 in the two *DegP* KO clones; clone G10 was used for the remainder of this study. PCR 2 (using primers P7 and 5) demonstrated a shorter product upon successful deletion of two exons. **c** Ring-stage survival assay, performed as above, using the Cam3.II^{WT}, Cam3.II^{Δ*PfDegP*}, and the K13 mutant Cam3.II^{R539T} lines. Results are mean \pm SEM for $n = 3$ independent replicates; p -values derive from two-tailed, unpaired t -tests. **d** Schizont-stage survival assay following a 4 h pulse of 700 nM DHA. Results are mean \pm SEM for $n = 4$ independent replicates; p -values derived from two-tailed unpaired t -test. **e–g** Heme measured from the free (**e**), hemoglobin-associated (**f**), and hemozoin (**g**) pools from trophozoites for various strains. Heme concentrations were calibrated to a standard curve and normalized to the number of parasites per sample to calculate fg/cell. Results are mean \pm SD for $n = 4$ independent replicates; p -values from one-way ANOVA.

relocate to the *P. falciparum* mitochondrion upon DHA treatment, indicating that in addition to its role in hemoglobin import, K13 may also influence mitochondrial metabolism⁹⁴. Such alternative functions of K13 are more likely to influence K13's effect on DHA susceptibility in *T. gondii*, given that heme import appears to play a minor role in this parasite compared to biosynthesis.

CRISPR-based screens can identify sensitizing mutations, which may help design combinatorial therapies. Screening for mutants that enhanced susceptibility to a sublethal dose of DHA, we identified an ortholog of TMEM14C, which has been proposed to import porphyrins across the inner mitochondrial membrane of mammalian cells⁴⁸. Although we could not establish a direct role for Tmem14c as a porphyrin transporter and cannot formally exclude alternative roles in mitochondrial metabolism, several lines of evidence lead us to propose that Tmem14c transports heme out of the mitochondrion in *T. gondii*. First, perturbations that decrease heme production decrease DHA susceptibility instead of increasing it, as occurs from Tmem14c disruption. Second, Δ Tmem14c parasites are most susceptible to

DHA during replication, when increased mitochondrial activity and higher demands on heme production, and export are likely taking place⁵¹. Third, Δ Tmem14c parasites have altered levels of glycine, a substrate for heme biosynthesis, which could be explained by negative feedback from excess accumulation of heme in the mitochondrion. ALAS, the enzyme that utilizes glycine to perform the first committed step in heme biosynthesis, has been shown to be regulated by excess heme through a variety of mechanisms^{95,96}. Finally, the mechanism and substrate specificity of TMEM14C remain uncharacterized in mammalian cells, leaving open the possibility that TMEM14C might simply mediate passive transport of porphyrins down their concentration gradient. The predicted role of Tmem14c as a porphyrin transporter leads us to propose that changes in heme availability, through its accumulation in the mitochondrion, may influence the susceptibility of parasites to DHA^{97,98}.

Screening for mutants with decreased DHA susceptibility identified the serine protease DegP2, whose knockout contributed to the survival of *T. gondii* and *P. falciparum* parasites exposed to

DHA. In both species, the activity of DegP2 or PfDegP could be linked to decreased porphyrin concentrations, and in *P. falciparum*, we extended these results to show that levels of free heme were affected by mutating *PfDegP*. *PfDegP* complements its ortholog in *Escherichia coli*, implying broad functional conservation⁹⁹.

Using TPP, we uncovered three mitochondrial proteins that may interact with DegP2. One of these hits, TGGT1_212930, contains a NifU domain that in other organisms transfers nascent iron–sulfur clusters to client proteins^{100,101}. In yeast, these clients include the TCA cycle enzymes aconitase and SDH2 (SDHB in *T. gondii*)—the latter also part of complex II of the ETC⁷⁰. Bacteria and yeast use chaperones to transfer iron–sulfur clusters from NifU domain-containing proteins to their clients^{102–104}, raising the possibility that DegP2 fulfills a similar role in *T. gondii*. The complex II inhibitor TTFA^{71,72} has an altered EC₅₀ when DegP2 is disrupted, which is consistent with DegP2 interacting with the complex II component SDHB, through TGGT1_212930. While this manuscript was in preparation, a study performed using in vitro evolution found that *T. gondii* parasites with point mutations in *DegP2* had decreased ART susceptibility¹⁰⁵. Interestingly, these researchers also found that such parasites had altered mitochondrial DNA copy number, which in yeast, has been linked to changes in aconitase¹⁰⁶.

In addition to TGGT1_212930, our TPP results revealed that DegP2 influenced the stability of two other mitochondrial proteins: the mitochondrial ATP synthase γ subunit (TGGT1_231910), and a protein annotated as hypothetical (TGGT1_226500). The γ subunit is part of the central stalk around which other components of the ATP synthase complex rotate, to generate ATP¹⁰⁷. In other systems, Deg-family proteins play roles in the folding, maintenance, and turnover of integral membrane proteins, such as those involved in the ETC^{108–110}, and a similar phenomenon may explain the apparent association between DegP2 and this ATP synthase subunit. TGGT1_226500 has not been studied extensively, although a global analysis of protein localization predicts it is mitochondrial⁶⁹ and perhaps localized to one of the mitochondrial membranes based on the presence of a predicted transmembrane domain¹¹¹. Our studies place DegP2's function at the intersection of the TCA cycle, the ETC, and heme biosynthesis. Despite its pleiotropic effects, parasites can survive without DegP2 under standard growth conditions, albeit with lower porphyrin concentrations that render them less susceptible to DHA.

We wondered whether, analogously to the mutation of K13, disruption of DegP2 would decrease DHA susceptibility in both *T. gondii* and *P. falciparum*. We therefore disrupted the homolog of *DegP2* in *P. falciparum*, *PfDegP*. As in *T. gondii*, these parasites exhibited decreased porphyrin levels and reduced DHA susceptibility. Our results complement recent studies pointing to a role for hemoglobin import in modulating DHA susceptibility^{14,15}, and suggest that mitochondrial heme dynamics can also have a measurable impact on DHA susceptibility.

Despite critical metabolic differences and over 350 million years of divergent evolution¹¹², our screens identified multiple genes involved in heme biosynthesis, as critical determinants of DHA susceptibility in *T. gondii*, echoing the results of recent studies that demonstrate that hemoglobin import greatly affects *P. falciparum*'s response to ART^{14,15}. Although the two organisms strike drastically different balances between heme import and biosynthesis, the availability of free heme emerges as a limiting determinant of the susceptibility of parasites to ARTs. Our study highlights the power of genome-wide CRISPR screens to identify conserved mechanisms of drug susceptibility and resistance, and points to their potential use in developing novel therapeutics.

Methods

***T. gondii* maintenance and strain construction.** *T. gondii* tachyzoites were grown in human foreskin fibroblasts (HFFs) maintained at 37 °C with 5% CO₂ in D3 (Dulbecco's modified Eagle's medium (DMEM, Life Technologies, 11965118) supplemented with 3% heat-inactivated fetal bovine serum and 10 μ g/ml gentamicin (Sigma Aldrich, G1272)). When appropriate, chloramphenicol (Sigma Aldrich, C3175) was used at 40 μ M and pyrimethamine (Sigma Aldrich, 46706) at 3 μ M.

Parasite lines were constructed using CRISPR/Cas9-mediated gene editing as described previously¹¹³. The Cas9-encoding plasmid pU6-Universal is available from Addgene (#52694). Gibson Assembly¹¹⁴ was used to clone gRNAs into the BsaI sites in pU6-Universal using homology arms of approximately 20 base pairs. Epitope tags and point mutations were introduced by transfecting repair oligos, bearing 40 base pairs of homology with the genome on each end of the mutation or insertion, along with CRISPR machinery. Such repair oligos were often created by heating oligonucleotides encoding complementary single-stranded DNA to 99 °C for 2 min in duplex buffer (100 mM potassium acetate, 30 mM HEPES, pH 7.5), then allowing DNA to cool slowly to room temperature (RT) over the course of several hours.

K13^{C627Y} mutant parasites were constructed by transfecting pU6-Universal encoding the protospacer TTGCTCCTCTCACCCTCCG (oligos P1 and P2 in Supplementary Data 7) into Δ KU80 parasites along with a repair oligo constructed by hybridizing the oligos P3 and P4. Converting the TGC that encodes C627 to TAC eliminated an Itai site, and restriction digests were used to confirm this mutation. We also introduced a silent CGG to CGA mutation at R667 to eliminate the protospacer adjacent motif and prevent re-cleavage by Cas9 after the initial mutation. Clonal K13^{C627Y} lines were isolated, and the mutation was confirmed by sequencing the locus using primers P5 and P6.

Δ DegP2 parasites were constructed by co-transfecting Δ KU80 parasites with two copies of pU6-Universal encoding gRNAs with the sequences GCAGTCCCC AGCATGGTCCG (P7 and P8 in Supplementary Data 7) and GCGCTCACAGA CCTCGCTGG (P9 and P10) to cleave the 5' and 3' ends of the ORF, respectively. These cuts were repaired using a template encoding YFP flanked by 40 nucleotides of homology to the 5' and 3'-UTRs of *DegP2*, constructed by amplifying the fluorescence marker with P11 and P12. YFP-positive parasites were selected by FACS, and the insertion was confirmed by PCR and Sanger sequencing, using primers P13 and P14.

DegP2-Ty parasites were constructed by transfecting pU6-Universal carrying the gRNA sequence GCGCTCACAGACCTCGCTGG, together with hybridized P15 and P16, into the Δ KU80 strain. Clonal lines were isolated using limiting dilution, and those carrying the Ty tag were identified using immunofluorescence microscopy¹¹⁵.

Δ DegP2 was complemented by integrating the plasmid pDegP2-HA into an intergenic region at position 14,87,300 on chromosome VI. pDegP2-HA was constructed by amplifying *DegP2* from cDNA using the primers P17 and P18, and assembling it with a portion of pDsRed¹¹⁶ that was amplified using the primers P19 and P20. A 200 nucleotide region surrounding the integration locus, with an NheI site at its center, was cloned into the PstI site of the resulting plasmid. We co-transfected NheI-linearized pDegP2-HA with a Cas9-expressing plasmid carrying a gRNA with the sequence GCCGTTCTGTCTCAGATGC⁴⁶, then selected for integrants using 40 μ M chloramphenicol. Clonal populations carrying DegP2-HA were confirmed using immunofluorescence microscopy with a mouse anti-HA antibody.

DegP2^{S569A}-Ty parasites were constructed by transfecting DegP2-Ty parasites with pU6-Universal encoding a protospacer with the sequence GCCATTAATCCT GGCAACAG (oligos P21 and P22), and a repair oligo constructed by annealing P23 and P24. Positive clones were selected based on destruction of a HpyCH4III restriction site, and confirmed by PCR and Sanger sequencing using primers P23 and P24.

DegP2 cKD parasites were constructed by transfecting DiCre parasites¹¹⁷, with pU6-Universal carrying the gRNA GCGCTCACAGACCTCGCTGG (P9 and P10) along with a repair template encoding an HA tag followed by the *T. gondii* CDPK3 3'-UTR flanked by two loxP sites, and followed by four U1 recognition sites and a DHFR resistance cassette. This repair template was PCR amplified from a custom-built plasmid using the primers P46 and P47. Following selection with pyrimethamine, clonal lines were selected based on the presence of the HA tag.

Δ Tmem14c parasites were constructed by co-transfecting Δ KU80 parasites with two copies of pU6-Universal encoding gRNAs with the sequence TCGGATTGC TATCTGACCAA (oligos P27 and P28) and ACGTCTGATGCCAAGGGCAT (primers P29 and P30), to cleave the 5' and 3' ends of the ORF, respectively. These cuts were repaired using a PCR product encoding a *TUB1* promoter, mNeonGreen coding sequence, and the *SAG1* 3'-UTR. This sequence was amplified using the primers P31 and P32. mNeonGreen-positive parasites were selected by FACS, and the insertion was confirmed by PCR and Sanger sequencing, using the primers P33 and P34, P35 and P36, and P37 and P38.

Tmem14c-Ty parasites were created by randomly integrating a plasmid containing Tmem14c-ty into RH parasites. Through PCR and Sanger sequencing of cDNA, the gene model on ToxoDB was found to be incorrect. The stop codon is instead found at the start of exon 2, creating a product of 330 bp. This product was amplified from cDNA using the primers P36 and P39, and assembled into the pSAG1-GCaMP5 (ref. ¹¹⁸) backbone, in which the chloramphenicol-resistance

cassette was replaced with *DHFR*, in frame with a Ty tag between the *SAG1* promoter and 3'-UTR. Parasites were selected using pyrimethamine, cloned by limiting dilution and positive clones selected by immunofluorescence microscopy for the Ty tag.

DiCre/*tdTomato* parasites were constructed by integrating a *tdTomato* expression cassette into an intergenic region at position 1487300 on chromosome VI. DiCre parasites¹¹⁹ were co-transfected with a Cas9-expressing plasmid carrying a gRNA with the sequence GCCGTTCTGTCTCACGATGC⁴⁶ and a repair template encoding a *TUB1* promoter, *tdTomato* coding sequence, and the *DHFR* 3'-UTR, which was amplified from a custom-built plasmid using the primers P44 and P45. *tdTomato*-positive parasites were selected by FACS, and a clonal population was isolated using limiting dilution and confirmed by flow cytometry.

Pooled genome-wide screens. Genome-wide CRISPR screens were performed based on the previously published method³³. Briefly, 500 µg of gRNA library linearized with AseI was transfected into $\sim 4 \times 10^8$ Cas9-expressing parasites⁴⁶ divided between ten individual cuvettes. Parasites were allowed to infect 10×15 cm² plates of confluent HFFs, and the medium changed 24 h post infection to contain pyrimethamine and 10 µg/ml DNaseI. Parasites were passaged upon lysis (between 48–72 h post transfection) and selection continued for three passages. At this point, parasites with integrated gRNA plasmids were split into two pools and either treated with indicated concentrations of DHA or left untreated. Untreated parasites were passaged onto fresh HFFs every 2 days, while the medium on treated parasites was changed for fresh DHA at the same time point. After a further three passages of the untreated population, parasites were collected, counted, and gDNA was extracted, using a DNeasy blood and tissue kit (Qiagen). When parasites were not limiting (e.g., in the untreated sample) DNA was extracted from 1×10^8 parasites. When DHA was used for positive selection, DNA was extracted from all recovered parasites. Integrated gRNA constructs were amplified from 500 ng of extracted DNA, using the primers P40 and P41 in two independent reactions and pooled. The resulting libraries were sequenced on a HiSeq 2500 (Illumina) with single-end reads, using primers P42 and P43.

CRISPR screen data analysis. Sequencing reads were aligned to the gRNA library. The abundance of each gRNA was calculated and normalized to the total number of aligned reads. To determine the fitness effect of each guide under DHA across biological replicates, we made use of the MAGeCK algorithm⁴⁹. Hits were selected based on FDR of <0.1 in at least one biological replicate. Metabolic pathways analysis on hits was performed using ToxoDB¹²⁰ against KEGG and MetaCyc pathways, and the Bonferroni-adjusted *p*-value reported.

Compounds used with *T. gondii*. DHA (VWR, TCD3793) was prepared at 10 mM in DMSO as single-use aliquots and used at the indicated concentration. Hemin (Sigma Aldrich, H9039) was prepared at 10 mM in 0.5 M NaOH. 2-DG (Sigma Aldrich, D6134) was prepared fresh at 10 mM in D3 and used at a final concentration of 5 mM. SA (Sigma Aldrich, D1415) was prepared in PBS as 200 mM stocks and used at a final concentration of 10 mM. ALA (Sigma Aldrich, A3785) was prepared fresh in PBS at 200 mM and used at a final concentration of 200 µM. NaFAc (Fisher Scientific, ICN201080) was prepared at 1 M in water and used at a final concentration 500 µM. ATQ (Sigma Aldrich, A7986) was prepared at 27 mM in DMSO and used at the indicated concentration. TTFA (Sigma Aldrich, T27006) was prepared as 10 mM stocks in DMSO and used at the indicated concentrations. MitoTracker Deep Red FM (Life Technologies, M22426) was used at a final concentration of 50 nM. Oligomycin (EMD Millipore, 495455) was used at a final concentration of 20 µM. Pyrimethamine (Sigma Aldrich, 46706) was prepared in ethanol at 10 mM. ADP (A2754-100MG) was prepared at 100 mM in water. FCCP (Sigma Aldrich C2920) was prepared at 50 mM in DMSO.

Lytic assay. A total of 50,000 parasites per well were spun down onto HFFs grown in 96-well plates. After 1 or 24 h, the medium was removed and replaced with medium containing vehicle or drug, and parasites were incubated for the indicated time before the wells were washed, the medium replaced, and the monolayers incubated until 72 h.p.i. Monolayers were rinsed with PBS, fixed in 95% ethanol or 100% ice-cold methanol for 10 min, and stained with crystal violet (Sigma, C6158) stain (2% crystal violet, 0.8% ammonium oxalate, and 20% ethanol) for 5 min before washing excess dye with water and allowing to dry. Absorbance of wells was read at 570 nm and normalized to drug treated, uninfected wells. Each experiment was performed with three technical replicates, and results show the mean of at least four independent experiments.

Pulsed treatment assay. Extracellular parasites were incubated in a total volume of 100 µl D3 with DHA for the indicated time, spun down, and resuspended in 600 µl of pre-warmed D3 before aliquoting 200 µl of parasites to HFF monolayers on a clear-bottomed plate and incubating for 24 h. Wells were then fixed in 4% formaldehyde for 10 min and stained using rabbit anti-PCNA, and detected using anti-rabbit Alexa 549. Images were acquired using a Cytation 3 high content imager, and the number of vacuoles and parasite nuclei per vacuole were quantified using an automated ImageJ macro. Vacuoles of two or more parasites were considered to be alive, and the number of such vacuoles in drug-treated wells was

normalized to the number in untreated wells to quantify the lethality of drug treatment.

Porphyrin assay. Based on published methods⁵⁵, $\sim 5 \times 10^7$ freshly egressed parasites were passed through a 3 µm filter, washed once in 10 ml of PBS, then pelleted and resuspended in 50 µl of H₂O, and flash frozen in liquid nitrogen. A total of 20 µl of parasite lysate was then mixed with 200 µl of pre-warmed 1.5 M oxalic acid (Sigma Aldrich, 75688) and incubated in a thermocycler at 99°C for 30 min. The total volume was then transferred to a clear-bottomed plate and fluorescence was detected at 662 nm following excitation at 400 nm. Porphyrin levels were calculated from a standard curve prepared as above using hemin. Total porphyrin was normalized to protein concentration, as calculated by Bradford assay (BioRad, 5000201). Experiments were performed with two technical replicates, and results are representative of at least three independent experiments.

Immunofluorescence microscopy. Infected cells were fixed in 4% formaldehyde for 10 min, then permeabilized with 0.25% Triton X-100 for 8 min. Staining was performed with mouse anti-Ty¹¹⁵, rabbit anti-mtHSP70 (ref. ¹²¹), and mouse anti-HA (1:1000; Biologends 901513) and detected with Alexa-Fluor-labeled secondary antibodies (1:1,000; Thermo Fisher). Nuclei were stained with Hoechst 33258 (Santa Cruz, SC-394039) and coverslips were mounted in Prolong Diamond (Thermo Fisher, P36961). Images were acquired using an Eclipse Ti epifluorescence microscope (Nikon) using the NIS elements imaging software. FIJI¹²² was used for image analysis and Adobe Photoshop for image processing.

Plaque formation. A total of 500 parasites per well were used to analyze the effect of drug treatment or gene deletion over the course of 8 days. The monolayers were then rinsed with PBS, fixed in 95% ethanol or 100% ice-cold methanol for 10 min, and stained with crystal violet (2% crystal violet, 0.8% ammonium oxalate, and 20% ethanol) for 5 min.

MitoTracker analysis of Δ DegP2. Parasites were suspended at 1×10^7 parasites per ml in D3 with or without 30 µM oligomycin. After 15 min at 37°C, the samples were mixed 2:1 with MitoTracker (Thermo Fisher Scientific, M7512) in D3, bringing the final concentration of oligomycin to 20 µM and MitoTracker to 12.5 nM. Parasites were incubated at 37°C for an additional 30 min, then pelleted, and resuspended in Ringer's solution (115 mM NaCl, 3 mM KCl, 2 mM CaCl₂, 1 mM MgCl₂, 3 mM NaH₂PO₄, 10 mM HEPES, 10 mM glucose, and 1% FBS), before analysis by flow cytometry.

Extraction of polar metabolites for LC-MS analysis. Parasites were harvested from HFFs when approximately half the vacuoles were lysed and prepared as for transcriptomics. Parasite pellets were quenched in 300 µl ice-cold 75% ACN supplemented with 0.5 µM isotopically labeled amino acids (Cambridge Isotopes, MSK-A2-1.2), and kept at -20°C. To extract polar metabolites, samples were sonicated for ten cycles in a Bioruptor (Diagenode) at 4°C with 30 s on and 30 s off, then incubated at 4°C for 10 min. After a 10 min, 10,000 r.p.m. spin in a tabletop centrifuge (Eppendorf), the supernatant was collected and the pellet was washed with 100 µl 75% ACN and spun again. The supernatants from the two spins were combined. Extracted metabolites were dried in a CentriVap concentrator equipped with a cold trap (Labconco, Kansas City, MO) and reconstituted in an appropriate volume of 75% ACN (30–100 µl).

LC-MS targeted analysis for polar metabolites. Polar samples were treated for small-molecule LC-MS as previously described¹²³. MS data acquisition on a Q Exactive benchtop orbitrap mass spectrometer equipped with an Ion Max source and a HESI II probe, which was coupled to a Dionex UltiMate 3000 UPLC system (Thermo Fisher Scientific, San Jose, CA) and was performed in a range of *m/z* = 70–1000, with the resolution set at 70,000, the AGC target at 1×10^6 , and the maximum injection time (Max IT) at 20 ms. For TSIM scans, the resolution was set at 70,000, the AGC target was 1×10^5 , and the max IT was 250 ms. Relative quantitation of polar metabolites was performed with XCalibur QuanBrowser 2.2 (Thermo Fisher Scientific) and TraceFinder software (Thermo Fisher Scientific, Waltham, MA), using a 5 p.p.m. mass tolerance and referencing an in-house library of chemical standards. Pooled samples and fractional dilutions were prepared as quality controls and only those metabolites were taken for further analysis, for which the correlation between the dilution factor and the peak area read was >0.95 (high-confidence metabolites). Normalization for relative parasite amounts was based on the total integrated peak area values of high-confidence metabolites within an experimental batch after normalizing to the averaged factor from all mean-centered areas of the isotopically labeled amino acids internal standards. It is of note that normalizing to protein content by Bradford analysis or the sum of all area reads from high-confidence metabolites lead to similar results. The data were further Pareto transformed for MetaboAnalyst-based statistical or pathway analysis¹²⁴.

Immunoblotting. Parasites were lysed in 20 mM HEPES, 137 mM NaCl, 10 mM MgCl₂, 1% Triton X-100 supplemented with Halt protease inhibitors (Thermo

Fisher 78430). Proteins were separated by SDS-PAGE and transferred to nitrocellulose membranes. CDPK1 was probed using a custom-made antibody¹²⁵ (1:20,000) and HA using mouse anti-HA (1:5000; Biogenders 901513).

Competition assays. DiCre/*tdTomato* and Degr2 cKD parasites were subjected to a 2-h treatment with 50 nM rapamycin or vehicle control 3 days prior to beginning competition assays. Rapamycin-treated DiCre/*tdTomato* parasites were then mixed with either treated or untreated Degr2 cKD parasites in a 1:1 ratio, and cultured in the presence of 0.5 μ M DHA or vehicle control. The population compositions were monitored every 2 days using a MACSQuant flow cytometer.

TPP sample preparation. For the purpose of processing biological replicates, parasites were grown in heavy (Lys8/Arg10) and light SILAC media for three passages prior to harvest. Between the second and third passage, intracellular parasites were treated with 50 nM rapamycin or vehicle control for 2 h. Two 15-cm dishes per treatment were harvested and passed through 0.2 μ m filters (EMD Millipore). The parasites were spun at 1000 \times g for 10 min at RT, were washed in 1 ml TPP buffer (142 mM KCl, 1 mM MgCl₂, 5.6 mM glucose, and 25 mM HEPES), and were spun again at 1000 \times g for 10 min at RT. The parasite pellet was resuspended in 1.2 ml TPP buffer, and 100 μ l was aliquoted into PCR-strip tubes. Parasites were heated at 37, 43, 47, 50, 53, 56, 59, 63, and 67 °C for 3 min using the gradient function on two 48-well thermal cyclers (BioRad). The tubes were placed on ice, and the parasites were combined with 20 μ l of 6 \times lysis buffer to a final concentration of 1% IGEAL CA-680, 1 \times Halt protease and phosphatase inhibitors, and 250 U/ml benzonase in TPP buffer. Lysates were spun at 100,000 \times g for 20 min in a TLA-100 rotor with a Beckman Ultra MAX ultracentrifuge. The concentration of soluble protein in the supernatant in the 37 °C samples was quantified with a DC Protein Assay (BioRad) by comparison to a standard curve of bovine serum albumin.

Protein digestion and peptide labeling. A volume corresponding to 50 μ g of protein from the 37 °C heavy and light SILAC sample was combined, for 100 μ g total. Equivalent volumes from the remaining temperatures were similarly pooled. Samples were reduced with 5 mM TCEP for 10 min at 55 °C, and were alkylated with 15 mM MMTS for 10 min at RT. The samples were desalted and cleared of detergent using the SP3 protocol¹²⁶. Proteins were digested at a 1:50 trypsin:protein ratio in 50 mM HEPES pH 8.5 overnight at 37 °C. Peptides were eluted and quantified using the Pierce Fluorometric Peptide Assay, and 50 μ g of peptides from the 37 °C sample and the equivalent volume from the remaining temperatures were labeled with TMT10plex at a 1:2 peptide:tag ratio according to manufacturer's instructions (Thermo Fisher Scientific). Labeled peptides from one treatment condition were pooled and desalted with a SepPak Light (Waters), eluted in 40% acetonitrile, 0.1% acetic acid, and lyophilized. Peptides were fractionated offline via reversed-phase high-performance liquid chromatography using Shimadzu LC-20AD pumps and a 10 cm \times 2.1 mm column packed with 2.6 μ m Aeris PEPTIDE XB-C18 media (Phenomenex). The gradient was isocratic 1% A buffer (20 mM ammonium formate, pH 10 in water) for 1 min at 150 μ l/min with increasing B buffer (100% acetonitrile) concentrations to 16.7% B at 20.5 min, 30% B at 31 min, and 45% B at 36 min. Fractions were collected with a FRC-10A fraction collector, and 15 samples were lyophilized for analysis.

LC-MS/MS data acquisition. Each fraction was resuspended in 0.1% formic acid and analyzed on an Orbitrap Q Exactive HF-X mass spectrometer in positive ion mode connected to an EASY-nLC chromatography system, using 0.1% formic acid as solvent A and 80% acetonitrile, 0.1% formic acid as solvent B (Thermo Fisher Scientific). Peptides were separated at 3 μ l/min on a gradient of 6–21% B for 41 min, 21–36% B for 20 min, 36–50% B for 10 min, and 50–100% B over 15 min. Full-scan spectra were acquired in profile mode with a scan range of 375–1400 m/z , resolution of 120,000, maximum fill time of 50 ms, and AGC target of 3E6 with a 15-s dynamic exclusion window. Precursors were isolated with 0.8 m/z window and fragmented with a NCE of 32. The top 20 MS2 spectra were acquired over a scan range of 350–1500 m/z with a resolution of 45,000, AGC target of 1E5, maximum fill time of 120 ms, and first fixed mass of 100 m/z . Raw data files have been deposited to the ProteomeXchange Consortium via the PRIDE partner repository^{127,128} with the dataset identifier PXD019917.

Protein MS data analysis. Peak lists and protein IDs were generated in Proteome Discoverer 2.2 using Sequest HT (Thermo Fisher Scientific) and the Toxodb-45 protein database (Toxodb.org). The search included the following posttranslational modifications for light samples: dynamic phospho/+79.966 Da (S, T, Y), dynamic oxidation/+15.995 Da (M), dynamic acetyl/+42.011 Da (N-terminus), dynamic TMT6plex/+229.163 Da (any N-terminus), dynamic TMT6plex/+229.163 Da (K), and static methylthio/+45.988 Da (C); and the following post-translational modifications for heavy samples: dynamic phospho/+79.966 Da (S, T, Y), dynamic oxidation/+15.995 Da (M), dynamic acetyl/+42.011 Da (N-terminus), dynamic TMT6plex/+229.163 Da (any N-terminus), dynamic Lys8-TMT6plex/+237.177 Da (N-terminus), static Lys8-TMT6plex/+237.177 Da (K), static label:13 C(6)15 N(4)/+10.008 Da (R), and static methylthio/+45.988 Da (C). Reporter ion intensities and ratios were quantified for unique peptides with a strict

1% FDR, co-isolation threshold of 50%, and S/N of 5. Protein abundance relative to the sample heated to 37 °C were used as input to the TPP R package⁶⁶. Input and output data are provided in Supplementary Data 5.

P. falciparum maintenance and strain construction. *P. falciparum* asexual blood-stage parasites were cultured in human erythrocytes (3% hematocrit) and RPMI-1640 medium supplemented with 2 mM L-glutamine, 50 mg/l hypoxanthine, 25 mM HEPES, 0.225% NaHCO₃, 10 mg/l gentamycin, and 0.5% (w/v) Albumax II (Invitrogen). Parasites were maintained at 37 °C in 5% O₂, 5% CO₂, and 90% N₂. Cultures were stained with Giemsa, monitored by blood smears fixed in methanol, and viewed by light microscopy.

Transfections were performed by electroporating ring-stage parasites at 5–10% parasitemia with 50 μ g of purified circular plasmid DNA resuspended in Cytomix¹²⁹. One day after electroporation, parasites were exposed to 2.5 nM WR99210 for 6 days to select for transformed parasites. Parasite cultures were monitored by microscopy for up to 6 weeks post electroporation, and recrudescence parasites were screened for editing by PCR. Positively edited bulk cultures were cloned by limiting dilution in 96-well plates, and flow cytometry was used to screen for positive parasites after 17–20 days. Parasites were stained with 1 \times SYBR Green (ThermoFisher) and 100 nM MitoTracker Deep Red (Invitrogen), and detected using an Accuri C6 flow cytometer (Becton Dickinson¹³⁰).

To generate the knockout construct for the serine protease *PfDegr* (PF3D7_0807700) a donor sequence (834 bp total) was synthesized (Genewiz) fusing homology regions located in exon 2 (HR1) and exon 5 (HR2), with the addition of one nucleotide to introduce a frameshift in exon 5. The donor fragment was cloned into the pDC2 plasmid¹³¹ by amplifying with primers p15 and p16 (Supplementary Data 7) using the restriction sites EcoRI and AatII. The pDC2 plasmid¹³² contains a codon-optimized Cas9 sequence under the regulatory control of the 5' calmodulin (PF3D7_1434200) promoter and the 3' *hsp86* (PF3D7_0708500) terminator, as well as the human *DHFR* (*hDHFR*) selectable marker that mediates resistance to the antiparasitodal agent WR99210 (Jacobus Pharmaceuticals). Two gRNA sequences (Supplementary Data 7) located in exon 4 were selected using chopchop¹³³ and cloned into pDC2 using an In-Fusion cloning kit (Takara Bio USA, Inc.). The final constructs pDC2-coCas9-*PfDegrPKO-hDHFR* were transfected into Cam3.II^{WT} parasites as described above. Primers for diagnostic PCRs, as well as sequencing primers are shown in Fig. 6b and listed in Supplementary Data 7.

Schizont-stage and ring-stage survival assays (SSA_{38h} and RSA_{0-3h}). These assays were carried out as previously described⁴³, with minor modifications. In brief, parasite cultures were synchronized one to two times using 5% sorbitol (Fisher). Drug was maintained throughout the assay until assessment of parasite growth. Synchronized schizonts were incubated in RPMI-1640 containing 15 units/ml sodium heparin for 15 min at 37 °C to disrupt agglutinated erythrocytes, then concentrated over a gradient of 75% Percoll (Fisher) and washed once in RPMI-1640. For the schizont-stage survival assay the concentrated schizonts were counted and seeded at 0.3% parasitemia followed by a 4 h exposure to 700 nM DHA or 0.1% DMSO (vehicle control). For the ring-stage survival assay purified schizonts were incubated for 3 h with fresh red blood cells, to allow time for merozoite invasion. Cultures were subjected again to sorbitol treatment to eliminate remaining schizonts. A total of 0–3 h post invasion rings were adjusted to 1% parasitemia and 2% hematocrit, and exposed to 700 nM DHA or 0.1% DMSO (vehicle control) for 4 h. Cells were washed to remove drug and returned to standard culture conditions for an additional 66 h. Parasite growth in each well was assessed using flow cytometry. Between 60,000 and 100,000 events were captured for each well. After 72 h, cultures generally expanded to 3–5% parasitemia in DMSO-treated controls. Percent survival of DHA-treated parasites was calculated relative to the corresponding DMSO-treated control.

Cellular heme fractionation assay. Heme fractionation was performed based on previously described methods^{75,76}. Briefly, sorbitol-synchronized early ring-stage parasites (<5 h post invasion) were incubated at 5% parasitemia and 2% hematocrit. Trophozoites were harvested at 20 h post incubation. Red blood cells were lysed with 0.05% saponin followed by multiple washes with PBS to remove traces of hemoglobin. The pellet was then resuspended in PBS and cell number quantified by flow cytometry. The remaining parasites were then lysed using hypotonic stress and sonication. Following centrifugation at 3600 r.p.m. for 20 min at RT, treatment with 0.2 M HEPES buffer (pH 7.4), 4% SDS (w/v), 0.3 M NaCl, 25% pyridine, 0.3 M NaOH, 0.3 M HCl, and distilled water, the fractions corresponding to hemoglobin, free heme, and hemozoin were recovered as solution. The UV-visible spectrum of each heme fraction as a Fe(III)heme-pyridine complex was measured using a multi-well plate reader (Spectramax 340PC; Molecular Devices). The total amount of each heme species was quantified using a standard curve prepared from a standard solution of porcine hematin (Sigma Aldrich) serially diluted in the same solvents used to process the pellets. The mass of each heme species in femtogram per cell (fg/cell) was then calculated by dividing the total amount of each heme species by the corresponding number of parasites. Statistical comparisons were made using one-way ANOVA (GraphPad Software Inc., La Jolla, CA, USA).

Statistics and reproducibility. All biological replicates were performed with independently derived parasite populations. Continuous variable data were presented as the mean \pm SD unless indicated. Where indicated, statistical tests were performed on raw data, prior to normalization. The significance of differences was assessed by unpaired, two-tailed Student's *t*-test. A one- or two-way ANOVA followed by Sidak's or Dunnett's multiple comparison tests were used where appropriate when the mean values of more than three groups were compared. *P*-values of <0.05 were defined as significant. All statistical analyses were performed and visualized by GraphPad Prism 8 (GraphPad Software Inc., La Jolla, CA, USA). Tables and results were visualized in Excel (Microsoft). All representative experiments were performed at least twice with comparable results.

Reporting summary. Further information on research design is available in the Nature Research Reporting Summary linked to this article.

Data availability

CRISPR screening raw data are available through the Gene Expression Omnibus with the accession number [GSE153785](https://www.ncbi.nlm.nih.gov/geo/query/acc.cgi?acc=GSE153785). Minimally processed CRISPR screen data are available in Supplementary Data 1. Raw thermal proteome profiling data are available through the ProteomeXchange Consortium via the PRIDE partner repository¹²⁷ with the dataset identifier [PXD019917](https://www.ebi.ac.uk/pride/archive/projects/PXD019917). Minimally processed thermal proteome profiling data is available in Supplementary Data 5. Additional data is available from the authors upon request. *T. gondii* genome information can be found in [ToxoDB](https://toxodb.org/). Source data are provided with this paper.

Code availability

All software used in this study is commercially available or sourced from cited publications.

Received: 4 September 2019; Accepted: 3 September 2020;

Published online: 23 September 2020

References

- Tilley, L., Straimer, J., Gnädig, N. F., Ralph, S. A. & Fidock, D. A. Artemisinin action and resistance in *Plasmodium falciparum*. *Trends Parasitol.* **32**, 682–696 (2016).
- Konstat-Korzenny, E., Ascencio-Aragón, J. A., Niezen-Lugo, S. & Vázquez-López, R. Artemisinin and its synthetic derivatives as a possible therapy for cancer. *Med. Sci.* **6**, 19 (2018).
- Meshnick, S. R., Thomas, A., Ranz, A., Xu, C. M. & Pan, H. Z. Artemisinin (qinghaosu): the role of intracellular hemozoin in its mechanism of antimalarial action. *Mol. Biochem. Parasitol.* **49**, 181–189 (1991).
- Wang, J. et al. Haem-activated promiscuous targeting of artemisinin in *Plasmodium falciparum*. *Nat. Commun.* **6**, 10111 (2015).
- Ismail, H. M. et al. Artemisinin activity-based probes identify multiple molecular targets within the asexual stage of the malaria parasites *Plasmodium falciparum* 3D7. *Proc. Natl Acad. Sci. USA* **113**, 2080–2085 (2016).
- Hartwig, C. L. et al. Accumulation of artemisinin trioxane derivatives within neutral lipids of *Plasmodium falciparum* malaria parasites is endoperoxide-dependent. *Biochem. Pharmacol.* **77**, 322–336 (2009).
- Heller, L. E., Goggins, E. & Roepke, P. D. Dihydroartemisinin–ferriprotoporphyrin IX adduct abundance in *Plasmodium falciparum* malarial parasites and the relationship to emerging artemisinin resistance. *Biochemistry* **57**, 6935–6945 (2018).
- Dondorp, A. M. et al. Artemisinin resistance in *Plasmodium falciparum* malaria. *N. Engl. J. Med.* **361**, 455–467 (2009).
- Noedl, H. et al. Evidence of artemisinin-resistant malaria in western Cambodia. *N. Engl. J. Med.* **359**, 2619–2620 (2008).
- van der Pluijm, R. W. et al. Determinants of dihydroartemisinin-piperazine treatment failure in *Plasmodium falciparum* malaria in Cambodia, Thailand, and Vietnam: a prospective clinical, pharmacological, and genetic study. *Lancet Infect. Dis.* **19**, 952–961 (2019).
- White, N. J. et al. Malaria. *Lancet* **383**, 723–735 (2014).
- Ariey, F. et al. A molecular marker of artemisinin-resistant *Plasmodium falciparum* malaria. *Nature* **505**, 50–55 (2014).
- Straimer, J. et al. Drug resistance. K13-propeller mutations confer artemisinin resistance in *Plasmodium falciparum* clinical isolates. *Science* **347**, 428–431 (2015).
- Yang, T. et al. Decreased K13 abundance reduces hemoglobin catabolism and proteotoxic stress, underpinning artemisinin resistance. *Cell Rep.* **29**, 2917–2928.e5 (2019).
- Birnbaum, J. et al. A Kelch13-defined endocytosis pathway mediates artemisinin resistance in malaria parasites. *Science* **367**, 51–59 (2020).
- Demas, A. R. et al. Mutations in *Plasmodium falciparum* actin-binding protein coronin confer reduced artemisinin susceptibility. *Proc. Natl Acad. Sci. USA* **115**, 12799–12804 (2018).
- Henriques, G. et al. Artemisinin resistance in rodent malaria-mutation in the AP2 adaptor μ -chain suggests involvement of endocytosis and membrane protein trafficking. *Malar. J.* **12**, 118 (2013).
- Rocamora, F. et al. Oxidative stress and protein damage responses mediate artemisinin resistance in malaria parasites. *PLoS Pathog.* **14**, e1006930 (2018).
- Henrici, R. C. et al. The Plasmodium falciparum Artemisinin Susceptibility-Associated AP-2 Adaptor μ Subunit is Clathrin Independent and Essential for Schizont Maturation. *mBio.* **11**, e02918–19 (2020).
- Xie, S. C. et al. Haemoglobin degradation underpins the sensitivity of early ring stage *Plasmodium falciparum* to artemisinins. *J. Cell Sci.* **129**, 406–416 (2016).
- Dogovski, C. et al. Targeting the cell stress response of *Plasmodium falciparum* to overcome artemisinin resistance. *PLoS Biol.* **13**, e1002132 (2015).
- Mok, S. et al. Drug resistance. Population transcriptomics of human malaria parasites reveals the mechanism of artemisinin resistance. *Science* **347**, 431–435 (2015).
- Breglio, K. F. et al. A single nucleotide polymorphism in the *Plasmodium falciparum* atg18 gene associates with artemisinin resistance and confers enhanced parasite survival under nutrient deprivation. *Malar. J.* **17**, 391 (2018).
- Mbengue, A. et al. A molecular mechanism of artemisinin resistance in *Plasmodium falciparum* malaria. *Nature* **520**, 683–687 (2015).
- Mukherjee, A. et al. Artemisinin resistance without pfkelch13 mutations in *Plasmodium falciparum* isolates from Cambodia. *Malar. J.* **16**, 195 (2017).
- Sutherland, C. J. et al. pfk13-independent treatment failure in four imported cases of *Plasmodium falciparum* malaria treated with artemether-lumefantrine in the United Kingdom. *Antimicrob. Agents Chemother.* **61**, e02382 (2017).
- Berens, R. L., Krug, E. C., Nash, P. B. & Curiel, T. J. Selection and characterization of *Toxoplasma gondii* mutants resistant to artemisinin. *J. Infect. Dis.* **177**, 1128–1131 (1998).
- Reynolds, M. G., Oh, J. & Roos, D. S. In vitro generation of novel pyrimethamine resistance mutations in the *Toxoplasma gondii* dihydrofolate reductase. *Antimicrob. Agents Chemother.* **45**, 1271–1277 (2001).
- Cowell, A. N. et al. Mapping the malaria parasite druggable genome by using in vitro evolution and chemogenomics. *Science* **359**, 191–199 (2018).
- Shalem, O. et al. Genome-scale CRISPR-Cas9 knockout screening in human cells. *Science* **343**, 84–87 (2014).
- Hou, P. et al. A genome-wide CRISPR screen identifies genes critical for resistance to FLT3 inhibitor AC220. *Cancer Res.* **77**, 4402–4413 (2017).
- Shi, C.-X. et al. CRISPR genome-wide screening identifies dependence on the proteasome subunit PSMC6 for bortezomib sensitivity in multiple myeloma. *Mol. Cancer Ther.* **16**, 2862–2870 (2017).
- Sidik, S. M., Huet, D. & Lourido, S. CRISPR-Cas9-based genome-wide screening of *Toxoplasma gondii*. *Nat. Protoc.* **13**, 307–323 (2018).
- Sidik, S. M. et al. A genome-wide CRISPR screen in *Toxoplasma* identifies essential apicomplexan genes. *Cell* **166**, 1423–1435.e12 (2016).
- Radke, J. B., Burrows, J. N., Goldberg, D. E. & Sibley, L. D. Evaluation of current and emerging antimalarial medicines for inhibition of *Toxoplasma gondii* growth in vitro. *ACS Infect. Dis.* **4**, 1264–1274 (2018).
- Nagamune, K., Moreno, S. N. J. & Sibley, L. D. Artemisinin-resistant mutants of *Toxoplasma gondii* have altered calcium homeostasis. *Antimicrob. Agents Chemother.* **51**, 3816–3823 (2007).
- Dunay, I. R., Chan, W. C., Haynes, R. K. & Sibley, L. D. Artemisone and artemiside control acute and reactivated toxoplasmosis in a murine model. *Antimicrob. Agents Chemother.* **53**, 4450–4456 (2009).
- Touquet, B. et al. High-content imaging assay to evaluate *Toxoplasma gondii* infection and proliferation: A multiparametric assay to screen new compounds. *PLoS ONE* **13**, e0201678 (2018).
- Montoya, J. G. & Liesenfeld, O. Toxoplasmosis. *Lancet* **363**, 1965–1976 (2004).
- Parapini, S., Olliaro, P., Navaratnam, V., Taramelli, D. & Basilio, N. Stability of the antimalarial drug dihydroartemisinin under physiologically relevant conditions: implications for clinical treatment and pharmacokinetic and in vitro assays. *Antimicrob. Agents Chemother.* **59**, 4046–4052 (2015).
- Ghorbal, M. et al. Genome editing in the human malaria parasite *Plasmodium falciparum* using the CRISPR-Cas9 system. *Nat. Biotechnol.* **32**, 819–821 (2014).
- Wang, Z. et al. Artemisinin resistance at the China-Myanmar border and association with mutations in the K13 propeller gene. *Antimicrob. Agents Chemother.* **59**, 6952–6959 (2015).
- Witkowski, B. et al. Novel phenotypic assays for the detection of artemisinin-resistant *Plasmodium falciparum* malaria in Cambodia: in-vitro and ex-vivo drug-response studies. *Lancet Infect. Dis.* **13**, 1043–1049 (2013).

44. Klonis, N. et al. Altered temporal response of malaria parasites determines differential sensitivity to artemisinin. *Proc. Natl Acad. Sci. USA* **110**, 5157–5162 (2013).
45. Radke, J. R. et al. Defining the cell cycle for the tachyzoite stage of *Toxoplasma gondii*. *Mol. Biochem. Parasitol.* **115**, 165–175 (2001).
46. Markus, B. M., Bell, G. W., Lorenzi, H. A. & Lourido, S. Optimizing systems for Cas9 expression in *Toxoplasma gondii*. *mSphere* **4**, e00386 (2019).
47. Zimmermann, L. et al. A completely reimplemented MPI bioinformatics toolkit with a new HHpred server at its core. *J. Mol. Biol.* **430**, 2237–2243 (2018).
48. Yien, Y. Y. et al. TMEM14C is required for erythroid mitochondrial heme metabolism. *J. Clin. Investig.* **124**, 4294–4304 (2014).
49. Li, W. et al. MAGeCK enables robust identification of essential genes from genome-scale CRISPR/Cas9 knockout screens. *Genome Biol.* **15**, 554 (2014).
50. Astner, I. et al. Crystal structure of 5-aminolevulinate synthase, the first enzyme of heme biosynthesis, and its link to XLSA in humans. *EMBO J.* **24**, 3166–3177 (2005).
51. MacRae, J. I. et al. Mitochondrial metabolism of glucose and glutamine is required for intracellular growth of *Toxoplasma gondii*. *Cell Host Microbe* **12**, 682–692 (2012).
52. Shanmugam, D., Wu, B., Ramirez, U., Jaffe, E. K. & Roos, D. S. Plastid-associated porphobilinogen synthase from *Toxoplasma gondii*: kinetic and structural properties validate therapeutic potential. *J. Biol. Chem.* **285**, 22122–22131 (2010).
53. Huet, D., Rajendran, E., van Dooren, G. G. & Lourido, S. Identification of cryptic subunits from an apicomplexan ATP synthase. *Elife* **7**, e38097 (2018).
54. Blume, M. et al. Host-derived glucose and its transporter in the obligate intracellular pathogen *Toxoplasma gondii* are dispensable by glutaminolysis. *Proc. Natl Acad. Sci. USA* **106**, 12998–13003 (2009).
55. Sinclair, P. R., Gorman, N. & Jacobs, J. M. Measurement of heme concentration. *Curr. Protoc. Toxicol.* **00**, 8.3.1–8.3.7 (1999).
56. Fujiwara, T. et al. Exploring the potential usefulness of 5-aminolevulinic acid for X-linked sideroblastic anemia. *Blood* **124**, 215–215 (2014).
57. Zhang, S. & Gerhard, G. S. Heme mediates cytotoxicity from artemisinin and serves as a general anti-proliferation target. *PLoS ONE* **4**, e7472 (2009).
58. Sigala, P. A., Crowley, J. R., Henderson, J. P. & Goldberg, D. E. Deconvoluting heme biosynthesis to target blood-stage malaria parasites. *Elife* **4**, e09143 (2015).
59. Lentini, G. et al. Characterization of *Toxoplasma* DegP, a rohoptry serine protease crucial for lethal infection in mice. *PLoS ONE* **12**, e0189556 (2017).
60. Carter, P. & Wells, J. A. Dissecting the catalytic triad of a serine protease. *Nature* **332**, 564–568 (1988).
61. Hedstrom, L. Serine protease mechanism and specificity. *Chem. Rev.* **102**, 4501–4524 (2002).
62. Sun, R. et al. Crystal structure of *Arabidopsis* Deg2 protein reveals an internal PDZ ligand locking the hexameric resting state. *J. Biol. Chem.* **287**, 37564–37569 (2012).
63. Pieperhoff, M. S. et al. Conditional UI gene silencing in *Toxoplasma gondii*. *PLoS ONE* **10**, e0130356 (2015).
64. Reinhard, F. B. M. et al. Thermal proteome profiling monitors ligand interactions with cellular membrane proteins. *Nat. Methods* **12**, 1129–1131 (2015).
65. Savitski, M. M. et al. Tracking cancer drugs in living cells by thermal profiling of the proteome. *Science* **346**, 1255784 (2014).
66. Frank, H. et al. Thermal proteome profiling for unbiased identification of direct and indirect drug targets using multiplexed quantitative mass spectrometry. *Nat. Protoc.* **10**, 1567–1593 (2015).
67. Herneisen, A. L. et al. Identifying the target of an antiparasitic compound in *Toxoplasma* using thermal proteome profiling. *ACS Chem. Biol.* **15**, 1801–1807 (2020).
68. Seidi, A. et al. Elucidating the mitochondrial proteome of *Toxoplasma gondii* reveals the presence of a divergent cytochrome c oxidase. *Elife* **7**, e38131 (2018).
69. Barylyuk, K. et al. A subcellular atlas of *Toxoplasma* reveals the functional context of the proteome. Preprint at <https://doi.org/10.1101/2020.04.23.057125> (2020).
70. Melber, A. et al. Role of Nfu1 and Bol3 in iron-sulfur cluster transfer to mitochondrial clients. *Elife* **5**, e15991 (2016).
71. Sun, F. et al. Crystal structure of mitochondrial respiratory membrane protein complex II. *Cell* **121**, 1043–1057 (2005).
72. Biagini, G. A., Viriyavejakul, P., O'Neill, P. M., Bray, P. G. & Ward, S. A. Functional characterization and target validation of alternative complex I of *Plasmodium falciparum* mitochondria. *Antimicrob. Agents Chemother.* **50**, 1841–1851 (2006).
73. Syafruddin, D., Siregar, J. E. & Marzuki, S. Mutations in the cytochrome b gene of *Plasmodium berghei* conferring resistance to atovaquone. *Mol. Biochem. Parasitol.* **104**, 185–194 (1999).
74. Korsinczyk, M. et al. Mutations in *Plasmodium falciparum* cytochrome b that are associated with atovaquone resistance are located at a putative drug-binding site. *Antimicrob. Agents Chemother.* **44**, 2100–2108 (2000).
75. Combrinck, J. M. et al. Optimization of a multi-well colorimetric assay to determine haem species in *Plasmodium falciparum* in the presence of anti-malarials. *Malar. J.* **14**, 253 (2015).
76. Combrinck, J. M. et al. Insights into the role of heme in the mechanism of action of antimalarials. *ACS Chem. Biol.* **8**, 133–137 (2013).
77. Zhang, S. & Gerhard, G. S. Heme activates artemisinin more efficiently than hemin, inorganic iron, or hemoglobin. *Bioorg. Med. Chem.* **16**, 7853–7861 (2008).
78. Basco, L. K. & B., J. L. In vitro activity of artemisinin derivatives against african isolates and clones of *Plasmodium falciparum*. *Am. J. Trop. Med. Hyg.* **49**, 301–307 (1993).
79. Witkowski, B. et al. Reduced artemisinin susceptibility of *Plasmodium falciparum* ring stages in western Cambodia. *Antimicrob. Agents Chemother.* **57**, 914–923 (2013).
80. D'Angelo, J. G., Bordón, C., Posner, G. H., Yolken, R., Jones-Brando, L. Artemisinin derivatives inhibit *Toxoplasma gondii* in vitro at multiple steps in the lytic cycle. *J. Antimicrob. Chemother.* **63**, 146–150 (2009).
81. Matsuu, A., Yamasaki, M., Xuan, X., Ikada, H. & Hikasa, Y. In vitro evaluation of the growth inhibitory activities of 15 drugs against *Babesia gamsi* (Aomori strain). *Vet. Parasitol.* **157**, 1–8 (2008).
82. Langreth, S. G. Feeding mechanisms in extracellular *Babesia microti* and *Plasmodium lophurae*. *J. Protozool.* **23**, 215–223 (1976).
83. van Dooren, G. G., Kennedy, A. T. & McFadden, G. I. The use and abuse of heme in apicomplexan parasites. *Antioxid. Redox Signal.* **17**, 634–656 (2012).
84. Shanmugasundram, A., Gonzalez-Galarza, F. F., Wastling, J. M., Vasieva, O. & Jones, A. R. Library of Apicomplexan Metabolic Pathways: a manually curated database for metabolic pathways of apicomplexan parasites. *Nucleic Acids Res.* **41**, D706–13 (2013).
85. Giacometti, A., Cirioni, O. & Scalise, G. In-vitro activity of macrolides alone and in combination with artemisin, atovaquone, dapsone, minocycline or pyrimethamine against *Cryptosporidium parvum*. *J. Antimicrob. Chemother.* **38**, 399–408 (1996).
86. Krishnan, A. et al. Functional and computational genomics reveal unprecedented flexibility in stage-specific *Toxoplasma* metabolism. *Cell Host Microbe* **27**, 290–306.e11 (2020).
87. Ke, H. et al. The heme biosynthesis pathway is essential for *Plasmodium falciparum* development in mosquito stage but not in blood stages. *J. Biol. Chem.* **289**, 34827–34837 (2014).
88. Kloehn, J., Harding, C. R. & Soldati-Favre, D. Supply and demand-heme synthesis, salvage and utilization by *Apicomplexa*. *FEBS J.* <https://doi.org/10.1111/febs.15445> (2020).
89. Nagaraj, V. A. et al. Malaria parasite-synthesized heme is essential in the mosquito and liver stages and complements host heme in the blood stages of infection. *PLoS Pathog.* **9**, e1003522 (2013).
90. Suroli, N. & Padmanaban, G. de novo biosynthesis of heme offers a new chemotherapeutic target in the human malarial parasite. *Biochem. Biophys. Res. Commun.* **187**, 744–750 (1992).
91. Sigala, P. A. & Goldberg, D. E. The peculiarities and paradoxes of *Plasmodium* heme metabolism. *Annu. Rev. Microbiol.* **68**, 259–278 (2014).
92. Dou, Z., McGovern, O. L., Di Cristina, M. & Carruthers, V. B. *Toxoplasma gondii* ingests and digests host cytosolic proteins. *MBio* **5**, e01188–14 (2014).
93. Tjhin, E. T., Hayward, J. A., McFadden, G. I. & van Dooren, G. G. Characterization of the apicoplast-localized enzyme TgUroD in *Toxoplasma gondii* reveals a key role of the apicoplast in heme biosynthesis. *J. Biol. Chem.* **295**, 1539–1550 (2020).
94. Gnädig, N. F. et al. Insights into the intracellular localization, protein associations and artemisinin resistance properties of *Plasmodium falciparum* K13. *PLoS Pathog.* **16**, e1008482 (2020).
95. Stojanovski, B. M. et al. 5-Aminolevulinate synthase catalysis: the catcher in heme biosynthesis. *Mol. Genet. Metab.* **128**, 178–189 (2019).
96. Ikushiro, H. et al. Heme-dependent inactivation of 5-aminolevulinate synthase from *Caulobacter crescentus*. *Sci. Rep.* **8**, 14228 (2018).
97. Hanna, D. A. et al. Heme dynamics and trafficking factors revealed by genetically encoded fluorescent heme sensors. *Proc. Natl Acad. Sci. USA* **113**, 7539–7544 (2016).
98. Abshire, J. R., Rowlands, C. J., Ganesan, S. M., So, P. T. C. & Niles, J. C. Quantification of labile heme in live malaria parasites using a genetically encoded biosensor. *Proc. Natl Acad. Sci. USA* **114**, E2068–E2076 (2017).
99. Sharma, S., Jadhav, M., Singh, A., Arora, K. & Malhotra, P. A secretory multifunctional serine protease, DegP of *Plasmodium falciparum*, plays an important role in thermo-oxidative stress, parasite growth and development. *FEBS J.* **281**, 1679–1699 (2014).
100. Navarro-Sastre, A. et al. A fatal mitochondrial disease is associated with defective NDU1 function in the maturation of a subset of mitochondrial Fe-S proteins. *Am. J. Hum. Genet.* **89**, 656–667 (2011).

101. Cameron, J. M. et al. Mutations in iron-sulfur cluster scaffold genes NFU1 and BOLA3 cause a fatal deficiency of multiple respiratory chain and 2-oxoacid dehydrogenase enzymes. *Am. J. Hum. Genet.* **89**, 486–495 (2011).
102. Cai, K., Frederick, R. O. & Markley, J. L. ISCU interacts with NFU1, and ISCU [4Fe-4S] transfers its Fe-S cluster to NFU1 leading to the production of holo-NFU1. *J. Struct. Biol.* **210**, 107491 (2020).
103. Uzarska, M. A., Dutkiewicz, R., Freibert, S.-A., Lill, R. & Mühlhoff, U. The mitochondrial Hsp70 chaperone Ssq1 facilitates Fe/S cluster transfer from Isu1 to Grx5 by complex formation. *Mol. Biol. Cell* **24**, 1830–1841 (2013).
104. Shakamuri, P., Zhang, B. & Johnson, M. K. Monothiol glutaredoxins function in storing and transporting [Fe 2S2] clusters assembled on IscU scaffold proteins. *J. Am. Chem. Soc.* **134**, 15213–15216 (2012).
105. Rosenberg, A., Luth, M. R., Winzeler, E. A., Behnke, M. & Sibley, L. D. Evolution of resistance in vitro reveals mechanisms of artemisinin activity in *Toxoplasma gondii*. *Proc. Natl. Acad. Sci. USA* **116**, 26881–26891 (2019).
106. Chen, X. J., Wang, X. & Butow, R. A. Yeast aconitase binds and provides metabolically coupled protection to mitochondrial DNA. *Proc. Natl. Acad. Sci. USA* **104**, 13738–13743 (2007).
107. Jonckheere, A. I., Smeitink, J. A. M. & Rodenburg, R. J. T. Mitochondrial ATP synthase: architecture, function and pathology. *J. Inherit. Metab. Dis.* **35**, 211–225 (2012).
108. Schuhmann, H. & Adamska, I. Deg proteases and their role in protein quality control and processing in different subcellular compartments of the plant cell. *Physiol. Plant* **145**, 224–234 (2012).
109. Chang, Z. The function of the DegP (HtrA) protein: protease versus chaperone. *IUBMB Life* **68**, 904–907 (2016).
110. Gao, T. & O'Brian, M. R. Control of DegP-dependent degradation of c-type cytochromes by heme and the cytochrome c maturation system in *Escherichia coli*. *J. Bacteriol.* **189**, 6253–6259 (2007).
111. Dobson, L., Reményi, I. & Tusnády, G. E. CCTOP: a consensus constrained TOPology prediction web server. *Nucleic Acids Res.* **43**, W408–12 (2015).
112. Escalante, A. A. & Ayala, F. J. Evolutionary origin of *Plasmodium* and other Apicomplexa based on rRNA genes. *Proc. Natl. Acad. Sci. USA* **92**, 5793–5797 (1995).
113. Sidik, S. M., Hackett, C. G., Tran, F., Westwood, N. J. & Lourido, S. Efficient genome engineering of *Toxoplasma gondii* using CRISPR/Cas9. *PLoS ONE* **9**, e100450 (2014).
114. Gibson, D. G. et al. Enzymatic assembly of DNA molecules up to several hundred kilobases. *Nat. Methods* **6**, 343–345 (2009).
115. Bastin, P., Bagherzadeh, Z., Matthews, K. R. & Gull, K. A novel epitope tag system to study protein targeting and organelle biogenesis in *Trypanosoma brucei*. *Mol. Biochem. Parasitol.* **77**, 235–239 (1996).
116. Lourido, S. et al. Calcium-dependent protein kinase 1 is an essential regulator of exocytosis in *Toxoplasma*. *Nature* **465**, 359–362 (2010).
117. Hunt, A. et al. Differential requirements for cyclase-associated protein (CAP) in actin-dependent processes of *Toxoplasma gondii*. *eLife* **8**, e50598 (2019).
118. Sidik, S. M. et al. Using a genetically encoded sensor to identify inhibitors of *Toxoplasma gondii* Ca²⁺ signaling. *J. Biol. Chem.* **291**, 9566–9580 (2016).
119. Hunt, A. et al. Differential requirements for cyclase-associated protein (CAP) in actin-dependent processes of *Toxoplasma gondii*. *eLife* **8**, e50598 (2019).
120. Gajria, B. et al. ToxoDB: an integrated *Toxoplasma gondii* database resource. *Nucleic Acids Res.* **36**, D553–6 (2008).
121. Pino, P. et al. Dual targeting of antioxidant and metabolic enzymes to the mitochondrion and the apicoplast of *Toxoplasma gondii*. *PLoS Pathog.* **3**, e115 (2007).
122. Schindelin, J. et al. Fiji: an open-source platform for biological-image analysis. *Nat. Methods* **9**, 676–682 (2012).
123. Birsoy, K. et al. An essential role of the mitochondrial electron transport chain in cell proliferation is to enable aspartate synthesis. *Cell* **162**, 540–551 (2015).
124. Xia, J., Sinelnikov, I. V., Han, B. & Wishart, D. S. MetaboAnalyst 3.0—making metabolomics more meaningful. *Nucleic Acids Res.* **43**, W251–W257 (2015).
125. Waldman, B. S. et al. Identification of a master regulator of differentiation in *Toxoplasma*. *Cell* **180**, 359–372.e16 (2020).
126. Hughes, C. S. et al. Single-pot, solid-phase-enhanced sample preparation for proteomics experiments. *Nat. Protoc.* **14**, 68–85 (2019).
127. Perez-Riverol, Y. et al. The PRIDE database and related tools and resources in 2019: improving support for quantification data. *Nucleic Acids Res.* **47**, D442–D450 (2019).
128. Huynh, M.-H. & Carruthers, V. B. Tagging of endogenous genes in a *Toxoplasma gondii* strain lacking Ku80. *Eukaryot. Cell* **8**, 530–539 (2009).
129. Fidock, D. A., Nomura, T. & Wellems, T. E. Cycloguanil and its parent compound proguanil demonstrate distinct activities against *Plasmodium falciparum* malaria parasites transformed with human dihydrofolate reductase. *Mol. Pharmacol.* **54**, 1140–1147 (1998).
130. Ekland, E. H., Schneider, J. & Fidock, D. A. Identifying apicoplast-targeting antimalarials using high-throughput compatible approaches. *FASEB J.* **25**, 3583–3593 (2011).
131. Fidock, D. A. et al. Mutations in the *P. falciparum* digestive vacuole transmembrane protein PfCRT and evidence for their role in chloroquine resistance. *Mol. Cell* **6**, 861–871 (2000).
132. Lee, M. C. S., Moura, P. A., Miller, E. A. & Fidock, D. A. *Plasmodium falciparum* Sec24 marks transitional ER that exports a model cargo via a diacidic motif. *Mol. Microbiol.* **68**, 1535–1546 (2008).
133. Labun, K. et al. CHOPCHOP v3: expanding the CRISPR web toolbox beyond genome editing. *Nucleic Acids Res.* **47**, W171–W174 (2019).

Acknowledgements

We would like to thank the MIT Genome Core and the Whitehead Metabolomics Core for technical assistance. Emily Shortt and Eric Spooner assisted with proteomics. Sheena Vasquez and Jade Bath helped with assay development. George Bell provided statistics advice. This study was supported by Sir Henry Wellcome and Sir Henry Dale fellowships (103972/Z/14/Z, 213455/Z/18/Z) to C.R.H., a Robert Black Fellowship from the Damon Runyon Cancer Research Foundation (DRG-2365-19) to E.A.B., a National Science Foundation Graduate Research Fellowship (174530) to A.L.H., an NIH R01 to D.A.F. (AI109023), a Discovery Award from the US Department of Defense (W81XWH1910086) to D.A.F., and an NIH Director's Early Independence Award (1DP5OD017892) and a grant from the Mallinckrodt Foundation to S.L.

Author contributions

Conceptualization, C.R.H., S.M.S., B.P., and S.L. Resources, B.M.M., A.L.H., and E.A.B. Investigation, C.R.H., S.M.S., B.P., A.L.H., N.F.G., J.O., and K.W. Writing—original draft, C.R.H., S.M.S., and B.P. Writing—review and editing, C.R.H., S.M.S., B.P., N.F.G., D.A.F., and S.L. Funding acquisition, D.A.F. and S.L. Supervision, D.A.F. and S.L.

Competing interests

The authors declare no competing interests.

Additional information

Supplementary information is available for this paper at <https://doi.org/10.1038/s41467-020-18624-0>.

Correspondence and requests for materials should be addressed to S.L.

Peer review information *Nature Communications* thanks the anonymous reviewers for their contribution to the peer review of this work. Peer reviewer reports are available.

Reprints and permission information is available at <http://www.nature.com/reprints>

Publisher's note Springer Nature remains neutral with regard to jurisdictional claims in published maps and institutional affiliations.



Open Access This article is licensed under a Creative Commons Attribution 4.0 International License, which permits use, sharing, adaptation, distribution and reproduction in any medium or format, as long as you give appropriate credit to the original author(s) and the source, provide a link to the Creative Commons license, and indicate if changes were made. The images or other third party material in this article are included in the article's Creative Commons license, unless indicated otherwise in a credit line to the material. If material is not included in the article's Creative Commons license and your intended use is not permitted by statutory regulation or exceeds the permitted use, you will need to obtain permission directly from the copyright holder. To view a copy of this license, visit <http://creativecommons.org/licenses/by/4.0/>.

© The Author(s) 2020

Annual Review of Microbiology
 Molecular Mechanisms of
 Drug Resistance in *Plasmodium
 falciparum* Malaria

Kathryn J. Wicht,¹ Sachel Mok,¹ and David A. Fidock^{1,2}

¹Department of Microbiology and Immunology, Columbia University Irving Medical Center, New York, New York 10032, USA; email: kathrynwicht@gmail.com, sm4223@cumc.columbia.edu, df2260@cumc.columbia.edu

²Division of Infectious Diseases, Department of Medicine, Columbia University Irving Medical Center, New York, New York 10032, USA

Annu. Rev. Microbiol. 2020. 74:431–54

The *Annual Review of Microbiology* is online at
micro.annualreviews.org

<https://doi.org/10.1146/annurev-micro-020518-115546>

Copyright © 2020 by Annual Reviews.
 All rights reserved

Keywords

antimalarial drug resistance, artemisinin-based combination therapy, piperazine, transport, hemoglobin, endocytosis, *pfprt*, *k13*

Abstract

Understanding and controlling the spread of antimalarial resistance, particularly to artemisinin and its partner drugs, is a top priority. *Plasmodium falciparum* parasites resistant to chloroquine, amodiaquine, or piperazine harbor mutations in the *P. falciparum* chloroquine resistance transporter (PfCRT), a transporter resident on the digestive vacuole membrane that in its variant forms can transport these weak-base 4-aminoquinoline drugs out of this acidic organelle, thus preventing these drugs from binding heme and inhibiting its detoxification. The structure of PfCRT, solved by cryogenic electron microscopy, shows mutations surrounding an electronegative central drug-binding cavity where they presumably interact with drugs and natural substrates to control transport. *P. falciparum* susceptibility to heme-binding antimalarials is also modulated by overexpression or mutations in the digestive vacuole membrane-bound ABC transporter PfMDR1 (*P. falciparum* multidrug resistance 1 transporter). Artemisinin resistance is primarily mediated by mutations in *P. falciparum* Kelch13 protein (K13), a protein involved in multiple intracellular processes including endocytosis of hemoglobin, which is required for parasite growth and artemisinin activation. Combating drug-resistant malaria urgently requires the development of new antimalarial drugs with novel modes of action.

ANNUAL
REVIEWS **CONNECT**

www.annualreviews.org

- Download figures
- Navigate cited references
- Keyword search
- Explore related articles
- Share via email or social media

Contents

1. INTRODUCTION	432
2. MOLECULAR MECHANISMS OF THE 4-AMINOQUINOLINES AND ARYLAMINOALCOHOLS	433
2.1. Mode of Action of the 4-Aminoquinolines and Arylaminoalcohols	433
2.2. PfCRT as a Primary Driver of Resistance to Chloroquine and Amodiaquine ..	435
2.3. PfMDR1 as a Modulator of <i>P. falciparum</i> Susceptibility to 4-Aminoquinolines and Arylaminoalcohols	437
2.4. Piperaquine Resistance Mechanisms	438
3. MECHANISM OF ARTEMISININ ACTION AND RESISTANCE IN <i>P. FALCIPARUM</i>	439
3.1. Mode of Action of Artemisinins	439
3.2. Origins, Spread, and Prevalence of Artemisinin Resistance	440
3.3. <i>k13</i> as the Primary Determinant of Artemisinin Resistance and Impact on Fitness	440
3.4. Mechanisms Underpinning K13-Mediated Artemisinin Resistance	442
3.5. Evidence of Non- <i>k13</i> Genetic Mediators of Artemisinin Resistance	443
3.6. Features of Artemisinin-Induced Dormancy and Recrudescence	444
4. CONCLUSIONS	445

1. INTRODUCTION

The persistence of the *Plasmodium falciparum* parasite, despite decades of clinical research and treatment protocols, has led to a global malaria disease burden that included over 200 million cases in 2018, according to the World Health Organization (157). These cases resulted in an estimated 405,000 deaths, including 272,000 (67%) children under 5 years, with an overwhelming 94% of mortalities occurring in sub-Saharan Africa. As the utilization and effectiveness of experimental vaccines have been very limited, there is a significant reliance on antimalarial drugs for prophylaxis as well as for treatment of infected patients (30). For thousands of years, malaria was treated with natural products found in bark, roots, or leaves of plants. Their active ingredients, however, were identified and used as isolated drug compounds only in the last century. Perhaps the most successful of these medicines was quinine, a quinoline-containing alkaloid from the bark of cinchona trees (101). Developments in the chemical synthesis of drug analogs led to the 4-aminoquinoline quinacrine and, after further toxicological and pharmacological studies, chloroquine. By the 1950s this fast-acting antimalarial was the frontline treatment for malaria. The use of chloroquine as a single-agent therapy continued globally for decades thanks to its efficacy, availability, low toxicity, and affordability (150). Antimalarials are some of the most commonly used medications in tropical regions, where the substantial need for treatment, exacerbated to a degree by incomplete patient compliance, puts immense drug selection pressure on *P. falciparum* parasites to evolve resistance mechanisms. When chloroquine resistance emerged in the early 1960s, malaria resurged, continuing for decades in most countries (151). High-throughput screening and drug discovery and development work by the US Army led to the discovery of pyrimethamine and the chloroquine analog amodiaquine, as well as the arylaminoalcohols mefloquine and halofantrine. They too suffered declining efficacy from the late 1980s, owing to the spread of resistant parasites. Another chloroquine derivative, piperaquine, developed under the Chinese National Malaria Elimination

Program as a *bis* 4-aminoquinoline that can overcome chloroquine resistance, has more recently been used in combination therapies in Southeast Asia (14).

The use of two or more compounds with different modes of action for malaria treatment is recommended by the World Health Organization, both to provide necessary cure rates and to delay the onset of resistance. Nonetheless, regions with low mixed-strain transmission rates, specifically in Southeast Asia, have historically been the first to show resistance to frontline drugs (86). Indeed, resistance to chloroquine, mefloquine, and sulfadoxine-pyrimethamine initially arose in that region (14, 112). More recently, artemisinin-based combination therapies (ACTs) have been successful in controlling malaria and have saved countless lives, with the global burden showing a 37% reduction from 2000 to 2015 (43). Artemisinin, originally extracted from the Chinese sweet wormwood *Artemisia annua*, and its derivatives artemether, artesunate, and dihydroartemisinin (DHA) are fast-acting compounds that contain a unique endoperoxide bridge. These are typically combined with a partner drug having a longer half-life such as lumefantrine, piperaquine, mefloquine, amodiaquine, or more recently pyronaridine, as recommended by the World Health Organization for the treatment of uncomplicated *P. falciparum* malaria. As early as 2008, emerging artemisinin resistance was detected in Southeast Asia, particularly in the Greater Mekong Subregion (GMS) (86, 153). The most problematic situation currently is the very rapid increase in failure rates for DHA + piperaquine, which has been the first-line treatment and the preferred ACT in most of Southeast Asia (106, 125, 142). The rise of these new DHA-and-piperaquine-resistant parasites threatens the recent progress made in malaria reduction and highlights the need for new interventions.

One initial consideration was to use the prophylactic combination drug atovaquone-proguanil (83). One caveat is that resistance to atovaquone can be readily acquired via mutations in cytochrome *b*, although these mutant parasites might no longer be transmissible (48). Proguanil is also of limited potency, and its active metabolite cycloguanil can encounter resistance via point mutations in the target dihydrofolate reductase (123). Mechanisms underlying resistance to atovaquone-proguanil and the antifolate combination pyrimethamine-sulfadoxine have recently been reviewed separately (53, 127). Our article instead focuses on modes of action of and mechanisms of resistance to ACT drugs.

2. MOLECULAR MECHANISMS OF THE 4-AMINOQUINOLINES AND ARYLAMINOALCOHOLS

2.1. Mode of Action of the 4-Aminoquinolines and Arylaminoalcohols

Since chloroquine resistance first emerged independently in Southeast Asia and South America, later spreading from Asia to Africa, scientists have been working to understand the mechanistic basis of drug action and resistance (115) (Supplemental Table 1). This work has converged on degradation of host hemoglobin and the subsequent detoxification of heme products. During the asexual blood stage of its life cycle, the developing trophozoite ingests up to 75% of the available hemoglobin, a major cytosolic host erythrocyte protein, by a process of endocytosis via cytostomes. Vesicles containing hemoglobin are transported to the digestive vacuole (DV), an acidic secondary lysosome with a pH of ~ 5.2 (70). In the DV, the parasite must degrade hemoglobin to acquire the amino acids required for its growth and maturation, a catabolic process mediated by multiple proteases (47). These include the aspartic proteases plasmepsins 1, 2, 4, and 3 (the latter is also known as histo-aspartic protease); the falcipain cysteine proteases; and the zinc protease falcilysin. This process produces denatured globin and a heme by-product, iron protoporphyrin IX [Fe(II)PPIX]. Fe(II)PPIX can be auto-oxidized by O_2 to cytotoxic Fe(III)PPIX, which is capable of lipid peroxidation. To mitigate this toxicity, Fe(III)PPIX is biomineralized into

ACT:
artemisinin-based
combination therapy

DHA:
dihydroartemisinin

GMS: Greater
Mekong Subregion

DV: digestive vacuole

Fe(II)PPIX: iron
protoporphyrin IX

Supplemental Material >

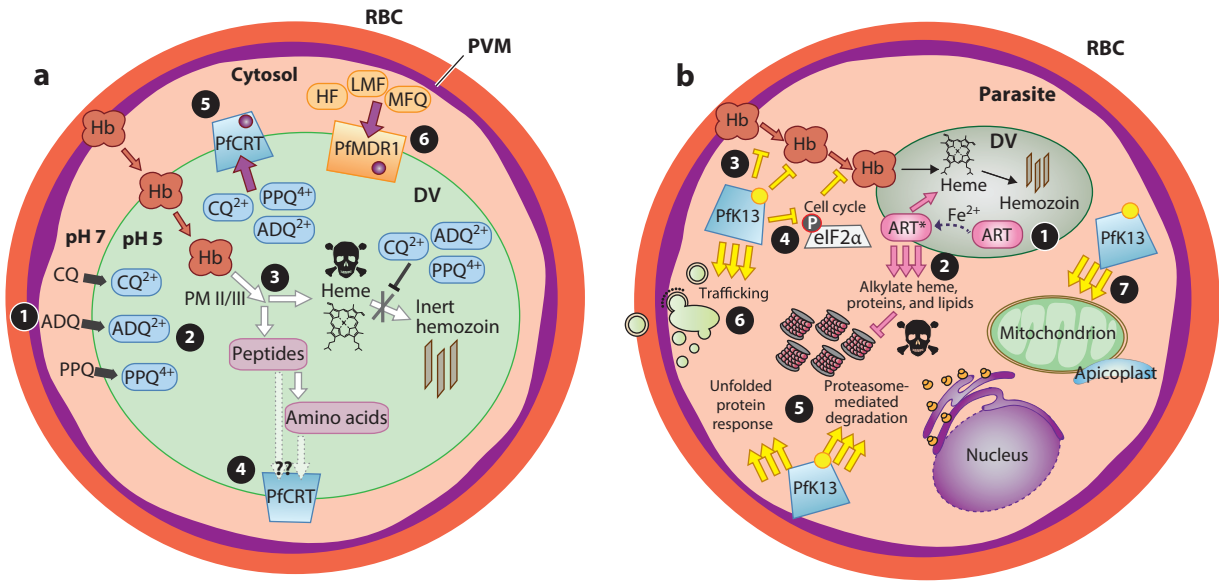


Figure 1

Mechanism of action of quinolines and artemisinins and resistance mechanisms mediated by PfCRT, PfMDR1, and K13 in *P. falciparum* asexual blood stage parasites. (a) During its asexual blood stage, the *P. falciparum* parasite, surrounded by its PVM, develops within the host red blood cell. (1) Quinoline-based antimalarials, including chloroquine, amodiaquine, and piperazine, concentrate from the parasite cytosol (neutral pH of ~7) into the DV (acidic pH of ~5.2). (2) Once inside the DV, these weak-base drugs are protonated, existing mostly as pH-trapped charged species that are unable to passively diffuse out through the DV membrane. (3) As additional molecules diffuse into the DV, their protonated forms bind to the high concentrations of toxic free heme by-product that result from the degradation of host hemoglobin, as well as to grooves on the surfaces of growing hemozoin crystals. The combination of pH trapping and heme binding accounts for the >1,000-fold drug accumulation inside the DV. (4) The DV membrane protein PfCRT is believed to be involved in transporting peptides released from hemoglobin digestion into the parasite cytosol. (5) In drug-resistant parasites, mutations in PfCRT enable the efflux of protonated drug molecules out of the DV, away from their heme target. (6) Mutations in the DV membrane transporter PfMDR1 can also influence parasite susceptibility to these compounds and are thought to enable transport of drugs such as halofantrine, lumefantrine, and mefloquine into the DV, away from their primary site of action. (b) (1) Artemisinin drugs are activated by cleavage of their endoperoxide by iron protoporphyrin IX (Fe^{2+} -heme), a product of parasite-digested hemoglobin. (2) The Fe^{2+} -heme-artemisinin carbon-centered radicals alkylate and damage a multitude of parasite proteins, heme, and lipids and inhibit proteasome-mediated protein degradation. K13 mutations, located primarily in the β -propeller kelch domain, confer artemisinin resistance in young rings. (3) The loss of K13 function provided by mutations has been shown to cause reduced endocytosis of host hemoglobin and (4) to extend the duration of ring-stage development, perhaps via PK4-mediated eIF2 α phosphorylation. These changes result in lowered levels of hemoglobin catabolism and availability of Fe^{2+} -heme as the drug activator and lead to reduced activation of artemisinin drugs. (5) K13 mutations may activate the unfolded protein response, maintain proteasome-mediated degradation of polyubiquitinated proteins in the presence of artemisinins, and (6) remove drugs and damaged proteins through an increase in PI3K-mediated vesicular trafficking. (7) K13 may also help regulate mitochondrial physiology and maintain membrane potential during drug-induced ring-stage quiescence. The asterisk signifies the activated form of ART. Abbreviations: ADQ, amodiaquine; ART, artemisinin; CQ, chloroquine; DV, digestive vacuole; eIF2 α , eukaryotic initiation factor 2 α ; Hb, hemoglobin; HF, halofantrine; LMF, lumefantrine; MFQ, mefloquine; PfCRT, *P. falciparum* chloroquine resistance transporter; PfMDR1, *P. falciparum* multidrug resistance 1 transporter; PPQ, piperazine; PVM, parasitophorous vacuole membrane; RBC, red blood cell.

hemozoin, an inert and highly insoluble crystalline material (Figure 1a). This brown birefringent crystal is formed mostly during the trophozoite stage, before merozoites develop (132).

Multiple studies have established that chloroquine and its 4-aminoquinoline analogs inhibit hemozoin formation in the DV, causing DV swelling and pigment clumping. Their activity can be reversed by inhibiting hemoglobin proteases (49, 131). 4-Aminoquinolines have also been shown

to inhibit the formation of β -hemozoin (synthetic hemozoin) in extracellular biomimetic assays (96). Furthermore, parasitized red blood cells treated with chloroquine, amodiaquine, or piperaquine show a dose-dependent increase in intracellular free heme with a corresponding decrease in hemozoin (26, 32). Chloroquine inhibits hemozoin formation by binding to the fastest-growing crystal face, possibly as a chloroquine-hemozoin complex (49, 100). The ability of quinoline antimalarials to strongly bind to Fe(II)PPIX, combined with pH trapping, allows for their >1,000-fold accumulation in the DV (16).

The arylaminoalcohols include antimalarials such as quinine, mefloquine, and lumefantrine. Generally, their mechanism of action is not as well understood as that of the 4-aminoquinolines; however, they may also partially interfere with hemozoin formation and detoxification of hemoglobin degradation by-products as a secondary aspect of their modes of action. Indeed, the arylaminoalcohols have been shown to form 1:2 drug:hemozoin μ -oxo dimer complexes in a similar manner to that of the 4-aminoquinolines, albeit with weaker binding constants (37). In a cell fractionation assay, there was a statistically significant increase in free heme and a decrease in hemozoin for parasites treated with quinine, mefloquine, and lumefantrine at 2.5 times their 50% inhibitory concentration (IC₅₀) values. However, these effects were not as pronounced as the divergent heme/hemozoin levels observed after treatment with chloroquine (27).

2.2. PfCRT as a Primary Driver of Resistance to Chloroquine and Amodiaquine

Chloroquine-resistant parasites display decreased accumulation of chloroquine in the DV, mediated via an energy-dependent drug efflux mechanism (73). The main causal determinant was reported in 2000, when the analysis of a genetic cross between chloroquine-sensitive and chloroquine-resistant strains identified mutations in the *P. falciparum* chloroquine resistance transporter gene, *pfcr*t (40). The 49-kDa drug/metabolite transporter protein PfCRT localizes to the DV membrane, consistent with its role in mediating chloroquine efflux out of the DV away from its heme target (29, 40, 81, 115). Very recently, single-particle cryogenic electron microscopy (cryo-EM) determined the PfCRT structure to 3.2 Å resolution, after successful screening of PfCRT-specific antigen-binding fragments (Fabs) that formed complexes with PfCRT as a means to overcome cryo-EM size and analytical limitations (67). The transporter contains 424 amino acids and 10 transmembrane helix domains arranged as five helical pairs that form two-helix hairpins with an inverted antiparallel topology, typical of drug/metabolite transporters, as well as two juxtamembrane helices. Together they form a negatively charged central cavity of around 3,300 Å³ that is open to the DV side in the solved antibody-bound conformation (**Figure 2**). This cavity is believed to accommodate positively charged drugs and other compounds/solutes that concentrate in the DV, allowing for their transport to the cytosol as PfCRT alternates conformations during its transport cycle. *trans*-Stimulation efflux experiments have demonstrated that extracellular chloroquine stimulates efflux of preloaded intracellular chloroquine, supporting the transporter or carrier model, as opposed to the channel model, for PfCRT-mediated drug efflux (117). The kinetics, efficiency, and mechanisms of this process are highly dependent on the specific mutations that give rise to a particular PfCRT isoform (16, 19, 67). Earlier studies reported genetic transformation via *pfcr*t allelic exchange and confirmed that chloroquine-resistant mutations in *pfcr*t-modified clones are sufficient for producing chloroquine-resistant phenotypes on different genetic backgrounds (122). An important and ubiquitous amino acid substitution in chloroquine-resistant alleles, regardless of origin, is lysine to threonine at position 76. This K76T mutation is always accompanied by multiple additional region-specific mutations. For example, the chloroquine-resistant South American 7G8, African GB4, and Southeast Asian Dd2 PfCRT isoforms harbor five, six, and eight mutations, respectively, compared to the chloroquine-sensitive

PfCRT: *Plasmodium falciparum* chloroquine resistance transporter

Cryo-EM: cryogenic electron microscopy

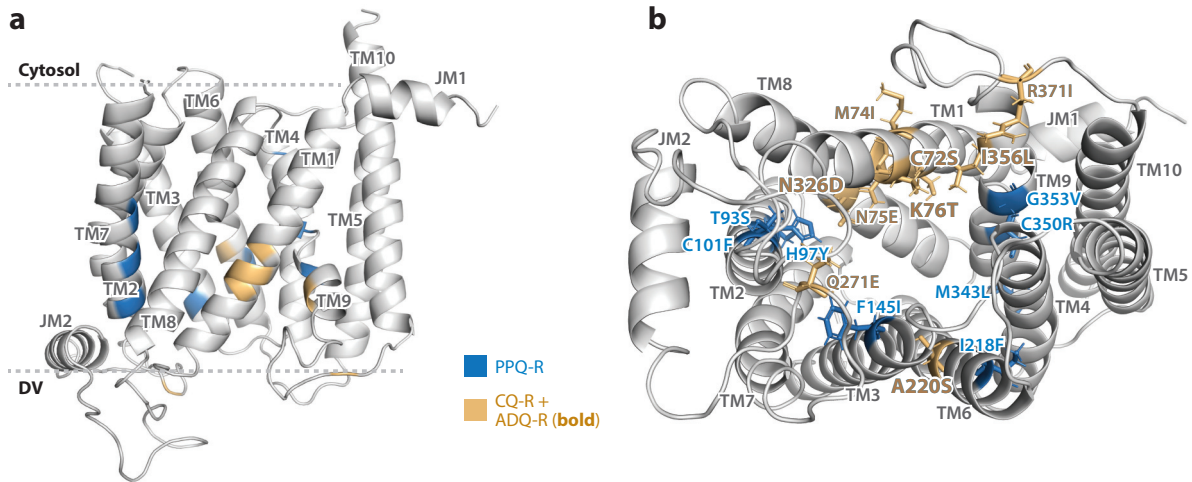


Figure 2

The structure of 7G8 PfCRT solved by cryogenic-electron microscopy showing the ten transmembrane helices (TM1–10) and two juxtamembrane helices (JM1–2) viewed (a) from the side and (b) from the DV into the central drug-binding cavity. Mutations associated with drug resistance are colored for piperavaquine (blue), chloroquine (gold), or amodiaquine (gold and bold). The substituted amino acids are represented as solid-colored sticks when viewed (b) from the DV only. Abbreviations: ADQ-R, amodiaquine resistance; CQ-R, chloroquine resistance; DV, digestive vacuole; PfCRT, *P. falciparum* chloroquine resistance transporter; PPQ-R, piperavaquine resistance.

wild-type 3D7 isoform. The cryo-EM structure of PfCRT was solved for the 7G8 isoform, revealing that all five of its mutations, namely, C72S, K76T, A220S, N326D, and I356L, line the central drug-binding cavity. A minimum of four of these mutations is required to confer chloroquine resistance, suggesting a codependent role for these additional amino acid substitutions (42). Although the 7G8, GB4, and Dd2 PfCRT isoforms are all considered chloroquine resistant, the South American SVMNT PfCRT haplotypes, as opposed to the African/Asian CVIET haplotypes, are equally associated with resistance to amodiaquine (116). Therefore, cross-resistance between chloroquine and amodiaquine is mainly observed on 7G8 backgrounds.

Transport studies have revealed that isoforms of PfCRT, expressed in *Xenopus* oocytes (10, 81), *Saccharomyces cerevisiae* yeast (8), or proteoliposomes (66), show a dose-dependent chloroquine or quinine uptake only when these resistance-conferring mutations are present, with K76T being a key transport requirement. This proton-coupled transport, which is dependent on a pH gradient and a positive membrane potential, is inhibited by other 4-aminoquinolines, including amodiaquine and piperavaquine. Transport is also inhibited by the chloroquine resistance reversal agent verapamil, which presumably competes for the PfCRT drug-binding site (67). PfCRT, which is essential to the parasite, might itself constitute a target of 4-aminoquinolines, which may act as competitive inhibitors of natural PfCRT substrates. Indeed, parasites expressing lower levels of mutant PfCRT are more sensitive to chloroquine, despite showing similar levels of chloroquine accumulation (74). Although the native function of PfCRT is not confirmed, studies have suggested its involvement in mediating the transport of hemoglobin-derived peptides and amino acids out of the DV, as well as glutathione, Cl⁻ ions, H⁺ ions, and iron (7, 73, 75, 81, 103, 162). PfCRT variants expressed in proteoliposomes transport basic amino acids such as arginine, lysine, and histidine, which would be positively charged upon entering PfCRT's cavity from the acidic DV (66). Notably, lumefantrine and atovaquone or neutral amino acids such as leucine do not compete for the drug-binding site, suggesting PfCRT's specificity for cationic or protonatable 4-aminoquinoline compounds (67).

Further evidence of PfCRT's role in transporting essential nutrients from the DV has been reported in metabolomics studies that evaluated the effects of mutations on peptide levels in parasite extracts. Metabolic quantitative trait locus analysis, which links the genome-wide contribution of individual alleles to metabolite concentration, demonstrates a correlation between elevated hemoglobin-derived peptides and the chloroquine-resistance-conferring *pfcr*t locus (75). Chloroquine-resistant K76T parasites show the largest accumulation of these peptides, such as PEEK, and a significant fitness disadvantage owing to compromised hemoglobin metabolism. Additional PfCRT mutations, including C101F and L272F, which arose in vitro under amantadine and blasticidin selection, respectively, show massively enlarged DVs in trophozoite and schizont stages and confer substantial fitness costs (108). The addition of these mutations on a chloroquine-resistant background causes reversal of chloroquine resistance, presumably by inhibiting PfCRT-mediated chloroquine transport, in agreement with chloroquine uptake data from *Xenopus* oocytes (32, 72, 108). Furthermore, parasites harboring an L272F mutation confer methionine auxotrophy to chloroquine-resistant Dd2 parasites, which become unable to metabolize and access this necessary amino acid (72).

PfMDR1: *Plasmodium falciparum* multidrug resistance 1 transporter

SNP: single-nucleotide polymorphism

2.3. PfMDR1 as a Modulator of *P. falciparum* Susceptibility to 4-Aminoquinolines and Arylaminoalcohols

Another factor that plays a role in resistance to heme-targeting antimalarials is the P-glycoprotein homolog PfMDR1 (also known as Pgh1), encoded by the *P. falciparum* multidrug resistance 1 transporter gene *pfmdr1* (109, 140). Like PfCRT, PfMDR1 lies on the DV membrane, but transport is predicted to be inwardly directed toward the DV (**Figure 1a**). Topologically, PfMDR1 resembles a typical P-glycoprotein-type ABC transporter, containing two membrane-spanning homologous domains, each consisting of six predicted helices followed by a hydrophilic nucleotide-binding pocket (118). This binding domain appears to be located on the cytosolic side of the DV, where it could first interact with antimalarials. Reducing *pfmdr1* copy number increases parasite susceptibility to mefloquine, halofantrine, lumefantrine, quinine, and artemisinin derivatives (121). The amino acid substitution N86Y, common in African strains, modulates drug susceptibility by enhancing parasite resistance to chloroquine and amodiaquine, while increasing susceptibility to mefloquine, lumefantrine, and DHA (144, 145). The use of artesunate + amodiaquine has been found to select for PfMDR1 N86Y and D1246Y in parasites that emerged after therapy, with decreased sensitivity to monodesethyl-amodiaquine, the active metabolite of amodiaquine (28, 98). PfMDR1 mutations in 7G8 South American parasites have more influence on chloroquine resistance than those in Asian Dd2 or African GB4 parasites, suggesting important isoform-specific relationships between PfCRT and PfMDR1.

Optimal access of drugs to their target is essential for their high activity. Mutations in PfMDR1 presumably inhibit the transport of antimalarials from the cytosol to the DV, thereby decreasing the concentration of heme-targeting drugs such as chloroquine and amodiaquine in the DV. On the other hand, antimalarials such as mefloquine, lumefantrine, and halofantrine that are likely to inhibit targets outside the DV become more potent when their transport by PfMDR1 away from the cytosol is restricted (111). Studies with *pfmdr1* complementary RNA-injected *Xenopus* oocytes revealed that PfMDR1 transports chloroquine, quinine, and halofantrine, with single-nucleotide polymorphisms (SNPs) affecting substrate specificity (118). For example, the mutation N86Y results in a transporter, Pgh-1^{Dd2}, that is unable to transport quinine and chloroquine but instead gains a halofantrine-transporting capability. It is possible that some antimalarial drugs, including quinine and mefloquine, not only are Pgh-1 substrates but also inhibit its regular function by occupying a common drug-binding site, thereby blocking the transport of other solutes (111, 118).

In Africa, *pfmdr1* gene amplification is very rare, probably owing to the less frequent drug pressure and the more frequent mixed infections that reinforce the impact of its known fitness cost, when compared with the situation in Asia, where fitness appears to be less of a dominating factor (113). The N86Y mutant and D1246 wild-type variants have the largest selective advantage in Uganda; however, SNPs in this gene generally have less impact on fitness than does copy number (99).

GWAS: genome-wide association study

***pm2-3*:** plasmepsin 2-3

2.4. Piperaquine Resistance Mechanisms

For several countries, particularly China, Vietnam, and Malawi, that have effectively prevented the use of chloroquine monotherapy, in vitro and in vivo parasite sensitivities to chloroquine have been frequently restored, along with a decrease in certain resistance-associated *pfcr1* and *pfmdr1* mutations (41, 52). Although the quinoline antimalarials are no longer used as monotherapies in most parts of the world, the widely adopted ACTs often rely on them as partner drugs. The earlier use of artesunate + mefloquine as the first-line therapy in some Southeast Asian countries resulted in selection for multicopy *pfmdr1*, associated with decreased efficacy, and led to the regional adoption of DHA + piperaquine (14, 28, 145). However, the decreased potency of the artemisinin derivatives in the GMS has augmented pressure on the partner drugs. By 2015, piperaquine resistance was being observed in Cambodia (2, 21, 38). In standard dose-response assays, piperaquine-resistant parasites often have biphasic or incomplete growth inhibition curves, complicating the calculation of the IC₅₀ or IC₉₀ values. A robust alternative has been the piperaquine survival assay, in which synchronized ring-stage parasites are exposed to a pharmacologically relevant dose of 200 nM piperaquine for 48 h followed by drug-free culture for an additional 24 h. Survival ratios are measured after 72 h and are calculated as the percentage of the ratio of drug-treated versus mock-treated live parasites (38). Survival rates $\geq 10\%$ are associated with an increased risk of piperaquine treatment failure and provide a threshold for determining piperaquine resistance in vitro (155).

Defining the genetic basis for piperaquine resistance has been a high priority, motivating genome-wide association studies (GWASs) that have uncovered several potential molecular markers. These include the amplification of the *plasmepsin 2* and *3* genes (*pm2-3*), which are involved in hemoglobin degradation (3, 15, 93, 155). It was proposed that overproduction of these plasmepsins might interfere with piperaquine's inhibition of heme detoxification processes in the DV (155). However, it was not possible to confirm whether plasmepsins were directly involved in mediating piperaquine resistance or whether they were compensatory mechanisms for fitness disadvantages of the actual resistance determinant(s) (78). Another study on 78 western Cambodian isolates sampled between 2011 and 2014 strongly suggested that other loci must be responsible for piperaquine resistance (102). Duru et al. (38) isolated artemisinin-resistant parasites that recrudesced from patients treated with DHA + piperaquine and showed piperaquine survival rates $\geq 10\%$ correlating with single-copy *pfmdr1* and several novel mutations in PfCRT, namely H97Y, M343L, or G353V, which arose on the Dd2 allele (**Figure 2**). Independently, genome-wide SNPs from 183 Cambodian isolates revealed an additional PfCRT mutation, F145I, that was associated with decreased piperaquine sensitivity in isolates harboring amplified *pm2-3* (1).

Evidence that PfCRT mutations might contribute to piperaquine resistance was initially provided when a PfCRT mutation, C350R, from French Guiana field isolates was found to be associated with decreased piperaquine susceptibility. This phenotype was confirmed via genetic editing in the 7G8 line, which resulted in a small but significant ~ 1.5 -fold shift in the piperaquine IC₅₀ value (105). Additionally, a SNP in *pfcr1* giving rise to the C101F substitution, identified from an in vitro piperaquine selection experiment, was genetically edited in Dd2 parasites and gave an ~ 140 -fold IC₉₀ increase relative to the Dd2 edited isogenic control, a biphasic dose-response

curve, and a 3-fold increase in the 50% lethal dose (LD_{50}) (32). Another study, confirmed via *pfprt*-modified parasites engineered in Dd2, found that the PfCRT mutations F145I, M343L, and G353V led to $\geq 10\%$ piperazine survival ratios and significant IC_{90} shifts, even without *pm2-3* amplification (114). Intriguingly, these mutations, which all occurred on chloroquine-resistant lines, caused a partial to full reversal of chloroquine resistance, highlighting the major influence of subtle physicochemical changes within the PfCRT transporter on drug associations and phenotypes (32, 105, 114). The prevalence of these different point mutations in the field appears to be driven largely by the relative parasite survival that they confer under a given drug pressure within the region, together with the fitness cost of the particular mutation (51, 142). Two PfCRT mutations that have expanded the most rapidly in the field in the last five years are T93S and I218F, which also line PfCRT's drug-binding cavity (**Figure 2**). These point mutations were recently shown via *pfprt*-edited parasites to individually give rise to $\sim 10\%$ parasite survival rates under high piperazine concentrations, while affording reasonable fitness levels relative to the more highly piperazine-resistant PfCRT mutation F145I (33).

PfCRT's interactions with piperazine and chloroquine have been studied by exposing variant isoforms of PfCRT harboring piperazine-resistance-associated mutations to radiolabeled piperazine or chloroquine, either in nanodiscs to assess drug binding or in proteoliposomes to measure drug uptake (67). Both chloroquine and piperazine show binding within the 0.1–0.2 μM K_d range at pH 5.5, regardless of isoform; however, drug uptake is significantly greater in resistant isoforms. For example, the chloroquine-resistant, piperazine-sensitive 7G8 and Dd2 isoforms show the largest chloroquine uptake and smallest piperazine uptake, while those with an F145I or C350R mutation show the opposite effect, relative to the wild type, which gives negligible uptake of both drugs. These findings reiterate the specificity of PfCRT for differentially mediating resistance to structurally distinct compounds, and they confirm that PfCRT point mutations give rise to contrasting drug phenotypes. This phenomenon could be leveraged by employing antimalarials such as chloroquine and piperazine in combination to exert opposing selective pressure on parasites (67). A longer-term approach would be to reverse resistance by identifying specific inhibitors of the PfCRT substrate-binding cavity that prevent it from transporting natural substrates and drugs (124).

3. MECHANISM OF ARTEMISININ ACTION AND RESISTANCE IN *P. FALCIPARUM*

3.1. Mode of Action of Artemisinins

Since the early 2000s, ACTs have been the first-line treatment for malaria, having quickly been adopted worldwide (151). The four main drug combinations comprising artemisinin derivatives are artesunate + mefloquine and DHA + piperazine, used in Southeast Asia, and artemether + lumefantrine (Coartem) and artesunate + amodiaquine, used in Africa. In the 1970s, a team led by Dr. Youyou Tu defined artemisinin's medicinal property and solved its chemical structure, for which she earned a Nobel Prize in Medicine (139). The compound's remarkable characteristics include rapid drug-activated killing of both the asexual blood stage and early sexual gametocyte forms of *P. falciparum* parasites within hours of exposure at low nanomolar concentrations, despite having a short half-life of < 1 h.

Most antimalarials such as sulfadoxine-pyrimethamine, atovaquone, and chloroquine inhibit either a single target or a single pathway, e.g., DHFR-mediated folate synthesis by sulfadoxine-pyrimethamine, atovaquone inhibition of cytochrome *bc*₁, and heme detoxification by chloroquine. On the other hand, artemisinins have been reported to bind to a very broad array of parasite proteins and appear to affect a multitude of organellar and cellular processes including hemoglobin

PCT_{1/2} (parasite clearance half-life): the time in hours that it takes for parasitemia to decrease by 50%

RSA: ring stage survival assay

endocytosis, glycolysis, protein synthesis and degradation, and cell cycle regulation (17, 64, 119, 148). This unique property is due to the cleavage of its endoperoxide bridge by free Fe(II)PPIX liberated from digested hemoglobin. Once activated, the heme-drug carbon-centered radical alkylates heme, proteins, and lipids, which accelerates the generation of more cytotoxic reactive oxygen species via a cluster bomb effect that eventually leads to cell death (64, 148) (**Figure 1b**). Independent studies have suggested that artemisinins may also target mitochondrial function by depolarizing this organelle's membrane potential (77, 147).

3.2. Origins, Spread, and Prevalence of Artemisinin Resistance

Delayed parasite clearance following artemisinin treatment was first observed in western Cambodia, the epicenter of emerging antimalarial multidrug resistance (36, 97). Clinical sites that had more than 30% of cases with microscopically positive parasites evident 72 h after initiating artemisinin or ACT treatment were categorized as areas of resistance by the World Health Organization. Subsequently, clinical artemisinin resistance was redefined as parasite clearance half-life (PCT_{1/2}) > 5 h. The PCT is the time required for the parasite density to be reduced by 50% along the log-linear portion of the normalized parasite clearance curve (152). This was the first instance where antimalarial resistance was recognized as a prolonged time to complete parasite clearance rather than an elevated dose of drug required to eliminate the parasite. Resistance has now been documented across multiple countries in the GMS, including Cambodia, Vietnam, Myanmar, Thailand, and Laos (86). This geographic diversification was attributed to artemisinin-resistant parasites disseminating through population migration as well as de novo emergence in new sites, abetted by permissive infections in local species of *Anopheles* mosquitoes (5, 126, 136). To date, clinical evidence of artemisinin resistance has not been robustly documented outside of Southeast Asia (28).

Resistance to artemisinin also spells a potential disaster for other antimalarial drugs, as it places increased pressure for these partner drugs to work quickly and effectively once artemisinin loses its efficacy. To combat artemisinin resistance, two malaria control strategies have been developed: triple ACTs (TACTs) and mass drug administration (MDA) (34, 146). While TACTs leverage on combining drugs that differ in their modes of action to prevent multidrug resistance from arising or eliminating infections resistant to one of the ACT partner drugs, MDA aims to eliminate pockets of asymptomatic malaria that serve as reservoirs for transmission and persistence of resistant parasites. Clinical testing of TACT efficacy is underway in the second-phase Tracking Resistance to Artemisinin Collaboration II (TRAC II) multiple-site study. Early indications are that the DHA + piperazine + mefloquine and the artemether + lumefantrine + amodiaquine combinations are promising and may help delay the onset of artemisinin resistance or restore antimalarial sensitivity in areas that were once artemisinin resistant (143).

3.3. *k13* as the Primary Determinant of Artemisinin Resistance and Impact on Fitness

In vitro artemisinin resistance is determined by performing a ring-stage survival assay (RSA) where young, 0–3 h postinvasion rings are exposed for 6 h to a pharmacologically relevant 700-nM concentration of the active artemisinin metabolite DHA. In artemisinin resistance, the loss of efficacy in early rings of resistant isolates has been characterized by a survival rate >1% without a change in sensitivity at the mature asexual blood stages (154). The parasite's *k13* gene (*kelch13*) as a genetic determinant of artemisinin resistance was first identified in a laboratory-based in vitro evolution study. By increasing artemisinin pressure stepwise on the Tanzanian strain F32 over 125 repeated drug cycles spanning 5 years, Ariey et al. (4) identified the M476I mutation in K13 and the D56V

mutation in the DNA-directed RNA polymerase II subunit RPB9 as early genetic changes that emerged after ~30 cycles of artemisinin pressure. Besides *k13*, mutations in six other genes also arose during further in vitro drug selection. This included a stop codon in falcipain 2 and SNPs in a cysteine protease involved in hemoglobin digestion, protein kinase PK7, gamete antigen 27/25 Pfg27, and two genes encoding unknown proteins.

A GWAS by several groups also implicated *k13* as a candidate marker of clinical artemisinin resistance (22, 89, 135). In the GWAS of ~1,500 clinical samples from the multiple-site TRAC study, ~26 mutations in the K13 protein were associated with delayed clearance, defined as a PCT_{1/2} > 5 h (5). While the *k13* gene was the only gene that converged using the two powerful approaches, the in vitro-derived M476I mutation has been observed only at a very low frequency of ~0.3% in one field study (158), providing evidence that in vitro selections can identify the correct gene but that the mutations can differ from those that succeed in the field. The latest extended pooled analyses of 3,250 isolates from a compilation of literature and new data by the WorldWide Antimalarial Resistance Network found 20 β -propeller mutations that were associated with a prolonged PCT_{1/2} in Asia, but this was not true for S522C, A578S, and Q613L mutations, which were observed in Africa (158). Only one nonpropeller mutation, E252Q, located in the apicomplexan-specific domain has been associated with a 1.5-fold-longer half-life, reaffirming the dominant role of propeller mutations in modulating artemisinin responses (158). Likewise, not all propeller mutations confer artemisinin resistance; for example, A578S was detected at low prevalence in Africa but did not confer resistance in vitro, at least in Dd2 parasites (87). Hence, the presence of propeller mutations cannot be used to predict the resistance phenotype. The reverse genetics approach of using gene-specific zinc-finger nucleases or CRISPR/Cas9 site-directed gene editing has been useful in proving the causal association of the most common K13 propeller mutations (C580Y, R539T, I543T, and Y493H) with in vitro artemisinin resistance (RSA > 1%) in Asian parasites (44, 130). The level of resistance differs between K13 mutations even on the same parasite background, suggesting that these point mutations may operate differently (130). Indeed, these four listed point mutations are scattered across the second, third, and fourth blades of the six-bladed β -propeller domain.

Varying responses to artemisinin also resulted when the same K13 variant codon was edited in different parasite backgrounds (130). This emphasized the important contribution of the genetic background to artemisinin resistance and the presence of secondary determinants that can modulate the degree of resistance. Candidate secondary loci suggested to modulate the artemisinin response were identified in various GWASs (22, 89, 135). Miotto et al. (89) identified the MDR2 (multidrug resistance protein 2) T484I, ferredoxin D193Y, PIB7 (phosphoinositide-binding protein 7) C1484F, ARPS10 (apicoplast ribosomal protein S10) V127M, and PfCRT I356T and N326S mutations as components of a genetic founder background in Southeast Asian isolates. However, their contribution to artemisinin resistance has yet to be validated experimentally. Another GWAS of 192 northeast Thai samples identified Kelch10 P623T as a potential modulator of artemisinin resistance via epistatic interactions with the K13 C580Y or E252Q isoforms (20).

K13 mutations that have independently emerged are associated with specific geographical origins (87, 136, 166). While F446I and more recently G533S dominate in Myanmar, and Yunnan, southern China, near the China-Myanmar border at 56% and 44% prevalence respectively, E252Q is found at the western Thai border and in Myanmar (59, 107, 163). R539T and Y493H mutations have been detected in Cambodia but not western Thailand (87). The most prevalent C580Y mutation is widespread in Western Cambodia, Thailand, and Vietnam and across the GMS (87, 158). The prevalence of each mutation is highly dynamic, with some fluctuating over time while others, such as C580Y in Cambodia, trend to fixation (107). The high prevalence of the C580Y mutation is driven by clonal expansion of the DHA- and piperaquine-resistant Pailin lineage. Originating in western Cambodia, this lineage spread to Thailand and Vietnam and then to

southern Laos and northeastern Thailand (51, 62). This lineage harbors the PLA1/KEL1 (K13 C580Y and *pm2-3* copy > 1) haplotype identified from microsatellite typing of a region from -31 kb up to +50 kb flanking the *k13* gene (63). In vitro comparative growth rate studies have shown significant differences between K13 mutations, with contemporary Cambodian parasites displaying less of a fitness cost than older strains, consistent with beneficial effects of secondary determinants (94, 129).

Recent reports document the emergence of K13 mutations in 2 isolates from Rwanda (P574L and A675V), 14 from Guyana (1.6%; C580Y), and 3 from Papua New Guinea (1.3%; C580Y). These appear to be distinct from the PLA1/KEL1 haplotype (24, 82, 90, 134). An earlier report of an M579I mutation linked to delayed clearance and low-level RSA survival (2.3%) (79) has not been independently confirmed. Moreover, the proportion of nonsynonymous to synonymous SNPs in *k13* is significantly lower in Africa than Southeast Asia, suggesting that *k13* is not undergoing selection in African countries to the degree observed in Southeast Asia (80). Presumably this is in part a result of the K13-mutant isolates having a fitness cost that is more detrimental to their survival in higher-transmission African settings with a greater prevalence of mixed infections and more cases of untreated infection. K13-mutant isolates from Papua New Guinea and French Guiana, adapted from the field or gene-edited to introduce the C580Y mutation, have exhibited elevated RSA survival rates of 6.8% and 27.6%, respectively (82, 90), showing that mutant K13 is able to impart resistance in those strains. However, there is no information on the clinical PCT_{1/2} outcome to suggest the emergence of clinically defined K13-mediated resistance to artemisinins in these regions.

3.4. Mechanisms Underpinning K13-Mediated Artemisinin Resistance

Similar to proteins encoded by other drug resistance genes, the K13 protein is essential for the parasite's intraerythrocytic development, although its level can be reduced up to 50% by regulating its mislocalization using a knock-sideways approach in transgenic parasites (12). K13 has been localized to cytosomes at the parasite periphery as well as to intracellular vesicles that associate with either endocytosis or vesicular trafficking of antigens including PfEMP1 or Rab-mediated protein transport (11, 13, 46, 160). K13 mutations have been thought to mediate artemisinin resistance in rings primarily via the reduced activation of artemisinin drugs and/or an enhanced parasite capacity to remove damaged proteins (**Figure 1b**). Lowered K13 levels resulting from mutations have been postulated to lead to reduced hemoglobin endocytosis and catabolism in young rings, resulting in lowered levels of free Fe(II)PPIX available to activate artemisinin (13, 160). In vitro edited K13-mutant 3D7 parasites were also more refractory to DHA-induced inhibition of proteasomal function and maintained protein turnover. Rings inherently tolerate >100-fold-higher levels of artemisinin than do the later trophozoite stages, where maximal activity occurs, validating the importance of hemoglobin endocytosis and digestion in artemisinin activation and subsequent cytotoxicity (68, 69). Perturbation of the pathway by disrupting falcipain 2a or adding the cysteine protease inhibitor E64 further demonstrated that reduced Fe(II)PPIX-mediated activation of the drug can lower parasite susceptibility to artemisinin (159). In addition, when artemisinin-resistant K13 mutant parasites were deprived of sufficient external amino acid sources, they were reported to be less fit and failed to developmentally progress compared with K13 wild-type parasites, providing further evidence that K13 mutations impact hemoglobin catabolism and intracellular liberation of globin-derived amino acids (18). K13-mutant field isolates also showed lowered heme levels at the trophozoite stage, and treatment with DHA generated fewer heme adducts, when compared with their isogenic K13 wild-type counterparts (54, 55).

Of note, no change in expression of *k13* transcript abundance was detected in K13 mutant clinical isolates (91). In addition, reduced expression of *k13* in rings was reported to result

in hypersensitivity to artemisinin as measured using 72-h dose-response assays (not RSAs) in *piggyBac* transposon-generated mutant parasite lines (45, 165), contrary to the expected increased tolerance if there were lower K13 steady-state protein levels. A reduced level of K13 protein was observed in early rings in the Cam3.II R539T mutant but not the Cam3.II C580Y mutant when compared to the isogenic wild-type line (11, 120). Further work is clearly required to evaluate whether K13 protein levels or functionalities are affected across all clinical isolates bearing mutations that associate with clinical resistance to artemisinin.

K13 also alters the cell cycle in K13 C580Y clinical isolates by conferring an extended period of ring-to-trophozoite stage development, which could also account for reduced Fe(II)PPIX-mediated drug activation (58, 91). K13 mutations have been proposed to destabilize the protein and to deregulate the phosphorylation of PfPK4, leading to downstream activation of transcriptional stress response pathways and modulation of growth via phosphorylation of the parasite's eukaryotic initiation factor 2 α (eIF2 α) (160, 164). Phosphorylation of eIF2 α has also been observed as a stress-sensing regulatory mechanism of reduced growth rates in cells deprived of the amino acid isoleucine (6).

Maintaining protein turnover is vital to cell survival upon treatment with artemisinin, which is known to cause the accumulation of damaged, unfolded, and polyubiquitinated proteins and to inhibit proteasome function (17). K13 mutations have been proposed to remove damaged proteins by upregulating the unfolded protein response (UPR), as shown with field isolates, and lowering the levels of ubiquitinated proteins as part of their enhanced cell stress response (35, 91) (**Figure 1b**). Several groups have observed synergy between artemisinin and proteasome inhibitors, providing a compelling potential avenue to overcome artemisinin resistance (35, 76, 128, 161). This synergy, however, is present in both K13-mutant and wild-type parasites (128), providing evidence that K13 mutations do not mediate resistance by modulating proteasomal activity. Alternatively, K13 mutations have been proposed to protect against artemisinin's proteostatic activity by reducing drug binding to and polyubiquitination of PI3K, thereby elevating the levels of PI3P-positive vesicles that engage in cellular processes of protein folding, vesicle-mediated protein export, and the UPR (11, 84).

Recent data also suggest that K13 function is linked to parasite mitochondria. Gnädig et al. (46) observed increased colocalization of K13 with mitochondria following a DHA pulse, especially in K13 mutants. We also observed reversal of mutant-K13-mediated artemisinin resistance upon coinubation with the mitochondrial cytochrome *bc*₁ inhibitor atovaquone (S. Mok, B.H. Stokes, N.F. Gnädig, L.S. Ross, T. Yeo, et al., unpublished data).

3.5. Evidence of Non-*k13* Genetic Mediators of Artemisinin Resistance

Several recent studies have shown that artemisinin resistance in *P. falciparum* can be driven by genes other than *k13*. Non-K13-mediated resistance in clinical studies has been limited to sporadic reports of delayed parasite clearance following ACT in a handful of clinical isolates in Southeast Asia and Africa (92, 133). On the other hand, in vitro selection studies with the Pikine and Thiès strains from Senegal yielded moderately artemisinin-resistant parasites that had acquired mutations in coronin. This protein contains a WD40 seven-bladed β -propeller domain similar in architecture to K13 (31). CRISPR-Cas9 editing of the coronin R100K, E107V, or G50E mutation into the wild-type parental lines reproduced the heightened RSA to similar levels (5–10%) as selected resistant lines. Separate selection studies with 3D7, another African line, yielded mutations in multiple genes including a stop mutation in the hemoglobinase falcipain 2A; however, genetic validation was not included in that report (110). UBP-1 has also been touted as a candidate artemisinin resistance mediator, based on linkage group selection analysis of a genetic cross in the rodent parasite *Plasmodium chabaudi* between a selected artemisinin-resistant parent and an

artemisinin-sensitive parent (60). Studies with *P. falciparum* revealed a V3275F mutation in *pfubp1* that was associated with resistance in vitro (56); however, this gene was not associated with in vivo resistance in Southeast Asian clinical isolates (61). The S160N mutation in the AP-2 adaptin μ subunit observed in post-ACT-treated African isolates also did not associate with elevated RSA values in vitro (56). None of the genes listed above, however, has been associated with delayed clearance rates of *P. falciparum* infections following artemisinin treatment in patients. More compelling is the GWAS of isolates from the China-Myanmar border region that found an association between decreased *P. falciparum* susceptibility to artemisinin derivatives and the T38I mutation in the PI3P-binding autophagy-related protein ATG18 (149). It will be interesting to determine whether these genes or others might act in the same functional pathway as *k13* and produce similar resistance levels independent of K13 mutations.

3.6. Features of Artemisinin-Induced Dormancy and Recrudescence

In bacterial systems, dormancy, i.e., the process where cells enter a low-energy resting state, has been utilized as a bet-hedging strategy to overcome unfavorable environmental conditions (65). Growth reinitiates once the cells sense that growth conditions have improved (39). This phenomenon has been observed in *Plasmodium* parasites following short-term treatment (6 to 144 h) with antimalarial compounds including artemisinin derivatives, atovaquone, proguanil, pyrimethamine, and mefloquine or exposure to stress-inducing conditions including cold shock or nutrient starvation (57, 71, 88, 95, 137, 138). Dormant parasites, characterized by condensed chromatin and reduced cytoplasm, are typically resistant to perturbations, suggesting that dormancy is a cell-adapted response to external stress (9). As an example, DHA treatment of *P. falciparum* parasites led to a temporary developmental arrest followed 9 to 20 days later by recrudescence of a small proportion (0.04–1.3%) of parasites (137). Interestingly, only asexual rings transitioned into dormant forms. Modeling studies have suggested that artemisinin-induced dormancy contributes to recrudescence of artemisinin-resistant parasites and treatment failure (25).

Artemisinin-treated dormant *P. falciparum* parasites were observed to have reduced metabolic levels yet maintained active apicoplasts and mitochondria (23, 104). Interestingly, atovaquone delayed the recovery of DHA-induced dormant parasites (104), suggesting that mitochondrial activity is critical for survival and regrowth of dormant parasites. Several studies have proposed mechanisms that underpin these processes. One study linked *P. falciparum* asexual blood stage cell cycle progression with the regulated expression of mitotic Ca^{2+} -dependent kinases (*cdpk4*, *pk2*, *nima*, and *ark2*) and the prereplicative complex (141). In another study, recovery from DHA-induced dormancy was associated with altered expression levels of cyclins (*pfcrk1*, *pfcrk4*) and cyclin-dependent kinases (50). Recovery following isoleucine starvation was also associated with stress-response GCN2-mediated eIF2 α phosphorylation, higher transcript levels of the RNA polymerase III repressor *PfMaf1*, and increased pre-tRNA expression to maintain translation of proteins (6, 85).

Over time, repeated drug pressures and induction of dormancy in wild-type parasite populations might progressively select for faster-recovering rings and lead to artemisinin-resistant parasites that no longer require dormancy, as postulated in a two-step process of artemisinin resistance acquisition (25). This would lead to longer times required for artemisinin treatment to clear parasites and result in higher rates of recrudescence. An in vitro example of this scenario may explain the establishment of an artemisinin-resistant K13 M476I mutant following multiple rounds of short-term artemisinin pressure and subsequent parasite recovery (4, 156). This mutant line was observed to form quiescent, nonpyknotic rings that could rapidly resume intraerythrocytic development upon removing artemisinin pressure, suggesting that mutant K13 obviated the need for parasites to enter dormancy as a survival mechanism (156).

4. CONCLUSIONS

The mechanisms of resistance to compounds that target parasite DV processes, such as hemoglobin degradation and hemozoin formation, are primarily linked to mutations in the transmembrane proteins PfCRT and PfMDR1. As mentioned above, these proteins transport drugs either away from or toward their primary site of action. Resistance to the endoperoxide artemisinins, mediated by mutations in K13, has been associated with reduced activation of the drug and an enhanced UPR. Sets of mutations or specific point mutations can confer a variety of fitness costs that together with the level of drug susceptibility under the relevant drug pressure influence which haplotypes dominate in field isolates. Combining suitable sets of drugs that apply opposing selective pressures in combination therapies provides important opportunities for mitigating drug resistance. This goal can only be achieved with a comprehensive understanding of the mechanisms by which parasites evade various drug pressures.

SUMMARY POINTS

1. Progress made in reducing malaria cases and fatalities worldwide is threatened by the emergence of multidrug-resistant *P. falciparum* parasites.
2. PfCRT is an essential drug/metabolite transporter, present on the parasite's DV membrane, that harbors an electronegative drug-binding cavity that presumably transports hemoglobin-derived peptides and that harbors unique, geographically dependent sets of mutations. These mutations can give rise to parasite resistance to chloroquine and in some cases amodiaquine. Resistance to piperaquine has also emerged in Southeast Asia through the gain of individual mutations that in many cases can result in loss of chloroquine resistance. These mutations confer fitness costs that influence their relative abundance within parasite populations.
3. Certain mutant PfCRT isoforms efficiently transport positively charged drugs, including chloroquine, amodiaquine, or piperaquine, that accumulate in the acidic DV and that prevent heme detoxification.
4. The other DV transporter, PfMDR1, modulates parasite susceptibility to certain heme-binding antimalarials including chloroquine, amodiaquine, lumefantrine, and mefloquine via copy number variations or point mutations.
5. Artemisinin derivatives are activated via Fe(II)PPIX-dependent cleavage of their endoperoxide bridge, thereby catalyzing the generation of cytotoxic reactive oxygen species. The activated drug affects multiple cellular processes by alkylating proteins, lipids, and heme.
6. Single point mutations in K13 constitute the primary genetic determinant of in vitro and in vivo artemisinin resistance. The C580Y mutation appears to be relatively fit in Southeast Asian parasites and is highly prevalent across the GMS.
7. Secondary genetic determinants in epistasis with *k13* appear to modulate the degree of artemisinin resistance.
8. K13 mutations have been proposed to reduce the protein's function and to mediate resistance by reducing artemisinin activation, prolonging the quiescent ring stage, upregulating the UPR, and augmenting the elimination of damaged proteins.

FUTURE ISSUES

1. Will K13 mutations begin to increase in prevalence in Africa, where malaria causes by far the most deaths, and compromise artemisinin efficacy? Is South America also at risk?
2. Will lumefantrine resistance arise in Africa? Can we predict the genetic basis and therefore generate candidate molecular markers for epidemiological screening and advance warning?
3. Can we combine new and past antimalarials into double or triple combination therapies to mitigate the spread of resistance by conferring opposing selective pressures on parasite populations?
4. Which approaches will be the most effective in identifying drug targets of antimalarials with complex modes of action such as artemisinin, as well as resistance mechanisms and markers, in order to gain a deeper insight into possibilities for overcoming drug resistance?
5. Experimental elucidation of molecular markers of emerging resistance to ACT drugs is empowered by genetic and genomic approaches that include the use of genome-wide association studies, genetic crosses between *P. falciparum* drug-resistant and drug-sensitive parasites in humanized mice, and CRISPR/Cas9-based gene editing.
6. New antimalarials with novel modes of action, or those that inhibit the transporters responsible for resistance, are urgently needed to replace artemisinins and current artemisinin-based combination therapies if or when they fail.

NOTE ADDED IN PROOF

Recent data from Rwanda show the emergence of K13 R561H mutants in *P. falciparum* parasites of local origin, and this mutation was shown to confer artemisinin resistance in gene-edited Dd2 parasites (139a).

DISCLOSURE STATEMENT

The authors are not aware of any affiliations, memberships, funding, or financial holdings that might be perceived as affecting the objectivity of this review.

ACKNOWLEDGMENTS

S.M. is grateful to receive support from a long-term fellowship funded by the Human Frontier Science Program Organization (LT000976/2016-L). D.A.F. gratefully acknowledges support from the NIH (R37 AI05234, R01 AI124678, R01 AI109023, R01 AI147628), the Bill & Melinda Gates Foundation (OPP1201387), the Department of Defense (W81XWH1910086), and the Medicines for Malaria Venture (MMV08/0015).

LITERATURE CITED

1. Agrawal S, Moser KA, Morton L, Cummings MP, Parihar A, et al. 2017. Association of a novel mutation in the *Plasmodium falciparum* chloroquine resistance transporter with decreased piperazine sensitivity. *J. Infect. Dis.* 216:468–76

2. Amaratunga C, Lim P, Suon S, Sreng S, Mao S, et al. 2016. Dihydroartemisinin-piperaquine resistance in *Plasmodium falciparum* malaria in Cambodia: a multisite prospective cohort study. *Lancet Infect. Dis.* 16:357–65
3. Amato R, Lim P, Miotto O, Amaratunga C, Dek D, et al. 2017. Genetic markers associated with dihydroartemisinin-piperaquine failure in *Plasmodium falciparum* malaria in Cambodia: a genotype-phenotype association study. *Lancet Infect. Dis.* 17:164–73
4. Ariey F, Witkowski B, Amaratunga C, Beghain J, Langlois AC, et al. 2014. A molecular marker of artemisinin-resistant *Plasmodium falciparum* malaria. *Nature* 505:50–55
5. Ashley EA, Dhorda M, Fairhurst RM, Amaratunga C, Lim P, et al. 2014. Spread of artemisinin resistance in *Plasmodium falciparum* malaria. *N. Engl. J. Med.* 371:411–23
6. Babbitt SE, Altenhofen L, Cobbold SA, Istvan ES, Fennell C, et al. 2012. *Plasmodium falciparum* responds to amino acid starvation by entering into a hibernatory state. *PNAS* 109:E3278–87
7. Bakouh N, Bellanca S, Nyboer B, Moliner Cubel S, Karim Z, et al. 2017. Iron is a substrate of the *Plasmodium falciparum* chloroquine resistance transporter PfCRT in *Xenopus* oocytes. *J. Biol. Chem.* 292:16109–21
8. Baro NK, Pooput C, Roepe PD. 2011. Analysis of chloroquine resistance transporter (CRT) isoforms and orthologues in *S. cerevisiae* yeast. *Biochemistry* 50:6701–10
9. Barrett MP, Kyle DE, Sibley LD, Radke JB, Tarleton RL. 2019. Protozoan persister-like cells and drug treatment failure. *Nat. Rev. Microbiol.* 17:607–20
10. Bellanca S, Summers RL, Meyrath M, Dave A, Nash MN, et al. 2014. Multiple drugs compete for transport via the *Plasmodium falciparum* chloroquine resistance transporter at distinct but interdependent sites. *J. Biol. Chem.* 289:36336–51
11. Bhattacharjee S, Coppens I, Mbengue A, Suresh N, Ghorbal M, et al. 2018. Remodeling of the malaria parasite and host human red cell by vesicle amplification that induces artemisinin resistance. *Blood* 131:1234–47
12. Birnbaum J, Flemming S, Reichard N, Soares AB, Mesen-Ramirez P, et al. 2017. A genetic system to study *Plasmodium falciparum* protein function. *Nat. Methods* 14:450–56
13. Birnbaum J, Scharf S, Schmidt S, Jonscher E, Hoeijmakers WAM, et al. 2020. A Kelch13-defined endocytosis pathway mediates artemisinin resistance in malaria parasites. *Science* 367:51–59
14. Blasco B, Leroy D, Fidock DA. 2017. Antimalarial drug resistance: linking *Plasmodium falciparum* parasite biology to the clinic. *Nat. Med.* 23:917–28
15. Bopp S, Magistrado P, Wong W, Schaffner SF, Mukherjee A, et al. 2018. Plasmeprin II–III copy number accounts for bimodal piperaquine resistance among Cambodian *Plasmodium falciparum*. *Nat. Commun.* 9:1769
16. Bray PG, Mungthin M, Hastings IM, Biagini GA, Saidu DK, et al. 2006. PfCRT and the *trans*-vacuolar proton electrochemical gradient: regulating the access of chloroquine to ferriprotoporphyrin IX. *Mol. Microbiol.* 62:238–51
17. Bridgford JL, Xie SC, Cobbold SA, Pasaje CFA, Herrmann S, et al. 2018. Artemisinin kills malaria parasites by damaging proteins and inhibiting the proteasome. *Nat. Commun.* 9:3801
18. Bunditvorapoom D, Kochakarn T, Kotanan N, Modchang C, Kumpornsin K, et al. 2018. Fitness loss under amino acid starvation in artemisinin-resistant *Plasmodium falciparum* isolates from Cambodia. *Sci. Rep.* 8:12622
19. Callaghan PS, Hassett MR, Roepe PD. 2015. Functional comparison of 45 naturally occurring isoforms of the *Plasmodium falciparum* chloroquine resistance transporter (PfCRT). *Biochemistry* 54:5083–94
20. Cerqueira GC, Cheeseman IH, Schaffner SF, Nair S, McDew-White M, et al. 2017. Longitudinal genomic surveillance of *Plasmodium falciparum* malaria parasites reveals complex genomic architecture of emerging artemisinin resistance. *Genome Biol.* 18:78
21. Chaorattanakawee S, Saunders DL, Sea D, Chanarat N, Yingyuen K, et al. 2015. *Ex vivo* drug susceptibility testing and molecular profiling of clinical *Plasmodium falciparum* isolates from Cambodia from 2008 to 2013 suggest emerging piperaquine resistance. *Antimicrob. Agents Chemother.* 59:4631–43
22. Cheeseman IH, Miller BA, Nair S, Nkhoma S, Tan A, et al. 2012. A major genome region underlying artemisinin resistance in malaria. *Science* 336:79–82

23. Chen N, LaCrue AN, Teuscher F, Waters NC, Gatton ML, et al. 2014. Fatty acid synthesis and pyruvate metabolism pathways remain active in dihydroartemisinin-induced dormant ring stages of *Plasmodium falciparum*. *Antimicrob. Agents Chemother.* 58:4773–81
24. Chenet SM, Akinyi Okoth S, Huber CS, Chandrabose J, Lucchi NW, et al. 2016. Independent emergence of the *Plasmodium falciparum* Kelch propeller domain mutant allele C580Y in Guyana. *J. Infect. Dis.* 213:1472–75
25. Cheng Q, Kyle DE, Gatton ML. 2012. Artemisinin resistance in *Plasmodium falciparum*: a process linked to dormancy? *Int. J. Parasitol. Drugs Drug Resist.* 2:249–55
26. Combrinck JM, Fong KY, Gibbard L, Smith PJ, Wright DW, Egan TJ. 2015. Optimization of a multi-well colorimetric assay to determine haem species in *Plasmodium falciparum* in the presence of anti-malarials. *Malar. J.* 14:253
27. Combrinck JM, Mabothe TE, Ncokazi KK, Ambele MA, Taylor D, et al. 2013. Insights into the role of heme in the mechanism of action of antimalarials. *ACS Chem. Biol.* 8:133–37
28. Conrad MD, Rosenthal PJ. 2019. Antimalarial drug resistance in Africa: the calm before the storm? *Lancet Infect. Dis.* 19:e338–51
29. Cooper RA, Ferdig MT, Su XZ, Ursos LM, Mu J, et al. 2002. Alternative mutations at position 76 of the vacuolar transmembrane protein PfCRT are associated with chloroquine resistance and unique stereospecific quinine and quinidine responses in *Plasmodium falciparum*. *Mol. Pharmacol.* 61:35–42
30. Cowell A, Winzeler E. 2018. Exploration of the *Plasmodium falciparum* resistome and druggable genome reveals new mechanisms of drug resistance and antimalarial targets. *Microbiol. Insights* 11:1178636118808529
31. Demas AR, Sharma AI, Wong W, Early AM, Redmond S, et al. 2018. Mutations in *Plasmodium falciparum* actin-binding protein coronin confer reduced artemisinin susceptibility. *PNAS* 115:12799–804
32. Dhingra SK, Redhi D, Combrinck JM, Yeo T, Okombo J, et al. 2017. A variant PfCRT isoform can contribute to *Plasmodium falciparum* resistance to the first-line partner drug piperazine. *mBio* 8:e00303-17
33. Dhingra SK, Small-Saunders JL, Menard D, Fidock DA. 2019. *Plasmodium falciparum* resistance to piperazine driven by PfCRT. *Lancet Infect. Dis.* 19:1168–69
34. Dini S, Zaloumis S, Cao P, Price RN, Fowkes FJI, et al. 2018. Investigating the efficacy of triple artemisinin-based combination therapies for treating *Plasmodium falciparum* malaria patients using mathematical modeling. *Antimicrob. Agents Chemother.* 62:e01068-18
35. Dogovski C, Xie SC, Burgio G, Bridgford J, Mok S, et al. 2015. Targeting the cell stress response of *Plasmodium falciparum* to overcome artemisinin resistance. *PLOS Biol.* 13:e1002132
36. Dondorp AM, Nosten F, Yi P, Das D, Phyto AP, et al. 2009. Artemisinin resistance in *Plasmodium falciparum* malaria. *N. Engl. J. Med.* 361:455–67
37. Dorn A, Vippagunta SR, Matile H, Jaquet C, Vennerstrom JL, Ridley RG. 1998. An assessment of drug-haematin binding as a mechanism for inhibition of haematin polymerisation by quinoline antimalarials. *Biochem. Pharmacol.* 55:727–36
38. Duru V, Khim N, Leang R, Kim S, Domergue A, et al. 2015. *Plasmodium falciparum* dihydroartemisinin-piperazine failures in Cambodia are associated with mutant K13 parasites presenting high survival rates in novel piperazine in vitro assays: retrospective and prospective investigations. *BMC Med.* 13:305
39. Dworkin J, Shah IM. 2010. Exit from dormancy in microbial organisms. *Nat. Rev. Microbiol.* 8:890–96
40. Fidock DA, Nomura T, Talley AK, Cooper RA, Dzekunov SM, et al. 2000. Mutations in the *P. falciparum* digestive vacuole transmembrane protein PfCRT and evidence for their role in chloroquine resistance. *Mol. Cell* 6:861–71
41. Frosch AE, Laufer MK, Mathanga DP, Takala-Harrison S, Skarbinski J, et al. 2014. Return of widespread chloroquine-sensitive *Plasmodium falciparum* to Malawi. *J. Infect. Dis.* 210:1110–14
42. Gabryszewski SJ, Modchang C, Musset L, Chookajorn T, Fidock DA. 2016. Combinatorial genetic modeling of *pfert*-mediated drug resistance evolution in *Plasmodium falciparum*. *Mol. Biol. Evol.* 33:1554–70
43. Gething PW, Casey DC, Weiss DJ, Bisanzio D, Bhatt S, et al. 2016. Mapping *Plasmodium falciparum* mortality in Africa between 1990 and 2015. *N. Engl. J. Med.* 375:2435–45

44. Ghorbal M, Gorman M, Macpherson CR, Martins RM, Scherf A, Lopez-Rubio JJ. 2014. Genome editing in the human malaria parasite *Plasmodium falciparum* using the CRISPR-Cas9 system. *Nat. Biotechnol.* 32:819–21
45. Gibbons J, Button-Simons KA, Adapa SR, Li S, Pietsch M, et al. 2018. Altered expression of K13 disrupts DNA replication and repair in *Plasmodium falciparum*. *BMC Genom.* 19:849
46. Gnädig NF, Stokes BH, Edwards RL, Kalantarov GF, Heimsch KC, et al. 2020. Insights into the intracellular localization, protein associations and artemisinin resistance properties of *Plasmodium falciparum* K13. *PLoS Pathog.* 16:e1008482
47. Goldberg DE. 2013. Complex nature of malaria parasite hemoglobin degradation. *PNAS* 110:5283–84. Erratum. 2013. *PNAS* 110(17):7097
48. Goodman CD, Siregar JE, Mollard V, Vega-Rodriguez J, Syafruddin D, et al. 2016. Parasites resistant to the antimalarial atovaquone fail to transmit by mosquitoes. *Science* 352:349–53
49. Gorka AP, de Dios A, Roepe PD. 2013. Quinoline drug-heme interactions and implications for anti-malarial cytostatic versus cytotoxic activities. *J. Med. Chem.* 56:5231–46
50. Gray KA, Gresty KJ, Chen N, Zhang V, Gutteridge CE, et al. 2016. Correlation between cyclin dependent kinases and artemisinin-induced dormancy in *Plasmodium falciparum* in vitro. *PLoS ONE* 11:e0157906
51. Hamilton WL, Amato R, van der Pluijm RW, Jacob CG, Quang HH, et al. 2019. Evolution and expansion of multidrug-resistant malaria in southeast Asia: a genomic epidemiology study. *Lancet Infect. Dis.* 19:943–51
52. Hayward R, Saliba KJ, Kirk K. 2005. *pfmdr1* mutations associated with chloroquine resistance incur a fitness cost in *Plasmodium falciparum*. *Mol. Microbiol.* 55:1285–95
53. Heinberg A, Kirkman L. 2015. The molecular basis of antifolate resistance in *Plasmodium falciparum*: looking beyond point mutations. *Ann. N. Y. Acad. Sci.* 1342:10–18
54. Heller LE, Goggins E, Roepe PD. 2018. Dihydroartemisinin-ferriprotoporphyrin IX adduct abundance in *Plasmodium falciparum* malarial parasites and the relationship to emerging artemisinin resistance. *Biochemistry* 57:6935–45
55. Heller LE, Roepe PD. 2018. Quantification of free ferriprotoporphyrin IX heme and hemozoin for artemisinin sensitive versus delayed clearance phenotype *Plasmodium falciparum* malarial parasites. *Biochemistry* 57:6927–34
56. Henrici RC, van Schalkwyk DA, Sutherland CJ. 2019. Modification of *pfap2mu* and *pfubp1* markedly reduces ring-stage susceptibility of *Plasmodium falciparum* to artemisinin in vitro. *Antimicrob. Agents Chemother.* 64:e01542-19
57. Henrici RC, van Schalkwyk DA, Sutherland CJ. 2019. Transient temperature fluctuations severely decrease *P. falciparum* susceptibility to artemisinin in vitro. *Int. J. Parasitol. Drugs Drug Resist.* 9:23–26
58. Hott A, Casandra D, Sparks KN, Morton LC, Castanares GG, et al. 2015. Artemisinin-resistant *Plasmodium falciparum* parasites exhibit altered patterns of development in infected erythrocytes. *Antimicrob. Agents Chemother.* 59:3156–67
59. Huang F, Takala-Harrison S, Jacob CG, Liu H, Sun X, et al. 2015. A single mutation in K13 predominates in Southern China and is associated with delayed clearance of *Plasmodium falciparum* following artemisinin treatment. *J. Infect. Dis.* 212:1629–35
60. Hunt P, Afonso A, Creasey A, Culleton R, Sidhu AB, et al. 2007. Gene encoding a deubiquitinating enzyme is mutated in artesunate- and chloroquine-resistant rodent malaria parasites. *Mol. Microbiol.* 65:27–40
61. Imwong M, Dondorp AM, Nosten F, Yi P, Mungthin M, et al. 2010. Exploring the contribution of candidate genes to artemisinin resistance in *Plasmodium falciparum*. *Antimicrob. Agents Chemother.* 54:2886–92
62. Imwong M, Hien TT, Thuy-Nhien NT, Dondorp AM, White NJ. 2017. Spread of a single multidrug resistant malaria parasite lineage (PfPailin) to Vietnam. *Lancet Infect. Dis.* 17:1022–23
63. Imwong M, Suwannasin K, Kunasol C, Sutawong K, Mayxay M, et al. 2017. The spread of artemisinin-resistant *Plasmodium falciparum* in the Greater Mekong subregion: a molecular epidemiology observational study. *Lancet Infect. Dis.* 17:491–97

64. Ismail HM, Barton V, Phanchana M, Charoensuththivarakul S, Wong MH, et al. 2016. Artemisinin activity-based probes identify multiple molecular targets within the asexual stage of the malaria parasites *Plasmodium falciparum* 3D7. *PNAS* 113:2080–85
65. Jones SE, Lennon JT. 2010. Dormancy contributes to the maintenance of microbial diversity. *PNAS* 107:5881–86
66. Juge N, Moriyama S, Miyaji T, Kawakami M, Iwai H, et al. 2015. *Plasmodium falciparum* chloroquine resistance transporter is a H⁺-coupled polyspecific nutrient and drug exporter. *PNAS* 112:3356–61
67. Kim J, Tan YZ, Wicht KJ, Erramilli SK, Dhingra SK, et al. 2019. Structure and drug resistance of the *Plasmodium falciparum* transporter PfCRT. *Nature* 576:315–20
68. Klonis N, Crespo-Ortiz MP, Bottova I, Abu-Bakar N, Kenny S, et al. 2011. Artemisinin activity against *Plasmodium falciparum* requires hemoglobin uptake and digestion. *PNAS* 108:11405–10
69. Klonis N, Xie SC, McCaw JM, Crespo-Ortiz MP, Zaloumis SG, et al. 2013. Altered temporal response of malaria parasites determines differential sensitivity to artemisinin. *PNAS* 110:5157–62
70. Kuhn Y, Rohrbach P, Lanzer M. 2007. Quantitative pH measurements in *Plasmodium falciparum*-infected erythrocytes using pHluorin. *Cell Microbiol.* 9:1004–13
71. LaCrue AN, Scheel M, Kennedy K, Kumar N, Kyle DE. 2011. Effects of artesunate on parasite recrudescence and dormancy in the rodent malaria model *Plasmodium vinckei*. *PLOS ONE* 6:e26689
72. Lee AH, Dhingra SK, Lewis IA, Singh MK, Siriwardana A, et al. 2018. Evidence for regulation of hemoglobin metabolism and intracellular ionic flux by the *Plasmodium falciparum* chloroquine resistance transporter. *Sci. Rep.* 8:13578
73. Lehane AM, Hayward R, Saliba KJ, Kirk K. 2008. A verapamil-sensitive chloroquine-associated H⁺ leak from the digestive vacuole in chloroquine-resistant malaria parasites. *J. Cell Sci.* 121:1624–32
74. Lehane AM, van Schalkwyk DA, Valderramos SG, Fidock DA, Kirk K. 2011. Differential drug efflux or accumulation does not explain variation in the chloroquine response of *Plasmodium falciparum* strains expressing the same isoform of mutant PfCRT. *Antimicrob. Agents Chemother.* 55:2310–18
75. Lewis IA, Wacker M, Olszewski KL, Cobbold SA, Baska KS, et al. 2014. Metabolic QTL analysis links chloroquine resistance in *Plasmodium falciparum* to impaired hemoglobin catabolism. *PLOS Genet.* 10:e1004085
76. Li H, O'Donoghue AJ, van der Linden WA, Xie SC, Yoo E, et al. 2016. Structure- and function-based design of *Plasmodium*-selective proteasome inhibitors. *Nature* 530:233–36
77. Li W, Mo W, Shen D, Sun L, Wang J, et al. 2005. Yeast model uncovers dual roles of mitochondria in action of artemisinin. *PLOS Genet.* 1:e36
78. Loesbanluechai D, Kotanan N, de Cozar C, Kochakarn T, Ansbro MR, et al. 2019. Overexpression of plasmepsin II and plasmepsin III does not directly cause reduction in *Plasmodium falciparum* sensitivity to artesunate, chloroquine and piperazine. *Int. J. Parasitol. Drugs Drug Resist.* 9:16–22
79. Lu F, Culleton R, Zhang M, Ramaprasad A, von Seidlein L, et al. 2017. Emergence of indigenous artemisinin-resistant *Plasmodium falciparum* in Africa. *N. Engl. J. Med.* 376:991–93
80. MalariaGen *Plasmodium falciparum* Community Proj. 2016. Genomic epidemiology of artemisinin resistant malaria. *eLife* 5:e08714
81. Martin RE, Marchetti RV, Cowan AI, Howitt SM, Broer S, Kirk K. 2009. Chloroquine transport via the malaria parasite's chloroquine resistance transporter. *Science* 325:1680–82
82. Mathieu LC, Cox H, Early AM, Mok S, Lazrek Y, et al. 2020. Local emergence in Amazonia of *Plasmodium falciparum* k13 C580Y mutants associated with *in vitro* artemisinin resistance. *eLife* 9:e51015
83. Maude RJ, Nguon C, Dondorp AM, White LJ, White NJ. 2014. The diminishing returns of atovaquone-proguanil for elimination of *Plasmodium falciparum* malaria: modelling mass drug administration and treatment. *Malar. J.* 13:380
84. Mbengue A, Bhattacharjee S, Pandharkar T, Liu H, Estiu G, et al. 2015. A molecular mechanism of artemisinin resistance in *Plasmodium falciparum* malaria. *Nature* 520:683–87
85. McLean KJ, Jacobs-Lorena M. 2017. *Plasmodium falciparum* Maf1 confers survival upon amino acid starvation. *mBio* 8:e02317-16
86. Menard D, Dondorp A. 2017. Antimalarial drug resistance: a threat to malaria elimination. *Cold Spring Harb. Perspect. Med.* 7:a025619

87. Menard D, Khim N, Beghain J, Adegnika AA, Shafiu-Alam M, et al. 2016. A worldwide map of *Plasmodium falciparum* K13-propeller polymorphisms. *N. Engl. J. Med.* 374:2453–64
88. Menard S, Ben Haddou T, Ramadani AP, Arieu F, Iriart X, et al. 2015. Induction of multidrug tolerance in *Plasmodium falciparum* by extended artemisinin pressure. *Emerg. Infect. Dis.* 21:1733–41
89. Miotto O, Amato R, Ashley EA, MacInnis B, Almagro-Garcia J, et al. 2015. Genetic architecture of artemisinin-resistant *Plasmodium falciparum*. *Nat. Genet.* 47:226–34
90. Miotto O, Sekihara M, Tachibana S-I, Yamauchi M, Pearson RD, et al. 2019. Emergence of artemisinin-resistant *Plasmodium falciparum* with *kelch13* C580Y mutations on the island of New Guinea. bioRxiv 621813
91. Mok S, Ashley EA, Ferreira PE, Zhu L, Lin Z, et al. 2015. Population transcriptomics of human malaria parasites reveals the mechanism of artemisinin resistance. *Science* 347:431–35
92. Mukherjee A, Bopp S, Magistrado P, Wong W, Daniels R, et al. 2017. Artemisinin resistance without *pfkelch13* mutations in *Plasmodium falciparum* isolates from Cambodia. *Malar. J.* 16:195
93. Mukherjee A, Gagnon D, Wirth DF, Richard D. 2018. Inactivation of plasmepsins 2 and 3 sensitizes *Plasmodium falciparum* to the antimalarial drug piperazine. *Antimicrob. Agents Chemother.* 62:e02309–17
94. Nair S, Li X, Arya GA, McDew-White M, Ferrari M, et al. 2018. Fitness costs and the rapid spread of *kelch13*-C580Y substitutions conferring artemisinin resistance. *Antimicrob. Agents Chemother.* 62:e00605–18
95. Nakazawa S, Maoka T, Uemura H, Ito Y, Kanbara H. 2002. Malaria parasites giving rise to recrudescence in vitro. *Antimicrob. Agents Chemother.* 46:958–65
96. Ncokazi KK, Egan TJ. 2005. A colorimetric high-throughput β -hematin inhibition screening assay for use in the search for antimalarial compounds. *Anal. Biochem.* 338:306–19
97. Noedl H, Se Y, Schaefer K, Smith BL, Socheat D, et al. 2008. Evidence of artemisinin-resistant malaria in western Cambodia. *N. Engl. J. Med.* 359:2619–20
98. Nsoby SL, Dokomajilar C, Joloba M, Dorsey G, Rosenthal PJ. 2007. Resistance-mediating *Plasmodium falciparum* *pfprt* and *pfmdr1* alleles after treatment with artesunate-amodiaquine in Uganda. *Antimicrob. Agents Chemother.* 51:3023–25
99. Ochong E, Tumwebaze PK, Byaruhanga O, Greenhouse B, Rosenthal PJ. 2013. Fitness consequences of *Plasmodium falciparum* *pfmdr1* polymorphisms inferred from *ex vivo* culture of Ugandan parasites. *Antimicrob. Agents Chemother.* 57:4245–51
100. Olafson KN, Ketchum MA, Rimer JD, Vekilov PG. 2015. Mechanisms of hematin crystallization and inhibition by the antimalarial drug chloroquine. *PNAS* 112:4946–51
101. Packard RM. 2014. The origins of antimalarial-drug resistance. *N. Engl. J. Med.* 371:397–99
102. Parobek CM, Parr JB, Brazeau NF, Lon C, Chaorattanakawee S, et al. 2017. Partner-drug resistance and population substructuring of artemisinin-resistant *Plasmodium falciparum* in Cambodia. *Genome Biol. Evol.* 9:1673–86
103. Patzewitz EM, Salcedo-Sora JE, Wong EH, Sethia S, Stocks PA, et al. 2013. Glutathione transport: a new role for PfCRT in chloroquine resistance. *Antioxid. Redox Signal.* 19:683–95
104. Peatey CL, Chavchich M, Chen N, Gresty KJ, Gray KA, et al. 2015. Mitochondrial membrane potential in a small subset of artemisinin-induced dormant *Plasmodium falciparum* parasites in vitro. *J. Infect. Dis.* 212:426–34
105. Pelleau S, Moss EL, Dhingra SK, Volney B, Casteras J, et al. 2015. Adaptive evolution of malaria parasites in French Guiana: Reversal of chloroquine resistance by acquisition of a mutation in *pfprt*. *PNAS* 112:11672–77
106. Phuc BQ, Rasmussen C, Duong TT, Dong LT, Loi MA, et al. 2017. Treatment failure of dihydroartemisinin/piperazine for *Plasmodium falciparum* malaria, Vietnam. *Emerg. Infect. Dis.* 23:715–17
107. Phy AP, Ashley EA, Anderson TJC, Bozdech Z, Carrara VI, et al. 2016. Declining efficacy of artemisinin combination therapy against *P. falciparum* malaria on the Thai-Myanmar border (2003–2013): the role of parasite genetic factors. *Clin. Infect. Dis.* 63:784–91
108. Pulcini S, Staines HM, Lee AH, Shafik SH, Bouyer G, et al. 2015. Mutations in the *Plasmodium falciparum* chloroquine resistance transporter, PfCRT, enlarge the parasite's food vacuole and alter drug sensitivities. *Sci. Rep.* 5:14552

109. Reed MB, Saliba KJ, Caruana SR, Kirk K, Cowman AF. 2000. Pgh1 modulates sensitivity and resistance to multiple antimalarials in *Plasmodium falciparum*. *Nature* 403:906–9
110. Rocamora F, Zhu L, Liong KY, Dondorp A, Miotto O, et al. 2018. Oxidative stress and protein damage responses mediate artemisinin resistance in malaria parasites. *PLoS Pathog.* 14:e1006930
111. Rohrbach P, Sanchez CP, Hayton K, Friedrich O, Patel J, et al. 2006. Genetic linkage of *pfmdr1* with food vacuolar solute import in *Plasmodium falciparum*. *EMBO J.* 25:3000–11
112. Roper C, Pearce R, Nair S, Sharp B, Nosten F, Anderson T. 2004. Intercontinental spread of pyrimethamine-resistant malaria. *Science* 305:1124
113. Rosenthal PJ. 2013. The interplay between drug resistance and fitness in malaria parasites. *Mol. Microbiol.* 89:1025–38
114. Ross LS, Dhingra SK, Mok S, Yeo T, Wicht KJ, et al. 2018. Emerging Southeast Asian PfCRT mutations confer *Plasmodium falciparum* resistance to the first-line antimalarial piperavaquine. *Nat. Commun.* 9:3314
115. Ross LS, Fidock DA. 2019. Elucidating mechanisms of drug-resistant *Plasmodium falciparum*. *Cell Host Microbe* 26:35–47
116. Sa JM, Twu O, Hayton K, Reyes S, Fay MP, et al. 2009. Geographic patterns of *Plasmodium falciparum* drug resistance distinguished by differential responses to amodiaquine and chloroquine. *PNAS* 106:18883–89
117. Sanchez CP, Rohrbach P, McLean JE, Fidock DA, Stein WD, Lanzer M. 2007. Differences in trans-stimulated chloroquine efflux kinetics are linked to PfCRT in *Plasmodium falciparum*. *Mol. Microbiol.* 64:407–20
118. Sanchez CP, Rotmann A, Stein WD, Lanzer M. 2008. Polymorphisms within PfMDR1 alter the substrate specificity for anti-malarial drugs in *Plasmodium falciparum*. *Mol. Microbiol.* 70:786–98
119. Shaw PJ, Chaotheing S, Kaewprommal P, Piriyaongsa J, Wongsombat C, et al. 2015. *Plasmodium* parasites mount an arrest response to dihydroartemisinin, as revealed by whole transcriptome shotgun sequencing (RNA-seq) and microarray study. *BMC Genom.* 16:830
120. Siddiqui G, Srivastava A, Russell AS, Creek DJ. 2017. Multi-omics based identification of specific biochemical changes associated with PfKelch13-mutant artemisinin-resistant *Plasmodium falciparum*. *J. Infect. Dis.* 215:1435–44
121. Sidhu AB, Uhlemann AC, Valderramos SG, Valderramos JC, Krishna S, Fidock DA. 2006. Decreasing *pfmdr1* copy number in *Plasmodium falciparum* malaria heightens susceptibility to mefloquine, lumefantrine, halofantrine, quinine, and artemisinin. *J. Infect. Dis.* 194:528–35
122. Sidhu AB, Verdier-Pinard D, Fidock DA. 2002. Chloroquine resistance in *Plasmodium falciparum* malaria parasites conferred by *pfprt* mutations. *Science* 298:210–13
123. Skinner-Adams TS, Fisher GM, Riches AG, Hutt OE, Jarvis KE, et al. 2019. Cyclization-blocked proguanil as a strategy to improve the antimalarial activity of atovaquone. *Commun. Biol.* 2:166
124. Small-Saunders JL, Hagenah L, Fidock DA. 2020. Turning the tide: targeting PfCRT to combat drug-resistant *P. falciparum*? *Nat. Rev. Microbiol.* 18:261–62
125. Spring MD, Lin JT, Manning JE, Vanachayangkul P, Somethy S, et al. 2015. Dihydroartemisinin-piperavaquine failure associated with a triple mutant including *kelch13 C580Y* in Cambodia: an observational cohort study. *Lancet Infect. Dis.* 15:683–91
126. St. Laurent B, Miller B, Burton TA, Amaratunga C, Men S, et al. 2015. Artemisinin-resistant *Plasmodium falciparum* clinical isolates can infect diverse mosquito vectors of Southeast Asia and Africa. *Nat. Commun.* 6:8614
127. Staines HM, Burrow R, Teo BH, Chis Ster I, Kreamsner PG, Krishna S. 2018. Clinical implications of *Plasmodium* resistance to atovaquone/proguanil: a systematic review and meta-analysis. *J. Antimicrob. Chemother.* 73:581–95
128. Stokes BH, Yoo E, Murithi JM, Luth MR, Afanasyev P, et al. 2019. Covalent *Plasmodium falciparum*-selective proteasome inhibitors exhibit a low propensity for generating resistance *in vitro* and synergize with multiple antimalarial agents. *PLoS Pathog.* 15:e1007722
129. Straimer J, Gnadig NF, Stokes BH, Ehrenberger M, Crane AA, Fidock DA. 2017. *Plasmodium falciparum* K13 mutations differentially impact ozonide susceptibility and parasite fitness *in vitro*. *mBio* 8:e00172-17
130. Straimer J, Gnadig NF, Witkowski B, Amaratunga C, Duru V, et al. 2015. K13-propeller mutations confer artemisinin resistance in *Plasmodium falciparum* clinical isolates. *Science* 347:428–31

131. Sullivan DJ. 2002. Theories on malarial pigment formation and quinoline action. *Int. J. Parasitol.* 32:1645–53
132. Sullivan DJ. 2013. *Plasmodium* drug targets outside the genetic control of the parasite. *Curr. Pharm. Des.* 19:282–89
133. Sutherland CJ, Lansdell P, Sanders M, Muwanguzi J, van Schalkwyk DA, et al. 2017. *pfk13*-independent treatment failure in four imported cases of *Plasmodium falciparum* malaria treated with artemether-lumefantrine in the United Kingdom. *Antimicrob. Agents Chemother.* 61:e02382–16
134. Tacoli C, Gai PP, Bayingana C, Sift K, Geus D, et al. 2016. Artemisinin resistance-associated K13 polymorphisms of *Plasmodium falciparum* in Southern Rwanda, 2010–2015. *Am. J. Trop. Med. Hyg.* 95:1090–93
135. Takala-Harrison S, Clark TG, Jacob CG, Cummings MP, Miotto O, et al. 2013. Genetic loci associated with delayed clearance of *Plasmodium falciparum* following artemisinin treatment in Southeast Asia. *PNAS* 110:240–45
136. Takala-Harrison S, Jacob CG, Arze C, Cummings MP, Silva JC, et al. 2015. Independent emergence of artemisinin resistance mutations among *Plasmodium falciparum* in Southeast Asia. *J. Infect. Dis.* 211:670–79
137. Teuscher F, Gatton ML, Chen N, Peters J, Kyle DE, Cheng Q. 2010. Artemisinin-induced dormancy in *Plasmodium falciparum*: duration, recovery rates, and implications in treatment failure. *J. Infect. Dis.* 202:1362–68
138. Thapar MM, Gil JP, Bjorkman A. 2005. *In vitro* recrudescence of *Plasmodium falciparum* parasites suppressed to dormant state by atovaquone alone and in combination with proguanil. *Trans. R. Soc. Trop. Med. Hyg.* 99:62–70
139. Tu Y. 2016. Artemisinin—a gift from traditional Chinese medicine to the world (Nobel lecture). *Angew. Chem. Int. Ed. Engl.* 55:10210–26
- 139a. Uwimana A, Legrand E, Stokes BH, Ndikumana J-LM, Warsame M, et al. 2020. Emergence and clonal expansion of *in vitro* artemisinin-resistant *Plasmodium falciparum* Kelch13 R561H mutant parasites in Rwanda. *Nat. Med.* In press
140. Valderramos SG, Valderramos JC, Musset L, Purcell LA, Mercereau-Puijalon O, et al. 2010. Identification of a mutant PfCRT-mediated chloroquine tolerance phenotype in *Plasmodium falciparum*. *PLOS Pathog.* 6:e1000887
141. van Biljon R, Niemand J, van Wyk R, Clark K, Verlinden B, et al. 2018. Inducing controlled cell cycle arrest and re-entry during asexual proliferation of *Plasmodium falciparum* malaria parasites. *Sci. Rep.* 8:16581
142. van der Pluijm RW, Imwong M, Chau NH, Hoa NT, Thuy-Nhien NT, et al. 2019. Determinants of dihydroartemisinin-piperaquine treatment failure in *Plasmodium falciparum* malaria in Cambodia, Thailand, and Vietnam: a prospective clinical, pharmacological, and genetic study. *Lancet Infect. Dis.* 19:952–61
143. van der Pluijm RW, Tripura R, Hoglund RM, Pyae Phy A, Lek D, et al. 2020. Triple artemisinin-based combination therapies versus artemisinin-based combination therapies for uncomplicated *Plasmodium falciparum* malaria: a multicentre, open-label, randomised clinical trial. *Lancet* 395:1345–60
144. Veiga MI, Dhingra SK, Henrich PP, Straimer J, Gnadig N, et al. 2016. Globally prevalent PfMDR1 mutations modulate *Plasmodium falciparum* susceptibility to artemisinin-based combination therapies. *Nat. Commun.* 7:11553
145. Venkatesan M, Gadalla NB, Stepniewska K, Dahal P, Nsanjabana C, et al. 2014. Polymorphisms in *Plasmodium falciparum* chloroquine resistance transporter and multidrug resistance 1 genes: parasite risk factors that affect treatment outcomes for *P. falciparum* malaria after artemether-lumefantrine and artesunate-amodiaquine. *Am. J. Trop. Med. Hyg.* 91:833–43
146. von Seidlein L, Peto TJ, Landier J, Nguyen TN, Tripura R, et al. 2019. The impact of targeted malaria elimination with mass drug administrations on falciparum malaria in Southeast Asia: A cluster randomised trial. *PLOS Med.* 16:e1002745
147. Wang J, Huang L, Li J, Fan Q, Long Y, et al. 2010. Artemisinin directly targets malarial mitochondria through its specific mitochondrial activation. *PLOS ONE* 5:e9582
148. Wang J, Zhang CJ, Chia WN, Loh CC, Li Z, et al. 2015. Haem-activated promiscuous targeting of artemisinin in *Plasmodium falciparum*. *Nat. Commun.* 6:10111

149. Wang Z, Cabrera M, Yang J, Yuan L, Gupta B, et al. 2016. Genome-wide association analysis identifies genetic loci associated with resistance to multiple antimalarials in *Plasmodium falciparum* from China-Myanmar border. *Sci. Rep.* 6:33891
150. Wellems TE, Plowe CV. 2001. Chloroquine-resistant malaria. *J. Infect. Dis.* 184:770–76
151. White NJ. 2004. Antimalarial drug resistance. *J. Clin. Investig.* 113:1084–92
152. White NJ. 2011. The parasite clearance curve. *Malar. J.* 10:278
153. White NJ, Pukrittayakamee S, Hien TT, Faiz MA, Mokuolu OA, Dondorp AM. 2014. Malaria. *Lancet* 383:723–35
154. Witkowski B, Amaratunga C, Khim N, Sreng S, Chim P, et al. 2013. Novel phenotypic assays for the detection of artemisinin-resistant *Plasmodium falciparum* malaria in Cambodia: *in-vitro* and *ex-vivo* drug-response studies. *Lancet Infect. Dis.* 13:1043–49
155. Witkowski B, Duru V, Khim N, Ross LS, Saintpierre B, et al. 2017. A surrogate marker of piperazine-resistant *Plasmodium falciparum* malaria: a phenotype-genotype association study. *Lancet Infect. Dis.* 17:174–83
156. Witkowski B, Lelievre J, Barragan MJ, Laurent V, Su XZ, et al. 2010. Increased tolerance to artemisinin in *Plasmodium falciparum* is mediated by a quiescence mechanism. *Antimicrob. Agents Chemother.* 54:1872–77
157. World Health Organ. 2019. *World malaria report 2019*. Rep., World Health Organ., Geneva. <https://www.who.int/publications-detail/world-malaria-report-2019>
158. WWARN K13 Genotype-Phenotype Study Group. 2019. Association of mutations in the *Plasmodium falciparum* Kelch13 gene (*Pf3D7_1343700*) with parasite clearance rates after artemisinin-based treatments—a WWARN individual patient data meta-analysis. *BMC Med.* 17:1
159. Xie SC, Dogovski C, Hanssen E, Chiu F, Yang T, et al. 2016. Haemoglobin degradation underpins the sensitivity of early ring stage *Plasmodium falciparum* to artemisinins. *J. Cell Sci.* 129:406–16
160. Yang T, Yeoh LM, Tutor MV, Dixon MW, McMillan PJ, et al. 2019. Decreased K13 abundance reduces hemoglobin catabolism and proteotoxic stress, underpinning artemisinin resistance. *Cell Rep.* 29:2917–28.e5
161. Zhan W, Visone J, Ouellette T, Harris JC, Wang R, et al. 2019. Improvement of asparagine ethylenediamines as anti-malarial *Plasmodium*-selective proteasome inhibitors. *J. Med. Chem.* 62:6137–45
162. Zhang H, Howard EM, Roepe PD. 2002. Analysis of the antimalarial drug resistance protein PfCRT expressed in yeast. *J. Biol. Chem.* 277:49767–75
163. Zhang J, Li N, Siddiqui FA, Xu S, Geng J, et al. 2019. *In vitro* susceptibility of *Plasmodium falciparum* isolates from the China-Myanmar border area to artemisinins and correlation with K13 mutations. *Int. J. Parasitol. Drugs Drug Resist.* 10:20–27
164. Zhang M, Gallego-Delgado J, Fernandez-Arias C, Waters NC, Rodriguez A, et al. 2017. Inhibiting the *Plasmodium* eIF2 α kinase PK4 prevents artemisinin-induced latency. *Cell Host Microbe* 22:766–76.e4
165. Zhang M, Wang C, Otto TD, Oberstaller J, Liao X, et al. 2018. Uncovering the essential genes of the human malaria parasite *Plasmodium falciparum* by saturation mutagenesis. *Science* 360:eaap7847
166. Zhu L, Tripathi J, Rocamora FM, Miotto O, van der Pluijm R, et al. 2018. The origins of malaria artemisinin resistance defined by a genetic and transcriptomic background. *Nat. Commun.* 9:5158

Review

Genomic and Genetic Approaches to Studying Antimalarial Drug Resistance and *Plasmodium* BiologyJohn Okombo,¹ Mariko Kanai,¹ Ioanna Deni,¹ and David A. Fidock^{1,2,*}

Recent progress in genomics and molecular genetics has empowered novel approaches to study gene functions in disease-causing pathogens. In the human malaria parasite *Plasmodium falciparum*, the application of genome-based analyses, site-directed genome editing, and genetic systems that allow for temporal and quantitative regulation of gene and protein expression have been invaluable in defining the genetic basis of antimalarial resistance and elucidating candidate targets to accelerate drug discovery efforts. Using examples from recent studies, we review applications of some of these approaches in advancing our understanding of *Plasmodium* biology and illustrate their contributions and limitations in characterizing parasite genomic loci associated with antimalarial drug responses.

Plasmodium Biology and Investigations into Antimalarial Resistance and Modes of Action

Malaria, caused by *Plasmodium* parasites, remains a leading cause of morbidity and mortality, especially in endemic resource-strained countries. According to World Health Organization (WHO) estimates, there were 229 million cases and 409 000 malaria-related deaths worldwide in 2019, the vast majority of which occurred in sub-Saharan Africa [1]. Of the six human-infecting *Plasmodium* species, *P. falciparum* is the most virulent and lethal [2]. This species has a complex life cycle in human and female *Anopheles* mosquito hosts, with human infections comprising a haploid asexual phase divided into a presymptomatic liver stage that produces an estimated 10 000–30 000 merozoites per parasite over a 1-week period, and an asexual blood stage (ABS) characterized by ~48 h cycles of invasion, differentiation, mitotic replication, and egress. A proportion of ABS parasites develop into male and female gametocytes that, when ingested by a feeding mosquito, form gametes that develop into zygotes, ookinetes, and subsequently oocysts on the midgut wall. Meiosis occurs during this period of sexual stage development in the mosquito. Inside these oocysts, haploid sporozoites form by sporogony and subsequently are released into the hemocoel, from where they migrate to the salivary glands. Sporozoites are then injected into a human host during a blood meal, where they enter the bloodstream and invade hepatocytes to initiate a new cycle of human infection. Strategies to control mosquito vector populations and to develop antimalarials active against ABS parasites and preferably additional life-cycle stages are essential to curtail the burden of disease.

Chemotherapy has been the mainstay of malaria control and prophylaxis, with antimalarial drugs endowed with different modes of action developed in the past century (Box 1). However, the ability of *P. falciparum*, in particular, to develop resistance to these treatments has compromised their efficacy and raised the importance of using combinations as well as developing new drugs and identifying novel targets. The current WHO-recommended first-line treatments of

Highlights

CRISPR/Cas9 and other site-specific gene-editing techniques enable rapid and efficient generation of knockouts, targeted integrants, and allelic replacements of genes associated with malaria pathogenesis and drug resistance.

Regulatable genetic systems that quantitatively and temporally modulate expression levels facilitate mechanistic studies, especially those involving essential genes, and help distinguish on-target from off-target effects.

New or refined whole-genome-based strategies, such as functional genomic screens and genetic crosses in humanized mice, now accompany traditional techniques, including genome-wide association studies (GWAS) and gene editing to identify and characterize genetic determinants of resistance.

¹Department of Microbiology & Immunology, Department of Medicine, Columbia University Irving Medical Center, New York, NY, USA

²Division of Infectious Diseases, Department of Medicine, Columbia University Irving Medical Center, New York, NY, USA

*Correspondence: df2660@cumc.columbia.edu (D.A. Fidock).



Box 1. Antimalarials: Mode of Action and Mechanisms of Resistance

Antimalarial drugs in current clinical use are endowed with different modes of action and mechanisms of resistance [5,8,113]. QN, a former frontline antimalarial for *P. falciparum* used since the early 17th century, has been slow to select for resistance. This drug is currently used to treat uncomplicated *P. falciparum* malaria in pregnant women and provides an alternative to artesunate for severe malaria. QN has a complex mode of action that includes the inhibition of heme detoxification. The mechanism of QN resistance is multifactorial and is partially associated with polymorphisms in *pfcr*, *pfmdr1*, and potentially other genes. Similar to QN, CQ diffuses inside the parasite's DV and prevents the biomineralization of toxic free heme into hemozoin. CQ^R is driven primarily by mutations in PfCRT (including K76T), which enable CQ efflux outside the DV, thus preventing drug accumulation at its primary site of action. ADQ, a 4-aminoquinoline structurally similar to CQ, also targets the heme detoxification pathway. Due to its ability to accumulate to high levels in the DV, ADQ and its metabolites are active against many CQ-resistant parasites. ADQ is currently an integral constituent of ACTs as a fixed-dose combination with artesunate. Reduced parasite sensitivity to ADQ has been associated with polymorphisms in PfMDR1, including N86Y and D1246Y, which have been selected for by ADQ therapy in different malaria-endemic settings. PPQ, another 4-aminoquinoline and ACT partner drug (used in combination with DHA), also targets heme detoxification. PPQ^R is driven by point mutations in PfCRT (including F145I, T93S, I218F on the background of the Dd2 haplotype) and appears to be augmented via amplifications in plasmepsins II and III.

Sulfadoxine plus pyrimethamine (SP) is a synergistic combination used for intermittent preventive treatment in pregnancy and infancy. SP interferes with folate biosynthesis, which is essential for DNA synthesis and parasite growth. Pyrimethamine inhibits PfDHFR while sulfadoxine inhibits PfDHPS. High-grade SP resistance occurs in mutant parasites harboring N51I, C59R, and S108N point mutations in PfDHFR and A437G and K540E in PfDHPS.

Artemisinins are the current frontline antimalarials and are effective at killing asexual rings and trophozoites. ART and its derivatives are activated by Fe²⁺-heme, a byproduct of hemoglobin, and kill parasites by alkylating heme, proteins, and lipids. ART^R is driven by point mutations in PfK13, which reduce ring-stage endocytosis of hemoglobin and enable parasite survival. The exact mechanism of action of the other ACT partner drugs, lumefantrine and MFQ, still remains unknown, although it might, in part, involve inhibition of hemoglobin endocytosis. Recent efforts to identify new antimalarial compounds with low propensity to succumb to resistance have led to the discovery of 'irresistible' compounds further discussed in Box 2.

uncomplicated malaria, caused by asexual parasites, depend on artemisinin-based combination therapies (ACTs). These treatments comprise fast-acting semisynthetic derivatives of the endoperoxide artemisinin (ART) that rapidly reduce parasite biomass, partnered with slower-acting but longer-lasting drugs to eliminate surviving parasites. The use of long-lasting insecticide-treated bed nets, indoor residual spraying, intermittent preventive treatment in infancy and pregnancy, and the global adoption of ACTs together have contributed to a significant reduction in malaria deaths between 2000 and 2015 [3]. However, this progress in malaria control has stalled, a situation aggravated by the spread of parasite and mosquito vector resistance to the front-line drugs and insecticides, respectively [4,5]. In addition, the persistent threat of asymptomatic chronic infections that serve as parasite reservoirs that maintain the life cycle and allow for onward transmission [6], and the limited efficacy of the **RTS,S/AS01** (see Glossary) candidate vaccine [7], necessitate sustained efforts towards achieving comprehensive malaria control. To expand the current antimalarial arsenal and overcome the shortcomings of ACTs, a detailed understanding of *P. falciparum* biology is crucial to identify druggable targets against which efficacious therapeutics can be developed.

The complexity of the *Plasmodium* life cycle presents opportunities to develop drugs with prophylactic (liver stage), curative (AS), and/or transmission-blocking (gametocyte stage) activity. Drug discovery efforts have focused predominantly on *P. falciparum* AS parasites in part because of the ease of *in vitro* culture, and challenges in generating sufficient numbers of liver stages and gametocytes required to screen large compound libraries. Indeed, several physiological processes in AS parasites, including host hemoglobin degradation and detoxification, folic acid biosynthesis, the mitochondrial electron transport chain, and pyrimidine biosynthesis, constitute important targets for antimalarials in clinical use or under development [8]. The development of reliable platforms for interrogating gametocytocidal and liver-stage inhibitors has now broadened

Glossary

BioID: a screening approach in which the protein of interest is fused to a biotin ligase that biotinylates proximal proteins, facilitating the identification of *in situ* protein interacting partners upon addition of biotin and subsequent biotin-avidin capture.

FRG-NOD human-liver chimeric (FRG huHep) mouse:

immunocompromised human liver-chimeric mouse that can be inoculated with *P. falciparum* sporozoites and later injected with human RBCs to facilitate the mosquito to liver to blood stage transitions for the progeny of *P. falciparum* genetic crosses.

Genome-wide association studies (GWAS):

a genetic approach involving an analysis of distinct field isolate genomes and their associated *in vitro* or *in vivo* phenotypes (including drug resistance) to determine genetic markers that strongly associate with those phenotypes and thus identify biomarkers for predictive purposes.

Homologous recombination:

a mechanism for exchanging genetic information between two homologous double-stranded DNA sequences. In AS parasites this mechanism can be leveraged to achieve allelic exchange following episomal plasmid-based single or double crossover events, or gene editing via the induction of ZFN- or CRISPR/Cas9-mediated double stranded breaks that trigger homology-directed repair using a donor template. Homologous recombination also creates recombinant progeny during meiosis between sexual stage parasites in mosquito midguts.

Hypermutator line: a *P. falciparum* Dd2 line with the D308A and E310A point mutations in the DNA polymerase δ that ablate the polymerase's proofreading (exonuclease) activity, which was earlier shown to increase the overall DNA mutation rate in *P. berghei* [112].

Quantitative trait locus (QTL)

mapping: a statistical method of localizing chromosomal regions that affect the variation in quantitative traits by linking genotypic data (e.g SNPs) to phenotypic data (e.g. *in vitro* drug responses).

RTS,S/AS01: a recombinant malaria vaccine containing part of the *P. falciparum* circumsporozoite protein, co-expressed with hepatitis B surface antigen to induce anti-circumsporozoite

the scope of antimalarial drug discovery, and high-throughput phenotypic screening has led to the identification of new broad-range antimalarial chemical scaffolds with multistage activity [9–15]. Research into the modes of action of hits identified in these high-throughput phenotypic screens can then drive subsequent drug development and help to identify mechanisms through which parasites can develop resistance.

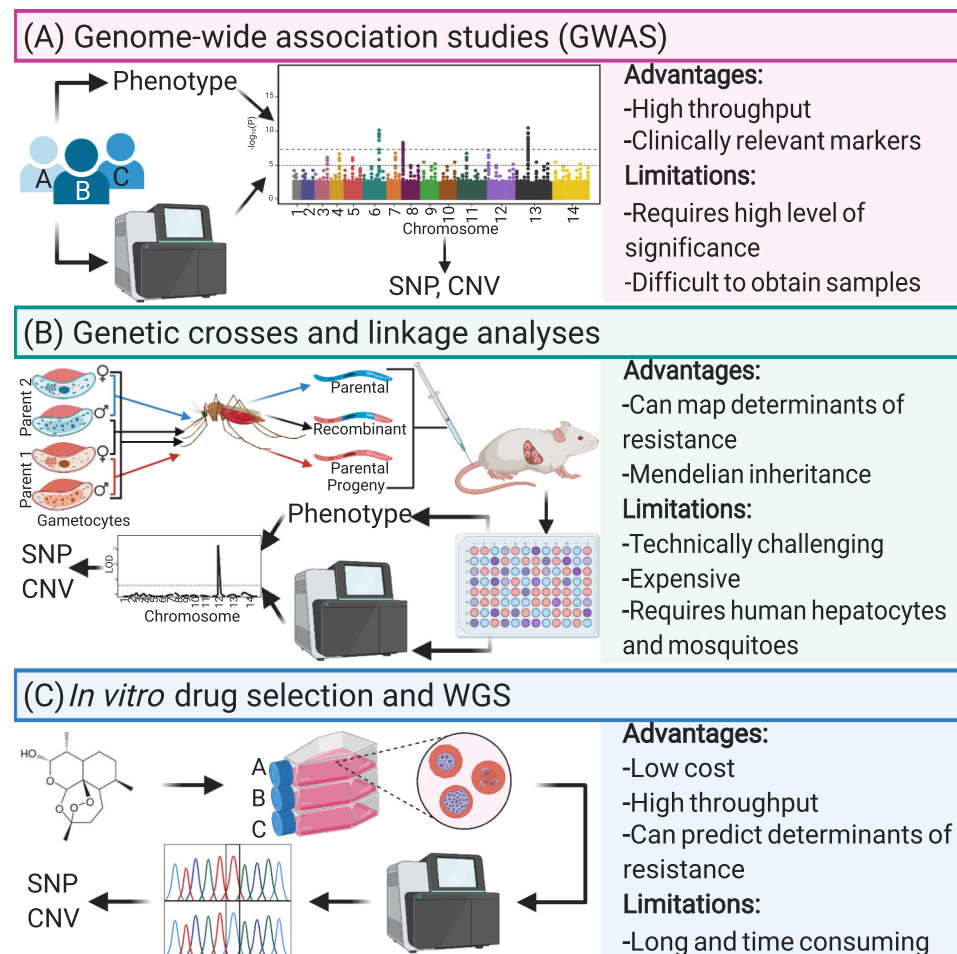
The rapid acceleration in generating *P. falciparum* genome sequences and the implementation of other 'omic' tools, including chemoproteomics and metabolic fingerprinting, have significantly enhanced approaches for studying critical physiological processes in *P. falciparum* parasites [16,17]. As examples, chemoproteomic profiling identified phosphatidylinositol 4-kinase and cGMP-dependent protein kinase (PfPKG) as targets of potent antiplasmodial targets, as confirmed using resistance selection and conditional knockdown approaches [18,19]. Genomic and genetic tools have also been invaluable in dissecting mechanisms of antimalarial drug resistance and other processes such as intracellular protein trafficking and red blood cell (RBC) egress and invasion [20–23]. This review recaps whole-genome approaches, including *in vitro* resistance evolution, genome-wide association studies (GWAS), and experimental genetic crosses, along with landmark genetic findings, which have set the stage for current investigations into antimalarial drug resistance and *Plasmodium* biology.

Harnessing *Plasmodium* Genomes to Map Antimalarial Resistance Determinants

GWAS of Antimalarial Resistance

Human-infecting *Plasmodium* species have compact genomes of approximately 23–34 Mb which, in *P. falciparum*, encode ~5400 protein-coding genes, along with a varying number of subtelomeric multigene families, spanning 14 chromosomes. These genomic data have enabled the identification of genes contributing to various parasite traits, particularly those of antimalarial drug responses. GWAS investigations constitute a powerful genome-based approach to elucidating genetic determinants of antimalarial resistance (Figure 1A). The first *P. falciparum* GWAS report used geographically diverse isolates to characterize the parasite population structure, recombination rates, and loci under recent positive selection [24]. Another GWAS search for loci correlated with resistance to 13 antimalarials identified a new halofantrine resistance locus, PF3D7_1036300, whose overexpression was associated with decreased sensitivity to halofantrine, mefloquine (MFQ) and lumefantrine, and whose copy number amplification also mediated resistance [25]. Subsequent functional validation analyses using Δ PF3D7_1036300 parasites revealed increased sensitivity to the aryl-amino alcohols but not unrelated antimalarials, suggesting chemical class specificity. Analyses of field isolates revealed that the C591S allele of this locus strongly associated with halofantrine sensitivity among Senegalese samples and was linked to reduced sensitivity to lumefantrine in Kenya (reviewed in [26]). In another GWAS on culture-adapted isolates from Kenya, *in vitro* responses to 22 antimalarials mapped to loci including *P. falciparum* dihydrofolate reductase (*pf dhfr*, PF3D7_0417200), dihydropteroate synthetase (*pf dhps*, PF3D7_0810800), multidrug resistance protein 1 (*pf mdr1*, PF3D7_0523000), chloroquine resistance transporter (*pf crt*, PF3D7_0709000), and the sodium/hydrogen exchanger (*pinhe-1*, PF3D7_1303500), and reported a putative association between amodiaquine (ADQ) activity and SNPs in cysteine desulfurase (PF3D7_0716600) [27]. Another study on ten common antimalarials, using isolates from the China–Myanmar border region with a history of ART usage, identified several loci associated with various drug responses including *pf crt* and *pf dhfr*. This study also associated the autophagy-related protein 18 (PF3D7_1012900) with decreased parasite sensitivities to dihydroartemisinin (DHA), artemether and piperaquine (PPQ) [28]. Genome-wide associations between *in vitro* chloroquine (CQ)-sensitive and PPQ-resistant phenotypes and the C350R mutation in *pf crt* have also been shown with isolates from French Guyana [29].

antibodies and circumsporozoite-specific CD4-positive T cells associated with protection from *P. falciparum* infection and episodes of clinical malaria. RTS,S (co-administered with AS01 as an adjuvant) is the only malaria vaccine to reach Phase III testing and is currently in WHO pilot implementation in Ghana, Kenya, and Malawi.



Trends in Parasitology

Figure 1. Genomic Approaches for Studying Drug Resistance (A) Genome-wide association studies (GWAS): *Plasmodium falciparum* parasites are isolated from infected patients, profiled *in vitro* against antimalarial drugs of interest, and genotyped (using whole-genome sequencing (WGS), microsatellite markers, or oligonucleotide arrays). These datasets are analyzed (as depicted visually in the Manhattan plot) to identify genetic variants associated with resistance. (B) Genetic crosses and linkage analyses: gametocytes from genetically distinct parental parasites are fed to *Anopheles* mosquitoes wherein they undergo sexual reproduction and genetic recombination, creating both parental and new recombinant genotypes. The resulting sporozoite haploid progeny are inoculated into FRG huHep mice by intravenous injection or mosquito bite, after which they develop inside the engrafted human hepatocytes and complete the liver- to blood-stage transition after injection of human RBCs 6 to 7 days later. Progeny are cloned by limiting dilution and then genotyped and phenotyped. QTL analysis is conducted (as shown in the log of the odds (LOD) plot) to localize the genetic determinant(s) of resistance and the polymorphisms that associate with the drug response variation. (C) *In vitro* drug selection and WGS (also known as *in vitro* evolution and whole-genome analysis [115]): antiplasmodial compounds are used to pressure *P. falciparum* parasites to select for recrudescence, resistant parasites. Genomic DNA of bulk cultures or their clones is sent for WGS, along with the parental strain, to identify genetic polymorphisms such as SNPs and CNVs that may underlie the resistance phenotype. Abbreviation: CNV, copy number variation.

Epidemiological investigations into antimalarial resistance have also benefited from large-scale genetic field studies that have corroborated clinical evidence of increasing rates of ACT treatment failure. These include reports associating *P. falciparum* kelch13 (*pfk13*, PF3D7_1343700) mutations with slow parasite clearance in ART-treated patients [30,31], and amplification of the hemoglobin protease plasmepsins II and III with PPQ resistance (PPQ^R) [32,33]. Analyses of

Box 2. Irresistible Compounds as Attractive Antimalarial Candidates

Antimalarial drug development is currently focused on the need to identify compounds that can rapidly lower parasite biomass to stop disease progression, have multistage activity, and possess low propensity to develop resistance. Physicochemical and structural features that confer fast-killing and multitarget inhibition profiles could help to make a compound less prone to succumbing to resistance. In a recent analysis of diverse antimalarial compounds, acquisition of resistant *P. falciparum* parasites was repeatedly unsuccessful for 24 of the 48 inhibitors assessed [114]. These compounds, fittingly dubbed ‘irresistibles’, present interesting candidates for drug development due to their lower likelihood of early failure from acquired drug resistance and strong correlation with fast-killing kinetics [114,115]. Recent attempts to evaluate their resistance mechanisms and targets have involved selections with parasites that present with different chemosensitivity profiles [116] or a **hypermutator line** with an enhanced mutation rate [117]. Proteomic and metabolomic approaches as well as selection experiments in a closely related organism like *Toxoplasma gondii* [118,119] or a surrogate species like *Saccharomyces cerevisiae* [120] can provide additional methods for studying these compounds.

whole-genome variation in *P. falciparum* clinical samples from Asia and sub-Saharan Africa have also identified patterns of parasite population structure shaped by antimalarial selection pressure [34] and tracked the origins and dissemination of drug-resistant lineages and mutations [35].

Using Experimental Genetic Crosses and Linkage Analysis to Map Determinants

Experimental genetic crosses, which involve sexual-stage recombination between two genetically distinct parasites to create recombinant progeny, are another powerful forward genetics tool to investigate the genetic basis of phenotypes including RBC invasion and growth, transmission, nutrient transport, and drug resistance, as well as studying the *Plasmodium* genome itself [14,26] (Box 3). Marker–trait associations between phenotypic and genotypic data can be invoked from linkage analyses using **quantitative trait locus (QTL) mapping**, and the identified locus scanned to narrow down candidate genes (Figure 1B) [36–38]. Genetic determinants can then be validated by gene editing and phenotype profiling and examined in subsequent functional experiments. Although earlier studies of *P. falciparum* genetic crosses (Table 1) utilized splenectomized chimpanzees and monkeys to complete the human stages of the life cycle [26], recent crosses have used **FRG-NOD human liver-chimeric (FRG huHep) mice** that support *P. falciparum* liver and ABS infections [14,39,40].

The first two genetic crosses, HB3×3D7 and HB3×Dd2, were used to map pyrimethamine and CQ resistance (CQ^R) to *pfdhfr* and *pfcr*, respectively [26]. Analysis of the HB3×Dd2 cross

Box 3. *P. falciparum* Crosses Using Humanized Mice and Linkage Analyses

In the published *P. falciparum* genetic cross protocol utilizing human-liver chimeric immunodeficient (*Rag2^{-/-}/IL2Rγ^{-/-}*) FRG huHep mice [14,40], sporozoites resulting from meiotic recombination between distinct strains in infected mosquitoes are isolated from *Anopheles* salivary glands and injected into FRG huHep mice. These mice lack fumaryl acetoacetate hydrolase (FAH) that catabolizes toxic metabolites in blood and other tissues, resulting in liver damage. Cycling of NTBC (Nitisinone) results in depletion of mouse hepatocytes and facilitates repopulation of the mouse liver with human hepatocytes. These mice receive infusions of human RBCs, allowing parasites that emerge from human hepatocytes to initiate ABS development. These parasites are recovered and cloned for subsequent phenotyping and genotyping. QTL analysis is used to map loci associated with inheritance of a quantifiable phenotypic trait. A major single-gene trait will segregate phenotypic data into two groups, as shown for *pfcr* for CQ^R, while a multigene, quantitative trait will exhibit a continuous phenotypic distribution, as seen for QN [46]. QTL is expressed as a log of the odds (LOD) score, which is the logarithm to base 10 of the ratio of the likelihood of a model with a QTL versus a model without a QTL. As exemplified in the cited studies, the QTL locus can be scanned for polymorphisms between parents in genes or gene expression levels to narrow down the candidate gene list. Candidate loci can then be validated by phenotyping genetically edited parasites. An alternative approach is to directly phenotype and genotype progeny in bulk populations by applying selective pressure (alongside controls) and assessing allele frequency changes that associate with selection via bulk segregant analysis (also known as linkage group selection) [14,26]. While the bulk segregant analysis is a high-throughput approach, only the clonal progeny QTL mapping can delineate how QTL loci interact. The expanded use of FRG huHep-based *P. falciparum* genetic crosses, complemented by emerging genomic tools, presents an exciting new frontier into research on antimalarial drug resistance and *Plasmodium* biology.

Table 1. Summary of Published *Plasmodium falciparum* Crosses^a

Parent 1		Parent 2		Vertebrate host	# of unique recombinant progeny	Main findings	Cross (Refs)
Name	Origin (year)	Phenotypes	Name				
HB3	Honduras (1980)	PYR ^R <i>in vitro</i>	3D7	Rwanda (1979) ^b	15	First to establish that <i>P. falciparum</i> genetic crosses can be conducted in non-human primates and mosquitoes; confirmed causal role of <i>dhfr</i> -fs SNPs in PYR resistance; associated <i>pfmdr1</i> mutations with parasite response to MFQ.	[121]
Dd2	Indochina (1980)	Verapamil-reversible CQ ^R <i>in vitro</i>	HB3	Honduras (1980)	35	SNPs in <i>pfcr1</i> mediate CQ resistance; SNPs in <i>pfmdr1</i> can modulate resistance to CQ; hemoglobin-derived peptide accumulation linked to CQ ^R <i>pfcr1</i> alleles; loci associated with QN response and intracellular accumulation levels; SNPs in <i>dhps</i> mediate resistance to sulfadoxine; high expression of <i>pfmdv-1</i> is important for gametocyte development; a region on chr.12 is involved in regulating ABS cell cycle duration; <i>cis</i> and <i>trans</i> transcriptional regulation occur in <i>P. falciparum</i> .	[122]
7G8	Brazil (1980)	Actus <i>nancymaae</i> non-virulent <i>in vivo</i>	GB4	Ghana (2000)	32	PRH5 is involved in ABS <i>P. falciparum</i> invasion of <i>A. nancymaae</i> ; an intergenic region between <i>pfhr2a</i> and <i>pfhr2b</i> is involved in <i>P. falciparum</i> alternative invasion pathways; SNPs in <i>pfcr1</i> and <i>pfmdr1</i> contribute to resistance to ADQ.	[123]
GB4	Ghana (2000)	CQ ^R <i>in vitro</i>	NF54HT-GFP-luc	Rwanda (1979)	4	Proof-of-concept that FRG-NOD hu-Hep mice can replace non-human primates for <i>P. falciparum</i> crosses.	[40]
7G8	Brazil (1980)		NF54HT-GFP-luc	Rwanda (1979)	15	Findings not yet reported.	[40]
NHP1/NHP4026	Thailand-Myanmar border (2007)	CQ ^R <i>in vitro</i> ; delayed clearance (but K13 WT)	NF54 (HT-GFP-luc)	Rwanda (1979)	84	Can use a fresh clinical isolate as a cross parent in the huHep host system; geographical origin of parents may affect inbreeding and allele segregation; regions in chrs. 2, 13, and 14 are differentially selected in AbuMAX vs serum media for ABS growth.	[40, 124]
803	Cambodia (2009-10)	Delayed clearance	GB4	Ghana (2000)	27	AS-treated K13 C580Y and C580 progeny showed similar <i>in vivo</i> clearance $t_{1/2}$ in ART-treated <i>Aotus</i> monkeys.	[44]
NHP1/337	Thailand-Myanmar border (2011)	Delayed clearance	MKK2835	Thailand-Myanmar border (2003)	60	Geographical origin of parents may affect inbreeding and allele segregation; regions on chrs. 12 and 14 may compensate for ABS ART resistance-associated fitness defects.	[39]

^aAbbreviations: ABS, asexual blood stage; ADQ, amodiaquine; ART^R, artemisinin-resistant; ART^S, artemisinin-sensitive; chr., chromosome; Clearance $t_{1/2}$, time it takes to reduce parasitemia by 50% (ART resistance is associated with a clearance $t_{1/2} > 5$ h); CQ, chloroquine; GFP, green fluorescent protein; luc, luciferase; MFQ, mefloquine; PYR, pyrimethamine; QN, quinone.

^bThe origin of 3D7, a clone of NF54, was recently mapped to Rwanda [36].

progeny also indicated that *pfmdr1* mutations can modulate the level of CQ^R [41] and linked hemoglobin-derived peptide accumulation to CQ-resistant *pfcr1* alleles [36]. The HB3×Dd2 cross also mapped segments putatively involved in quinine (QN) resistance, and *pfdhps* mutations that govern sulfadoxine resistance [14,26,37]. Investigations using the third cross, 7G8×GB4, mapped *P. falciparum* ABS invasion of *Aotus nancymae* RBCs to reticulocyte binding protein homolog 5 (*prfh5*, PF3D7_0424100) and implicated an intergenic region between *prfh2a* (PF3D7_1335400) and *prfh2b* (PF3D7_1335300) in mediating an alternative invasion pathway [26,38]. The 7G8×GB4 cross progeny also associated mutations in *pfcr1* and *pfmdr1* with ADQ and CQ resistance [42]. A more recent cross between NF54(HT-GFP-luc) and NHP* (later called NHP4026) established that FRG huHep mice can replace nonhuman primates for *P. falciparum* crosses, and that fresh clinical isolates can be used as cross parents [40]. This cross was also used to map nutritional determinants, and identified regions in chromosomes 2, 13, and 14 that were differentially selected for ABS growth in lipid-enriched bovine serum albumin (Albumax) media versus media containing human serum [43]. In the fifth experimental cross between the 803 (PfK13 C580Y) and GB4 (PfK13 C580) strains, artesunate-treated PfK13 C580Y and C580 progeny displayed similar parasite clearances in *Aotus* monkeys despite their differential ART resistance (ART^R) phenotypes *in vitro* [44]. ABS progeny from the sixth reported cross between NHP1337 (PfK13 C580Y; ART-resistant) and MKK2835 (PfK13 C580; ART-sensitive) revealed QTLs on chromosomes 12 and 14 favoring selection against the ART-resistant parent, which may indicate regions that compensate for fitness defects associated with *in vitro* mutant PfK13-mediated ART^R [39].

In characterizing the *P. falciparum* genome, genetic crosses have also been harnessed to assess recombination frequency, allele variability, *de novo* versus inherited copy number variations (CNVs), and transcriptional regulation using gene expression QTL [14,26,45]. Collective analyses of multiple crosses have indicated that indels are the most common form of polymorphism in the genome, and that crossover events are twice as frequent as non-crossover events. Furthermore, they showed that meiotic recombination can occur within CNVs encompassing drug resistance genes, revealing a mechanism for how parasites may compensate for fitness costs associated with resistance-conferring polymorphisms [45]. One advantage of genetic cross analysis in *Plasmodium* is that it is 'simplified' due to the Mendelian inheritance pattern with these haploid stages, as recombinant progeny will have a known allele of either parent at any locus. However, cost and demand for technical expertise with humanized mice and mosquitoes limit the routine use of *P. falciparum* genetic crosses, and inconsistencies in whether ABS parasites can maintain their ability to generate mature gametocytes is a complicating factor [14]. Genetic crosses with human *Plasmodium* spp. also require an *in vitro* culture system to obtain and phenotype progeny clones, excluding *P. vivax* from potential future crosses, and restrict genotypes to two parents, which may cause genetic determinants to be missed and/or limit the influence of the genetic background. The genetic cross procedure itself introduces an unknown selective pressure that may also bias the resulting progeny pool [46].

Functional Genomic Analyses Using Mutant Parasite Screens

Phenotype-driven functional *Plasmodium* mutant screens have also revealed genes involved in all developmental stages [47–49], gametocytogenesis [50], apicoplast biogenesis [51], host cell remodeling [52], and mosquito transmission [53]. Three genome-wide *Plasmodium* mutant screens have been completed thus far, one in *P. falciparum* and two in the rodent malaria model species, *P. berghei*. A *P. falciparum* *piggyBac* transposon insertion saturation mutagenesis in the NF54 strain generated over 38 000 mutants created with mostly a single insertion per genome [49]. A mutagenesis index score and a mutagenesis fitness score were created to identify 2680 of 5399 genes as essential for ABS growth. Chemogenomic profiling of *piggyBac* mutants from a

Trends in Parasitology

prior mutant library helped to identify a group of seven DHA-sensitive mutants, including a *pfk13* mutant that had a maximal expression in mid to late ring stages instead of the wild-type early ring stage. This altered timing of expression was likely driven by the promoter of the drug selection cassette, as this cassette and its flanking *piggyBac* inverted terminal repeats were inserted into the endogenous putative *pfk13* promoter [54]. This screen highlighted the power of the *piggyBac* genome-wide mutant library in identifying determinants of parasite susceptibility to selective agents. Genome-wide mutagenesis screens have also been completed in *P. berghei* with barcoded knockout mutants, and subsequent barcode counting on a next-generation sequencer [47,48]. Analysis of the relative abundance of barcodes identified genes essential for ABS *P. berghei* growth and for the gametocyte to mosquito to liver to blood-stage transitions. This system also enabled modeling of *P. berghei* liver-stage metabolism to show major reprogramming at this stage, including 27 genes that represented seven metabolic systems – type II fatty acid synthesis and elongation, tricarboxylic acid, amino sugar, heme, lipoate, and shikimate metabolism – that were deemed essential specifically in liver stages [48]. It is important to note, however, that these observed essentialities in the *P. berghei* model might not necessarily mirror those in *P. falciparum*. For example, while knockout mutants for genes encoding uridine-acetylglucosamine or *N*-acetylglucosamine-phosphate mutase show that UDP-*N*-acetyl-glucosamine synthesis is non-essential for *P. berghei* ABS parasites [47], unsuccessful attempts to knock out glucosamine-phosphate *N*-acetyltransferase [55] and the under-representation of transposon insertions into glucosamine-phosphate *N*-acetyltransferase, uridine-acetylglucosamine or *N*-acetylglucosamine-phosphate mutase genes [49] suggest that this biosynthetic pathway is essential for *P. falciparum*. Collectively, these functional genomic screens provide important insights into the essentiality and function of unannotated genes and help to prioritize gene candidates identified in orthogonal screening experiments. Furthermore, barcoding of the mutant libraries allows for high-throughput profiling to investigate genetic determinants of phenotypes such as antimalarial drug resistance that may be elusive using *in vitro* selections.

In Vitro Drug Selection and Whole-Genome Sequence Analysis

Whole-genome sequencing (WGS) of parasite clones from *in vitro* evolution of resistance also exploits genome-wide information in identifying the genetic determinants that underlie antimalarial drug responses. [56]. During resistance selections, parasites are exposed to sublethal, continuous, or dose-escalating drug pressure until the emergence of recrudescence resistant populations that show an increase in EC₅₀ (the concentration required to inhibit parasite proliferation by 50%), characterized by a rightward shift in the concentration–response curves. Comparing genomes of the resistant clonal parasites to that of their untreated parent helps to identify genome-encoded changes such as SNPs and CNVs that may underlie the resistance phenotype (Figure 1C). For instance, WGS analysis of resistant clones from *in vitro* selections using structurally diverse compounds identified CNVs and SNPs in 83 genes associated with resistance [57]. Drug pressuring with AN13762 [58], DSM265 [59], bortezomib or WLL [60–62], or DHA [63] has also traced *in vitro* resistance-conferring mutations to *P. falciparum* prodrug activation and resistance esterase (PF3D7_0709700), dihydroorotate dehydrogenase (PF3D7_0603300), the 20S proteasome β 5 subunit (PF3D7_1011400), or coronin (PF3D7_1251200), respectively (Table 2). Selections with the imidazolopiperazines KAF156 and GNF179 also associated resistance with SNPs in the cyclic amine resistance locus (PF3D7_0321900), acetyl-CoA transporter (PF3D7_1036800), and UDP-galactose transporter (PF3D7_1113300) [21]. Other reports have demonstrated PfK13-independent resistance phenotypes arising from ART selections *in vitro* [64], increased copy number and mutations in *P. falciparum* purine nucleoside phosphorylase (PF3D7_0513300) that conferred resistance to transition-state analog inhibitors [65], and *pfmdr1* mutations that confer resistance to hexahydroquinolines [66]. These examples, while not

exhaustive of the large repertoire of *in vitro* evolution and WGS analysis, highlight the versatility of this approach.

WGS of clones from *in vitro* selections can also inform target identification studies. For example, genome sequence data have revealed the Na⁺-dependent ATPase PfATP4 as the target of multiple chemotypes including the recently described methylisoquinoline MB14 [67], cleavage and polyadenylation specificity factor subunit 3 as the target of benzoxaboroles [68], and PfPKG as the primary target of ML10 and MMV030084 [19,69] (Table 2). As this approach is limited to compounds against which resistance can be easily generated, alternative methods are necessary for 'irresistible' compounds (Box 2). Additionally, *in vivo* responses depend on the pharmacokinetics and pharmacodynamics of the drug, thus restricting the translational value of this strategy. A recent proof-of-concept to compare the *in vitro* development of resistant *P. falciparum* parasites to that in an *in vivo* mouse model of *P. falciparum* infection [70] offers a good platform to interrogate the clinical relevance of identified genomic changes.

Genome Editing Approaches to Studying Antimalarial Resistance and Mode of Action

To demonstrate the power of genome-wide studies in elucidating functionally important loci in the *P. falciparum* genome, validation experiments using genetically engineered parasites are critical. The advent of transfection-based genetic modification of *P. falciparum* enabled the first use of allelic exchange to confirm causal roles of drug resistance mediators, as shown for *pf dhfr* and *pf dhps* point mutations that mediate parasite resistance to pyrimethamine and sulfadoxine, respectively [71,72]. Later, mutations in *pf crt* were confirmed by allelic exchange to be the primary mediator of CQ^R [73]. Allelic exchange studies with polymorphic codons in *pf mdr1* also implicated this ABC transporter in mediating resistance to MFQ and halofantrine [74]. Genetically edited parasites can now be generated in a relatively efficient and scalable manner. One such method is site-specific zinc-finger nuclease (ZFN)-based editing in which parasites are transfected with a construct that encodes for pairs of customized DNA sequence-specific zinc-finger proteins linked to a split endonuclease [75]. These DNA-binding proteins trigger double-stranded breaks in the target sequence that trigger homology-directed DNA-repair mechanisms using a plasmid-encoded donor sequence. This method of gene editing has helped to elucidate the role of specific *pf crt* and *pf mdr1* mutations in multiple antimalarial resistance phenotypes [76–78], and also confirmed the essentiality of phosphatidylinositol 4-kinase and its role as a target of imidazopyrazines [79]. ZFNs also enabled the first and only documented evidence of gene editing in the human parasite *P. vivax* [80].

Gene disruptions in *P. falciparum* formerly involved extended culture periods of assessing integration via **homologous recombination** and single-site or double crossovers of an episomal plasmid, thus precluding large-scale genome manipulation efforts. Clustered regularly interspaced short palindromic repeats/Cas9 (CRISPR/Cas9) editing has circumvented this drawback by modifying a prokaryotic viral defense system to cleave a specific genomic sequence containing a unique 3' protospacer-adjacent motif (PAM) [81]. High-fidelity homologous recombination between the cleaved genomic locus and a donor sequence subsequently enables integration of the donor DNA [81,82]. As examples, evaluation of PfPKG as a target of the imidazole compound MMV030084 [19], interaction of PfMDR1 with the piperazine-containing compound ACT-451840 [83], and the contribution of the PfK13 C580Y and R561H mutations to ART^R *in vitro* [82,84], have all leveraged CRISPR/Cas9-based genome editing. CRISPR/Cas9 editing has also confirmed SNPs that confer resistance to the experimental antimalarials DSM265 [59], KAF156 and GNF179 [21], benzoxaboroles [68], and hexahydroquinolines [66]. In *P. berghei*, CRISPR/Cas9 editing was recently used to

Table 2. Select Antiplasmodial Compounds Identified by Recent Drug Discovery Efforts

Compound ID	Compound class	Stage in development	Putative target	Target location	Biological pathway	Pf strain(s) for ABS selection	Resistance mediator(s)	Refs
ACT-451840	Piperazine	Phase I (NCT02223871, NCT02186002) ^a	Multidrug resistance 1 (PfMDR1) ^b	DV membrane	Unknown	Dd2, 7G8, NF54	<i>pfmdr1</i> (PF3D7_0523000)	[82]
AN13762	Benzoxaborole	Pre-clinical	Cleavage and specificity factor homolog (PfCPSF3)	Nucleus	mRNA maturation	Dd2, 3D7	Prodrug activation and resistance esterase (<i>pfpare</i> , PF3D7_0709700); SUMO-activating enzyme subunit 2 (<i>pfuba2</i> , PF3D7_123700); E3 SUMO ligase (<i>pfpias</i> , PF3D7_1360700); ring zinc-finger E3 ubiquitin ligase (PF3D7_0529900); ubiquitin-activating enzyme 1 (PF3D7_1350400); cleavage and polyadenylation specificity factor subunit 3 (<i>pfpsf3</i> , PF3D7_1438500)	[57]
Bortezomib, WLL, WLW	Bortezomib: peptidyl boronic acid; WLL and WLW: peptide vinyl sulfones	Pre-clinical	<i>P. falciparum</i> 20S proteasome ($\beta 5$ and $\beta 2$ for WLL, $\beta 2$ for WLW)	Proteasome	Ubiquitin-regulated protein degradation	Bortezomib: 3D7, WLL, and WLW; Cam3.II K13 ^{WT} , Cam3.II K13 ^{C580Y} , V1/S K13 ^{WT} , V1/S K13 ^{C580Y}	Bortezomib: Pf20S $\beta 5$ (PF3D7_1011400); WLL: Pf20S $\beta 6$ (PF3D7_0518300) and $\beta 5$; WLW: Pf20S $\beta 2$ (PF3D7_1328100), Pf26S proteasome 19S regulatory particles (<i>pfpra4</i> , PF3D7_1306400), (<i>pfprt5</i> , PF3D7_1130400), (<i>pfprn6</i> , PF3D7_1402300)	[59–61]
DSM265	Triazopyrimidine	Phase I/II (NCT02389348, NCT02573857, NCT02123290) ^a	Dihydroorotate dehydrogenase (PfDHODH)	Mitochondrion	Pyrimidine biosynthesis	Dd2, K1	<i>pfdhodh</i> (PF3D7_0603300)	[58]
GNF-Pf-5640	Hexahydroquinoline	Pre-clinical	Unknown	Unknown	Unknown	Dd2-B2	<i>pfmdr1</i> (PF3D7_0523000)	[65]
KAF156 and GNF179	Imidazolo-piperazines	KAF156: Phase II (NCT01753823, NCT04546633, NCT03167242) ^a ; GNF179: Pre-clinical	Unknown	Endoplasmic Reticulum/Golgi apparatus	Endoplasmic Reticulum-dependent protein processing	3D7, Dd2	Cyclic amine resistance locus (<i>pfcarl</i> , PF3D7_0321900); UDP-galactose transporter (<i>pfugt</i> , PF3D7_1113300); acetyl-CoA transporter (<i>pfact</i> , PF3D7_1036800)	[20]
MB14	4-cyano-3-methylisoquinoline	Pre-clinical	Na ⁺ efflux pump (PfATP4)	Parasite plasma membrane	ATP4-regulated Na ⁺ homeostasis	3D7	non-SERCA-type Ca ²⁺ -transporting P-ATPase (<i>pfatp4</i> , PF3D7_1211900)	[66]
ML10 and MMV030084	ML10: imidazopyridine; MMV030084: trisubstituted imidazole	Pre-clinical	cGMP-dependent protein kinase (PfPKG)	Cytosol and early secretory pathway	Parasite egress and host cell invasion	Dd2-B2 ^{WT} , Dd2-B2 TKL3 ^{K60}	Tyrosine kinase-like protein 3 (<i>tk3</i> , PF3D7_1349300)	[18,68]

^aClinicalTrials.gov Identifier^bUnknown if this is the primary target or resistance mediator.

demonstrate that PfK13 mutations confer *in vivo* ART^R [85], and that ubiquitin hydrolase (PBANKA_0208800) can modulate parasite susceptibility to ART and CQ [86].

CRISPR/Cas9 editing can also introduce epitope tags into genes of interest and help to investigate their biological features. For example, CRISPR/Cas9 editing of a triple hemagglutinin (3xHA) epitope tag onto the adaptor protein 2 μ subunit (AP-2 μ), followed by fluorescent and immunoelectron microscopy, localized this trafficking protein to a compartment adjacent to the digestive vacuole (DV) and plasma membrane and enabled the identification of interacting partners including other AP-2 subunits, the K10 kelch-domain protein, and PfEHD, an effector of endocytosis and lipid mobilization [87]. Similarly, affinity purification of the *Plasmodium* translocon of exported (PTEX) protein with a CRISPR/Cas9-engineered 3xFLAG tag enabled its native structure to be solved by cryo-electron microscopy [88]. These direct observations of the PTEX structure provided evidence of its role as the gateway for the parasite's exportome and yielded insights into the unique interactions between constituent proteins necessary for PTEX function. Nevertheless, transfection efficiency for *P. falciparum* remains low, and complete editing of all transfected parasites is rare [81].

Selection-linked integration (SLI) has been developed as an alternative approach to generate parasites with targeted genomic integration events [89]. In this strategy, a promoter-less targeting region on the plasmid used for integration is linked with an additional selectable marker, separated by a 2A skip peptide that cleaves a single messenger RNA (mRNA) transcript into separate polypeptides. This additional selectable marker can be expressed only after single crossover recombination into the target locus, but because of the skip peptide, the marker is not attached to the target itself. Parasites carrying the integration can therefore be selected by using the additional integration-linked resistance marker (denoted as the SLI-resistance marker). The robustness of SLI has been validated via successful green fluorescent protein (GFP) fusion-based localization of native proteins, disruption of genes, knocking in an allele conferring ART^R, and functional analyses of known and newly identified essential genes at the protein level [89,90].

Regulatable Systems in Antimalarial Resistance and Asexual Blood-stage Development

Typically, gene knockouts are only practical for dispensable genes or those whose products can be chemically and/or genetically compensated. Conditional expression systems that permit inducible regulation of RNA and protein levels offer promising alternatives to study essential genes. Target genes bearing a glucosamine-6-phosphate riboswitch (*glmS*) ribozyme in the 3' untranslated region (UTR) can be efficiently knocked down in response to a glucosamine-6-phosphate inducer, leading to reduced protein levels [91] (Figure 2A). This system has enabled assessments of parasite sensitivity to the *Plasmodium* export element mimetic WEHI-916 using plasmepsin V knockdown lines [92], and hypersensitivity to pyrimethamine in parasites with attenuated expression of *pfdhfr* [91]. Target validation efforts through *glmS* ribozyme-mediated modification have also demonstrated deoxyhypusine synthase as a potential antiplasmodial target [93]. In addition, *glmS*-attenuated expression of eukaryotic translation initiation factor 2 α kinase (PF3D7_0628200) has demonstrated its role in DHA-induced stress responses in the parasite endoplasmic reticulum [94]. This technique, however, can be confounded by glucosamine cytotoxicity due to its acidity and consequent ability to lower the pH of the medium [95].

Genetic modification can also leverage sequence-specific recombination using the Cre recombinase that recognizes 34-nucleotide *loxP* sites and mediates excision or inversion of *loxP*-flanked sequences depending on the *loxP* orientation. The dimerizable Cre (DiCre) system (Figure 2B) involves expression of inactive Cre as two polypeptide moieties that fuse to FK506-

Trends in Parasitology

binding protein (FKBP) 12 and FKBP rapamycin-binding (FRB) protein, respectively, with rapamycin-induced heterodimerization of the two Cre components restoring recombinase activity [96]. Following proof-of-principle experiments in *P. falciparum* ABS parasites, reports demonstrated the abrogation of merozoite invasion through DiCre-mediated conditional knockdown of cyclic AMP-dependent protein kinase A catalytic subunit (PF3D7_0934800) and actin-1 (PF3D7_1246200) expression [97,98]. A marker-free NF54::DiCre parasite line has also been developed to conditionally delete genes across the life cycle [99]. More recently, a report on DiCre-mediated conditional disruption and allelic replacement of PfPKG demonstrated that the protein has no scaffolding or adaptor role in ABS development and acts solely during merozoite egress [100]. Despite the relatively high efficiency of DiCre excision in *P. falciparum*, its removal of 3' UTRs may not always reduce target protein levels if there is an alternative polyadenylation site that can stabilize the target mRNA [96]. Furthermore, given the low transfection efficiency in *P. falciparum*, it can take time to introduce two *loxP* sites that flank the desired target sequence. One recent innovation has been to introduce *loxP* sites as a part of silent synthetic introns (loxPint) [101]. The combined usage of loxPint-flanked kinase domains and the aforementioned NF54::DiCre parasite background has allowed the conditional knockdown of all 18 FIKK serine/threonine kinases, and the subsequent phosphoproteomic analyses of each kinase [102].

Protein levels can also be regulated by introducing unstable destabilizing domains, such as FKBP-based destabilization domain (DD) or an *Escherichia coli* DHFR destabilizing domain (DDD), into a protein of interest, thereby triggering proteasomal degradation (Figure 2C). This instability can be reversed by stabilizing compounds (Shield-1 and trimethoprim for DD and DDD fusion proteins, respectively), thus allowing tunable expression of protein levels. An earlier use of a FKBP protein destabilization domain (ddFKBP) in *P. falciparum* demonstrated that the swollen DV phenotype in falcipain-2 knockout lines could be rescued by expression of Shield-1-dependent falcipain-2-ddFKBP [103]. Transfected parasites expressing GFP fused to a DD have also been used to investigate the antiproteasome activity of novel peptidyl boronate hit compounds from a library of human proteasome inhibitors [61]. This strategy has also been used to assess the roles and essentialities of heat shock protein 70x and the receptor for activated c-kinase 1 [104,105]. However, for some proteins, the degree of degradation may not be sufficient to produce a phenotype, in which case combining this system with another regulatable expression may tighten regulation. In addition, some proteins mistarget or do not function when tagged with DD, while others may not be degraded well as fusions [103].

Rapid mislocalization of proteins by the knock-sideways (KS) approach can also be used to study function [89]. KS is based on ligand-induced dimerization whereby the endogenous target is fused with FKBP, and FRB is fused to a signal that mediates trafficking to a different cellular location (Figure 2D). Upon addition of the ligand (often rapamycin or its analogs) that dimerizes FKBP and FRB, the target protein is directed away from its native site of action. This approach was validated through mislocalization and inducible inactivation of PfK13 [89]. More recently, the KS approach has been harnessed to investigate proteins within the PfK13 compartment that are essential for parasite survival. The combined use of KS and a quantitative **BioID** approach led to the identification of candidate proteins within the ART^R interactome [90]. Conditional inactivation through KS also enabled the evaluation of the role of vacuolar protein sorting-associated protein 45 (PF3D7_0216400) in host cell cytosol uptake [106] and phosphoinositide-binding PH domain-containing protein in merozoite attachment and invasion [107].

Blocking or permitting transcription of genes and then measuring the resulting cellular phenotype is also achievable using the tetracycline repressor protein (TetR) which binds to its associated DNA operator sequences, thereby blocking transcription [108]. This repression is reversible

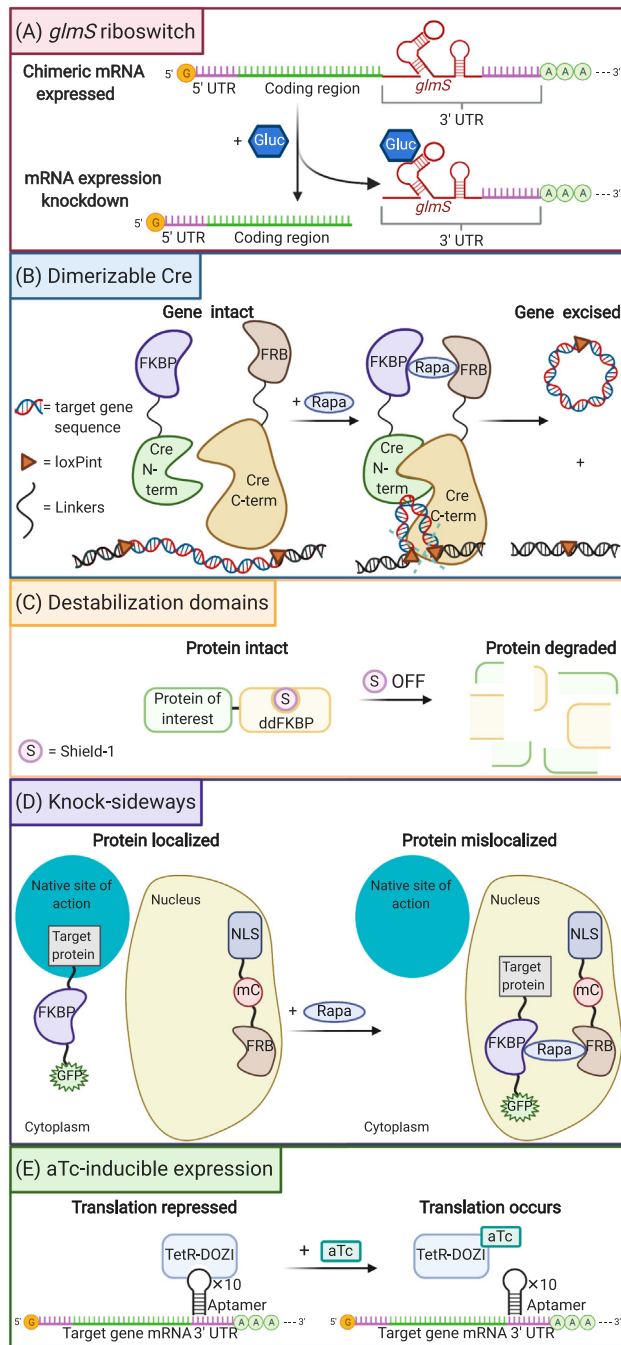


Figure 2. Schematic Representation of *Plasmodium* Regulatable Expression Strategies (A) *glmS* riboswitch-based

gene expression system: the targeting construct contains the *glmS* ribozyme at the 3' end of the gene of interest. Addition of glucosamine activates the ribozyme, leading to cleavage of the mRNA and removal of the 3' UTR, triggering rapid mRNA degradation by the proteasome and a reduction in protein levels.

(B) Dimerizable Cre (DiCre) system: the Cre recombinase is expressed as two inactive polypeptide moieties fused to FKBP12 and FRB, respectively. Rapamycin-induced dimerization leads to the association of the complementing Cre components and reconstitution of enzymatic activity. The Cre recombinase recognizes *loxP* sites (herein introduced via synthetic introns) to catalyze the excision (or insertion) of *loxP*-flanked DNA segments. This approach can be tailored to conditionally silence genes, introduce point mutations or generate fusions.

(C) Destabilization domain-based regulation of protein expression, using Shield-1-protected protein-ddFKBP fusion proteins that degrade upon removal of Shield-1.

(D) Knock-sideways system: FRB-mCherry fusion is localized in one sub-cellular compartment (in this example the nucleus) by a localization signal while the target protein, tagged with a FKBP-GFP fusion, is elsewhere in its native site of action (denoted herein as the cytoplasm). Addition of rapamycin stimulates heterodimerization of FRB and FKBP and results in mislocalization of the protein of interest, with possible phenotypic consequences.

(E) aTc-inducible system: in this example a 10× tetracycline repressor protein (TetR) aptamer array is genetically encoded within the 3' UTR of the target gene. A TetR-ATP-dependent RNA helicase DDX6 (DOZI) fusion protein is also expressed and binds the aptamer mRNA, repressing translation of the target transcript. Addition of the tetracycline analog anhydrotetracycline (aTc) induces reversible allosteric interaction with the TetR-DOZI protein, disrupting the TetR-DOZI-aptamer interaction, and enables mRNA expression of the target gene. Translation stops upon removal of aTc. Alternative designs include engineering aptamer arrays

in the 5' UTR or 5' and 3' UTRs [108]. Abbreviations: aTc, anhydrotetracycline; FKBP, FK506-binding protein; FRB, binding domain of the FKBP-rapamycin-associated protein; loxPint, *loxP* site encoded in a synthetic intron; mC, mCherry; NLS, nuclear localization signal; Rapa, rapamycin; S, Shield-1; term, terminus.

through allosteric interaction of TetR with tetracycline or its analog anhydrotetracycline (aTc). A recent adaptation of this approach is the TetR-DOZI aptamer system [108,109] in which aTc-regulatable binding occurs between the TetR-DOZI fusion protein and 10×TetR RNA

aptamer arrays encoded in the 3' UTR of the gene of interest, leading to translation inhibition (Figure 2E). The TetR-DOZI system has been successfully leveraged in recent investigations of the druggability of plasmepsins V, IX, and X, as well as the nutrient-permeable channel EXP2 and the *P. falciparum* Niemann–Pick type C1-related protein [110,111].

Concluding Remarks

Recent advances in genomic and genetic approaches to investigate *Plasmodium* biology have provided powerful tools to elucidate molecular determinants of antimalarial resistance and identify novel drug targets. The possibility of coupling site-specific editing techniques such as CRISPR/Cas9 with inducible systems heralds unprecedented robustness in validating genetic determinants of phenotypes, including drug resistance, while the high-throughput scaling of genomic strategies enables increased analytical power (see Outstanding Questions). An established approach to studying antimalarials with an unknown mechanism of resistance is to first conduct *in vitro* selections with *P. falciparum* ABS parasites (the Dd2 B2 clone is often used), including a hypermutator line if needed. Uniquely barcoded panels of lines with SNPs or CNVs in known resistance determinants can also be drug-pulsed as mixed cultures and the pool of surviving parasites barcode-sequenced to assess whether known determinants can confer resistance. Libraries of knockout parasites (such as the *piggyBac* transposon-tagged library [49]) can also be screened, with the caveat that mutants of essential genes may not be available for profiling. A more resource-demanding, but high-yield alternative is to conduct genetic crosses between genotypically and phenotypically distinct clinical isolates, to investigate mechanisms of drug resistance that are elusive through *in vitro* drug selection, as well as other biological processes of interest. Candidate genes obtained by these methods can then be narrowed down by markers identified in GWAS, evidence of positive selection in field isolates, and targeted profiling of select mutants if available. Candidates can then be validated in a relatively high-throughput manner by conditional knockdown or editing of these genes (ideally in more than one genetic background). The continued refinement and use of these tools can be a powerful catalyst for ongoing research into discovering and developing new, safe, and efficacious antimalarials.

Acknowledgments

D.A.F. gratefully acknowledges support from the Medicines for Malaria Venture, the Bill & Melinda Gates Foundation (OPP1201387), the Department of Defense (W81WXH-15-2-0033 and W81XWH-19-1-0086), and the NIH (R01 AI109023, R01 AI124678, R01 AI147628, R33 AI127581). M.K. gratefully acknowledges support from the Japan Student Services Organization. The authors also thank members of the Malaria Drug Accelerator (MalDA) Consortium (funded by the Bill & Melinda Gates Foundation (OPP1054480) and led by Dr Elizabeth Winzeler, OPP1054480) for their collaboration and stimulating discussions. Figures were created with BioRender.com.

Declaration of Interests

There are no interests to declare.

References

- World Health Organization (2020) *World Malaria Report 2020*, WHO
- Cowman, A.F. *et al.* (2016) Malaria: Biology and disease. *Cell* 167, 610–624
- Gething, P.W. *et al.* (2016) Mapping *Plasmodium falciparum* mortality in Africa between 1990 and 2015. *N. Engl. J. Med.* 375, 2435–2445
- malERA Refresh Consultative Panel on Insecticide and Drug Resistance (2017) malERA: An updated research agenda for insecticide and drug resistance in malaria elimination and eradication. *PLoS Med.* 14, e1002450
- Blasco, B. *et al.* (2017) Antimalarial drug resistance: linking *Plasmodium falciparum* parasite biology to the clinic. *Nat. Med.* 23, 917–928
- Chen, I. *et al.* (2016) Asymptomatic malaria: A chronic and debilitating infection that should be treated. *PLoS Med.* 13, e1001942
- Duffy, P.E. and Gorres, J.P. (2020) Malaria vaccines since 2000: progress, priorities, products. *NPJ Vaccines* 5, 48
- Phillips, M.A. *et al.* (2017) Malaria. *Nat. Rev. Dis. Primers* 3, 17050
- Alam, M.M. *et al.* (2019) Validation of the protein kinase PfCLK3 as a multistage cross-species malarial drug target. *Science* 365, eaau1682
- Antonova-Koch, Y. *et al.* (2018) Open-source discovery of chemical leads for next-generation chemoprotective antimalarials. *Science* 362, eaat9446
- Baragana, B. *et al.* (2015) A novel multiple-stage antimalarial agent that inhibits protein synthesis. *Nature* 522, 315–320

Outstanding Questions

How can we increase experimental throughput in the identification of drug modes of action and mechanisms of resistance?

How can we close the gap between the laboratory and the field so that we can predict clinical resistance markers *in vitro*, and identify causal mechanisms as resistance emerges in real time? How can we best incorporate genetic crosses and functional genomic screens into this process, alongside the traditional GWAS and gene-editing studies?

How does the genetic background influence parasite response to antimalarial treatment, and are there common genetic factors that make some parasites intrinsically less susceptible to drugs than others?

What methods can best maximize recombination and genetic diversity amongst progeny and minimize self-fertilization?

12. Brancucci, N.M. *et al.* (2015) An assay to probe *Plasmodium falciparum* growth, transmission stage formation and early gametocyte development. *Nat. Protoc.* 10, 1131–1142
13. Roth, A. *et al.* (2018) A comprehensive model for assessment of liver stage therapies targeting *Plasmodium vivax* and *Plasmodium falciparum*. *Nat. Commun.* 9, 1837
14. Vendrely, K.M. *et al.* (2020) Humanized mice and the rebirth of malaria genetic crosses. *Trends Parasitol.* 36, 850–863
15. Dorjsuren, D. *et al.* (2021) Chemoprotective antimalarials identified through quantitative high-throughput screening of *Plasmodium* blood and liver stage parasites. *Sci. Rep.* 11, 2121
16. Cowell, A.N. and Winzeler, E.A. (2019) Advances in omics-based methods to identify novel targets for malaria and other parasitic protozoan infections. *Genome Med.* 11, 63
17. Kloehn, J. *et al.* (2016) Using metabolomics to dissect host-parasite interactions. *Curr. Opin. Microbiol.* 32, 59–65
18. Paquet, T. *et al.* (2017) Antimalarial efficacy of MMV390048, an inhibitor of *Plasmodium* phosphatidylinositol 4-kinase. *Sci. Transl. Med.* 9, eaad9735
19. Vanaerschot, M. *et al.* (2020) Inhibition of resistance-refractory *P. falciparum* kinase PKG delivers prophylactic, blood stage, and transmission-blocking antiplasmodial activity. *Cell Chem. Biol.* 27, 806–816 e808
20. Flueck, C. *et al.* (2019) Phosphodiesterase beta is the master regulator of cAMP signalling during malaria parasite invasion. *PLoS Biol.* 17, e3000154
21. Lim, M.Y. *et al.* (2016) UDP-galactose and acetyl-CoA transporters as *Plasmodium* multidrug resistance genes. *Nat. Microbiol.* 1, 16166
22. Marapana, D.S. *et al.* (2018) Plasmepsin V cleaves malaria effector proteins in a distinct endoplasmic reticulum translocation interactome for export to the erythrocyte. *Nat. Microbiol.* 3, 1010–1022
23. Ross, L.S. *et al.* (2018) Emerging Southeast Asian PfCRT mutations confer *Plasmodium falciparum* resistance to the first-line antimalarial piperazine. *Nat. Commun.* 9, 3314
24. Mu, J. *et al.* (2010) *Plasmodium falciparum* genome-wide scans for positive selection, recombination hot spots and resistance to antimalarial drugs. *Nat. Genet.* 42, 268–271
25. Van Tyne, D. *et al.* (2011) Identification and functional validation of the novel antimalarial resistance locus *PF10_0355* in *Plasmodium falciparum*. *PLoS Genet.* 7, e1001383
26. Su, X.Z. *et al.* (2019) *Plasmodium* genomics and genetics: New insights into malaria pathogenesis, drug resistance, epidemiology, and evolution. *Clin. Microbiol. Rev.* 32, e00019
27. Wendler, J.P. *et al.* (2014) A genome wide association study of *Plasmodium falciparum* susceptibility to 22 antimalarial drugs in Kenya. *PLoS One* 9, e96486
28. Wang, Z. *et al.* (2016) Genome-wide association analysis identifies genetic loci associated with resistance to multiple antimalarials in *Plasmodium falciparum* from China–Myanmar border. *Sci. Rep.* 6, 33891
29. Pelleau, S. *et al.* (2015) Adaptive evolution of malaria parasites in French Guiana: Reversal of chloroquine resistance by acquisition of a mutation in *pfcr*. *Proc. Natl. Acad. Sci. U. S. A.* 112, 11672–11677
30. Ariey, F. *et al.* (2014) A molecular marker of artemisinin-resistant *Plasmodium falciparum* malaria. *Nature* 505, 50–55
31. Miotto, O. *et al.* (2015) Genetic architecture of artemisinin-resistant *Plasmodium falciparum*. *Nat. Genet.* 47, 226–234
32. Amato, R. *et al.* (2017) Genetic markers associated with dihydroartemisinin-piperazine failure in *Plasmodium falciparum* malaria in Cambodia: A genotype-phenotype association study. *Lancet Infect. Dis.* 17, 164–173
33. Witkowski, B. *et al.* (2017) A surrogate marker of piperazine-resistant *Plasmodium falciparum* malaria: A genotype-phenotype association study. *Lancet Infect. Dis.* 17, 174–183
34. Amambua-Ngwa, A. *et al.* (2019) Major subpopulations of *Plasmodium falciparum* in sub-Saharan Africa. *Science* 365, 813–816
35. Cerqueira, G.C. *et al.* (2017) Longitudinal genomic surveillance of *Plasmodium falciparum* malaria parasites reveals complex genomic architecture of emerging artemisinin resistance. *Genome Biol.* 18, 78
36. Lewis, I.A. *et al.* (2014) Metabolic QTL analysis links chloroquine resistance in *Plasmodium falciparum* to impaired hemoglobin catabolism. *PLoS Genet.* 10, e1004085
37. Sanchez, C.P. *et al.* (2014) A HECT ubiquitin-protein ligase as a novel candidate gene for altered quinine and quinidine responses in *Plasmodium falciparum*. *PLoS Genet.* 10, e1004382
38. Campino, S. *et al.* (2018) A forward genetic screen reveals a primary role for *Plasmodium falciparum* reticulocyte binding protein homologue 2a and 2b in determining alternative erythrocyte invasion pathways. *PLoS Pathog.* 14, e1007436
39. Li, X. *et al.* (2019) Genetic mapping of fitness determinants across the malaria parasite *Plasmodium falciparum* life cycle. *PLoS Genet.* 15, e1008453
40. Vaughan, A.M. *et al.* (2015) *Plasmodium falciparum* genetic crosses in a humanized mouse model. *Nat. Methods* 12, 631–633
41. Patel, J.J. *et al.* (2010) Chloroquine susceptibility and reversibility in a *Plasmodium falciparum* genetic cross. *Mol. Microbiol.* 78, 770–787
42. Sa, J.M. *et al.* (2009) Geographic patterns of *Plasmodium falciparum* drug resistance distinguished by differential responses to amodiaquine and chloroquine. *Proc. Natl. Acad. Sci. U. S. A.* 106, 18883–18889
43. Kumar, S. *et al.* (2020) Bulk segregant approaches to nutritional genomics in *Plasmodium falciparum*. *bioRxiv* Posted online September 12, 2020. <http://doi.org/10.1101/2020.09.12.294736>
44. Sa, J.M. *et al.* (2018) Artemisinin resistance phenotypes and K13 inheritance in a *Plasmodium falciparum* cross and *Aotus* model. *Proc. Natl. Acad. Sci. U. S. A.* 115, 12513–12518
45. Miles, A. *et al.* (2016) Indels, structural variation, and recombination drive genomic diversity in *Plasmodium falciparum*. *Genome Res.* 26, 1288–1299
46. Sen, S. and Ferdig, M. (2004) QTL analysis for discovery of genes involved in drug responses. *Curr. Drug Targets Infect. Disord.* 4, 53–63
47. Bushell, E. *et al.* (2017) Functional profiling of a *Plasmodium* genome reveals an abundance of essential genes. *Cell* 170, 260–272 e268
48. Stanway, R.R. *et al.* (2019) Genome-scale identification of essential metabolic processes for targeting the *Plasmodium* liver stage. *Cell* 179, 1112–1128 e1126
49. Zhang, M. *et al.* (2018) Uncovering the essential genes of the human malaria parasite *Plasmodium falciparum* by saturation mutagenesis. *Science* 360, eaap7847
50. Ikadai, H. *et al.* (2013) Transposon mutagenesis identifies genes essential for *Plasmodium falciparum* gametocytogenesis. *Proc. Natl. Acad. Sci. U. S. A.* 110, E1676–E1684
51. Tang, Y. *et al.* (2019) A mutagenesis screen for essential plastid biogenesis genes in human malaria parasites. *PLoS Biol.* 17, e3000136
52. Maier, A.G. *et al.* (2008) Exported proteins required for virulence and rigidity of *Plasmodium falciparum*-infected human erythrocytes. *Cell* 134, 48–61
53. Tewari, R. *et al.* (2010) The systematic functional analysis of *Plasmodium* protein kinases identifies essential regulators of mosquito transmission. *Cell Host Microbe* 8, 377–387
54. Pradhan, A. *et al.* (2015) Chemogenomic profiling of *Plasmodium falciparum* as a tool to aid antimalarial drug discovery. *Sci. Rep.* 5, 15930
55. Cova, M. *et al.* (2018) The Apicomplexa-specific glucosamine-6-phosphate N-acetyltransferase gene family encodes a key enzyme for glycoconjugate synthesis with potential as therapeutic target. *Sci. Rep.* 8, 4005
56. Rocamora, F. and Winzeler, E.A. (2020) Genomic approaches to drug resistance in malaria. *Annu. Rev. Microbiol.* 74, 761–786
57. Cowell, A.N. *et al.* (2018) Mapping the malaria parasite druggable genome by using *in vitro* evolution and chemogenomics. *Science* 359, 191–199
58. Sindhe, K.M.V. *et al.* (2020) *Plasmodium falciparum* resistance to a lead benzoxaborole due to blocked compound activation and altered ubiquitination or sumoylation. *mBio* 11, e02640-19
59. White, J. *et al.* (2019) Identification and mechanistic understanding of dihydroorotate dehydrogenase point mutations in *Plasmodium falciparum* that confer *in vitro* resistance to the clinical candidate DSM265. *ACS Infect. Dis.* 5, 90–101

60. Li, H. *et al.* (2016) Structure- and function-based design of *Plasmodium*-selective proteasome inhibitors. *Nature* 530, 233–236
61. Xie, S.C. *et al.* (2018) Target validation and identification of novel boronate inhibitors of the *Plasmodium falciparum* proteasome. *J. Med. Chem.* 61, 10053–10066
62. Stokes, B.H. *et al.* (2019) Covalent *Plasmodium falciparum*-selective proteasome inhibitors exhibit a low propensity for generating resistance *in vitro* and synergize with multiple antimalarial agents. *PLoS Pathog.* 15, e1007722
63. Demas, A.R. *et al.* (2018) Mutations in *Plasmodium falciparum* actin-binding protein coronin confer reduced artemisinin susceptibility. *Proc. Natl. Acad. Sci. U. S. A.* 115, 12799–12804
64. Rocamora, F. *et al.* (2018) Oxidative stress and protein damage responses mediate artemisinin resistance in malaria parasites. *PLoS Pathog.* 14, e1006930
65. Ducati, R.G. *et al.* (2018) Genetic resistance to purine nucleoside phosphorylase inhibition in *Plasmodium falciparum*. *Proc. Natl. Acad. Sci. U. S. A.* 115, 2114–2119
66. Vanaerschot, M. *et al.* (2017) Hexahydroquinolines are antimalarial candidates with potent blood-stage and transmission-blocking activity. *Nat. Microbiol.* 2, 1403–1414
67. Gilson, P.R. *et al.* (2019) A 4-cyano-3-methylisoquinoline inhibitor of *Plasmodium falciparum* growth targets the sodium efflux pump PfATP4. *Sci. Rep.* 9, 10292
68. Sonoiki, E. *et al.* (2017) A potent antimalarial benzoxaborole targets a *Plasmodium falciparum* cleavage and polyadenylation specificity factor homologue. *Nat. Commun.* 8, 14574
69. Baker, D.A. *et al.* (2020) Targeting the malaria parasite cGMP-dependent protein kinase to develop new drugs. *Front. Microbiol.* 11, 602803
70. Mandt, R.E.K. *et al.* (2019) *In vitro* selection predicts malaria parasite resistance to dihydroorotate dehydrogenase inhibitors in a mouse infection model. *Sci. Transl. Med.* 11, eaav1636
71. Triglia, T. *et al.* (1998) Allelic exchange at the endogenous genomic locus in *Plasmodium falciparum* proves the role of dihydroorotate synthase in sulfadoxine-resistant malaria. *EMBO J.* 17, 3807–3815
72. Wu, Y. *et al.* (1996) Transformation of *Plasmodium falciparum* malaria parasites by homologous integration of plasmids that confer resistance to pyrimethamine. *Proc. Natl. Acad. Sci. U. S. A.* 93, 1130–1134
73. Sidhu, A.B. *et al.* (2002) Chloroquine resistance in *Plasmodium falciparum* malaria parasites conferred by *pfcr* mutations. *Science* 298, 210–213
74. Reed, M.B. *et al.* (2000) Pgh1 modulates sensitivity and resistance to multiple antimalarials in *Plasmodium falciparum*. *Nature* 403, 906–909
75. Straimer, J. *et al.* (2012) Site-specific genome editing in *Plasmodium falciparum* using engineered zinc-finger nucleases. *Nat. Methods* 9, 993–998
76. Dhingra, S.K. *et al.* (2019) *Plasmodium falciparum* resistance to piperazine driven by PfCRT. *Lancet Infect. Dis.* 19, 1168–1169
77. Kim, J. *et al.* (2019) Structure and drug resistance of the *Plasmodium falciparum* transporter PfCRT. *Nature* 576, 315–320
78. Veiga, M.J. *et al.* (2016) Globally prevalent PfMDR1 mutations modulate *Plasmodium falciparum* susceptibility to artemisinin-based combination therapies. *Nat. Commun.* 7, 11553
79. McNamara, C.W. *et al.* (2013) Targeting *Plasmodium* Pf(4)K to eliminate malaria. *Nature* 504, 248–253
80. Moraes Barros, R.R. *et al.* (2015) Editing the *Plasmodium vivax* genome, using zinc-finger nucleases. *J. Infect. Dis.* 211, 125–129
81. Lee, M.C.S. *et al.* (2019) Cutting back malaria: CRISPR/Cas9 genome editing of *Plasmodium*. *Brief. Funct. Genomics* 18, 281–289
82. Ghorbal, M. *et al.* (2014) Genome editing in the human malaria parasite *Plasmodium falciparum* using the CRISPR-Cas9 system. *Nat. Biotechnol.* 32, 819–821
83. Ng, C.L. *et al.* (2016) CRISPR-Cas9-modified *pfmdr1* protects *Plasmodium falciparum* asexual blood stages and gametocytes against a class of piperazine-containing compounds but potentiates artemisinin-based combination therapy partner drugs. *Mol. Microbiol.* 101, 381–393
84. Uwimana, A. *et al.* (2020) Emergence and clonal expansion of *in vitro* artemisinin-resistant *Plasmodium falciparum* kelch13 R561H mutant parasites in Rwanda. *Nat. Med.* 26, 1602–1608
85. Simwela, N.V. *et al.* (2020) *Plasmodium berghei* K13 mutations mediate *in vivo* artemisinin resistance that is reversed by proteasome inhibition. *mBio* 11, e02312-20
86. Simwela, N.V. *et al.* (2020) Experimentally engineered mutations in a ubiquitin hydrolase, UBP-1, modulate *in vivo* susceptibility to artemisinin and chloroquine in *Plasmodium berghei*. *Antimicrob. Agents Chemother.* 64, e02484-19
87. Henrici, R.C. *et al.* (2020) The *Plasmodium falciparum* artemisinin susceptibility-associated AP-2 Adaptor μ subunit is clathrin independent and essential for schizont maturation. *mBio* 11, e02918-19
88. Ho, C.M. *et al.* (2018) Malaria parasite translocan structure and mechanism of effector export. *Nature* 561, 70–75
89. Birnbaum, J. *et al.* (2017) A genetic system to study *Plasmodium falciparum* protein function. *Nat. Methods* 14, 450–456
90. Birnbaum, J. *et al.* (2020) A Kelch13-defined endocytosis pathway mediates artemisinin resistance in malaria parasites. *Science* 367, 51–59
91. Prommana, P. *et al.* (2013) Inducible knockdown of *Plasmodium* gene expression using the *gImS* ribozyme. *PLoS One* 8, e73783
92. Sleebs, B.E. *et al.* (2014) Inhibition of Plasmeprin V activity demonstrates its essential role in protein export, PfEMP1 display, and survival of malaria parasites. *PLoS Biol.* 12, e1001897
93. Aroonsri, A. *et al.* (2019) Validation of *Plasmodium falciparum* deoxyhypusine synthase as an antimalarial target. *PeerJ* 7, e6713
94. Bridgford, J.L. *et al.* (2018) Artemisinin kills malaria parasites by damaging proteins and inhibiting the proteasome. *Nat. Commun.* 9, 3801
95. Naik, R.S. *et al.* (2003) Glucosamine inhibits inositol acylation of the glycosylphosphatidylinositol anchors in intraerythrocytic *Plasmodium falciparum*. *J. Biol. Chem.* 278, 2036–2042
96. Collins, C.R. *et al.* (2013) Robust inducible Cre recombinase activity in the human malaria parasite *Plasmodium falciparum* enables efficient gene deletion within a single asexual erythrocytic growth cycle. *Mol. Microbiol.* 88, 687–701
97. Das, S. *et al.* (2017) Multiple essential functions of *Plasmodium falciparum* actin-1 during malaria blood-stage development. *BMC Biol.* 15, 70
98. Wilde, M.L. *et al.* (2019) Protein kinase A is essential for invasion of *Plasmodium falciparum* into human erythrocytes. *mBio* 10, e01972-19
99. Tiburcio, M. *et al.* (2019) A novel tool for the generation of conditional knockouts to study gene function across the *Plasmodium falciparum* life cycle. *mBio* 10, e01170-19
100. Koussis, K. *et al.* (2020) Simultaneous multiple allelic replacement in the malaria parasite enables dissection of PKG function. *Life Sci. Alliance* 3, e201900626
101. Jones, M.L. *et al.* (2016) A versatile strategy for rapid conditional genome engineering using *loxP* sites in a small synthetic intron in *Plasmodium falciparum*. *Sci. Rep.* 6, 21800
102. Davies, H. *et al.* (2020) An exported kinase family mediates species-specific erythrocyte remodelling and virulence in human malaria. *Nat. Microbiol.* 5, 848–863
103. Armstrong, C.M. and Goldberg, D.E. (2007) An FKBP destabilization domain modulates protein levels in *Plasmodium falciparum*. *Nat. Methods* 4, 1007–1009
104. Blomqvist, K. *et al.* (2017) Receptor for activated C-kinase 1 (PfRACK1) is required for *Plasmodium falciparum* intraerythrocytic proliferation. *Mol. Biochem. Parasitol.* 211, 62–66
105. Cobb, D.W. *et al.* (2017) The exported chaperone PfHSP70x is dispensable for the *Plasmodium falciparum* intraerythrocytic life cycle. *mSphere* 2, e00363-17
106. Jonscher, E. *et al.* (2019) PVP545 is required for host cell cytosol uptake by malaria blood stage parasites. *Cell Host Microbe* 25, 166–173
107. Ebrahimzadeh, Z. *et al.* (2019) A pan-apicomplexan phosphoinositide-binding protein acts in malarial microneme exocytosis. *EMBO Rep.* 20, e47102
108. Ganesan, S.M. *et al.* (2016) Synthetic RNA-protein modules integrated with native translation mechanisms to control gene expression in malaria parasites. *Nat. Commun.* 7, 10727
109. Rajaram, K. *et al.* (2020) Redesigned TetR-aptamer system to control gene expression in *Plasmodium falciparum*. *mSphere* 5, e00457-20

110. Batista, F.A. *et al.* (2020) New directions in antimalarial target validation. *Expert Opin. Drug Discov.* 15, 189–202
111. Nasamu, A.S. *et al.* (2017) Plasmeepsins IX and X are essential and druggable mediators of malaria parasite egress and invasion. *Science* 358, 518–522
112. Honma, H. *et al.* (2016) Mutation tendency of mutator *Plasmodium berghei* with proofreading-deficient DNA polymerase δ . *Sci. Rep.* 6, 36971
113. Wicht, K.J. *et al.* (2020) Molecular mechanisms of drug resistance in *Plasmodium falciparum* malaria. *Annu. Rev. Microbiol.* 74, 431–454
114. Corey, V.C. *et al.* (2016) A broad analysis of resistance development in the malaria parasite. *Nat. Commun.* 7, 11901
115. Yang, T. *et al.* (2021) MalDA, accelerating malaria drug discovery. *Trends Parasitol.* 21, 493–507
116. Goodman, C.D. *et al.* (2020) A single point mutation in the *Plasmodium falciparum* FtsH1 metalloprotease confers actinonin resistance. *eLife* 9, e58629
117. Yoo, E. *et al.* (2020) The antimalarial natural product salinipostin A identifies essential α/β serine hydrolases involved in lipid metabolism in *P. falciparum* parasites. *Cell Chem. Biol.* 27, 143–157
118. Harding, C.R. *et al.* (2020) Genetic screens reveal a central role for heme metabolism in artemisinin susceptibility. *Nat. Commun.* 11, 4813
119. Rosenberg, A. *et al.* (2019) Evolution of resistance *in vitro* reveals mechanisms of artemisinin activity in *Toxoplasma gondii*. *Proc. Natl. Acad. Sci. U. S. A.* 116, 26881–26891
120. LaMonte, G.M. *et al.* (2020) Pan-active imidazolopiperazine antimalarials target the *Plasmodium falciparum* intracellular secretory pathway. *Nat. Commun.* 11, 1780
121. Walliker, D. *et al.* (1987) Genetic analysis of the human malaria parasite *Plasmodium falciparum*. *Science* 236, 1661–1666
122. Wellem, T.E. *et al.* (1990) Chloroquine resistance not linked to *mdr*-like genes in a *Plasmodium falciparum* cross. *Nature* 345, 253–255
123. Hayton, K. *et al.* (2008) Erythrocyte binding protein PfPRH5 polymorphisms determine species-specific pathways of *Plasmodium falciparum* invasion. *Cell Host Microbe* 4, 40–51
124. Button-Simons, K.A. *et al.* (2019) Surprising variation in the outcome of two malaria genetic crosses using humanized mice: Implications for genetic mapping and malaria biology. *bioRxiv* Published online December 13, 2019. <http://doi.org/10.1101/2019.12.13.871830>